Terahertz homodyne self-mixing and its application to tomographic imaging

Selbsthomodyne Erzeugung & Detektion von Terahertzstrahlung und deren Anwendung in der Tomographie

Zur Erlangung des Grades eines Doktors der Naturwissenschaften (Dr. rer. nat.)
genehmigte Dissertation von M.Sc. Till Mohr aus Frankfurt am Main
April 2018 – Darmstadt – D 17

TECHNISCHE UNIVERSITÄT DARMSTADT

Fachbereich Physik
Institut für Angewandte Physik
Semiconductor Optics Group

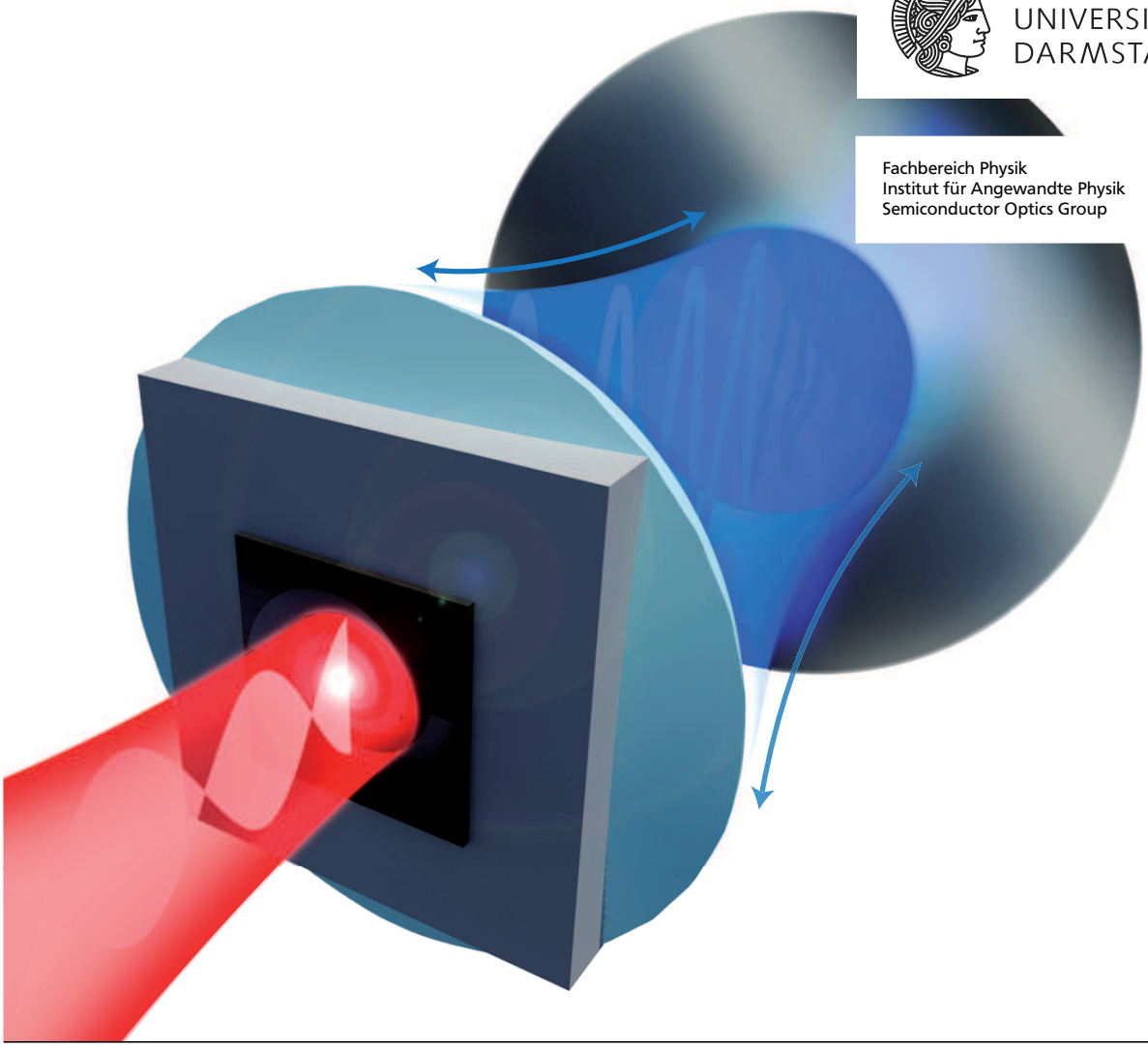

Terahertz homodyne self- mixing and its application to tomographic imaging
Selbsthomodyne Erzeugung & Detektion von Terahertzstrahlung und deren Anwendung in der Tomographie

Genehmigte Dissertation von M.Sc. Till Mohr aus Frankfurt am Main

Version: Dissertation_Mohr_v2.0

Referent:	Prof. Dr. W. Elsäßer
Korreferent:	Prof. Dr. Th. Walther

Tag der Einreichung:	15.11.2017
Tag der Prüfung:	10.01.2018

Darmstadt – D 17

Bitte zitieren Sie dieses Dokument als:

URN: urn:nbn:de:tuda-tuprints-73626
URL: tuprints.ulb.tu-darmstadt.de/id/eprint/7362

Dieses Dokument wird bereitgestellt von tuprints,
E-Publishing-Service der TU Darmstadt

tuprints.ulb.tu-darmstadt.de
tuprints@ulb.tu-darmstadt.de

Die Veröffentlichung steht unter folgender Creative Commons Lizenz:
Namensnennung – Keine kommerzielle Nutzung – Keine Bearbeitung 4.0 International

creativecommons.org/licenses/by-nc-nd/4.0/

Institut für Angewandte Physik
Technische Universität Darmstadt

Terahertz homodyne self- mixing and its application to tomographic imaging

Vom Fachbereich Physik
der Technischen Universität Darmstadt

zur Erlangung des Grades
eines Doktors der Naturwissenschaften
(Dr. rer. nat.)

genehmigte
Dissertation

von
M.Sc. Till Mohr
aus Frankfurt am Main

Darmstadt 2018
D 17

Table of contents

1. Introduction

In the second half of the 19th century J. C. Maxwell developed the famous Maxwell equations [1], which are the fundamental equations to describe phenomena of the electromagnetism. From these equations the existence of electromagnetic radiation is theoretically predicted and shortly thereafter H. Hertz succeeded in the first experimental demonstration of electromagnetic waves with a frequency of approximately 0.5 GHz. With these findings, the foundations of the research field of electromagnetic waves were set. With the development of many components like transmitter antennas, polarizers, and point-contact detectors J. C. Bose made a great contribution to this research field [2]. Thus, J. C. Bose was able to increase the frequency of the electromagnetic waves to frequencies up to 60 GHz, which correspond to a wavelength of 5 mm [2]. In the infrared region of the electromagnetic spectra H. Rubens and O. Baeyer [3] used thermal incoherent light sources like the quartz mercury lamp to extend the spectrum towards longer wavelengths. In order to make precise measurements of the spectra in the infrared wavelength range, H. Rubens and E. F. Nichols developed spectrometers which enable the observation of wavelengths beyond 50 μm using the reststrahlen effect of dielectric materials [4]. These very accurate spectra provided a deep insight into the radiation emitted from a blackbody, which finally led to the radiation law formulated by M. Planck [5]. The spectral gap between electrically and optically generated radiation provoked H. Rubens and E. F. Nichols to the following statement [6]:

"*Since we have become accustomed to think of waves of electrical energy and light waves as forming component parts of a common spectrum, the attempt has often been made to extend our knowledge over the wide region that separates the two phenomena.*"

This quotation can be regarded as the first remark of a gap in the electromagnetic spectrum between microwaves generated by electronic sources and infrared radiation produced by optical technologies. The electromagnetic spectrum spanning from the radio waves to the x-rays is depicted in Fig. 1.1. In the center between the microwaves and infrared region the terahertz domain is located. This domain comprises the frequencies from 0.1 THz to 10 THz and corresponds to the gap mentioned by H. Rubens and E. F. Nichols.

In order to approach the terahertz domain from the long wavelengths in the microwave regime, new electric devices like the resonant tunnel diode [8] and frequency multiplication and mixing [9] are used. One challenge of these electrical approaches is the decrease in output power with higher frequencies [10]. The cut-off frequency f_c of electrical devices is smaller than the ratio between the velocity v of the charge carriers inside the material caused by the acceleration of an electric field and the length l, which the charge carriers have to travel inside the device. This limitation is found, because the phase of the generated radiation has to advance only by a small fraction while an electron travels the length l. Since the velocity of charge carriers in semiconductors is limited, the devices have to shrink to very small dimensions to reach the terahertz frequency domain. However, due to the small size of the devices the applied electric field has to reach the maximum possible breakdown field E_b of the material. This is important to achieve a high voltage V, which is needed to accelerate the charge carriers to their maximum possible velocity in

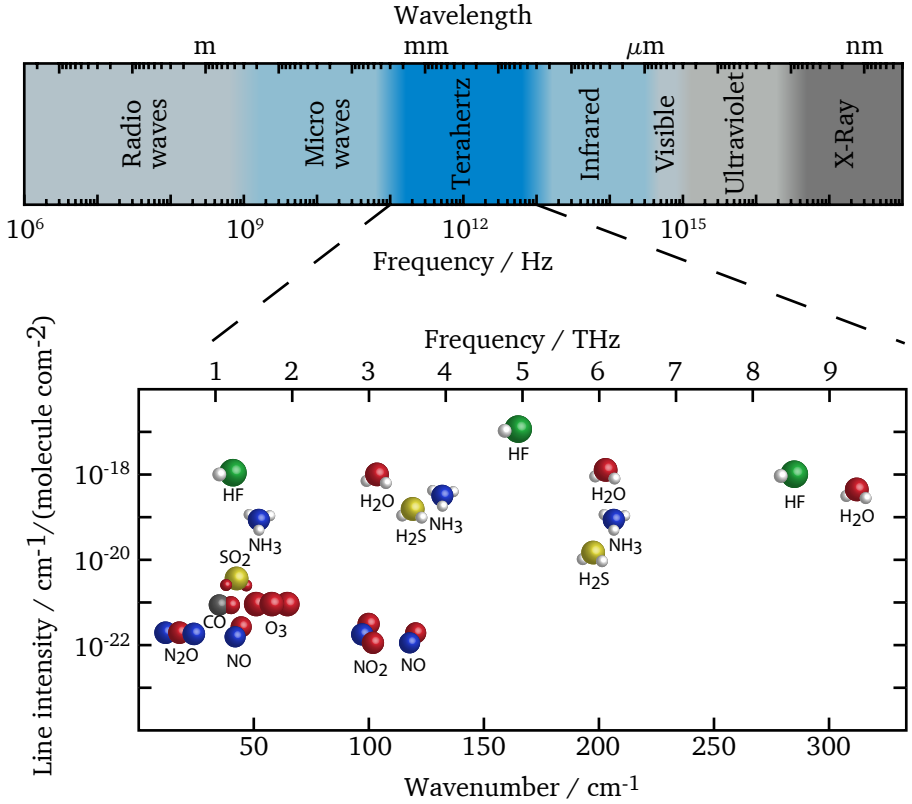

Figure 1.1.: (top) Part of the electromagnetic spectrum ranging from radio waves to x-rays. Between the microwaves and infrared region the so-called terahertz gap is located within a frequency span of 0.1 to 10 THz. (bottom) Absorption line intensities of prominent gas molecules used for fingerprint spectroscopy taken from the HITRAN database [7] in the terahertz spectrum.

order to gain the maximum output power. The output power P of such an electric device is given by the fraction of the squared voltage and the load resistance R [10]

$$P = \frac{V^2}{R} = \frac{1}{R}(E_b l)^2 = \frac{1}{R}\left(\frac{v E_b}{f_c}\right)^2 \sim \frac{1}{{f_c}^2}. \tag{1.1}$$

It can be seen that the output power is decreasing rapidly with the square of the frequency, and therefore is limiting the maximum achievable frequency of electric devices.

On the other side of the terahertz gap the mercury arc lamp as used by H. Rubens and others was the favorable source for infrared and terahertz radiation for a long time. The first experimental demonstration of the laser in 1960 by T. H. Maiman using a ruby crystal to produce light at 694 nm [11] has been the most significant development of optical sources in the 20^{th} century. This key technology allowed also for the further development of high power sources in the terahertz frequency domain. In 1964 A. Crocker et al. developed a water vapor laser emitting at various lines from 23 μm to 79 μm and reaching peak

output powers of up to 15 W [12]. Beginning with these first findings, a plurality of molecular-gas [13] and solid-state terahertz lasers [14] have been realized. The latest development is the quantum cascade laser (QCL), which was theoretically proposed by R. F. Kazarinov and R. A. Suris [15] and was first experimentally realized by J. Faist and F. Capasso in the mid-infrared wavelength region [16]. Shortly after this first demonstration of a QCL at the end of the 20^{th} century, the concept was extended to the terahertz frequency domain [17]. In addition to this direct generation of terahertz radiation, a promising technique is the conversion of near-infrared (NIR) femtosecond pulses to short terahertz pulses. This can be realized by employing photoconductive antennas (PCA) [18] or nonlinear crystals [19], which transfer the NIR pulse into the terahertz frequency domain by different physical processes. The generated terahertz pulses are spectrally broadband and can extend in a spectral range of several terahertz. In combination with a coherent detection scheme, both amplitude and phase information of the terahertz pulse can be measured. When a sample object is placed into the terahertz beam path, this terahertz time-domain spectroscopy method can yield the complex refractive index of the sample object [20]. Instead of NIR femtosecond pulses, which generate pulsed terahertz radiation, two continuous wave (CW) single mode lasers with a frequency detuning to each other in the THz range can be used to generate narrowband CW terahertz radiation. For this purpose, the electric fields of the two lasers are superimposed and generate an optical beat signal. This NIR beat signal is then converted into single frequency terahertz radiation by photomixers [21] or crystals with a non-linear susceptibility [22].

Although only limited methods for the generation and detection of the terahertz radiation were available, first applications were developed at the beginning of the 20^{th} century. In 1935 R. B. Barnes mapped the absorption of atmospheric water vapor between the wavelength of 38 μm and 170 μm [23]. In succession, discoveries were made that many more gas molecules possess a major spectral fingerprint in the terahertz domain, which can be used to identify these molecules. The vibrational and rotational states of the gas molecules cause spectral absorption features from the mid-infrared to the terahertz domain and have been therefore explored by many scientists. These observations led to databases and are used as spectral fingerprint lookup tables. One of these databases is the high-resolution transmission molecular absorption (HITRAN) database [7]. The bottom graph of Fig. 1.1 shows some strong characteristic absorption lines of a plurality of gas molecules in the region from 0.1 to 10 THz taken from the HITRAN database [7]. Not only gas molecules, but also many substances that are of specific interest for biological, medical or security applications possess characteristic spectral fingerprints in the terahertz domain. Thus, terahertz imaging can not only provide an image of an object composed of different substances, each with different absorption properties, but using fingerprint spectroscopy these substances can additionally be identified. This identification is a major advantage of using terahertz radiation in imaging applications and has been demonstrated for different substances like glucose and lactose embedded in plastic containers [24, 25]. Further, terahertz fingerprint spectroscopy provides a non-destructive method to detect illegal contraband, such as drugs and explosives. The transparency of materials like e.g. paper, cloth and plastics at terahertz frequencies is used to look through these materials and identify illegal drugs [26] and explosives [27, 28]. Even letters written on different overlapping sheets of paper in a closed envelope have been revealed using terahertz imaging [28]. Besides the spectral fingerprints of many molecules, terahertz radiation can be classified as non-ionizing [29]. The energy of terahertz photons is several orders of magnitude below the energy level required to ionize biological molecules. This is very advantageous, because non-ionizing and ionizing (e.g. x-rays) radiation generate vastly different effects in biological tissue. The ionization of water and biomolecules generate highly reactive free radicals. They can be very harmful to biological

structures by causing secondary or indirect damage to other biomolecules. The irradiation with terahertz radiation causes heating of the tissue and this, for example, can result in structural protein damage and cell death. However, the biocompatible amount of deposited energy and the explicit effects depend on the biological material under irradiation. The non-ionizing nature of terahertz radiation is of notably use for medical applications such as the differentiation of basal cell carcinoma, the most common form of skin cancer, from normal tissue [30]. The diseased tissue shows an increased absorption in the terahertz spectral domain compared to healthy tissue. This is a result of increased water content in the diseased tissue or a change in the vibrational modes of the water molecules. The sensitivity of terahertz radiation to measure the water content is also used to perform non-destructive in-vivo studies of the water content of leaves [31, 32]. These studies revealed that plants suffering from water deficit show different water losses on long timescales depending on the used substrate. This is of particular interest for the agricultural industry [33]. The water content of paper is also of special interest during the drying process in its production, because properties of the paper such as shrinkage, curling and strength are influenced by its drying dynamics [34]. Hence, terahertz radiation offers remote sensing capability with superior spatial resolution compared to microwaves, but is still insensitive to scattering processes in the paper due to of its long wavelength [34]. The long wavelength of the terahertz radiation allows the detection of rather large defects like cracks, bubbles and inhomogeneities using interferometric techniques in material quality observations [35, 36]. In order to realize an insight into a sample, rather than imaging a projection, graphic imaging techniques can be applied. In this way, defects, foreign objects or inhomogeneities can be exactly located inside the sample. This for example is useful in security applications and a plurality of industrial processes [37]. As previously discussed the photon energy of terahertz radiation is non-ionizing and therefore lower safety requirements exist for the implementation of terahertz systems compared to x-rays. This eases the implementation of such systems, which is one reason why tomographic terahertz imaging can become an alternative to x-ray tomography in several fields of application.

This introduction pursues the same structural guideline as this thesis. The generation and detection of terahertz radiation is in the center of discussion, using the photomixing technique as introduced by K. A. McIntosh et al. [21]. This technique stands out by its excellent signal-to-noise ratio (SNR), room temperature operation and broad frequency tunability. Conventionally it relies on two individual PCAs, one for the generation and one for the detection of the terahertz radiation. These two PCAs are unified to a single PCA by a compact homodyne self-mixing (HSM) terahertz spectroscopy concept developed in the first part of this thesis. The developed method combines both CW-terahertz radiation generation and phase-sensitive detection in a single PCA. This eases measurements in reflection configuration and results in a significantly reduced complexity and cost of the terahertz spectroscopy set-up. Subsequently, two-dimensional tomographic terahertz imaging is investigated, which revealed specific challenges for the image reconstruction in the terahertz frequency domain. These challenges include optical effects like refraction, reflection as well as diffraction. The experiments are therefore accompanied by ray tracing studies and a specially developed model, which considers all of these optical effects by a hybrid ansatz using ray tracing and scalar diffraction theory. This model enables the calculation of projections and allows the formulation of an optimization problem and thus offers an approach for tomographic reconstruction using the developed model.

In detail, this thesis is structured as follows.

Chapter 2 gives a state-of-the-art overview of different techniques for the generation and detection of terahertz radiation. The different techniques are compared with each other regarding various aspects such as output power, frequency tuneability, and operation temperature. Subsequently, a more detailed description of the photomixing method is given. At last, the fundamentals of tomographic imaging and the recently developed single-pixel imaging technique are discussed.

In Chapter 3 the developed laser systems, necessary for the photomixing approach, are presented and characterized. Two external cavity diode lasers (ECDL) using an interference filter as frequency selective element and one ECDL using a grating are investigated. Important properties of the laser systems concerning the terahertz experiments are the relative intensity noise (RIN), the spectral linewidth, the frequency tunability and the long-term stability. Under these considerations, both ECDL configurations are compared and advantages and disadvantages of these systems are discussed.

Chapter 4 presents the basic characterization of different photomixer devices. The devices possess different geometries and are examined by their characteristic output power and frequency response. The selection of photomixers include one commercial available low-temperature (LT) grown Gallium Arsenide (GaAs) photomixer provided by TOPTICA Photonics AG and two self-packaged photomixers, with LT-GaAs chips provided by M. Mikulics from the Forschungszentrum Jülich.

Chapter 5 discusses the first experimental realization of the HSM method using a revolving chopper wheel to back reflect the terahertz radiation towards the photomixer. Transmission experiments involving Teflon samples of different thickness demonstrate the phase-sensitive detection of the method. In addition, a first estimation of the SNR is given by the contrast of the signal amplitude with the noise baseline measured with an electrical spectrum analyzer (ESA).

In Chapter 6 the HSM method is applied to two-dimensional tomographic terahertz imaging. A hollow-core Teflon cylinder filled with α-Lactose monohydrate powder is studied at two individual terahertz frequencies, one far away and one at a specific absorption line of the powder. The influence of refraction related to the HSM set-up is accompanied with ray tracing simulations and is discussed by means of the measured 1D projections. Following, different imaging techniques are investigated theoretically by ray tracing simulations. These techniques involve imaging using raster scanning of the object with a small and large area detector, a multi-pixel detector and the single-pixel imaging approach. Motivated by the ray tracing result, the single-pixel imaging approach is experimentally realized to achieve two-dimensional tomographic imaging. Furthermore, a model is developed, which considers refraction and diffraction effects by a hybrid ansatz using ray-tracing and scalar diffraction theory. This model enables the calculation of projections and allows the formulation of an optimization problem offering an approach for tomographic image reconstruction.

Finally, Chapter 7 closes the thesis with a short summary highlighting the achieved results and an outlook.

2. Fundamentals

This chapter can be divided into three parts, dealing with the fundamentals of terahertz generation and detection in section 2.1, a more detailed look onto the photomixing approach in section 2.2 and finally terahertz imaging in section 2.3.

2.1. Generation and detection of terahertz radiation

As already stated in the introduction, there exists a variety of possible methods for the generation and detection of terahertz radiation. This section discusses some of the most common methods and gives a state-of-the-art overview on the generation of terahertz radiation. At the end of this section a comparison of these terahertz generation methods is given with respect to important properties like e.g operation temperature, spectral tuning and output power.

Generally, methods for the generation of terahertz radiation can be divided into two groups. The first group produces short pulses of terahertz radiation, which are spectrally broadband and can easily span several THz in the frequency domain. The second group generates narrow band CW terahertz radiation, concentrating the total optical power in a single frequency.

Already shortly after the realization of the first laser, molecular gas lasers emitting CW terahertz radiation were introduced [12]. Conceptually these lasers are very similar to gas lasers operating in the visible spectral region, but make use of transitions between rotational states of the gas molecules. Figure 2.1(a) schematically shows the concept of an optically pumped far-infrared gas laser [38]. The active medium commonly consists of a molecular gas with a permanent dipole moment like CH_3OH, CH_3F or NH_3 [13]. This constant dipole moment is necessary because the transitions between rotational states must couple directly to the electromagnetic radiation. The active medium is placed in a resonator and is optically pumped from the thermally populated bottom vibrational state to the first excited vibrational state by a CO_2 laser. This induces a population inversion between two rotational states and as a result the exited molecules undergo a transition to a lower rotational state by emitting terahertz radiation. By changing the molecular gas species or the investigated rotational transitions a plurality of different laser devices each operating at a specific terahertz frequency between 0.2 and 8 THz [39] with output powers in the W regime [13] are realized. Even though these lasers cover nearly the whole terahertz frequency domain, one single laser is limited to a specific molecular transition, such that no tuning of the device is possible. Furthermore, these devices are bulky, require a lot of power for their operation and the optical power conversion from pump light to terahertz radiation is quite inefficient.

Another laser source capable to generate CW terahertz radiation is the so-called P-Type Germanium laser. This kind of device is an all-solid-state laser and relies on the emission of terahertz radiation from stimulated transitions between different Landau levels. The Landau levels are discrete energy levels

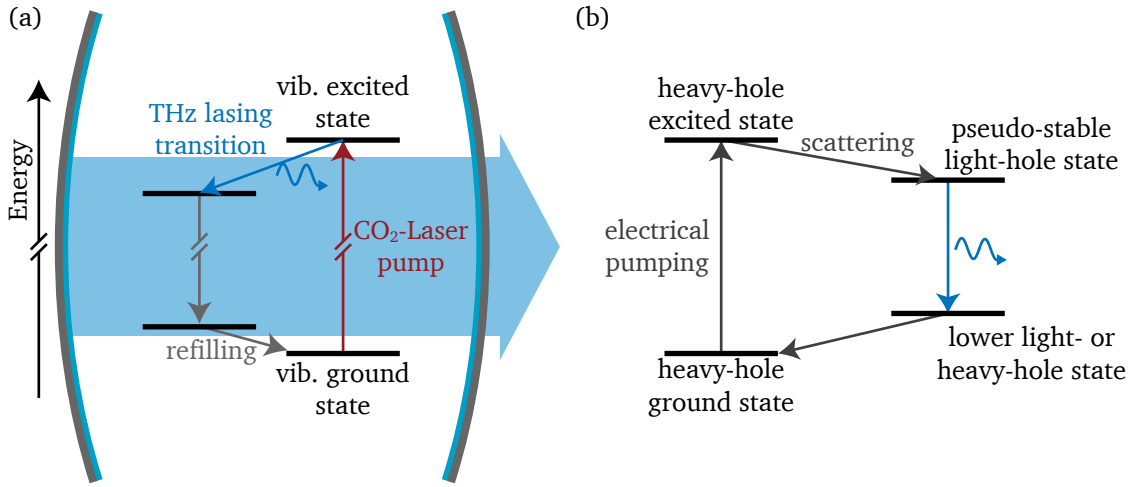

Figure 2.1.: (a) Schematic of a far-infrared gas laser optically pumped by a CO_2 laser. The active medium commonly is a molecular gas with a permanent dipole moment like CH_3OH, CH_3F or NH_3. (b) Concept of a P-Type Germanium Laser. This laser is based on stimulated emission between different Landau levels. The population inversion is generated between a pseudo-stable level and a lower light- or heavy-hole level.

generated by an external magnetic field surrounding the doped germanium. Additional an electric field perpendicular to the magnet field is applied, which accelerates the heavy holes of the germanium to an exited state. At the same time this electric field ensures the generation of so-called pseudo-stable Landau levels in the light-hole band. Some of the accelerated heavy holes scatter into this pseudo-stable level, where a population inversion between the pseudo-stable level and a lower-light- or heavy-hole level is generated as depicted in Fig. 2.1(b) [40]. Stimulated transitions between the pseudo-stable level and the lower-light- or heavy-hole level constitute the lasing process of the P-Type Germanium laser. The emitted terahertz radiation can be frequency-tuned from 1 to 4 THz by a variation of the electric- or magnet-field [41]. Achieved output powers range from tens of mW up to 10 W under pulsed operation conditions, but need strong magnetic- and electric-fields [41]. Also, a proper operation of these laser devices requires cryogenic cooling below 80K [41].

The latest laser operating at terahertz frequencies is the QCL, which was first experimentally realized by R. Köhler et al. [17]. The first demonstration of the QCL already operated at a temperature of up to 50 K and emits a power of 2 mW at 4.4 THz [17]. Most semiconductor lasers rely on an optical transition between the conduction band and the valence band. For these kind of lasers, the energy gap between the conduction and valence band determines its emission wavelength. In order to produce lasers with different emission wavelengths, a multitude of material combinations are investigated for "band-gap engineering", as e.g. GaAs for NIR laser diodes (LD) [42] or GaN for blue LDs [43]. In contrast, QCLs use intersubband transitions, which are carefully engineered by alternating layers of different materials [44]. These alternating layers form quantum wells of discrete energy levels, while the energy values of the levels are given by the thickness of the layers. In that way, the energy of a transition between different energy levels does not depend on the chosen material, rather it depends on the layer thickness grown for

example with molecular beam epitaxy. Thereby, different QCL devices are developed to operate in a large area of different spectral regions ranging from the mid-infrared at 2.3 μm [45] to the terahertz domain at 360 μm [46]. By successive repetition of the quantum wells, separated by an injector, a cascade of quantum wells is created, which are energetically aligned in space by applying a bias voltage. This is illustrated in Fig. 2.2(a) [47]. The electron undergoes an optical transition from the energy level 2 to the level 1 and thereby emits a terahertz photon. Subsequently, the electron is recycled by the injector to the next quantum well, where it undergoes an additional transition. A typical QCL can consist of $30-40$ of these emitting stages, which in turn are built up by a multitude of nm thick layers of different semiconductors [44]. Essentially two main challenges exist in the development of new QCL terahertz sources [40]:

- The energy of a photon with a freqeuncy of 1 THz is sufficiently low that it is difficult to achieve the required population inversion at high temperatures.
- On the one hand, the induced emission strongly depends on the radiation intensity inside the gain medium. On the other hand it is difficult to confine the laser modes to a small volume as the gain medium because of the long wavelength of the terahertz radiation.

Nevertheless, terahertz emission of a QCL near 200 K has been achieved under pulsed operation conditions [48] and output powers above 1 W (pulsed) [49] and 140 mW (CW) [50] have been demonstrated. Spectral tuning in the order of 165 GHz has been reported without [51] and with a grating in an external cavity configuration [52]. Another promising approach involving two mid-infrared QCLs is the generation of terahertz radiation based on the direct intracavity difference-frequency generation (DFG) [53]. This technique offers room temperature generation in a single compact device combined with a broad frequency tunability between 1.2 and 5.9 THz [54].

Coming from the microwave region of the electromagnetic spectrum, electric sources are continuously approaching towards the terahertz domain. One promising device is the resonant-tunneling diode (RTD), which reaches frequencies up to 1.5 THz [55, 56] and output powers of 610 μW at 0.6 THz [57]. An RTD consists of two barriers forming a quantum well as depicted in Fig. 2.2(b) I. Without and with low bias voltages no current can flow through the barriers, however by applying a sufficiently high bias voltage the energy bands get tilted strong enough leading to an increasing current flow. This is schematically shown in Fig. 2.2(b) II. If the bias voltage is increased further on, suddenly no current can flow through the barriers because the energy states of the quantum well shift below the conduction-band bottom at the emitter side and no more elastic tunneling is possible [58]. The described Voltage-Current behavior of such an RTD is depicted in Fig. 2.2(b) III for an ideal (red) and real (green dashed) device. This curve shows that under specific biasing conditions the RTD possess a negative-differential-conductance (NDC). By connecting such an NDC device (R_{NDC}) in parallel to the load resistor R_L of a resonant circuit (LC-circuit) as depicted in Fig. 2.2(b) IV, the total resistance of the LC-circuit can become negative. Consequently, a small oscillation inside the LC-circuit gets amplified until the damping of the LC-circuit and the amplification of the NDC are equal and a steady-state oscillation occurs. Due to this oscillating current radiation at the frequency of the oscillation is emitted by the LC-circuit. Usually the LC-circuit is represented by a hollow core resonator or a planar resonant antenna [58]. In order to achieve high oscillation frequencies, the size of the whole circuit has to be in the same order as the emitted wavelength.

Another method of generating terahertz radiation entirely employing electronic technologies is the fre-

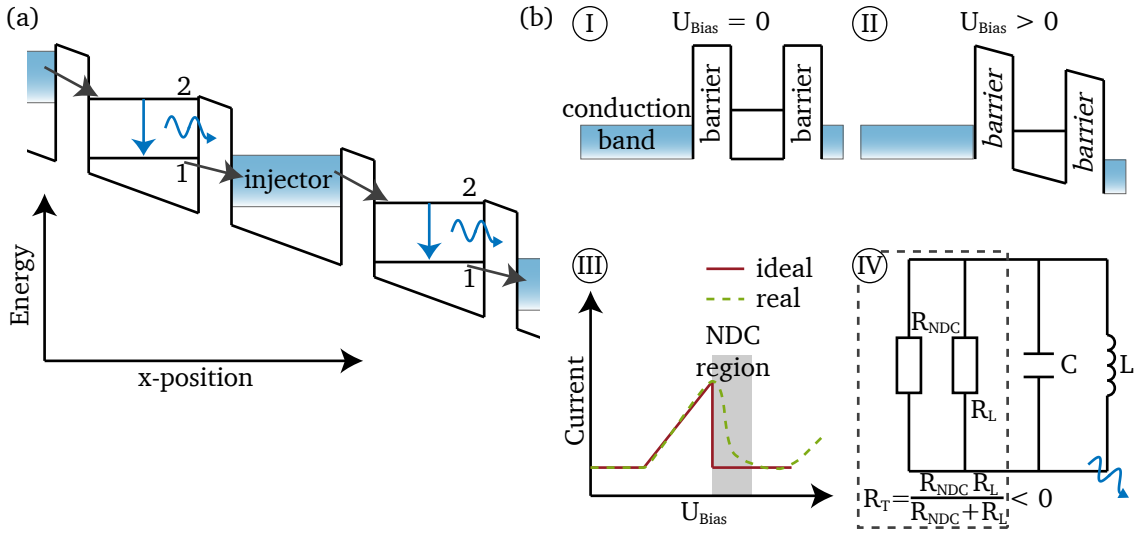

Figure 2.2.: (a) Two cascaded quantum wells, separated by an injector, which are aligned by an applied bias voltage. Lasing occurs by a transition of an electron between the energy levels 2 and 1. After that the electron is recycled by the injector to the adjacent quantum well, where it undergoes an subsequent transition. (b) Operation principle of an RTD. (I) An RTD consists of two barriers forming a quantum well, which prevents a current flow in the absence of a sufficiently high bias voltage. (II) By applying a sufficient high bias voltage the energy bands get tilted and a current can flow until a cutoff voltage at which suddenly no more current can flow. (III) Voltage-Current behavior of an RTD for an ideal (red) and real (green dashed) device. (IV) By connecting an RTD to an LC-circuit, the total resistance of the circuit can become negative. A small oscillation inside the LC-circuit gets amplified until the damping of the LC-circuit and the amplification of the NDC are equal and a steady-state oscillation occurs.

quency upconversion by multiplier chains. This technique uses nonlinear devices like Schottky diodes to generate higher harmonics of the input signal [59]. State-of-the-art microwave technologies like Gunn or IMPATT oscillators are capable to generate radiation with frequencies up to approximately 150 GHz and with output powers of several hundreds of mW [60]. By using these oscillators as source with a frequency upconversion afterwards an output power of 100 mW at 250 GHz is achieved [58]. But with increasing frequency, the output power decreases fast and for example reaches only 50 μW at 2.2 THz [58].

What the upconversion is for the electronic technologies is the DFG and optical rectification for the field of optical technologies. These methods use a nonlinear crystal to downconvert the frequency of radiation, which initially is mostly located in the near- [61] or mid-infrared [53] spectral region. If such a nonlinear crystal is exposed to a strong electromagnetic field a large displacement of the electrons from equilibrium is induced and second order nonlinear effects become apparent. The non-symmetric potential energy function of the nonlinear crystal, as schematically depicted in Fig. 2.3(a) [40], induces a non-symmetric motion of the electrons under the influence of a strong electromagnetic field as shown in Fig. 2.3(b). This motion can be separated into a linear part (dashed, blue), the second harmonic process (dash-dotted

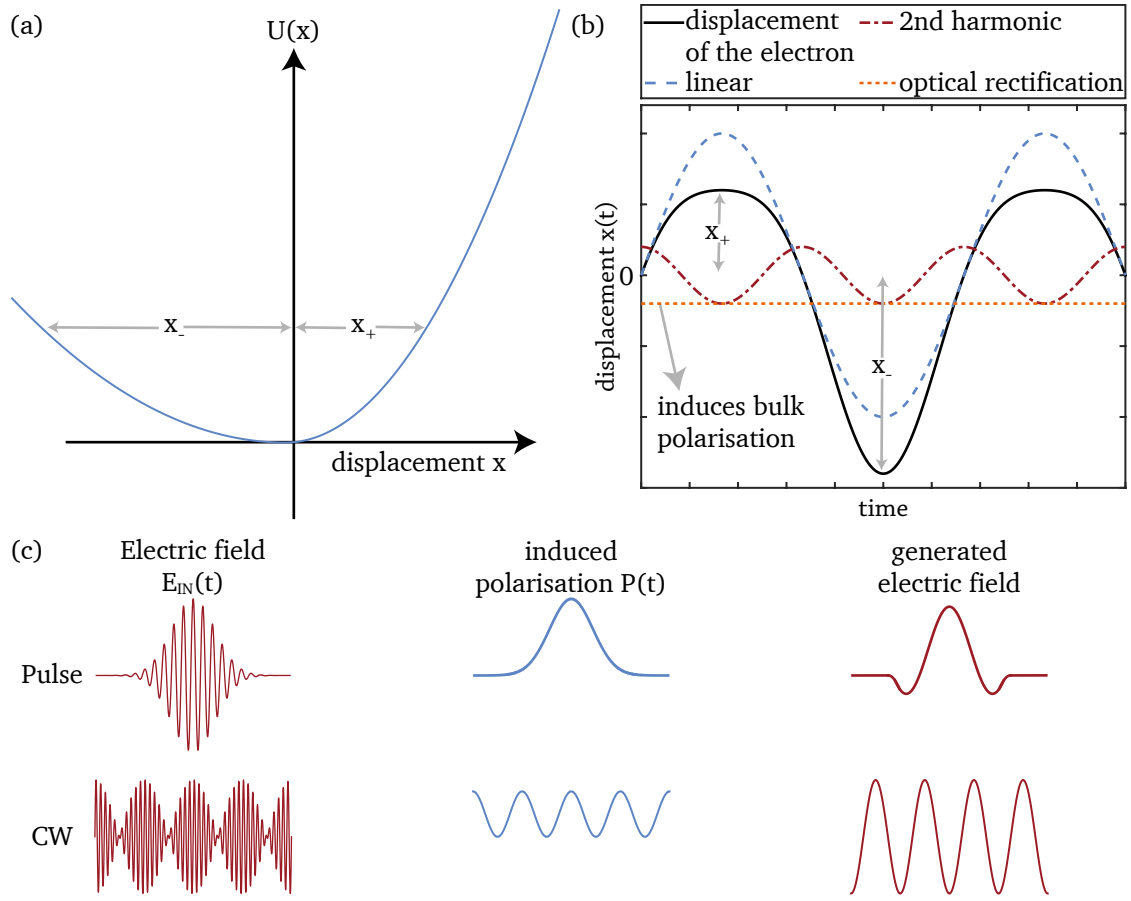

Figure 2.3.: (a) The non-symmetric potential energy function of a nonlinear crystal, induces (b) a non-symmetric motion of the electrons under the influence of a strong electromagnetic field. (c) Due to an electric field in the shape of a Gaussian pulse or an optical beat signal, the optical rectification gives rise to a time dependent polarization in the nonlinear crystal and this time varying polarization generates an electromagnetic field.

red), which oscillates with the double frequency of the original electromagnet field and a constant part representing the optical rectification process (dotted, orange). The optical rectification gives rise to a constant polarization in the nonlinear crystal. If the so far as constant considered incident electromagnetic field is replaced by a temporal Gaussian pulse (Fig. 2.3(c), top) or an optical beat signal (Fig. 2.3(c), bottom) the induced polarization gets time-dependent and is given by the envelope of the optical pulse or beat signal. This temporally varying polarization in turn generates an electromagnetic field. In case of an incident optical pulse, the generated radiation is a short electromagnetic pulse with a spectral bandwidth corresponding to the inverse of the optical pulse duration. For the generation of CW radiation, the incident electromagnetic wave has to be realized by an optical beat signal. Here, the polarization undergoes a sinusoidal modulation at the difference frequency of the optical beat signal and therefore generates radiation at this difference frequency. Commonly used nonlinear crystals for the generation of terahertz radiation are CdSe, GaSe, $LiNbO_3$, GaAs and ZnTe [62, 63]. One major challenge in the generation of

terahertz radiation by nonlinear effects is the difference in the refractive indices of the nonlinear crystal at the frequency of the incident electromagnetic field and the terahertz radiation. In a non-dispersive media both the incident radiation and terahertz radiation would travel at the same speed through the nonlinear crystal. Under this circumstance, the amplitude of the terahertz wave is continuously growing while traveling through the nonlinear crystal because of constructive interference with terahertz radiation generated continuously by the induced polarization. In reality, the dispersion of the crystal produces a phase difference between the incident electromagnetic field and the terahertz radiation while traveling through the crystal. Hence, the terahertz radiation interferes constructively and destructively with the continuously generated radiation and averages to zero when traveling over a long distance through the crystal. The phase matching conditions are met by using thin crystals [64] or by appropriate tilting of the crystal [65] and making use of the birefringence of the crystals. Phase matching can also be achieved by a periodic sequence of differently oriented crystals [66]. Another process, which limits the spectral bandwidth of this technique is the absorption of terahertz radiation at low and high terahertz frequencies by the nonlinear crystal. Nevertheless, terahertz radiation over a huge frequency span of several terahertz has been generated with average output powers ranging from the μW to the mW [67–69].

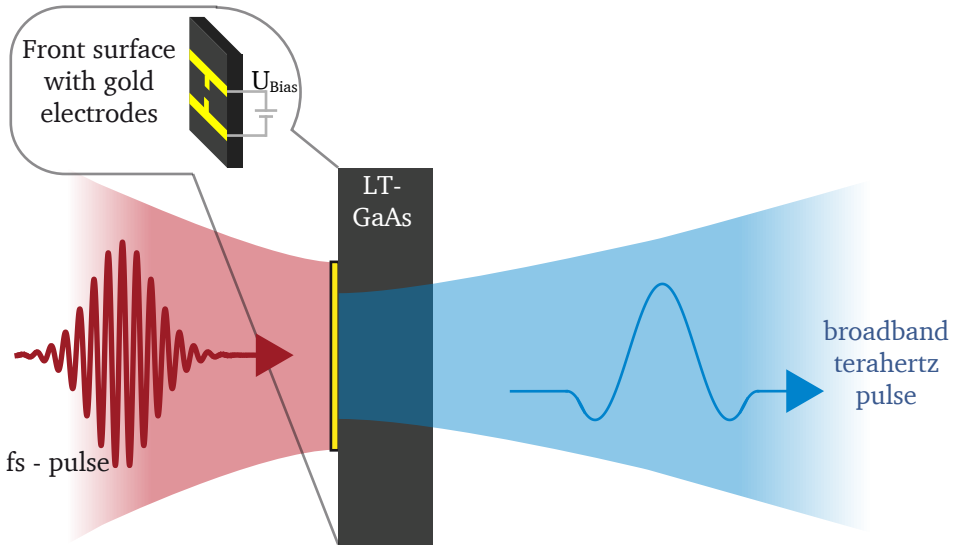

Figure 2.4.: Terahertz generation using a PCA. An optical fs-pulse is irradiating the gap between two electrodes (inset) and generates there electron-hole pairs in the semiconductor. By a bias voltage these electron-hole pairs get accelerated and form a short current pulse, which generates a short spectrally broadband electromagnetic pulse.

A technique closely related to optical rectification by short optical pulses is the generation of terahertz radiation using a PCA. The necessary PCA consists of an antenna and two metal electrodes deposited on a semiconductor substrate as e.g. LT-GaAs. Commonly, the electrodes consist of gold and are separated by a small semiconductor gap of several micrometres length as schematically depicted in the inset of Fig. 2.4. By applying a bias voltage to the electrodes only a small current, the so-called dark current, flows across

the semiconductor as its resistance is in the order of 1 MΩ [70]. If the gap is now illuminated by radiation with an energy higher than the band-gap of the semiconductor, electron-hole pairs are generated inside the semiconductor. These charge carriers are accelerated by the bias voltage and contribute to the current flow. After turning off the radiation recombination of the electron-hole pairs leads to a current drop back to the dark current. In that way, a fast optical-switch is realized. In order to generate terahertz radiation from such a switch, the PCA is illuminated by fs-pulses, which generate electron-hole pairs on short time-scales. After the fs-pulse excitation the electron-hole pairs recombine on picosecond time-scales. This consequently short current pulse generates a short spectrally broadband electromagnetic terahertz pulse. The leading edge of the electromagnetic pulse is mostly governed by the duration of the fs-pulse, whereas the tail is determined by the recombination time of the semiconductor. To obtain short electromagnetic pulses, and therefore terahertz pulses with a high bandwidth, both short fs-pulses and fast recombination times are important. The most commonly used substrates for PCAs are LT-GaAs, radiation-damaged silicon-on-sapphire, semi-insulating GaAs, indium phosphide and amorphous silicon [47]. Besides fast recombination times, the electric field breakdown voltage of the semiconductor must be sufficiently high, because the output power of the terahertz pulse depends quadratically on the bias voltage. State-of-the-art PCA systems achieve high average terahertz output powers of 3.8 mW [71], a large spectral bandwidth of 0.3 to 20 THz [72] and high optical-to-terahertz conversion efficiencies of up to 7.5% [73].

The photomixing technique is based on a similar concept as the previously introduced generation of pulsed terahertz radiation using a PCA [74]. But instead of broadband terahertz pulses, single-frequency CW radiation is generated. The technique is capable to generate moderate output powers ranging from several μW to 0.8 mW at 1 THz [75]. Further, the generated radiation offers a narrow linewidth down to the Hz regime [76] and is suitable for high resolution spectroscopy with tuning ranges of up to 3.8 THz [77, 78]. Last but not least, because of its compact set-up and room temperature operation, this method is chosen as a source for the terahertz radiation generation in this thesis and will be introduced in detail in section 2.2.

Table 2.1 offers a summary of the introduced techniques used to generate terahertz radiation. Important properties like operation temperature, spectral tuning and output power are summarized. Apart from gas lasers, techniques emitting high output powers at frequencies above 1 THz are almost always in need of cryogenic cooling. A drawback of terahertz gas lasers is the inability of frequency tuning, because the lasing process is based on specific transitions of different rotational states. Electronic sources are capable to generate high output powers in the microwave regime, but with increasing frequency the output power decreases fast and frequencies above 2 THz are difficult to achieve. Techniques completely covering the terahertz domain involve PCAs and pulsed optical rectification. These techniques produce spectrally broadband terahertz pulses spanning the whole terahertz domain and optical rectification can even extend into the mid-infrared spectral region. A high spectral resolution with moderate output powers and large frequency tuneability is achieved by DFG and photomixing. Additionally to the discussed advantages in the terahertz generation, optical rectification, DFG, photomixing and PCAs all incorporate the possibility for phase sensitive detection schemes offering a good dynamic range and a high SNR as will be discussed in the following.

The scheme for sensing short terahertz pulses using a PCA is similar to the generation process involving a PCA as shown in Fig. 2.4. In contrast to the generation scheme, the PCA used for detection is not biased

Table 2.1.: Comparison of different techniques used to generate terahertz radiation (RT = room temperature, SF = single frequency, MM = multi frequency, BB = broadband).

	Operation mode	Spectral coverage (THz)	Spectral tuning	Operation temperature	Average output power
Photoconductive antenna	BB	$0.3-20$ [72]	x	RT	μW–mW [71]
Photomixing	SF	up to 5 [77, 79]	whole spectral coverage	RT	μW–mW [75]
Terahertz gas lasers	SF	$0.2-8$ [39]	x	RT	several Watt [13]
P-Type Germanium lasers	SF	$1-4$ [41]	whole spectral coverage	< 80 K [41]	mW to 10 W [41]
QCL	SF / MF	$0.68-5$ [80]	165 GHz [51]	< 200 K (pulsed) [48]	1 W (pulsed) [49] 140 mW (CW) [50]
Resonant-tunneling diode	SF	up to 1.5 [55]	x	RT	610 μW @ 0.6 THz [57]
Frequency multiplication	FW	up to 2.2 [58]	$\sim$ 1 THz [58]	RT	100 mW @ 250 GHz [58] 50 μW @ 2.2 THz[58]
Optical rectification	BB	up to 41 [81]	x	RT	μW–mW [67–69]
DFG	SF	$0.02-20$ [82]	whole spectral coverage	RT	μW–mW [83, 84]

and an incoming terahertz pulse is focused onto the PCA. On the opposite side of the PCA, a fs-pulse (in general a part of the same pulse used for the generation) is focused onto the gap between the electrodes and generates electron-hole pairs inside the semiconductor. If the fs-pulse and the terahertz pulse overlap temporally at the PCA, the generated free carriers are accelerated by the terahertz field and a current proportional to the field strength is observed. In case the two pulses are not temporally overlapping no current is generated. Further, the fs-pulse must be shorter and the recombination of electron-hole pairs must be faster than the duration of the terahertz pulse. In this way, the terahertz pulse is sampled by changing the phase between the two pulses. By a Fourier transformation of the measured pulse the terahertz spectra is calculated. The PCA only provides a signal if both pulses are temporally overlapping. Therefore, background radiation, which is not in phase with the pulses averages to zero, which enables high SNR values of this detection scheme.

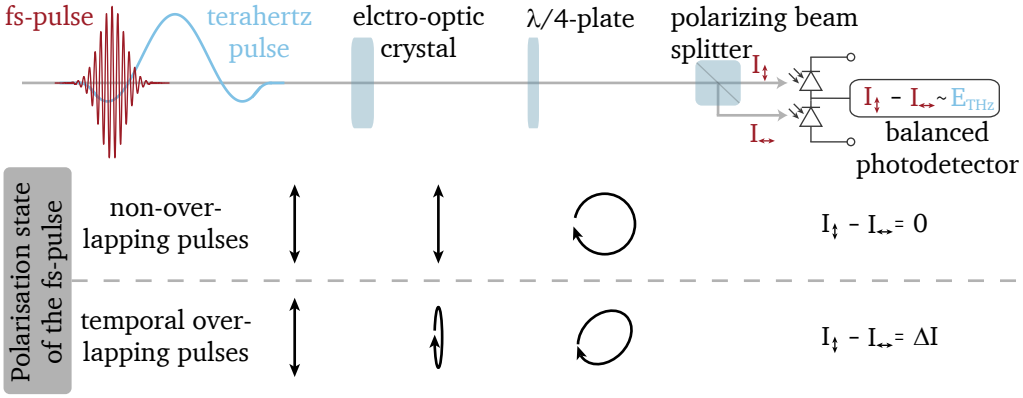

Figure 2.5.: A short terahertz pulse impinging on an electro-optic crystal changes its birefringence proportional to the field strength. This means that the strength of the electric field can be measured by a measurement of the birefringence of the EO crystal, which is done with an optical fs-pulse.

A second method to measure the electric field of the terahertz radiation relies on the Pockels effect in electro-optic (EO) crystals. An electric field applied to such a crystal changes its birefringence linearly proportional to the field strength. Consequently, this implies that the strength of the electric field can be measured by a measurement of the birefringence of the EO crystal. A schematic set-up of the method is depicted in Fig. 2.5. The linearly polarized fs-pulse and the terahertz pulse incident on the EO crystal. While both pulses propagate through the crystal, the terahertz pulse induces a birefringence in the crystal proportional to its field strength, which changes the polarization state of the fs-pulse. To achieve a maximum change of the polarization state and to temporally sample the terahertz pulse, the group velocity of both pulses must be the same inside the crystal and measurements with different phases between the pulses must be performed. Subsequent to the EO-crystal a $\lambda/4$-plate is placed, which induces a phase shift of $\pi/2$ to the polarization components of the fs-pulse. In the absence of the terahertz field the fs-pulse is still in a linear polarization state, which is converted to a pure circular polarization state by the $\lambda/4$-plate. A polarizing beamsplitter is used to separate the fs-pulse in its horizontal and vertical linear polarization states. The intensity difference of the two linear polarization states is then measured by a balanced photodetector resulting in a current signal of zero, if no terahertz radiation is

present. In case the terahertz radiation is in phase with the fs-pulse, the polarization state of the fs-pulse is slightly elliptical after the $\lambda/4$-plate. Therefore, the balanced photodetector measures a current, which is proportional to the field strength of the terahertz radiation. The terahertz pulse is sampled by changing the phase between the two pulses via an optical delay line. Afterwards, the measured electric field is Fourier transformed to receive the optical spectra of the terahertz pulse.

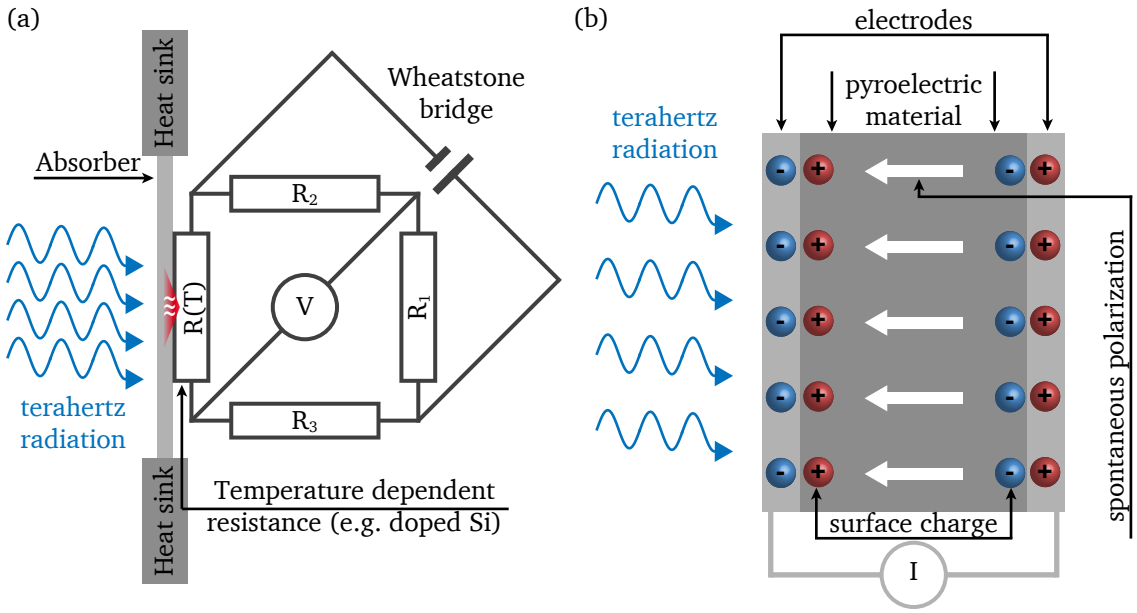

Figure 2.6.: (a) Schematic of the operation principle of a bolometer. The incoming radiation is directly converted into heat and a resistance measurement of a temperature dependent resistor $R(T)$ provides information about the power of the incident radiation. (b) The operation of a pyroelectric detector is based on a temperature change of a pyroelectric crystal, which results in a change of its polarization and in turn a variation of the surface charge. By placing two electrodes on top of the crystal surfaces these surface charges can be measured by a compensating current flowing through the circuit.

Besides these special measurement techniques, which measure the full electric field consisting of amplitude and phase information, instruments like Bolometers, Golay-Cells and pyroelectric detectors are only able to measure the intensity of the terahertz radiation. Often, the incoming radiation is directly converted into heat, which afterwards is measured by different concepts. Bolometers for example are thermal detectors, which make use of heating induced by the radiation. One way to realize this is a temperature-dependent resistance as found in some materials to measure the radiation induced temperature change. For this purpose, the bolometer is cooled down to or even below the temperature of liquid helium. The main parts of a bolometer are the absorber, the heat sink, the temperature-dependent resistor and the resistance measurement circuit. A typical arrangement using a Wheatstone bridge to measure the resistance is depicted in Fig. 2.6(a). The absorber must offer a constant and high absorption coefficient and a low reflectivity in the terahertz frequency domain. Materials offering a good temperature-dependent resistance are strongly doped Si and Ge. The temperature dependent resistance R of a doped semiconductor is given

by $R = R_0 exp\left(\sqrt{A/T}\right)$ [85] and offers a large change of the resistance for small temperature changes at low temperatures.

Pyroelectric detectors operate at room temperature and make use of the pyroelectric effect, which occurs in crystals like triglycine sulfate (TGS), deuterated triglycine sulfate (DTGS), lithium tantalate ($LiTaO_3$), and barium titnate ($BaTiO_3$) [40]. These crystals possess a spontaneous polarization along a specific crystal axis, which also induces surface charges. A temperature change of the crystal results in a change of the polarization and in turn a variation of the surface charge. By placing two electrodes on top of the crystal surfaces as depicted in Fig. 2.6(b) these surface charges can be measured due to a compensating current which flows through the circuit formed by the electrodes. However, the surface charges are compensated by free carriers, which means that only changes of the temperature can be measured. In general, pyroelectric detectors possess a lower SNR and sensitivity in the terahertz frequency domain as compared to bolometers. But their room temperature operation and small size make them excellent detectors for terahertz radiation with optical powers down to the tens of nW [86].

2.2. Photomixing

The photomixing technique is closely related to the generation of short terahertz pulses using a PCA. Instead of a fs-pulse impinging on the PCA an optical beat signal is focused onto the gap between the two metal electrodes. Conventionally, the beat signal is generated by a superposition of two single-mode lasers possessing the same polarization. But also a single laser emitting radiation at two neighboring frequencies at the same time is used to generate the optical beat signal [87, 88]. The total electric field of the two lasers emitting the same optical power at the frequencies ω_1 and $\omega_2 = \omega_1 - 2\pi\nu_{THz}$ is given by

$$E(t) = E_0 \cdot e^{i\omega_1 t} + E_0 \cdot e^{i\omega_2 t + \Delta\phi} + c.c. \tag{2.1}$$

with E_0 being the field strength of both lasers and $\Delta\phi$ being the phase between the two lasers, which is assumed to be zero in the following considerations. The electric field of each laser is shown in Fig. 2.7(a) together with the corresponding optical beat signal (b) and the time-varying optical intensity (c). The optical beat signal exhibits a periodicity, which is also visible in the time dependent intensity. The intensity of the optical beat signal generated by the two lasers, which emit radiation of the same polarization and output power, is given by

$$I_{opt}(t) = 2E_0^2 \left[2 + cos\left(2\omega_1 t\right) + cos\left(2\omega_2 t\right) + 2cos\left(\left[\omega_1 + \omega_2\right] t\right) + 2cos\left(\underbrace{\left[\omega_1 - \omega_2\right]}_{2\pi\nu_{THz}} t \right) \right] \tag{2.2}$$

$$I_{opt}(t) \sim I_{opt,0}\left(1 + cos\left(2\pi\nu_{THz} t\right)\right) \tag{2.3}$$

Here, four different frequency components can be recognized. The first two are the doubled frequency ($2\omega_{1,2}$) of each laser, while the third one is the sum frequency ($\omega_1 + \omega_2$). These three frequencies are responsible for the fast intensity oscillations in Fig.2.7(c) and are too fast for the free carriers of the semiconductor to follow. The last frequency component is the difference frequency ($\nu_{THz} = (\omega_1 - \omega_2)/2\pi$) of the two lasers. This frequency can be seen in Fig.2.7(c) by the slowly, compared to the other oscillations, varying intensity. In fact, the two lasers are chosen to possess a difference frequency in

the terahertz frequency domain.

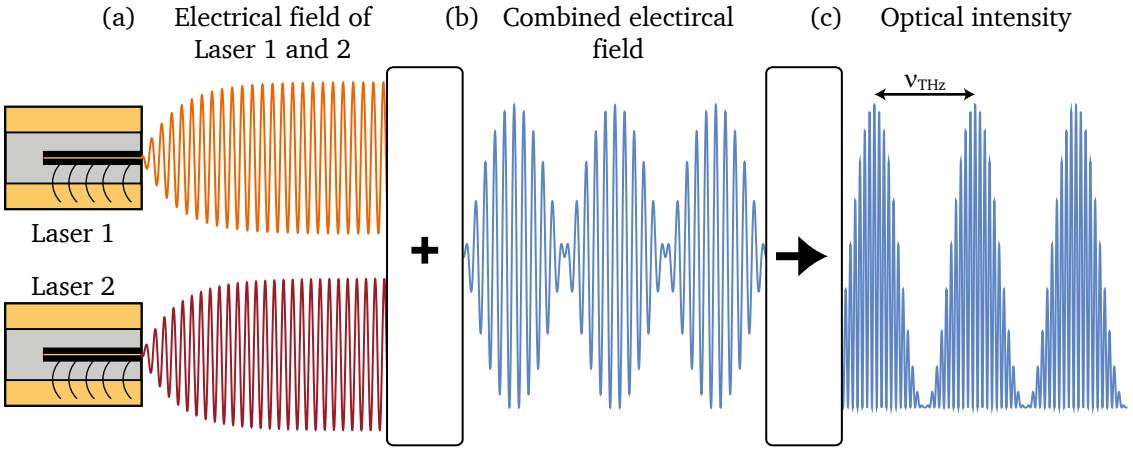

Figure 2.7.: (a) Electric field of the two lasers emitting at the frequencies ω_1 and ω_2. (b) The superposition of these two electric fields leads to an optical beat signal with (c) a time-varying optical intensity.

In order to convert this difference frequency to a real electromagnetic terahertz wave, the beat signal is focused onto the gap of the PCA. Here the radiation induces free carriers inside the semiconductor, which typically have lifetimes in the order of several hundreds of fs [89]. By applying a bias voltage to the electrodes of the PCA, these free carriers get accelerated and as a result a current is generated. Because of the short lifetimes, the number of free carriers is able to follow the difference frequency modulated intensity of the optical beat signal. The time-dependent induced current at the PCA $I_{PCA}(t)$ is given by a convolution of the intensity $I_{opt}(t)$ of the optical beat signal and the impulsive current density [40]

$$I_{PCA}(t) = \int_0^\infty I_{opt}(t-t') \left[e\, n(t')\, v(t') \right] dt' \tag{2.4}$$

$$n(t) = exp\left(-\frac{t}{\tau_{cl}}\right)$$
$$v(t) = \mu_e E_{DC}\left[1 - exp\left(-\frac{t}{\tau_{mr}}\right)\right]$$

where e is the charge of the electron, $n(t)$ is the carrier density, τ_{cl} is the carrier lifetime, $v(t)$ is the average velocity of the electrons, τ_{mr} is the momentum relaxation time, E_{DC} is the bias field and μ_e is

the electron mobility. Since the momentum relaxation time is much shorter than the carrier lifetime this integral reduces to [40]

$$I_{PCA}(t) = \tau_{cl}\mu_e E_{DC} I_{opt,0} + \frac{\tau_{cl}\mu_e E_{DC} I_{opt,0}}{\sqrt{1+4\pi^2\nu_{THz}^2\tau_c^2}} cos\left(2\pi\nu_{THz}t - tan^{-1}\left(2\pi\nu_{THz}\tau_{cl}\right)\right) \tag{2.5}$$

$$I_{PCA}(t) = I_{DC} + \frac{I_{AC}}{\sqrt{1+4\pi^2\nu_{THz}^2\tau_c^2}} cos\left(2\pi\nu_{THz}t - \phi\right). \tag{2.6}$$

The current at the PCA can be divided into a constant part I_{DC} and a part alternating at the difference frequency ν_{THz}, from which the CW terahertz field

$$E_{THz} \sim \frac{dI_{PCA}(t)}{dt} \tag{2.7}$$

is radiated. Usually the electrodes are connected to an antenna, which possess a radiation resistance R_A. The average terahertz output power emitted by this antenna is given by the product of the average AC current times the radiation resistance of the antenna

$$< P_{THz}(\nu_{THz}) > = < I_{PCA}^2 > \cdot R_A = \frac{1}{2} R_A \left(E_{DC}^2 I_{opt,0}^2\right) \frac{\tau_{cl}^2\mu_e^2}{1+4\pi^2\nu_{THz}^2\tau_{cl}^2}. \tag{2.8}$$

The emitted output power depends quadratically on the incident intensity of the optical beat signal and the applied bias voltage. The maximal applicable bias voltage is given by the breakdown voltage of the investigated semiconductor material, which for example is 500 kV/cm for LT-GaAs [79]. To generate CW terahertz radiation the PCA is irradiated continuously by the optical beat signal, which also generates thermally dissipated heat in the semiconductor. This thermal heat deposition limits the maximal incident optical power to the PCA, which is further decreased duo to the weak thermal conductance of LT-GaAs [90].

A typically antenna structure used for photomixing is the logarithmic spiral antenna, shown in the inset of Figure 2.8. One of the outstanding properties of this antenna is their spectrally broad emission characteristic [91]. However, the ability of broad frequency tuning of such a PCA is achieved at the expense of the output power of the device caused by the relatively low radiation resistance R_A of the antenna. In applications requiring radiation at a specific terahertz frequency it is often desirable to optimize the device for this frequency. This can be achieved by using a PCA with a dipole antenna, which shows a higher output power at the design frequency compared to a PCA with a logarithmic spiral antenna [91, 92]. Apart from the design frequency the output power of the PCA with dipole antenna decreases fast and finally is below the output power of a PCA with logarithmic spiral antenna.

Contrary to the emitted terahertz radiation depicted in Fig. 2.8, an electric dipole as the PCA would irradiate the terahertz radiation in both directions (into the free space and the LT-GaAs crystal). But since LT-GaAs possess a large refractive index of 3.4 in the terahertz domain most of the radiation is directly radiated into the substrate (right side of the PCA in Fig. 2.8) and not into free space (left side of the PCA in Fig. 2.8) [93]. This is a desirable effect for the generation of directional radiation, but the high refractive index also leads to some challenges. After traveling through the substrate, the terahertz radiation must be outcoupled into free space on (right side of the LT-GaAs crystal in Fig. 2.8). Coming from the optically

thicker medium to air total reflection of the radiation occurs at an angle of $\theta_C = sin^{-1}(1/n_{LT-GaAs}) \approx 17°$. This would lead to a dramatic decrease of the outcoupled terahertz power, since the generated radiation is highly divergent because of the small source size compared to its wavelength. To overcome this issue, a substrate lens is attached to the backside of the PCA as shown in Fig. 2.8, which is capable to decrease the divergence or even collimate the radiation [94, 95]. A material well suitable for the production of low loss high quality lenses in the terahertz frequency domain is high resistivity float zone silicon (HRFZ-Si). HRFZ-Si features a low absorption in the terahertz domain, a refractive index matching to the refractive index of GaAs and a low dispersion in the range from 0.5 to 4.5 THz [96].

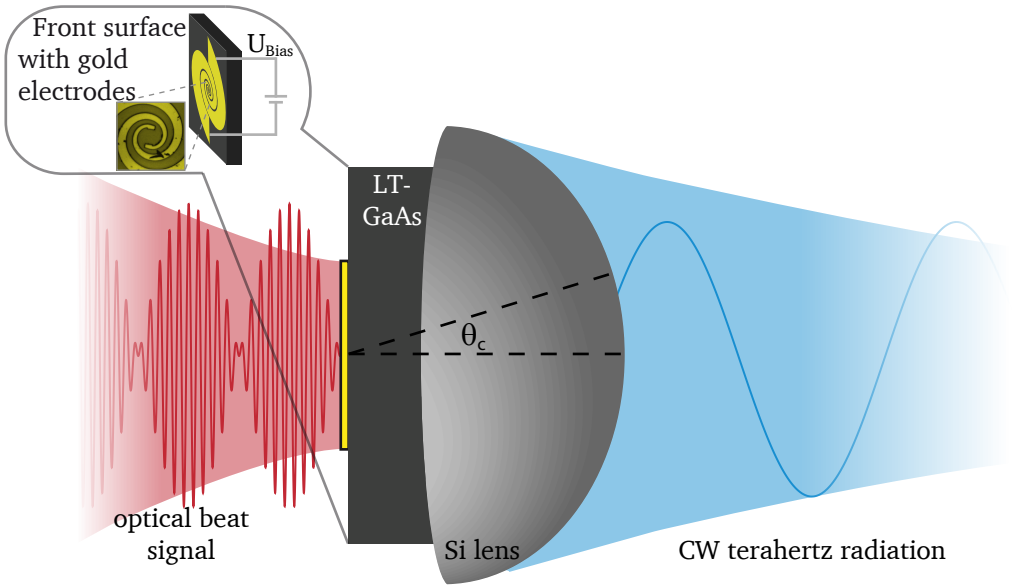

Figure 2.8.: Terahertz generation using the photomixing approach. An optical beat signal is irradiated on the gap between two electrodes (inset) and generates free carriers inside the semiconductor. By applying a bias voltage these electron-hole pairs get accelerated and oscillate with the frequency of the beat signal, which leads to the radiation of a CW terahertz electric field. A Si-lens is used to improve the out-coupling of the radiation.

Besides the generation of terahertz radiation, the PCA can also be used as a detector for CW terahertz radiation as depicted in Fig. 2.9. For this purpose, the PCA is not biased and is irradiated by the same optical beat signal as used for the generation. The optical beat signal still modulates the number of free carriers in the semiconductor, but as no bias voltage is applied these carriers do not contribute to a current flow. If an incident terahertz field, generated by the same optical beat signal, impinges on the detector PCA a bias proportional to the electric field of the terahertz radiation is generated. As a result, the free carriers are accelerated and a mean current $< I_{THz} >$ flows which is proportional to the product of the electric field and the incident laser power [58]

$$< I_{THz} > \sim < E_{THz}(t) \cdot I_{opt}(t) > \sim \; E_{THz,0} \cdot I_{opt,0} \cdot cos(\varphi). \tag{2.9}$$

Here, φ denotes a phase difference between the optical beat signal and the terahertz radiation. The measured current at the PCA used for detection is proportional to the field strength of the terahertz radiation, but also depends on the phase of the terahertz radiation making phase sensitive measurements possible.

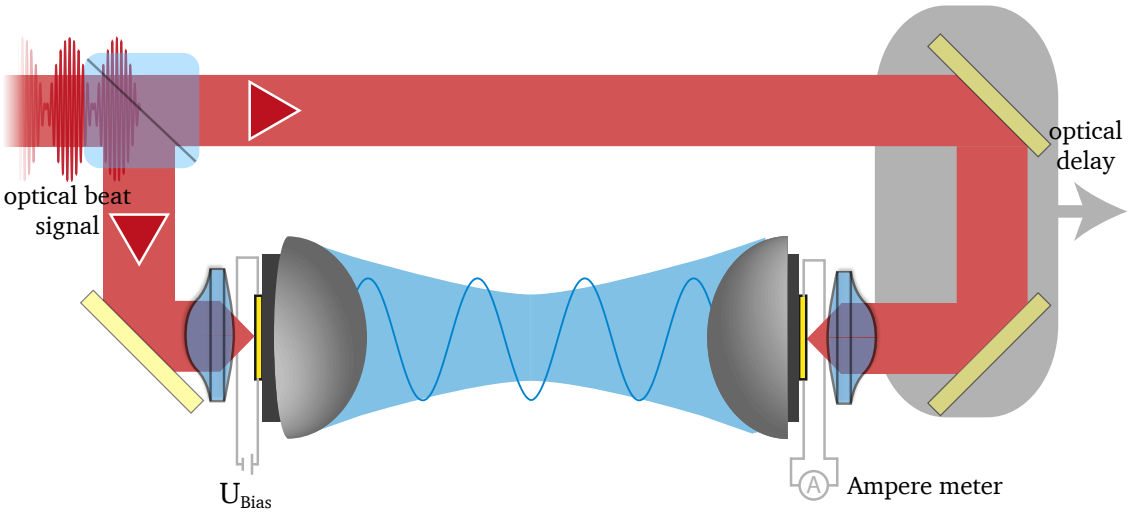

Figure 2.9.: Scheme of the phase sensitive detection of terahertz radiation using a PCA as detector. The optical beat signal is split into two parts. One part irradiates on the PCA for the terahertz generation, while the other passes an variable optical delay and is focused on the detection PCA. In contrast to the PCA used for generation, the detection PCA is not biased but connected to an ampere meter, which measures the current generated by the simultaneously irradiated terahertz radiation and optical beat signal.

The introduced techniques for the generation and detection of terahertz radiation allow the implementation of a multitude of different applications. One of these application fields is terahertz imaging, which benefits from the non-ionizing nature of the terahertz radiation and the opacity of many packaging materials in this spectral domain.

2.3. Terahertz imaging

Terahertz imaging techniques are evolving towards excellent tools for a plurality of industrial and research applications [97–100]. Besides the opacity of many materials, the specific spectral fingerprints of a multitude of materials in the terahertz domain are used to determine the spatial chemical composition of sample objects. These properties are utilized for example in security imaging, where the opacity of textiles and synthetic materials and the absorption of metal is used to detect hidden objects [101] or the spectral fingerprint of explosives reveal directly and doubtless the presence of these substances [102]. Further, terahertz imaging techniques can be applied for medical diagnostics [103, 104] or quality control [105]. In these fields of applications, the spectrum of available implementations varies from all-optical [106], over electro-optical [103] to fully electrical [107] schemes for the generation and detection of the terahertz

radiation. Imaging of a coin is achieved by a set-up using a terahertz QCL for the simultaneous generation and detection of terahertz radiation [106]. The coin back reflects a portion of the terahertz radiation into the QCL cavity and induces a voltage change, which depends on the amplitude and phase of the back-reflected radiation. By a translation of the coin, the amplitude and phase of the back-reflected terahertz radiation changes and thus the surface morphology of the coin can be recognized. Terahertz imaging techniques can also be used to achieve images containing spectral information. This for example can be realized using broadband terahertz pulses [108]. Here, the spectral fingerprints in the terahertz frequency domain are used to distinguish between different biological substances, incapable with an image taken in the visible spectrum.

Most of the images taken in the terahertz frequency domain rely on the raster scanning of the object under investigation. This often leads to recording times of several minutes, depending on the desired spatial resolution. To improve the recording time multi-pixel detectors involving a large number of pixels [109] and with high frame rates of up to 450 frames per second [110] can be used. Another promising imaging method is the single-pixel imaging, which uses a non-spatially resolving so-called 'bucket' detector and does not require any mechanically raster scanning of the object. This method reconstructs an image of the object by a set of measurements of the total intensity transmitted, reflected or scattered from the object under illumination with differently spatial patterned radiation. Real time videos, simultaneously taken in the visible and short-wavelength infrared have been realized [111] and 3D imaging [112] has been demonstrated using a single-pixel camera in the visible spectral domain. The concept of a single-pixel camera and its adaption to the terahertz frequency domain is discussed in section 2.3.2 demonstrating that raster scanning of the object and multi-pixel detectors are not mandatory for imaging applications.

2.3.1. Tomographic imaging

In order to realize an insight into an object, rather than imaging a projection, tomographic reconstruction techniques can be applied. This for example is necessary and useful in security applications and a plurality of industrial processes [37]. Since the photon energy of terahertz radiation is non-ionizing, there are lower safety requirements compared to x-rays, easing the implementation of terahertz systems.

To receive the two-dimensional shape of a sample object, a plurality of projections under different rotation angles of the object under investigation need to be recorded. Figure 2.10 shows a sample object consisting of two circular shapes with homogenous absorption coefficients. The sample has an absorption coefficient distribution $f(x,y)$, which is measured under different rotation angles θ as shown for two exemplary projections at 0° and 70°. By assuming straight rays from the source, through the sample to the detector, which is located opposite the source, an absorption value $P_\theta(t)$ of a projection is given by the line integral

$$P_\theta(t_\theta) = \int_{-\infty}^{\infty} f(t_\theta, s_\theta)\, ds_\theta \tag{2.10}$$

with t_θ and s_θ being the rotated coordinate system of a projection given by

$$\begin{pmatrix} t_\theta \\ s_\theta \end{pmatrix} = \begin{pmatrix} cos(\theta) & sin(\theta) \\ -sin(\theta) & cos(\theta) \end{pmatrix} \begin{pmatrix} x \\ y \end{pmatrix}. \tag{2.11}$$

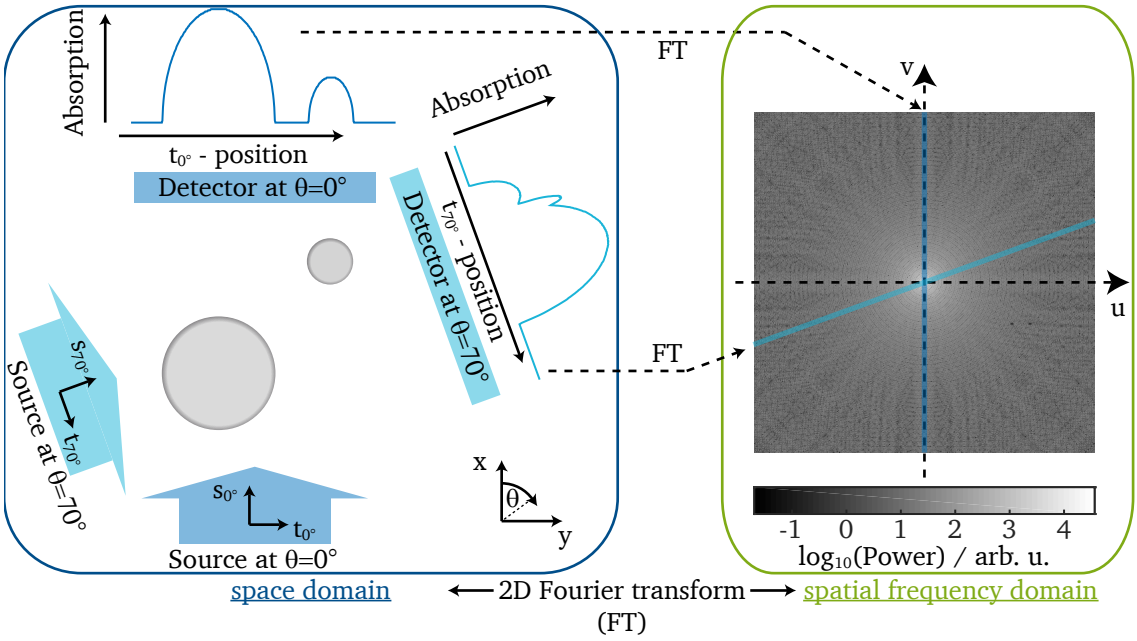

Figure 2.10.: The principle of tomographic imaging is based on the measurement of projections of the sample object under different rotation angles θ. The Fourier transform of each projection is used to fill up the spatial frequency domain (u, v) of the object image.

Next the projection is transformed into the frequency domain using the Fourier transform,

$$FT_\theta(w) = \int_{-\infty}^{\infty} P_\theta(t_\theta) e^{-2\pi i w t}\, dt = \int_{-\infty}^{\infty}\int_{-\infty}^{\infty} f(t_\theta, s_\theta) e^{-2\pi i w t_\theta}\, ds_\theta\, dt_\theta \tag{2.12}$$

By transforming this equation into the original coordinate system of the object (x, y) and the corresponding coordinate system of the spatial frequency domain (u, v)

$$FT_\theta(u, v) = \int_{-\infty}^{\infty}\int_{-\infty}^{\infty} f(x, y) e^{-2\pi i w(x\cos(\theta)+y\sin(\theta))}\, dx\, dy \tag{2.13}$$

$$= \int_{-\infty}^{\infty}\int_{-\infty}^{\infty} f(x, y) e^{-2\pi i x u} e^{-2\pi i y v}\, dx\, dy, \tag{2.14}$$

the two-dimensional Fourier transform of the image at the spatial frequencies $(u = w\,cos(\theta), v = w\,sin(\theta))$ is derived. This derivation represents the basic mechanism of tomographic image reconstruction and is called Fourier Slice Theorem [113, 114]. Equation 2.14 reveals, that by measuring the projection of an object and taking the Fourier transform of that projection, a radial line of the spatial frequency space of the object is determined. This is illustrated in the right hand side of Fig. 2.10, which represents the spatial frequency domain of the object. The Fourier transform of the particular projection represents a line in the 2D spatial frequency domain of the object as illustrated in the right hand side of Fig. 2.10 inside the (u, v) coordinate system. By taking an infinite number of projections of the sample under the rotation angles θ_1, θ_2, ..., θ_∞ the complete spatial frequency domain of the object is determined. Knowing $FT(u, v)$, the

object absorption coefficient distribution $f(x, y)$ can be calculated by the inverse Fourier transform. In practice only a limited number of measurements can be performed and therefore the frequency domain is only known along a limited number of radial lines. Between these lines the frequency space must be approximated by interpolation methods. Further away from the center, the density of known points even gets more sparse, leading to a lack of information in the high frequency parts of the reconstructed image. This leads to a smoothing of the transitions between different image elements and further the overall image appears blurred due to the absence of fine image details.

For this reason a plurality of additional reconstruction techniques have been developed. One of the most commonly used reconstruction algorithms is the filtered back projection [115]. This algorithm is derived from the Fourier Slice Theorem and consists of two parts, the back projection and the filtering. The algorithm takes a projection and smears it out over the space domain of the object. In that way all measured projections are superimposed and with an increasing number of smeared projections the shape of the object gets clearer. However, the borders of the sample are blurred, which is a result of the sparse sampling of the high frequency components. The high frequency components of an image are responsible for the fine details and sharp edges, while the low frequencies represent smooth surfaces. In the measurements the high frequencies are under-represented, which is corrected by a filter applied to the frequency domain of each projection. Typically, the applied filter suppresses the low frequencies and amplifies the high frequencies. After the filtering, the projection is inversely Fourier transformed and smeared over the space domain of the object image. By superimposing all of the filtered projections a much sharper image is reconstructed. However, quality of the reconstructed image using the filtered back projection algorithm suffers if only a small number of projections are available [107]. It is well accepted that iterative algorithms are superior to the filtered back projection algorithm for low numbers of projections [107]. Therefore, the approach of the algebraic reconstruction technique (ART) was first proposed by Gordon et al. [116]. It relies on an algebraic formulation of the rays intersecting the image $f(x, y)$, which is represented in a sequential order f_j with total of N pixels. The final value p_i of one ray casted through the image is given as the sum of all pixels, in which each is multiplied by a weight value w_{ij}. Most of these weight values will be zero, since the ray does not hit the corresponding pixel. But the weight of pixels hitten by the ray can be calculated by multiple methods, each with its own trade-off between accuracy and speed. For example, in Fig. 2.11(a) the weighting is done by the distance the ray travels through the corresponding pixel. By taking all M rays of every projection into account, the projection process can be described by the following system of equations:

$$\begin{array}{ccccccccccc} w_{11}f_1 & + & w_{12}f_2 & + & w_{13}f_3 & + & \dots & + & w_{1N}f_N & = & p_1 \\ w_{21}f_1 & + & w_{22}f_2 & + & w_{23}f_3 & + & \dots & + & w_{2N}f_N & = & p_2 \\ \vdots & & & & & & & & & & \\ w_{M1}f_1 & + & w_{M2}f_2 & + & w_{M3}f_3 & + & \dots & + & w_{MN}f_N & = & p_M \end{array} \tag{2.15}$$

In this system, an image is represented by a point in a N-dimensional space and each of the above equations describe a hyperplane in this space. The image f, which is determined by the projections $p_1 \dots p_M$, is given by the point in which all the hyperplanes intersect. Generally, this point can be calculated by multiplying the inverse of the matrix of weights $\mathbf{w}$ with the projection vector $\vec{p}$

$$\vec{f} = \mathbf{w}^{-1} \cdot \vec{p}, \tag{2.16}$$

but first the dimension of this matrix is $M \times N$ is very large and second it is not invertible because the matrix is not square. In order to visualize the iterative approach used in the ART, an image consisting of two pixels and two projection measurements is used as example. The set of equations then simplifies to

$$w_{11}f_1 + w_{12}f_2 = p_1 \tag{2.17}$$
$$w_{21}f_1 + w_{22}f_2 = p_2. \tag{2.18}$$

Each of the two equations represent a line, which are schematically shown in Fig. 2.11(b). The reconstructed image corresponds to the intersection of these two lines. To find the intersection point first an initial guess $\vec{f}^0$ is done. In the first iteration, this guess is projected onto the first line given by Eq. 2.17. In the second iteration, the resulting vector $\vec{f}^1$ is projected onto the second line given by Eq. 2.18, which again is projected on the first line in the third iteration and so on. The k^{th} projection can be calculated using

$$\vec{f}^k = \vec{f}^{k-1} - \frac{\vec{f}^{k-1} \cdot \vec{w}_i - p_i}{\|\vec{w}_i\|} \vec{w}_i, \tag{2.19}$$

with the index i given by the modulo of N and $k+1$. In this manner, the algorithm iteratively approaches the intersection of the two lines, yielding the solution.

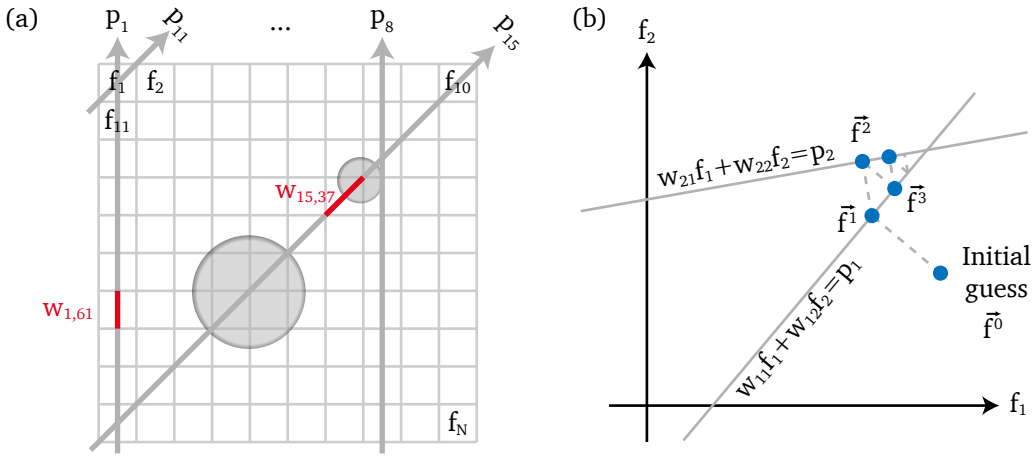

Figure 2.11.: (a) Illustration of Eq. 2.15, two exemplary weights $w_{1,61}$ and $w_{15,37}$ are shown for the image $(f_1, f_2, \ldots, f_N)$. Rays traveling through the image are labeled p_M. (b) Visualization of the iterative procedure applied to find the solution of Eq. 2.17 and Eq. 2.18.

The ART algorithm presents a computationally efficient way to perform the tomographic reconstruction but it suffers from salt and pepper noise [114], which means that the image is randomly covered with white and black pixels [117]. On the cost of computational time, the quality of the reconstructed image can be improved by e.g. the simultaneous iterative reconstructive technique. This algorithm projects a guess of the image onto all rays p_i and updates the guess by the average image change. Generally, this approach leads to better reconstruction result but the convergence is slower [114]. A trade-off between these two approaches is the simultaneous algebraic reconstruction technique (SART) [118]. This algorithm uses all

rays of a specific projection angle in one iteration to perform the correction of the guessed image. As a result, the algorithm achieves fast convergence with a good quality of the reconstructed image.

An additional benefit that all the algebraic reconstruction algorithms share, is the opportunity to incorporate a priori information about the image and ray distortions like refraction effects into the reconstruction process [114]. This is of particular interest in the terahertz frequency domain, since refraction, diffraction and reflection effects have a huge impact on the measured projections [119, 120]. The reconstructed images often show distortions or even are poorly correlated to the physical shape of the object. The main reason for the distortions of the reconstructed images originate in the used reconstruction algorithm, which actually has been developed for x-ray tomography, i.e. wavelengths between 5 and 60 pm, thus much smaller than the object dimensions. Moreover, the refractive index of matter differs very little from unity in the x-ray spectral domain, hence the algorithm assumes straight rays, which penetrate the sample object and get attenuated depending on the spatially distributed absorption coefficient and the optical path length through the object. This circumstance is not given in case of tomographic terahertz imaging, because refraction of the rays, losses due to reflection and diffraction effects occur and strongly influence the measured projections. For this purpose, a lot of efforts are done to improve the quality of reconstructed images in terahertz tomography. Both new concepts for the field of tomographic terahertz imaging have to be developed, and improvements of the experimental set-ups, like for example refractive index matching [121], or special reconstruction algorithms [119, 122] are needed. Also, a good understanding of the impact of refraction, reflection and diffraction effects on terahertz tomography is required in the latter case, in order to include these effects to the tomographic reconstruction.

An important component of the tomographic imaging set-up is the detection scheme, which must be capable to measure the spatially resolved projections of the sample object. For this purpose, imaging schemes involving raster scanning of the object or multi-pixel detectors are often used. Because multi-pixel detector arrays are not widely available in the terahertz frequency domain, commonly the projection is obtained by raster scanning the object. An alternative concept is given by the single-pixel imaging technique, which allows the measurement of spatially resolved projections without raster scanning of the object and by using a non-spatially resolving 'bucket' detector. This concept will be introduced in more detail in the following section.

2.3.2. Hadamard imaging

Nowadays it is not implicitly necessary to make use of multi-pixel detectors or raster scanning in order to get spatially resolved images of an object. With the advance in computational capacity and new methods for the generation of spatially patterned radiation, the application of single-pixel detectors appears more frequently in the scope of imaging. This method uses a non-spatially resolving 'bucket' detector, which integrates the total incident intensity. The image of the object is reconstructed by a set of n measurements of the total intensity transmitted, reflected or scattered from the object under illumination with differently

spatial patterned radiation as illustrated in Fig. 2.12. Mathematically this can be expressed in the following system of equations

$$\left.\begin{aligned} M_1 &= \vec{P}_1 \cdot \vec{f} \\ M_2 &= \vec{P}_2 \cdot \vec{f} \\ &\vdots \\ M_n &= \vec{P}_n \cdot \vec{f} \end{aligned}\right\} \vec{M} = \mathbf{P} \cdot \vec{f} \tag{2.20}$$

where M_1 to M_n denote the measured intensities at the bucket detector and $\vec{f}$ is the mask of the object, which is illuminated by the nth pattern $\vec{P}_n$. $\mathbf{P}$ represents the pattern matrix, in which the nth row is represented by the transposed pattern $\vec{P}_n^{\,T}$. The transmission mask of the object is received by the multiplication of Eq. 2.20 with the inverse of $\mathbf{P}$

$$\mathbf{P} \cdot \vec{f} = \vec{M} \tag{2.21}$$

$$\mathbf{P}^{-1} \cdot \mathbf{P} \cdot \vec{f} = \mathbf{P}^{-1} \cdot \vec{M} \tag{2.22}$$

$$\vec{f} = \mathbf{P}^{-1} \cdot \vec{M}. \tag{2.23}$$

The system of Eqs. 2.20 can only be solved by applying Eq. 2.23 if the number of measurements are equal or larger than the total number of pixels.

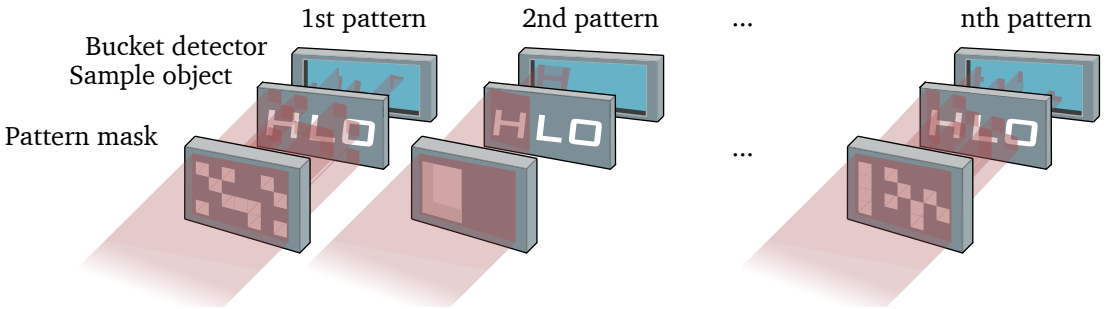

Figure 2.12.: A multitude of different patterns are used to illuminate a sample object while the bucket detector measures the total intensity transmitted through the object under illumination of one pattern. An image of the object can be calculated from these n intensities, although a detector with no spacial resolution is used.

The kind of employed spatial patterns is variable and depends on the specific implementation. One possibility is the application of random patterns, which are often used in the framework of compressed sensing [123, 124]. Compressive sensing offers the possibility to perform a reconstruction of the image with a reduced number of measurements. The number of needed measurements can be reduced to 25−30% of the total number of pixels [124, 125], which enables short measurement times. This of course is achieved by a trade-off between the number of measurements and the quality of the reconstructed image. By increasing the number of measurements, at first the image quality increase quite fast and with a higher amount of measurements slowly converges as shown in [124]. However, Eq. 2.23 cannot be used to reconstruct the image of the object. Instead computationally more complex optimization algorithms like the minimization of the total variation (min-TV) [126] must be used.

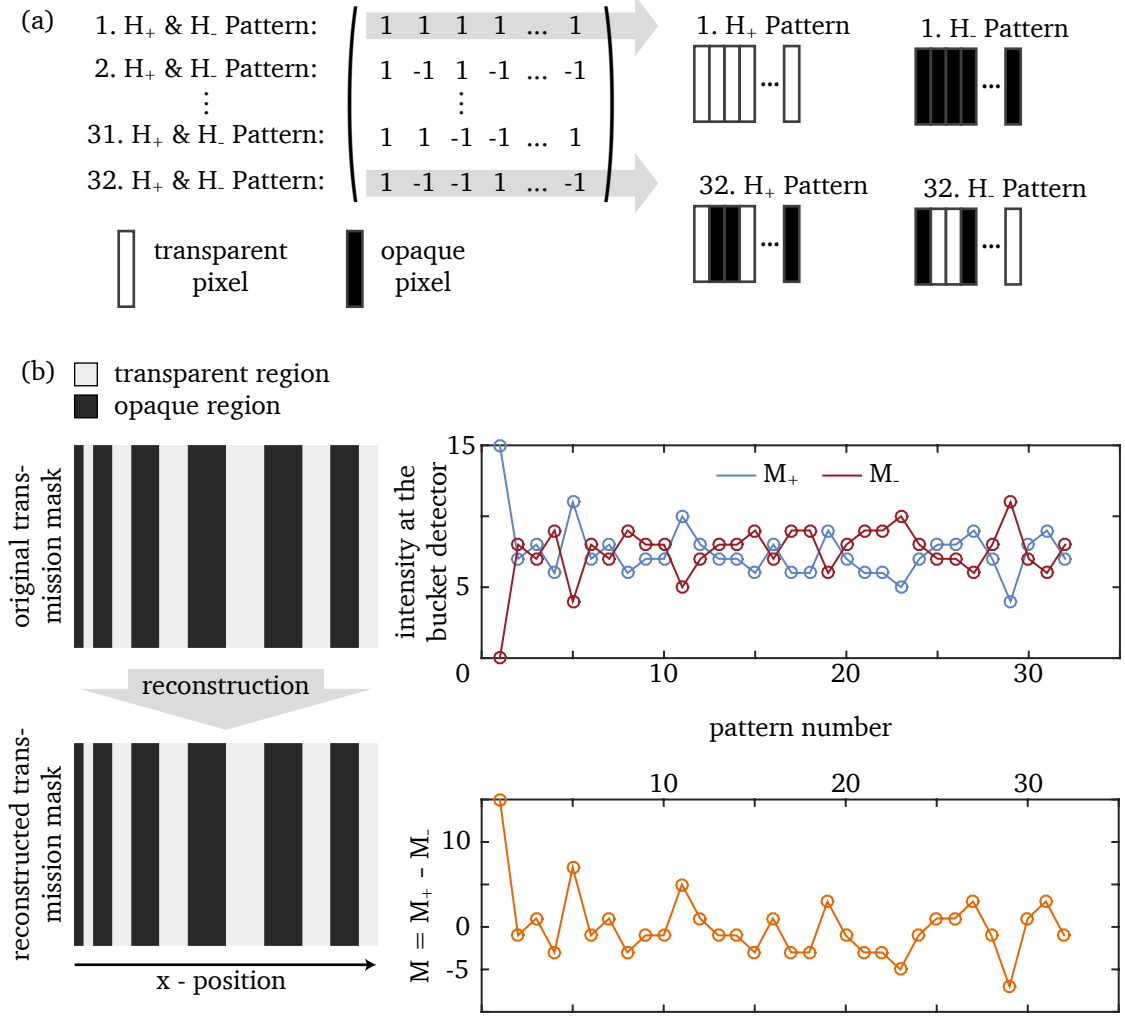

Figure 2.13.: (a) Illustration of the pattern generation instructions of a 32×32 Hadamard matrix used for single-pixel imaging. Each row of the Hadamard matrix represents two patterns. The H_+ patterns are created by transparent regions represented by $+1$ entries and opaque regions for the -1 entries, while this is reversed for the H_- patterns. (b) Simulation of the Hadamard single-pixel imaging scheme. The measurement vectors $\vec{M}_+$ and $\vec{M}_-$ are calculated using Eq.2.20 from the original transmission mask and afterwards the transmission mask is reconstructed using Eq. 2.23.

A set of patterns which enable the image reconstruction described in Eq.2.23 can be derived from the Hadamard matrices [127]. This group of matrices are squared matrices containing only the values 1 and -1. Further, the matrices are orthogonal, meaning that the rows/columns of these matrices are all orthogonal to each other. As a consequence, the inverse of a Hadamard matrix is given by its transpose divided by its dimension. Besides the faster computational time and possibility to exactly calculate the image using Eq. 2.23, in general single-pixel imaging based on Hadamard patterns achieves higher image

quality [125] on the cost of measurement time. A Hadamard matrix of the dimension $2n$ can be created by using the following recursive construction rule

$$\mathbf{H_1} = 1,\ \mathbf{H_2} = \begin{pmatrix} 1 & 1 \\ 1 & -1 \end{pmatrix},\ \ldots,\ \mathbf{H_n} = \begin{pmatrix} \mathbf{H_{n-1}} & \mathbf{H_{n-1}} \\ \mathbf{H_{n-1}} & -\mathbf{H_{n-1}} \end{pmatrix}.$$

As can be seen a Hadamard matrix is composed of the entries 1 and -1, but the available intensity values to form radiation patterns can only take values from 0 (no radiation) to 1 (full intensity). Therefore, the Hadamard matrix must be split into two matrices containing only the entries 0 and 1. This is done by adding and subtracting the Hadamard matrix $H^{n\times n}$ to the matrix of ones $\mathbb{1}_{nn}$

$$\begin{pmatrix} \vec{M}_+ \\ \vec{M}_- \end{pmatrix} = \begin{pmatrix} 0.5 \cdot (\mathbb{1}_{nn} + \mathbf{H}) \cdot \vec{f} \\ 0.5 \cdot (\mathbb{1}_{nn} - \mathbf{H}) \cdot \vec{f} \end{pmatrix} = \begin{pmatrix} \mathbf{H}_+ \cdot \vec{f} \\ \mathbf{H}_- \cdot \vec{f} \end{pmatrix}. \tag{2.24}$$

Now, the measurement vector $\vec{M}$ is given by the difference between the two newly defined measurement vectors $\vec{M}_+$ and $\vec{M}_-$

$$\begin{aligned} \vec{M}_+ - \vec{M}_- &= \left(0.5 \cdot (\mathbb{1}_{nn} + \mathbf{H}) \cdot \vec{f}\right) - \left(0.5 \cdot (\mathbb{1}_{nn} - \mathbf{H}) \cdot \vec{f}\right) && (2.25)\\ &= 0.5 \cdot (\mathbb{1}_{nn} + \mathbf{H} - \mathbb{1}_{nn} + \mathbf{H}) \cdot \vec{f} && (2.26)\\ &= \mathbf{H} \cdot \vec{f} && (2.27)\\ &= \vec{M} && (2.28) \end{aligned}$$

Therefore, $2n$ measurements are needed to achieve Hadamard pattern based single-pixel imaging with a resolution of n pixels. The patterns projected on the sample object are formed by the rows of the Hadamard matrix. This is shown in Fig. 2.13(a) for a 32×32 dimensional Hadamard matrix in the one-dimensional case. The H_+ patterns are created by transparent regions represented by $+1$ entries and opaque regions for the -1 entries, while this is reversed for the H_- patterns. For example, the first row of $\mathbf{H}$ only consists of ones and therefore the first H_+ pattern is fully transparent whereas the H_- pattern is fully opaque. The object under investigation is then illuminated with patterned radiation defined by the rows of the Hadamard matrix one by one. The integrated intensities $\vec{M}_+$ (blue) and $\vec{M}_-$ (red) for a transmission mask as depicted in Fig. 2.13(b) are calculated using Eq. 2.24 and are shown in the right side of the figure. The sample mask is either fully transparent, which corresponds to a transmission value of 1, or fully opaque, which corresponds to a transmission value of 0. Since the first pattern of H_+ is fully transparent the first intensity in $\vec{M}_+$ corresponds to the maximum possible transmission through the sample mask. Contrary, the first $\vec{M}_-$ value is zero, since the pattern is fully opaque. Afterwards only smaller differences in the values of $\vec{M}_+$ and $\vec{M}_-$ are recognizable, which is also visible in the measurement vector $\vec{M}$ shown in the bottom right of Fig. 2.13(b). The reconstruction is performed using Eq. 2.23 and the resulting reconstructed transmission mask is shown in the left bottom of Fig. 2.13(b). The reconstructed transmission mask is reproduced very well.

This chapter has introduced basic methods for the generation and detection of terahertz radiation. These methods involve electrical, optical or electro-optical technology to close the terahertz gap of the electromagnetic spectrum. These developments pave the way for terahertz applications as the introduced tomographic and single-pixel imaging. The emphasis of terahertz generation and detection has been on

the photomixing concept. This concept transfers an optical beat signal to the terahertz frequency domain using a PCA. One requirement of this approach is the source of the optical beat signal, which will be discussed in the next chapter.

3. External cavity diode laser sources for photomixing

The laser source presents an important part for the generation and detection of terahertz radiation using the photomixing technique. According to Eq. 2.8 the terahertz output power from the PCA is directly related to the square of the optical intensity of the utilised laser source. To achieve the highest possible terahertz output power, the laser source must typically provide an optical output power from tens to several hundreds of milliwatt depending on the actual PCA [128]. But not only does the emitted terahertz power increase with higher laser intensities, also the noise of the terahertz power is linked to the intensity noise of the laser source due to the relation in Eq. 2.8. One advantage of photomixing is the possibility to generate highly coherent single frequency terahertz radiation necessary for high resolution spectroscopy. However, the spectral resolution is limited by the linewidth of the terahertz radiation, which is given by the laser source [129]. Of particular interest is the tuning of the emitted terahertz frequency and therefore the difference frequency in spectroscopic applications. To exploit the full spectral bandwidth provided by the PCA, the laser system has to offer the ability to tune the difference frequency between approximately 0.1 and 5 THz. This corresponds to a wavelength tuning of approximately 10 nm at a central wavelength of 800 nm.

There exist a plurality of different laser systems used for the photomixing technique [88, 130–132]. Due to its compactness and relative low cost the semiconductor LD has proven to be an excellent laser for the photomixing technique [131]. These lasers enable the opportunity to create a very compact single-chip terahertz emitter using a monolithically integrated dual-wavelength LD [133]. These LDs use dual Distributed Bragg Reflectors (DBR) [134] or Distributed-Feedbacks (DFB) [133] to achieve single mode emission on two wavelengths. The linewidth of these lasers are in the MHz regime and frequency tuning is achieved by a change of the pump current or temperature. However, the frequency tuning range of these devices is limited to approximately 1 THz [133]. To achieve a higher frequency tuning two or even three separate distributed-feedback LDs can be used [78]. To even increase the tuning range to more than 100 nm [135], which exceeds the bandwidth of the PCA, ECDLs can be used. Compared to DFB and DBR lasers ECDLs provide a smaller spectral linewidth, which even can be in the single Hertz regime employing sophisticated stabilization schemes [136].

The ECDL configuration relies on optical self-feedback, coupling a portion of the emitted light back into the LD after the light is spectrally filtered by either an optical grating or interference filter (IF). This is illustrated in Fig. 3.1 for the two configurations used in this thesis. In the Littrow configuration (a) a LD with an anti-reflective (AR) coated facet and a facet as cleaved is used. On both sides the emitted light is collimated by a lens[D1] with a high numerical aperture. The light from the AR coated side is irradiated onto a tilted optical grating[D2], from which the radiation is back-reflected under a wavelength dependent angle. Because of this dispersive reflectance of the grating only a specific wavelength is coupled back into

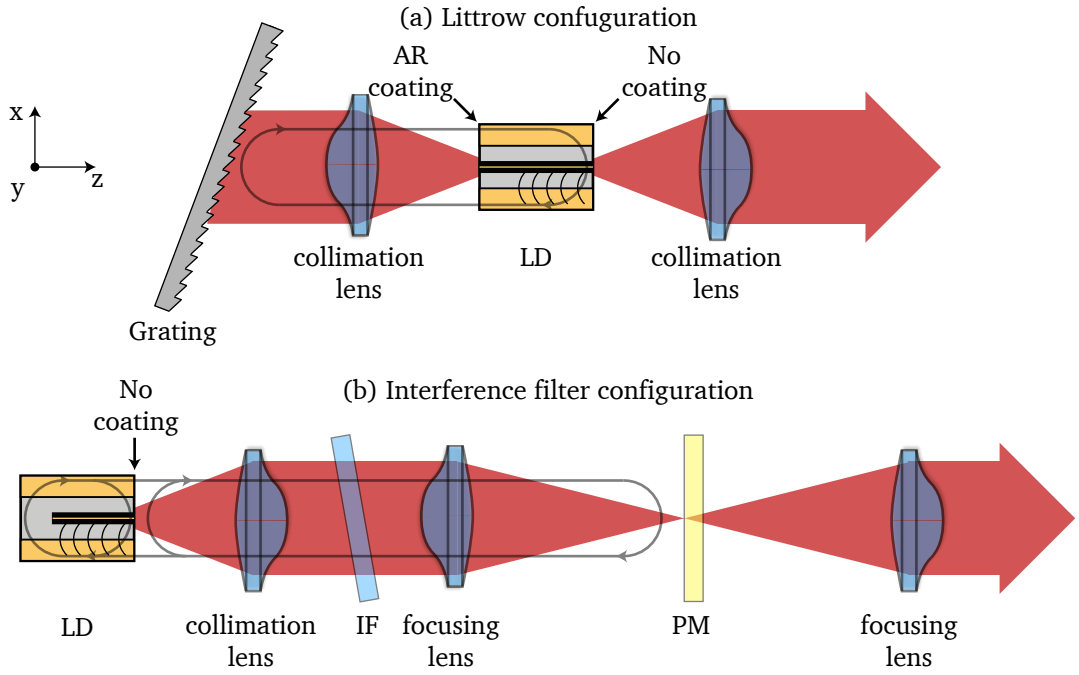

Figure 3.1.: Illustration of two different ECDL concepts using (a) the Littrow and (b) the Interference filter configuration.

the LD, enabling spectrally filtered self-feedback. The grating and the as cleaved facet form the cavity of the ECDL with a free spectral range $\Delta\nu$ of

$$\Delta\nu = \frac{c}{2L} \tag{3.1}$$

with c the speed of light and L the cavity length. By displacing the grating in beam propagation direction the ECDL can be tuned mode jump free about the free spectral range, which for example amounts to 3.7 GHz for a cavity length of 4 mm. By rotating the grating about the y-axis the wavelength can be tuned over a broad spectral range described by

$$\lambda = 2g \cdot sin(\alpha) \tag{3.2}$$

where g is the grating spacing, λ is the desired back-reflected wavelength and α is the tilting angle of the grating.

The second approach followed in this thesis is depicted in Fig. 3.1(b) . Here an IF[D3] is used inside the cavity to spectrally filter the light which is back-reflected by a partially reflective mirror[D4](PM). Due to the packaging of the investigated LD, only one facet is accessible and the LD exhibits no AR coated facet. The emitted light is collimated by a lens[D1] and passes the slightly tilted IF. Afterwards a second lens[D5] with a long focal length is used to focus the radiation onto the reflective surface of the PM. A portion of the light is back-reflected into the LD by the PM, while the rest of the light is collimated by a

second lens[D5] with a long focal length. Thus, the system possesses three cavities, one inside the LD, a second between the back-facet of the LD and the PM and a third between the front-facet of the LD and the PM. Depending on the optical feedback strength different emission regimes of such a three cavity ECDL have been reported [137, 138]. The regimes vary from stable single-mode emission to a chaotic intensity output and random mode jumps. For this reason, the feedback strength of the developed IF based ECDLs is designed to achieve emission in the stable single mode emission regime.

The transmission profile of the IF is measured using the Bruker Vertex 80V spectrometer. An exemplary transmission profile for a rotation angle of 0° is shown as inset in Fig. 3.2(a). The IF possesses a Gaussian shape with a transmission maximum at a central wavelength of 829 nm. Aside from this central wavelength, the transmission symmetrically declines fast on both sides of the IF transmission profile with a full width at half maximum (FWHM) of 3.6 nm. By tilting the IF the central wavelength is varied as shown in Fig. 3.2(a). In this way, the wavelength of the light back-reflected into the LD can be varied over a broad region of wavelengths. Here it should be noted that the tuning of the central wavelength is roughly linear in the range from −5° to −20°. A tilt of the IF between 0° and −5° only has a small impact on the central wavelength. With larger rotation angles, the transmission at the central frequency is continuously decreasing to values below 60% as shown in Fig. 3.2(b). Further the FWHM of the transmission profile increase from 3.6 nm at a rotation angle of 0° to 5.5 nm at −20°. The decreasing transmission values and increasing FWHM of the IF transmission profile are limitations on the maximum achievable tunability of the ECDL.

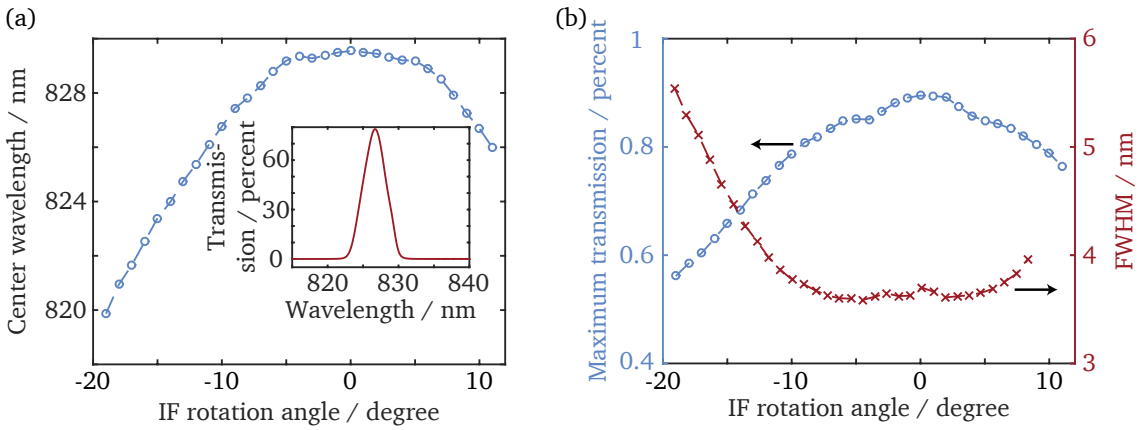

Figure 3.2.: (a) Tuning characteristics of the central wavelength by a rotation of the IF. The inset shows the transmission through the IF for a rotation angle of 0°. (b) Influence of the rotation angle on the peak transmission through the IF and on the FWHM of the IF.

The overall cavity length of the ECDL realized using an IF is much longer compared to the ECDL employing a grating, which makes the free spectral range much smaller. Indeed, this limits the mode jump free frequency tuning range of the ECDL, but its mechanical robustness is superior compared to the ECDL using a grating because of the utilized optical components and arrangement [139]. First, the feedback is realized by a focusing lens and a PM as depicted in Fig. 3.3(b). This so-called cat-eye reflector ensures, that a tilt of the PM has a smaller influence on the feedback strength compared to a tilt of the grating.

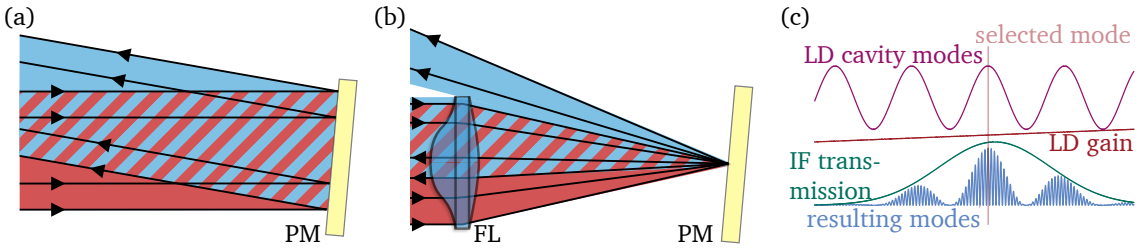

Figure 3.3.: A collimated beam gets back-reflected at a mirror, which is misaligned by an angle of 5°, in the (a) ordinary and (b) cat-eye configuration. Despite the large misalignment of the mirror approximately half of the beam gets back-reflected in the same direction using the cat-eye configuration. (c) Visualization of the mode selection process in an IF-based ECDL.

This is illustrated in Fig. 3.3(a,b), where the PM is rotated by 5°. Compared to the single PM configuration a much larger portion of the radiation is back-reflected in the original direction. Second, due to the long focal length of the lens and the hereof resulting long Rayleigh length, the feedback strength is less sensitive to translations of the PM in beam propagation direction. And third, the frequency of the back-reflected light of the IF-based ECDL is less sensitive to vibrations of the IF. A change of the rotation angle causes a displacement of the centre wavelength of $(d\lambda/d\theta)$ of 0.04 nm/mrad. In case of the grating, a corresponding much larger value amounts to 0.8 nm/mrad according to Eq. 3.2 for a grating with 1200 lines/mm and a central wavelength of 830 nm.

The single-frequency emission of the IF-based ECDL relies on the interaction of several selection mechanisms. The cavity of the LD is in the order of millimetres, which results in a relatively large spacing between possible modes of this resonator. This is illustrated in Fig. 3.3(c) by the purple sinusoidal curve. However, the external cavity with its length in the order of several centimetres, exhibits a very narrow mode spacing as shown by the spacing between two maxima of the blue curve in Fig.3.3(c). Further, each possible mode experiences a different gain, because of the non-constant gain of the LD material and the transmission profile of the IF placed into the external cavity. The resulting modes and their gain are schematically shown in Fig.3.3(c) by the blue curve. With respect to the highest possible gain, there is clearly one mode favored and therefore the ECDL emits on this single mode.

In order to characterize and compare the grading- and IF-based ECDLs, a variety of measurement methods are needed. These range from long-term stability measurements to noise measurements of the output power and emission wavelength and are introduced in the next section.

3.1. Characterization methods

Based on the requirements discussed in the introduction of the previous section the developed ECDLs are now characterized. First the dependency of the LD bias voltage and optical output power on the pump current of the ECDLs are measured using the experimental set-up shown in Fig. 3.4. Further this set-up is used to investigate the wavelength tuning and the long-term stability of the optical output power and wavelength of the ECDLs. The collimated light of an ECDL is transmitted through an optical isolator[D6] (ISO) to prevent back-reflections of the components in the experimental set-up. Afterwards the beam is split into three parts by two 50 : 50 beam splitters[D7]. One part of the beam is fiber coupled and connected to the input of an optical spectrum analyzer (OSA)[D8] to measure the emitted absolute wavelength within a resolution of 50 pm. The second part is irradiated on a Fabry-Pérot interferometer[D9], which possesses a free spectral range of 10 GHz and measures the relative optical frequency with a high resolution. The remaining portion of the light is used to measure the optical output power of the ECDL with a power meter[D10]. To get rid of the losses due to the ISO and the beam splitters, the power meter is calibrated to the optical power just in front of the ISO.

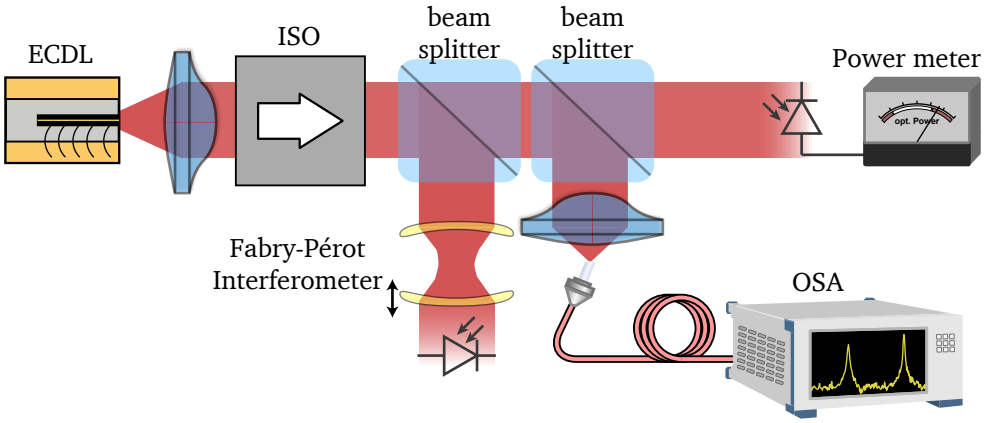

Figure 3.4.: Scheme of the experimental set-up, which is used to determine the frequency tuning and the long-time stability regarding the optical output power and wavelength of the developed ECDLs.

A central measure describing the fluctuations of the emitted intensity is the relative intensity noise (RIN). The RIN is defined as the ratio between the mean squared fluctuations of the optical power $\Delta P(t)$ and the squared average optical power P_0^2

$$RIN = \frac{\left\langle \Delta P(t)^2 \right\rangle}{P_0^2}. \tag{3.3}$$

The experimental set-up for RIN measurements is shown in Fig. 3.5. The radiation of a light source impinges on a self-made specially designed photodetector, which is described in detail in appendix C. This photodetector is capable to split the photocurrent induced at the photodiode under illumination of light in its DC and AC fractions and provides an amplified voltage proportional to the photocurrent at its DC

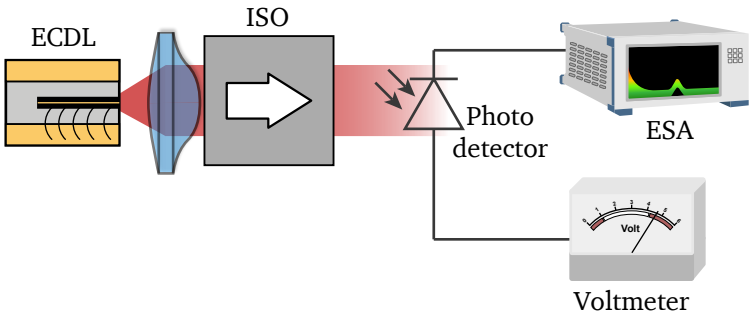

Figure 3.5.: Scheme of the experimental set-up, which is used to measure the RIN of the developed ECDLs.

and AC outputs. Because the incident optical power is proportional to the generated photocurrent at the photodiode Eq. 3.3 can be written as

$$RIN = \frac{\left\langle I^2_{photo,AC} \right\rangle}{I^2_{photo,DC}}. \tag{3.4}$$

The denominator is directly accessible by connecting the DC output of the photodetector to a multimeter which measures the DC output voltage U_{DC}. The AC photocurrent is measured frequency resolved in the range from 100 Hz to 1 MHz by connecting the AC output of the photodetector to an ESA[D11]. The ESA measures the electrical power P_{ESA} of the AC output of the photodetector, therefore the RIN can be calculated using

$$RIN = \frac{(P_{ESA}(f) - P_{noise}(f)) \cdot G(f)}{RBW \cdot U^2_{DC}} \cdot 1Hz, \tag{3.5}$$

where $P_{noise}(f)$ is the frequency dependent noise of the photodetector, $G(f)$ the gain factor correlating the AC power to the DC voltage and the RBW is the resolution bandwidth of the ESA. The lowest RIN value which can be measured is the shot-noise limit, which is proportional to $I^{-1}_{photo,DC}$

$$RIN_{SN} = \frac{2eB}{I_{photo,DC}}, \tag{3.6}$$

with e the elementary charge and B the detector bandwidth of 1 Hz. Besides shot noise there are several noise sources for LDs which can increase the intensity noise level, such as thermal, generation recombination, 1/f and random-telegraph noise [140]. Also the amount of optical feedback into a LD has an influence on its RIN values [141].

Another important characteristic of the developed ECDLs is the spectral linewidth, which is the width, typically the FWHM, of the optical spectrum. A popular method to obtain the linewidth of a laser is the so-called self-heterodyne linewidth technique developed by Okoshi et al. [142]. A scheme of the experimental set-up is shown in Fig. 3.6. At first, the output of the laser is split into two equal parts, from

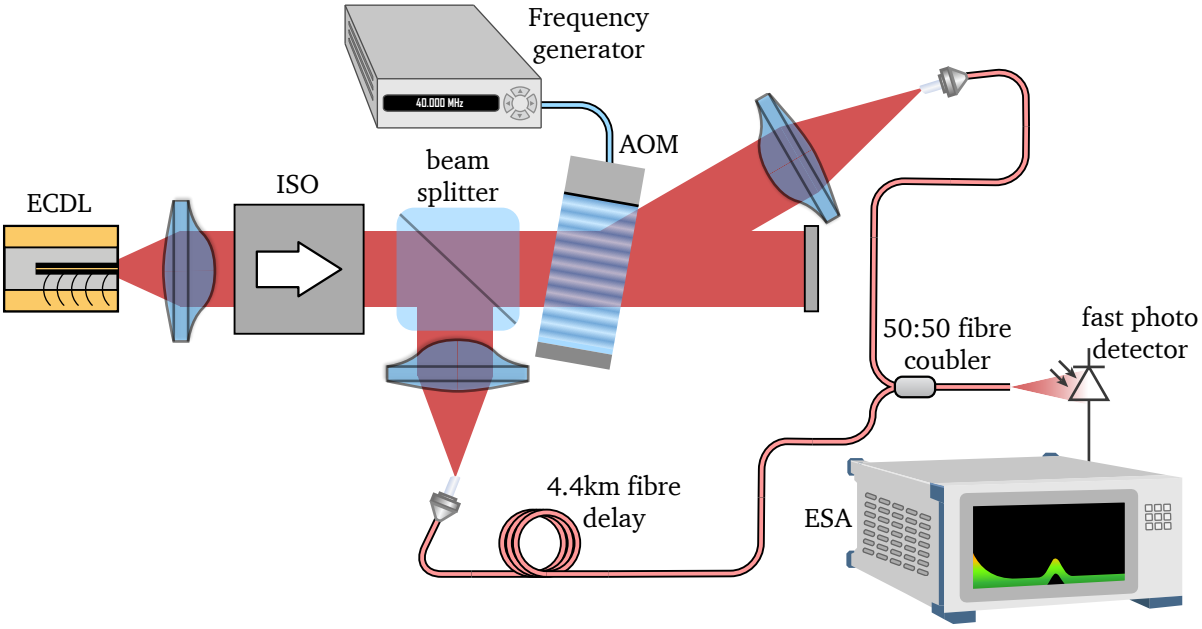

Figure 3.6.: Scheme of the self-heterodyne linewidth method, which is used to measure the spectral linewidth of the developed ECDLs.

which one part passes a sufficient long delay line of several kilometres. In this context sufficient long means a delay length longer than the coherence length of the laser, which in turn is directly correlated to the linewidth. The second part of the laser beam is sent through an acousto-optic modulator[D12] (AOM), which is driven by a constant frequency. The AOM causes a wavelength shift of the laser beam by its driving frequency and subsequently both parts of the laser beam are again superimposed. To ease the alignment and to provide a sufficient long delay line the beams are fiber coupled. The delay is realized by a 4.4 km long optical fiber and afterwards the beams are superimposed by a fiber beamsplitter[D13]. The resulting beat note is located at the driving frequency of the AOM and is measured using a fast photodetector[D14] and an ESA[D15]. Due to the long delay of one of the beams, the superimposed beams are uncorrelated and therefore the width of the beat note is twice the laser linewidth.

3.2. Experimental results

In this section, the results of the previously introduced characterization techniques are presented for the different laser systems. In total three different ECDLs are characterized and their capability to serve as laser source for the photomixing technique is examined. One LD[D16] (i) is integrated in the ECDL scheme using a grating as shown in Fig. 3.1(a). The second and third ECDLs consist of different LDs[D17],[D18] (ii & iii) and are extended by an external cavity using an IF as shown in Fig. 3.1(b). In order to investigate the possibility of a cost reduction of such an ECDL system one LD[D17] with a low and one LD with a moderate[D18] price is investigated. The price of LD[D18] used for ECDL (iii) amounts to 210€, while the LD[D17] used for ECDL (ii) only costs 15€.

3.2.1. Optical output power and spectra

First, the influence of the pump current on the optical output power and voltage of each ECDL is investigated. These characteristic curves are recorded using the experimental set-up shown in Fig. 3.4. The results for the grating ECDL and the two ECDLs using the IF are depicted in Fig. 3.7(a-c), respectively. The voltage curve (blue) for all the ECDLs exhibits the typical shape of a LD and is located between 1.4 and 2 V, from which on a current can flow thought the LD. This critical voltage depends on the semiconductor material bandgap. In the curve of the optical output power (red) first a small amount of amplified spontaneous emission is recognized for low pump currents. By increasing the current above the lasing threshold of the ECDL the optical output power increases fast. The deviation from a linear dependence between the intensity and the pump current originates from mode jumps during the measurement. The threshold current of ECDL (ii) and (iii) is located at 28 and 25 mA, respectively. Due to the optical feedback, these threshold currents are lower as in case of the free running LDs, which amount to 32 and 38 mA. At the maximum permitted pump current both ECDLs exhibit an optical output power above 70 mW. The grating-based ECDL (i) shows a higher threshold current as the previous two ECDLs. The threshold current amounts to 40 mA and the maximum achievable power reaches 26 mW.

After investigating the V-I and P-I curves, the spectral properties of the ECDLs are analysed. The wavelength of the grating-based ECDL (i) can be tuned either by a tilt of the grating or a displacement of the grating in z-direction via a piezo actuator. The first method allows a large tuning range of 14.5 THz as can be seen in Fig. 3.8(a). However, the tuning involves many mode jumps and is rather coarse. To achieve a much finer and mode jump free tuning of the ECDL the grating can be displaced via a piezo actuator. This is done by applying a voltage to the piezo actuator as can be seen in the inset of Fig. 3.8(b). The fine displacement of the grating causes a small mode hop-free frequency shift of the ECDL, which is measured using a Fabry-Pérot interferometer. Figure 3.8(b) reveals a linear dependency between the frequency shift and the applied voltage. A maximum tuning of 2 GHz is achieved by changing the voltage by 2.5 V. Beyond this tuning range, a further voltage increase leads to a mode jump as the free spectral range of the ECDL is exceeded. Such a fine-tuning mechanism is missing in the IF-based ECDLs. Here, only a coarse tuning of the frequency is achieved by a rotation of the IF. Also, the tuning range of 3.5 and 3.8 THz for the ECDL (ii) and (iii) is considerably smaller compared to the grating-based ECDL. This is especially caused by the decreasing transmission of the IF with larger rotation angles as can be seen in Fig. 3.2 and the AR coated LD of the grating-based ECDL. Besides the different frequency tuning ranges, all the developed ECDLs share a good side-mode suppression. As can be seen from the spectra in Fig. 3.8(a,c,d) no side modes are visible, which implies a suppression of greater than 40 dB.

The optical output power and wavelength of the three ECDLs monitored over a period of 8 hours are shown in Fig. 3.9 and Fig. 3.10, respectively. The grating-based ECDL (Fig. 3.9(a)) shows a complex behaviour of its output power during the whole time span. First, the laser emits on a single frequency and the power rises to a maximum from which on it decreases until multi-mode operation occurs. This pattern is repeated several times during the observation time, whereby the single-frequency emission time intervals increase. At the beginning of the measurement, one single-mode operation period lasts approximately 25 minutes, which increases to a duration of over 105 minutes. During the measurement time of 8 hours, the output power shifts by a total of ±5 % from the mean output power. While ECDL (i) oscillates around the mean output power and performs several switches between single- and multi-mode operation, ECDL (ii) and (iii) exhibit a slow drift towards lower output powers. With a slope of 0.1 %/h and a total drift smaller than 1 % in 8 hours, the output power of ECDL (ii) is very stable as can be seen in Fig. 3.9(b). Initially, ECDL (iii) exhibits a slow intensity drift of 0.04 %/h, which increase to 0.28 %/h

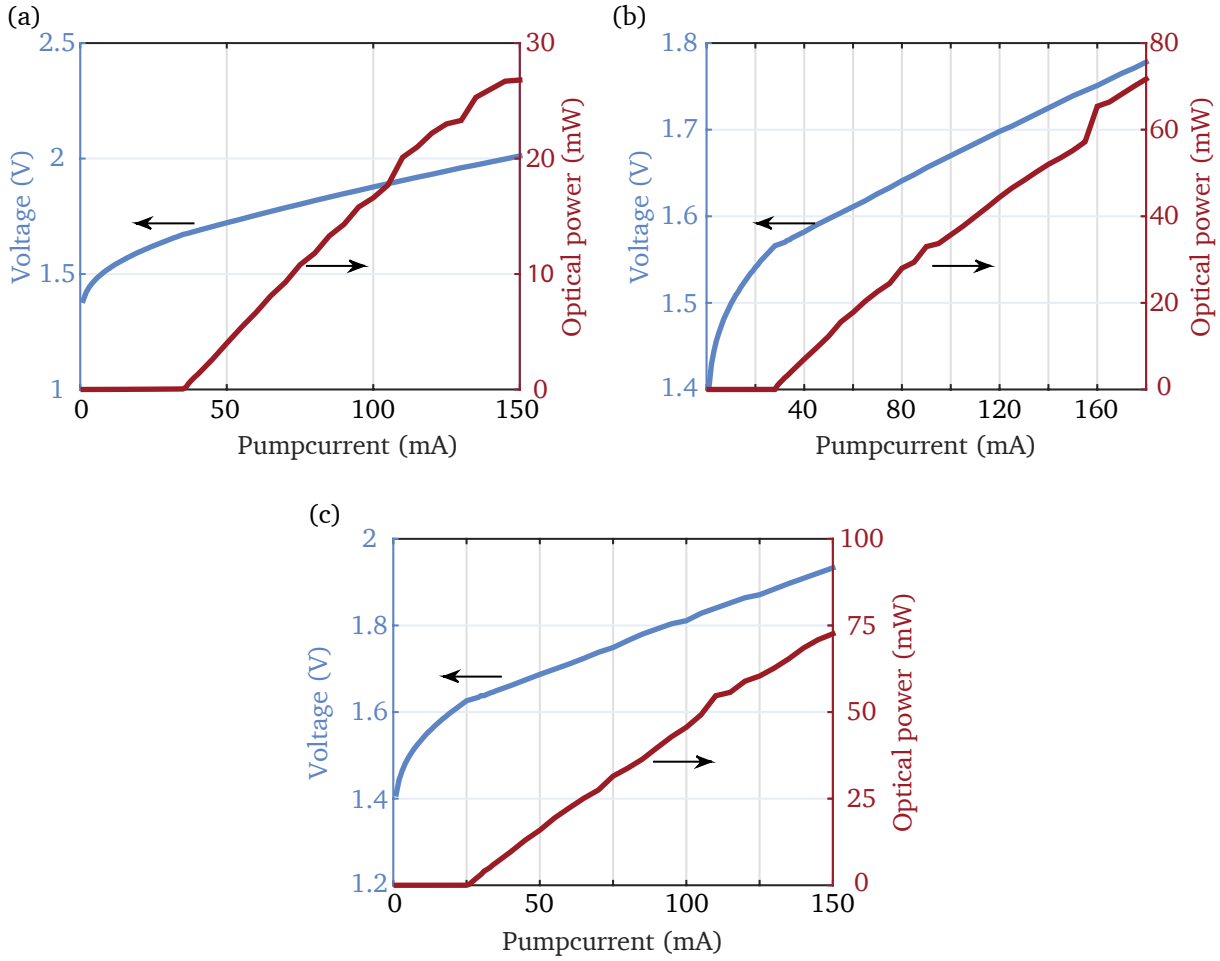

Figure 3.7.: Characteristic V-I (blue) and P-I (red) curves of the developed ECDLs. The graphs correspond to (a) the grating ECDL[D16] (i), (b) the first IF ECDL[D17] (ii) and (c) the second IF ECDL[D18] (iii).

after 150 minutes. Thus, a very low variation of the output power of 2 % over the full measurement time is achieved.

Next, the wavelength of the ECDLs is recorded over a period of 8 hours using an OSA. The central wavelength positions are obtained by a Gaussian curve fit to the measured spectra and are shown in Fig. 3.10(a)-(c) as drift from the initial wavelength at the beginning of the measurement. The zones of multi-mode emission of the grating-based ECDL are indicated by red areas in Fig. 3.10(a). While the periods of single-mode emission of the laser become longer, it seems that the duration of the multi-mode emission change randomly. During the measurement time, the ECDL performs several mode jumps, which

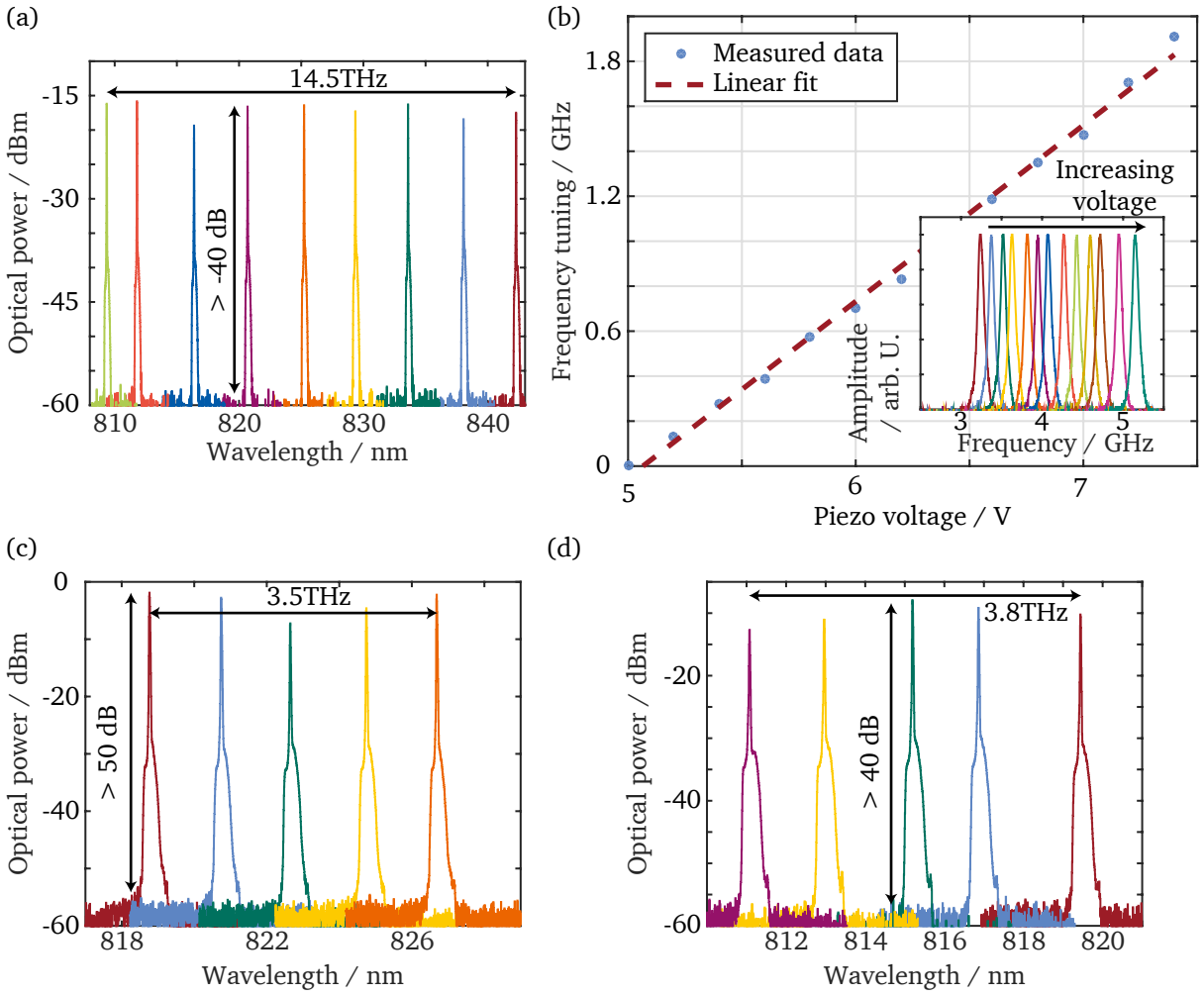

Figure 3.8.: Coarse (a) and fine (b) frequency tuning of the grating-based ECDL (i). The IF-based ECDLs only exhibit the possibility of coarse frequency tuning as shown for (c) ECDL (ii) and (d) ECDL (iii). The broad skirts at the bottom of the waveforms originate from a deviation of the ideal filter shape of the monochromator and the dynamic range of the OSA [143, 144].

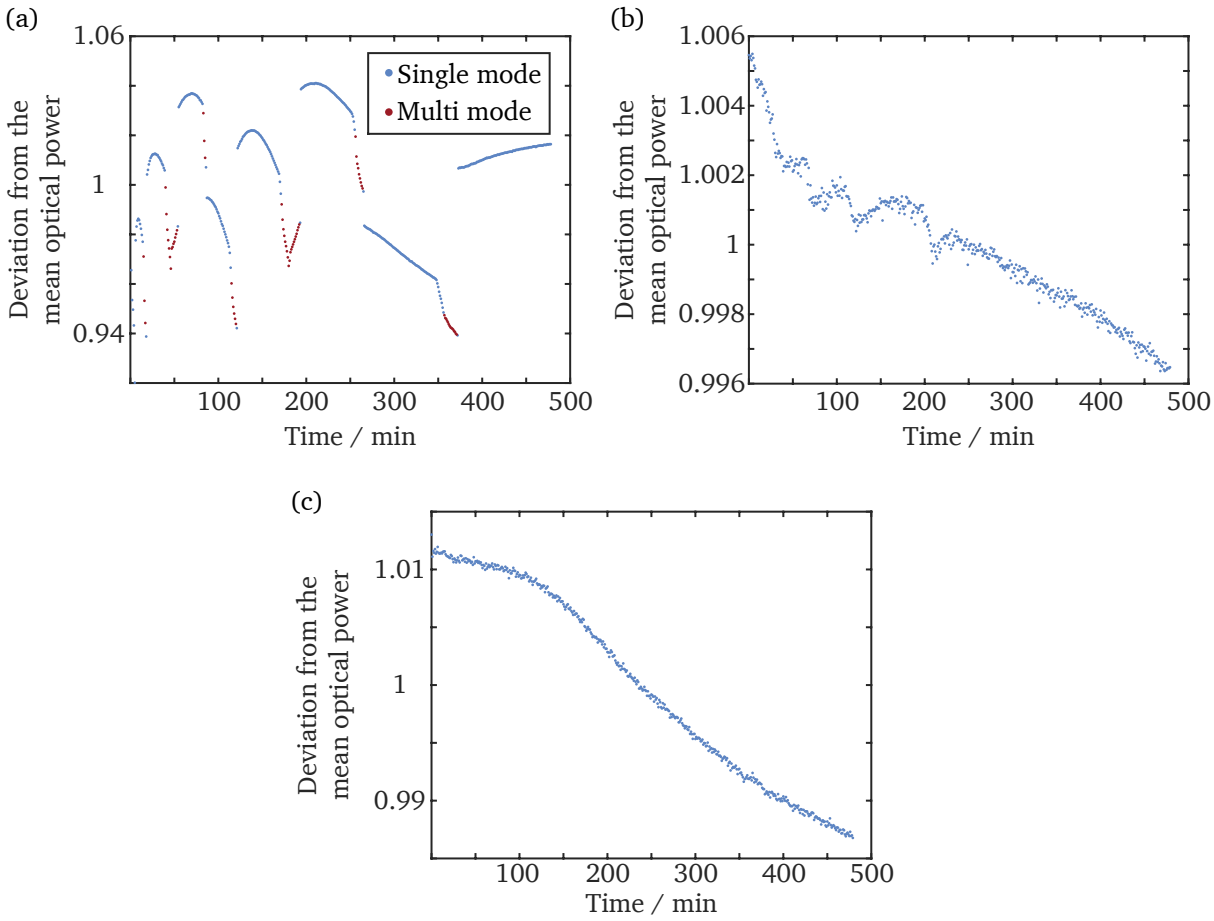

Figure 3.9.: Long time power stability of (a) ECDL (i), (b) ECDL (ii) and (c) ECDL (iii).

lead to a maximum deviation of 100 GHz from the initial laser frequency. During a stable single-mode emission period the frequency of the ECDL drifts only by several GHz, while this drift gets smaller with elapsed time. As also observed in the stability of the optical output power, the frequency drift of the IF-based ECDLs is significant smaller compared to the grating-based ECDL. Single-mode emission of both IF-based ECDLs is observed during the whole measurement time. In the first 150 minutes, the emission wavelength of ECDL (ii) undergoes a redshift of 4.8 GHz as shown in Fig. 3.10(b). Afterwards the emission frequency slowly drifts by approximately 1 GHz in the opposite direction. The smallest frequency drift is observed for ECDL (iii). Here, a constant drift towards higher frequencies is measured as shown in Fig. 3.10(c). During the observation time of 8 hours the ECDL only drifts by 1.6 GHz, which corresponds to a frequency drift of 3.3 MHz per minute.

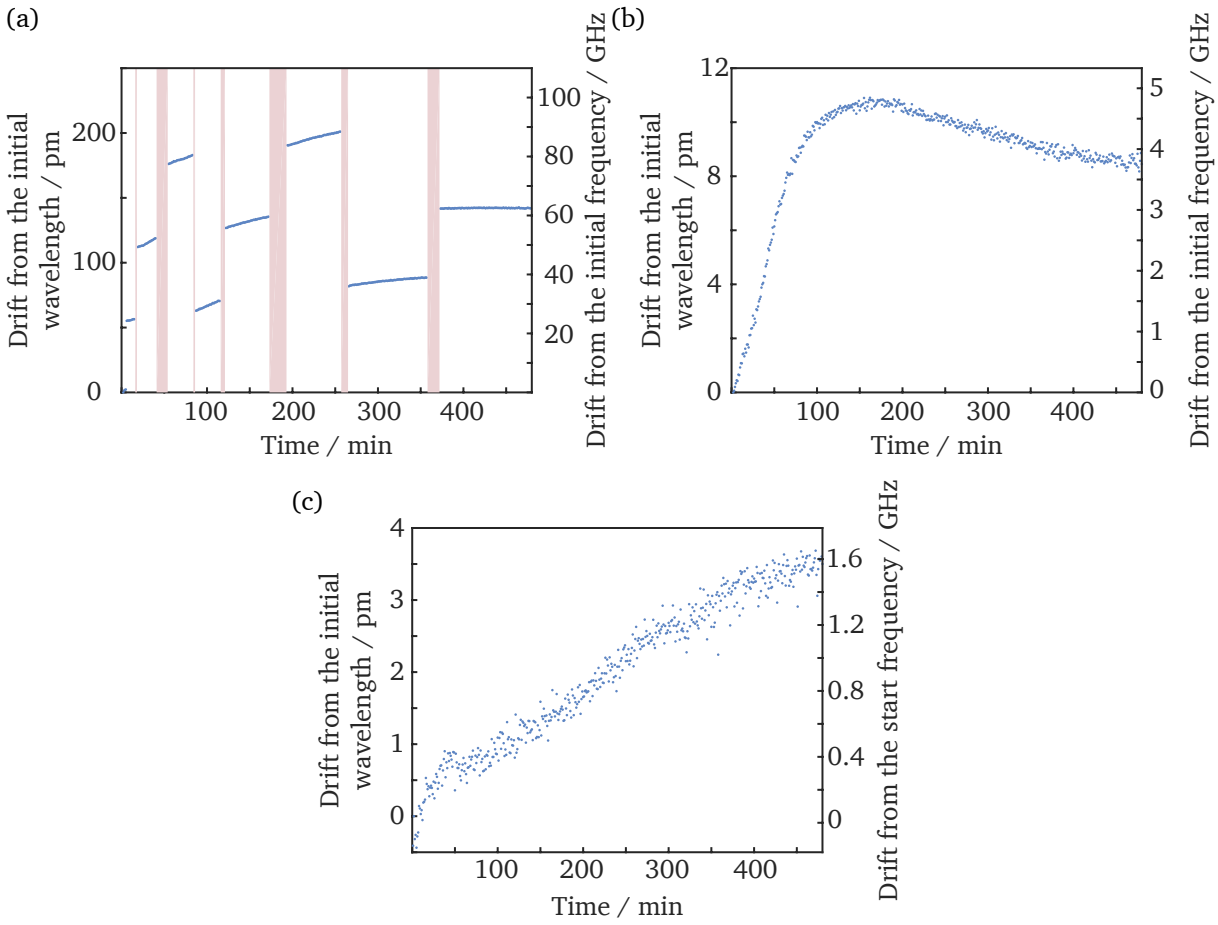

Figure 3.10.: Long time wavelength stability of (a) ECDL (i), (b) ECDL (ii) and (c) ECDL (iii).

3.2.2. Relative intensity noise and laser linewidth

Now that the temporal behaviour on long time scales regarding the optical spectrum and output power is known, the RIN and the linewidth of the developed lasers are investigated. The RIN and the linewidth represent fluctuations of the emitted intensity and frequency on short timescales, respectively. The RIN is measured within the frequency range of 100 Hz to 1 MHz and shown for the three ECDLs in Fig. 3.11. The shot noise RIN limit for each measurement amounts to −132 dB and the pump current of each ECDL is 150 mA. This low RIN value is still above the detection limit, as shot noise limited RIN measurements of the output of an LED is demonstrated down to −136 dB in appendix C using the developed detector. Starting with RIN values between −50 and −90 dB at a frequency of 100 Hz, all the ECDLs show a decreasing RIN with a 1/f dependency. A minimum RIN value of −100 dB is reached by each ECDL at a different threshold frequency. From this threshold frequency on the RIN remains constant at −100 dB until the maximum measured frequency of 1 MHz. However, the threshold frequency varies for each ECDL. With a threshold frequency of 10 kHz, the smallest value is achieved by the grating-based ECDL, followed by ECDL (iii) with a threshold frequency of 100 kHz. The highest threshold frequency with a value of 300 kHz is observed for ECDL (ii).

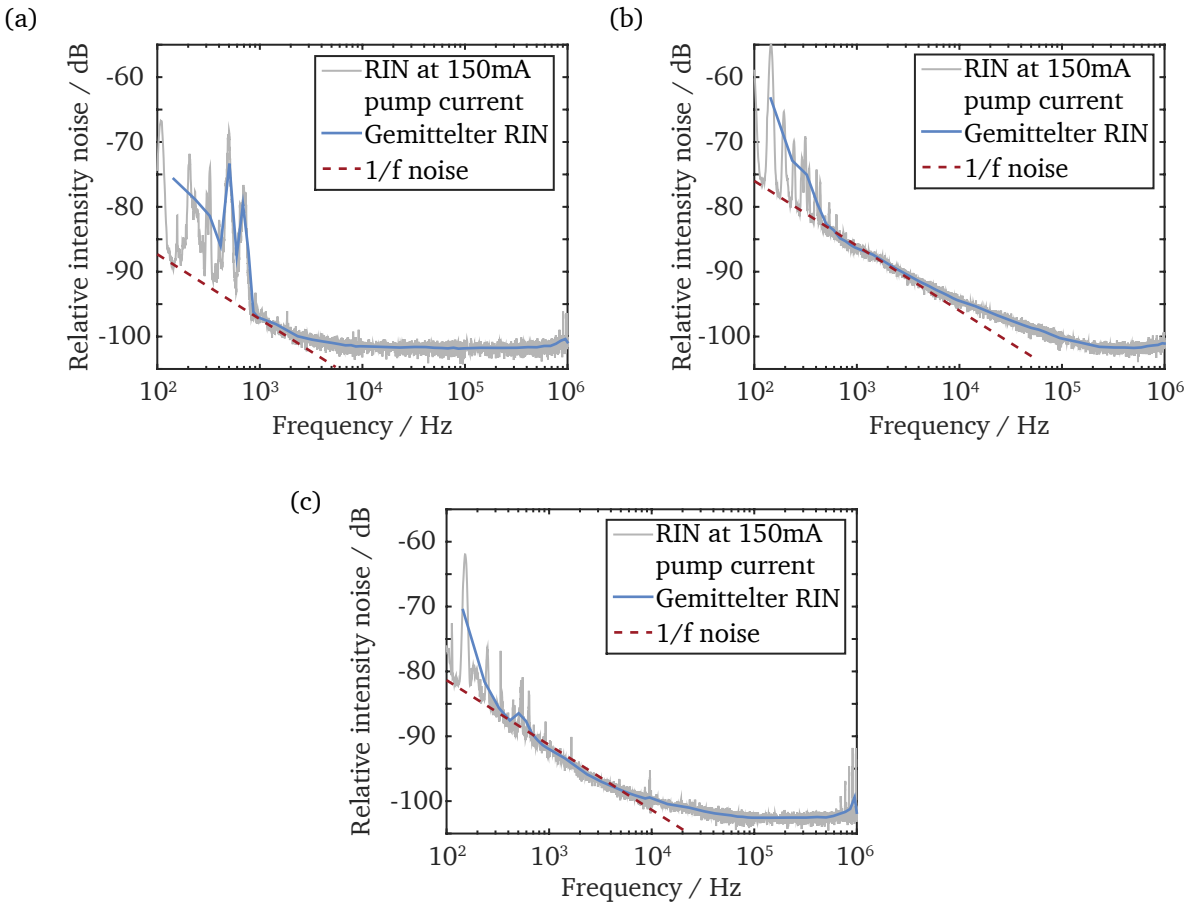

Figure 3.11.: RIN measured in the frequency range from 100 Hz to 1 MHz for (a) ECDL (i), (b) ECDL (ii) and (c) ECDL (iii), each pumped with a current of 150 mA. The grey curve represents the measured RIN, an average of 100 points is shown in blue and a 1/f behaviour is indicated by the dashed red line. In each case the shot noise limit amounts to −132 dB.

By using the self-heterodyne technique as described in the previous section, the beat signals for the three ECDLs are measured and are depicted in Fig. 3.12. A curve fitting using a Voigt profile is applied to the experimental data, from which the FWHM of each beat note is obtained. The curve fitting results are shown as dashed red curves in Fig. 3.12. The grating-based ECDL shows a relative broad beat note and a good agreement between the curve fitting and the measured data. From the FWHM of the beat note the linewidth Δf of the laser is calculated using [145]

$$\Delta f \approx 0.5 \cdot \left(0.5346 f_L + \sqrt{0.2166 f_L^2 + f_G^2}\right). \tag{3.7}$$

Here, f_L and f_G are the FWHM of the Lorentzian and Gaussian curves associated with the Voigt profile. For the grating-based ECDL, the spectral linewidth is calculated to 128 kHz. Compared to that relatively broad linewidth, both IF-based ECDLs show much narrower beat signals. The ECDLs (ii) and (iii) achieve low spectral line widths of 7.5 and 17 kHz, respectively. These two linewidth correspond to the coherence

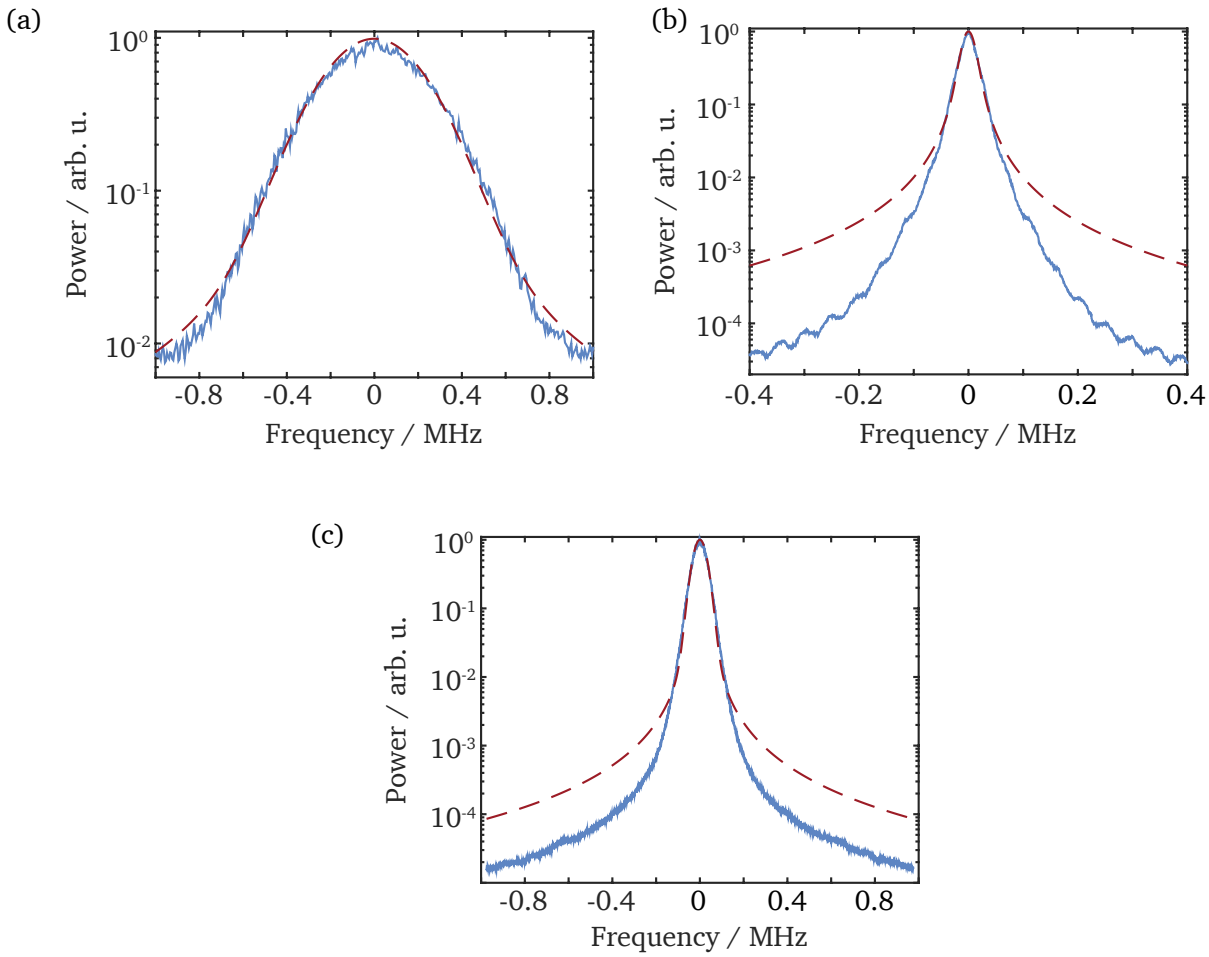

Figure 3.12.: Self-heterodyne beat signal for (a) ECDL (i), (b) ECDL (ii) and (c) ECDL (iii) pumped with a current of 150 mA. The measured data are plotted in blue, while the curve fitting of the measurements to a Voigt profile is presented as dashed red curve.

lengths of 12.7 and 5.6 km, which in the first case is longer and in the second case is in range of the fiber delay length. The fiber delay is realized by a 4.4 km long optical fiber, which corresponds to a delay length of approximately 6.4 km assuming a refractive index of 1.45 for the fiber core. As mentioned in the previous section the self-heterodyne technique gets inaccurate if the delay length is smaller than the coherence length of the laser, because the superimposed laser beams are still correlated to each other. This can be modeled using a sophisticate model as introduced in [146, 147]. As can be seen in Fig. 3.12(c), the shape of the beat note first falls apart from the Voigt profile at its left and right tail, if the coherence length of the laser matches the delay length. By further increasing the coherence length of the laser, the tails of the beat note show small oscillations [147] as can be seen in Fig. 3.12(b). In general, the linewidth calculated using the FWHM of the Voigt profile is too small if the coherence length of the laser exceeds the delay length. The length of the used fiber, and the resultant delay time can be described as a maximum achievable measurement time or a corresponding minimum frequency. This implies that the impact on

the line width of frequencies below this minimum frequency is not comprised in the measurements. As a result the obtained line width is too small due to the existence of low frequency noise as it is often found for LDs [148]. This is the case for the beat notes measured for ECDL (ii) and (iii). Therefore their linewidth is estimated to be in the range of 15 kHz, which corresponds to a coherence length equal to the fiber delay length.

3.3. Summary and conclusion

Two different ECDL designs, one including a grating and one including an IF, were investigated in this chapter. Table 3.1 summarizes the results of the characterization methods applied to the three developed ECDLs. The ECDLs (ii) and (iii) use the same IF-based scheme as depicted in Fig. 3.1(b) but incorporate different LDs. However, the performance of both IF-based ECDLs was found to be quite similar. Both provided a high optical output power with a good long term stability and a low RIN. Also, their spectral long term stability with a drift in the range of several GHz during 8 hours of observation was found to be sufficient for the targeted photomixing experiments. The small spectral linewidth of the ECDLs which was located in the lower kHz frequency range paves the way for high resolution spectroscopy in the terahertz wavelength region using the photomixing technique.

The grating-based ECDL exhibited a spectral linewidth of 128 kHz, which was found to be ten times higher than the linewidth of the IF-based ECDLs. Nevertheless, this is sufficient for the targeted photomixing experiments and the ECDL (i) convinced with its large coarse frequency tuning range of 14.5 THz and a fine tuning of 2 GHz. Such a fine tuning mechanism is completely missing in the IF-based ECDLs and also the coarse frequency tuning range of the devices are by far lower. Further, the grating-based ECDL convinced with its low $1/f$ threshold frequency in its RIN spectra. But a main concern was the long term stability of the device. Here, the ECDL switched between single- and multi-mode emission and performed several mode jumps during the observation time. From the long term stability investigations it seemed that the ECDL needs a relatively long warm up phase before operating constantly in the single-mode operation regime. Since the targeted terahertz imaging experiments require measurement times of a few hours, the IF-based ECDLs are here clearly superior.

The following investigations on the photomixing technique in the next chapters require two laser sources emitting radiation near a central wavelengths of 820 nm. Further the wavelength difference of the two lasers needs to be tunable from 0.2 to 2.2 nm to generate terahertz radiation in a frequency range of 0.1 to 1 THz. To operate the PCAs an optical power of up to 30 mW will be required. These demands are all fulfilled by the investigated ECDLs, allowing for the generation of terahertz radiation using the photomixing technique.

Table 3.1.: Comparison between the grating-based (i), the IF-based ECDL[D17] (ii) and the IF-based ECDL[D18] (iii).

	grating-based ECDL (i)	IF-based ECDL (ii)	IF-based ECDL (iii)
Maximum optical output power	26 mW	70 mW	75 mW
Frequency tuning	14.5 THz coarse and 2 GHz fine	3.5 THz coarse	3.8 THz coarse
Side-mode suppression	> 40 dBm	> 50 dBm	> 40 dBm
Long term stability of the output power	±5%, switches between single- and multi-mode emission	1%	2%
Long term stability of the frequency	100 GHz, switches between different modes	4.8 GHz	1.6 GHz
RIN	1/f behavior until a threshold frequency of 10 kHz. Afterwards −100 dB	1/f behavior until a threshold frequency of 300 kHz. Afterwards −100 dB	1/f behavior until a threshold frequency of 100 kHz. Afterwards −100 dB
Linewidth	128 kHz	$\leqslant 15$ kHz	$\leqslant 15$ kHz

4. Photomixing

After the detailed characterization of the laser systems, the output of two ECDLs is superimposed to generate an optical beat signal. As descried in section 2.2 this beat signal is then converted into terahertz radiation using the photomixing technique. Three PCAs with different "gap" designs and packaging are investigated in this section. The first two PCAs are based on LT-GaAs chips with a gold structure deposited on one side, which are kindly provided by Dr. M. Mikulics from the Institute of Thin Films and Interfaces at the Research Centre Jülich. The gold structures consist of a logarithmic spiral antenna with different gap designs in its center. An image taken under a microscope of the two investigated LT-GaAs chips B08 and M75/117 is shown in Fig. 4.1. The logarithmic spiral antennas possess a diameter of approximately 1.13 mm and have three turns. In its center, the antennas are separated into two parts by a gap of 16 μm

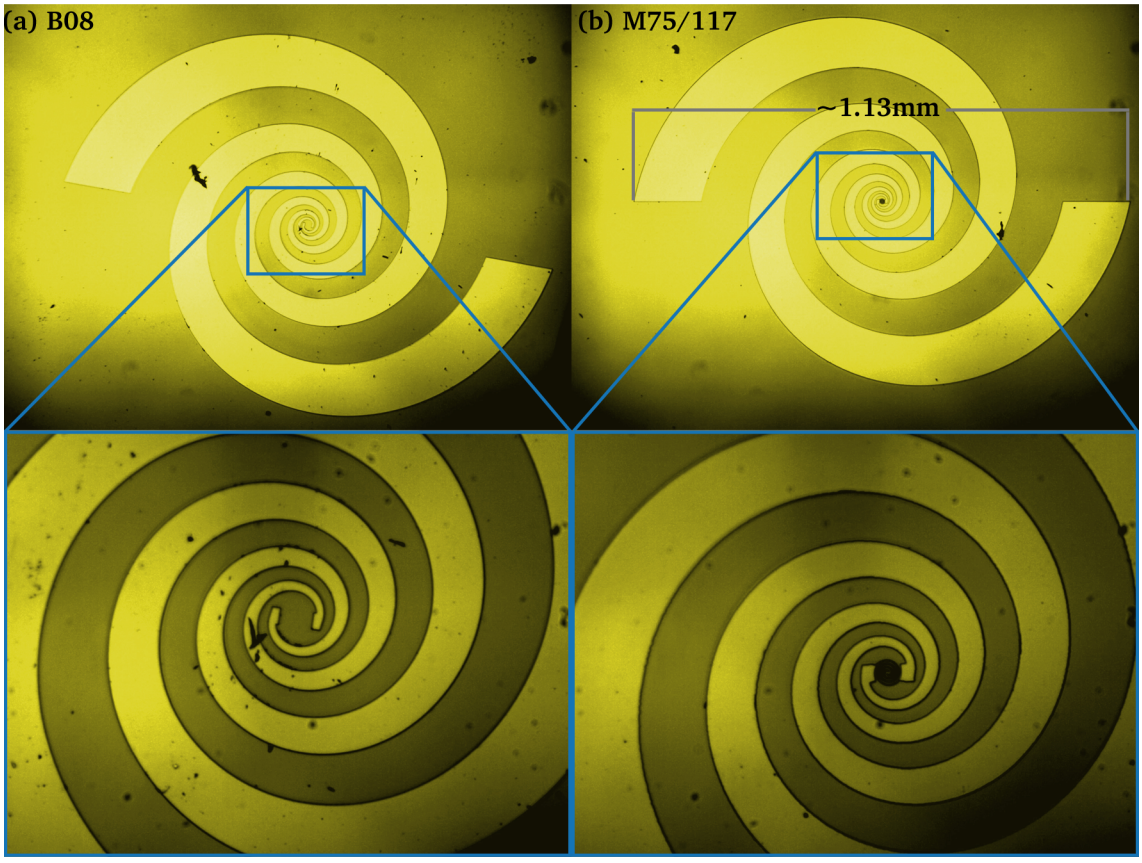

Figure 4.1.: Photograph of the two investigated LT-GaAs chips B08 and M75/117 taken under the microscope. On both chips a golden logarithmic spiral antenna with three turns is deposited. In its center, the antennas are separated into two parts by differently designed gaps.

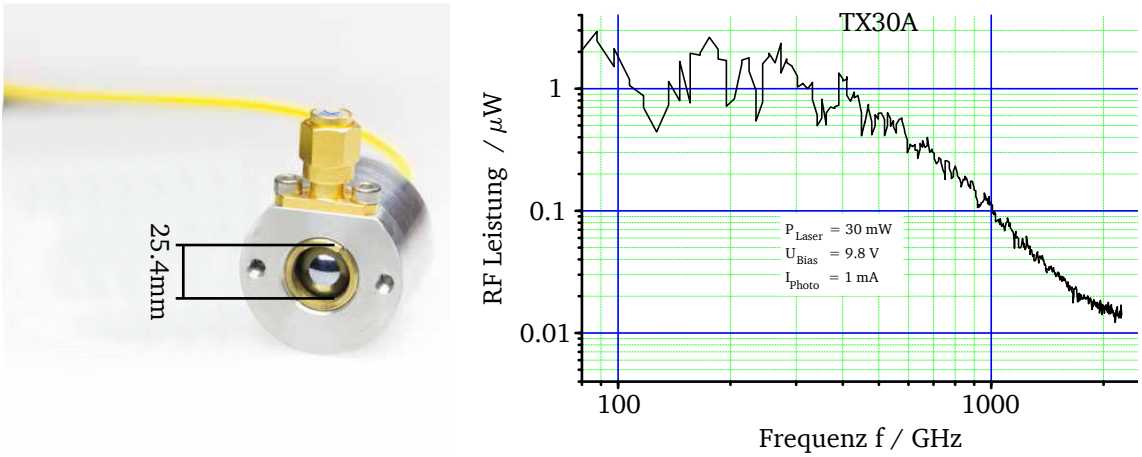

Figure 4.2.: (left) Photograph of the commercially available packaged TOPTICA Photonics PCAs. (right) Measured output power of the investigated TOPTICA Photonics PCA TX30A in dependence on the radiation frequency. Both images are provided by TOPTICA Photonics.

and 12μm width for the chips B08 and M75/117, respectively. While chip B08 exhibits a blank gap between the two antenna parts, chip M75/117 shows a tiny spiral structure between the two antenna parts, which only gets apparent with a further microscope magnification as can be seen in the bottom of Fig. 4.1(b).

To improve the handling of the small LT-GaAs chips and in order to realize an electrical contact, the chips are mounted on a printed circuit board (PCB). For this purpose, a hole with a diameter slightly larger than the PCA antenna diameter is drilled in the center of a 4×4 cm large PCB. Then, the PCA chip is glued on the insulating backside of the PCB with the golden antenna structure looking through the hole. The conducting side of the PCB is separated into two electrically isolated parts. Each end of the antenna is electrically contacted to one of the electrical parts of the PCB by a tiny gold wire using a wire bonder[D19] machine, which was kindly provided by Prof. Alff and introduced by Dr. Komissinskiy both from the Technische Universität Darmstadt. The packaging of the PCA chips is completed by a focusing silicon lens[D20] with a focal length of 50 mm, which is mounted on the plain GaAs side of the chips. The focusing HRFZ-Si lens is pressed on the GaAs surface using four springs and focuses the terahertz radiation 50 mm in front of the PCA. Further the lens is important to improve the out-coupling efficiency on the plain GaAs backside of the PCA chip as described in section 2.2.

The third investigated PCA is a commercially available fully packaged and fiber coupled PCA[D21] provided by TOPTICA Photonics in collaboration with Dr. A. Deninger. A photograph of the packaged device is shown on the left side of Fig. 4.2. Like the chips B08 and M75/117, the TOPTICA PCA also consists of an LT-GaAs chip and a logarithmic spiral gold antenna with three turns. But the gap between the two antenna parts is designed with interdigitated finger electrodes. Further the PCA is also equipped with a focusing HRFZ-Si lens, generating a focal point of the terahertz radiation at a distance of 40 mm in front

of the PCA.

A characterization of the output power of the PCA at a bias voltage of 9.8 V and with an impinging optical power of 30 mW of the laser beat signal is shown on the right hand side of Fig. 4.2. This measurement is provided by TOPTICA Photonics and in the following serves as benchmark for the Jülich PCAs. The PCA exhibits a very high terahertz output power of up to 3μW below 300 GHz. For higher frequencies the output power rapidly decreases and reaches approximately 20 nW at 2 THz.

4.1. Experimental set-up

A scheme of the experimental set-ups used for the characterization of the investigated PCAs is shown in Fig. 4.3 and Fig. 4.4. In both cases the light of two ECDLs passes each an ISO and is subsequently fiber coupled. The radiation inside the fibers is superimposed by a fiber beamsplitter[D13], generating the optical beat signal at the difference frequency of the two ECDLs. One part of the radiation is coupled to the emitter PCA, where the polarization of the radiation is controlled by two 3-paddle polarization controllers attached to the fibers before the fiber beamsplitter. In case of PCA B08 and M75/117, the radiation is focused onto the gap of one of the emitter PCAs using a lens[D22] with a focal length of 11 mm.

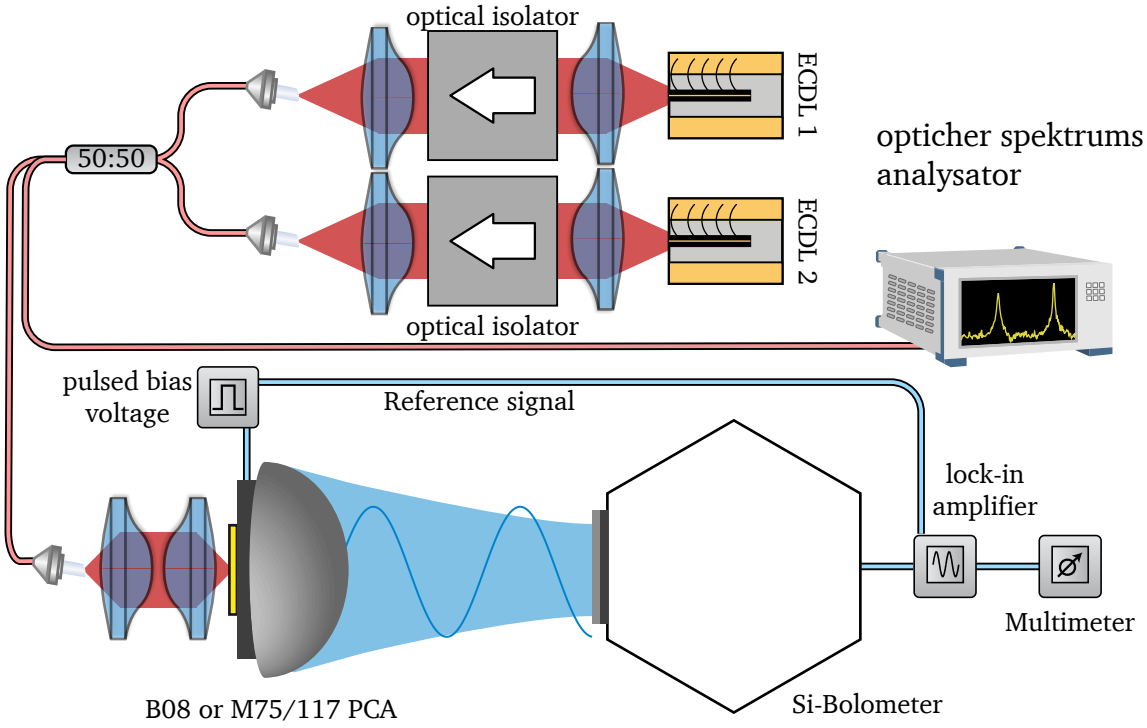

Figure 4.3.: Experimental set-up used for the characterization of the PCAs B08 and M75/117. The optical beat signal is focused onto the gap of a biased PCA, while the output power of the generated terahertz radiation is measured using a Si-Bolometer[D24].

Further, in both cases the PCAs are biased with a pulsed AC voltage using a pulse generator[D23]. The modulation frequency is given by the cutoff frequency of the employed detection technique. Therefore, a modulation frequency of 80 Hz is chosen for the detection scheme using the bolometer[D24] shown in Fig. 4.3 and 20 kHz for the heterodyne experiment shown in Fig. 4.4. In both cases a duty cycle of 50% is chosen.

In case of the intensity measurement using the bolometer (Fig. 4.3), the second output of the fiber beamsplitter is directly connected to an OSA[D8] to monitor the emitted wavelength and power of the ECDLs. The terahertz radiation generated by the PCA B08 or M75/117 is directly focused onto the bolometer by the mounted Si-lens. The voltage output of the bolometer and the reference signal of the pulse generator are connected to a lock-in amplifier[D25], which extracts the amplitude of the voltage signal at the given reference frequency. According to the manual of the bolometer, this amplitude is correlated to the power of the detected terahertz radiation by $\approx 2.4 \times 10^5 \frac{V}{W}$. In order to read out the voltage with the computer, the voltage of the lock-in amplifier monitor output is measured using a digital multimeter[D26].

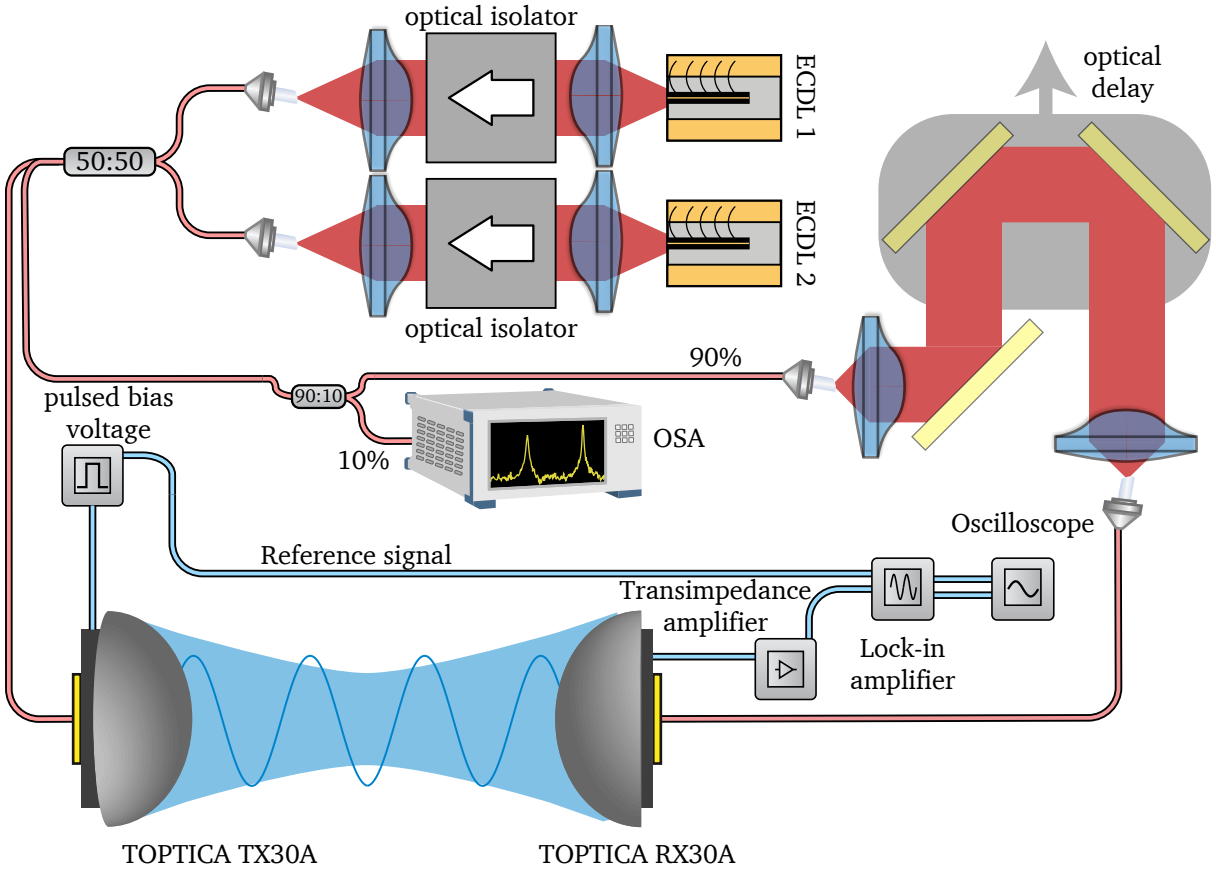

Figure 4.4.: Scheme of a heterodyne experiment employing the fiber coupled TOPTICA TX30A PCA as emitter and the RX30A as receiver. This set-up is used for a phase sensitive detection of the generated terahertz radiation.

For the heterodyne experiment, the second output of the fiber beamsplitter is further split using a 90 : 10 fiber beamsplitter[D27]. The output providing 10% of the radiation is used to monitor the emitted wavelength and power of the ECDLs using an OSA[D8]. The remaining 90% are out-coupled using a fiber collimation package[D28] and pass an optical delay line. The delay line is realized by two mirrors mounted on a linear translation stage[D29] as shown in Fig. 4.4. After the linear translation stage the light is again coupled into a polarization-maintaining optical fiber and connected to the receiver PCA. By the linear translation of these two mirrors the phase of the optical beat signal relative to the phase of the generated terahertz radiation both impinging on the receiver PCA can be varied. In contrast to the emitter PCA, the receiver PCA is not biased and the current generated by the simultaneously impinging terahertz radiation and beat signal at the receiver PCA is amplified by a transimpedance amplifier[D30]. The output of the transimpedance amplifier and the reference signal of the pulse generator are connected to a lock-in amplifier[D25], which extracts the amplitude and phase of the voltage signal at the given reference frequency. In order to simultaneously record the amplitude and phase of the lock-in amplifier, both monitor outputs are connected to an oscilloscope[D31].

4.2. Results and discussion

First, the two Jülich PCAs B08 and M75/117 are investigated using the experimental set-up depicted in Fig. 4.3. Since no specifications for the PCAs are given, the maximum optical power of the beat signal and applied bias voltage are kept low to avoid damage to the PCAs. The output power of the generated terahertz radiation is measured for increasing bias voltages at a beat signal power of 15 mW. The bias voltage is increased from 0.1 to a maximum of 5 V and the terahertz power is measured using the bolometer. The resulting measured terahertz powers are shown in Fig. 4.5(a) for the PCA B08 (blue) and PCA M75/117 (red) for a difference frequency of 0.15 THz. Each measurement point represents the mean value of 60 successively in an interval of 1 s taken measurements of the bolometer voltage. The error bars in Fig. 4.5(a) are given by the standard deviation of these 60 measuremnts. As a guide to the eye, the solid lines represent a curve fitting to

$$P_{THz} = a \cdot V^2 + b, \tag{4.1}$$

where a and b are the curve fitting parameters and V is the bias voltage of the PCA. As predicted by Eq. 2.8, both PCAs show a quadratic dependency of their output power as a function of the applied bias voltage. PCA M75/117 exhibits a maximum output power of 0.96 nW at a bias voltage of 5 V, whereas the irradiated terahertz power from PCA B08 is 17 % smaller and amounts to a maximum of 0.82 nW.

Next the difference frequency of the two ECDLs is gradually tuned from 0.15 to 1.05 THz and for each frequency the emitted power of the PCAs is measured by the bolometer. The results are shown in Fig. 4.5(b). Again each measurement point represents the mean value of 60 measurements, but the error bars are omitted in the plot to preserve clarity. Over the entire frequency span PCA M75/117 exhibits a higher or even output power compared to PCA B08. The maximum output power for PCA M75/117 and PCA B08 is achieved at about 0.2 THz and amounts to 9 nW and 5 nW, respectively. Going to higher difference frequencies, the output power of both PCAs rapidly drops with $1/f^2$. Due to the higher output power of PCA M75/117 a signal at the bolometer is still detectable until a frequency of 0.8 THz, while the maximum frequency of PCA B08 amounts to 0.5 THz. It is notable that the frequency dependent

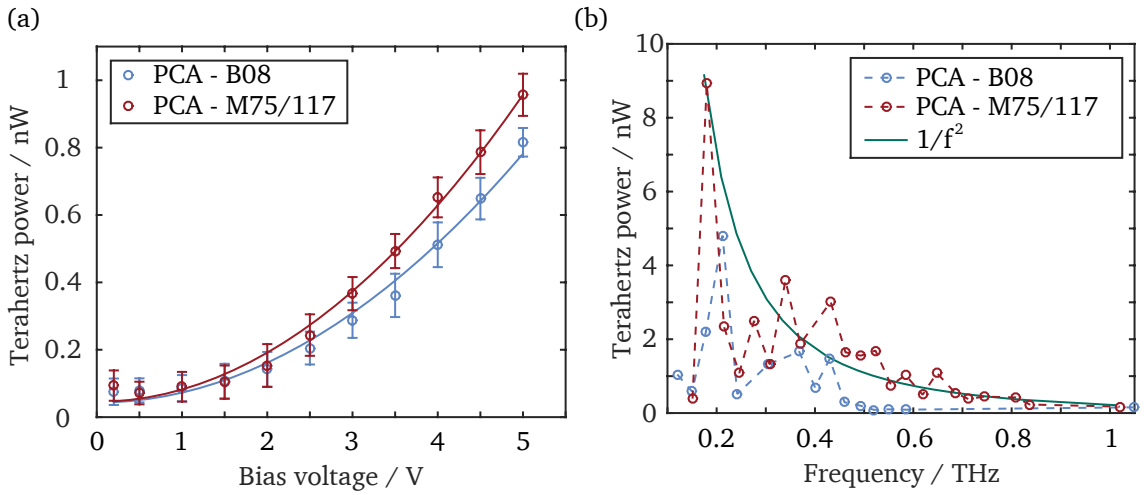

Figure 4.5.: Characteristics of the investigated PCA structures B08 and M75/117. (a) Dependency of the irradiated terahertz power of both PCAs at a difference frequency of 0.15 THz on the applied bias voltage. (b) Frequency dependent emission of both investigated PCAs at a bias voltage of 5 V. In all measurements the intensity of the optical beat signal amounts to 15 mW.

output power of PCA M75/117 exhibits local power maxima displaced by frequencies between 60 and 90 GHz. The reason for this modulation of the output power is unclear at this point and needs further investigations. On the one hand, the reason for this observation could be a resonance of the structure of the investigated PCA, but on the other hand effects of the bonding and mounted Si-lens can not be excluded.

A second method to detect the terahertz radiation generated by a PCA, is the so called heterodyne detection. Here, the amplitude and phase of the terahertz radiation is detected by a second PCA serving as receiver as depicted in Fig.4.4. A bias voltage of 9 V and an optical power of 22 mW is applied to the emitter PCA, while no bias and an optical power of 15 mW is applied to the receiver PCA. The terahertz radiation generated at the emitter is focused between the two PCAs and again collected by the receiver PCA. While the optical beat signal generates free carriers at the receiver PCA, the impinging terahertz radiation accelerates these carriers resulting in a current flow. This current is proportional to the power of the terahertz field P_{THz} and depends on the phase between the optical beat signal and the electric field of the terahertz radiation, which is given by the optical delay z. Further the current is amplified by a transimpedance amplifier with the gain G_{TIA}, such that the measured voltage is given by

$$V_{THz}(z) = G_{TIA} \cdot I_0(P_{THz}) \cdot cos\left(2\pi \frac{z + z_0}{\lambda}\right) + a. \tag{4.2}$$

Here, $I_0(P_{THz})$ is the current generated by the terahertz field at the receiver, z_0 is the initial phase difference introduced by the optical delay, λ is the wavelength of the terahertz radiation and a includes a small offset of the signal introduced by the lock-in amplifier and needed for the curve fitting.

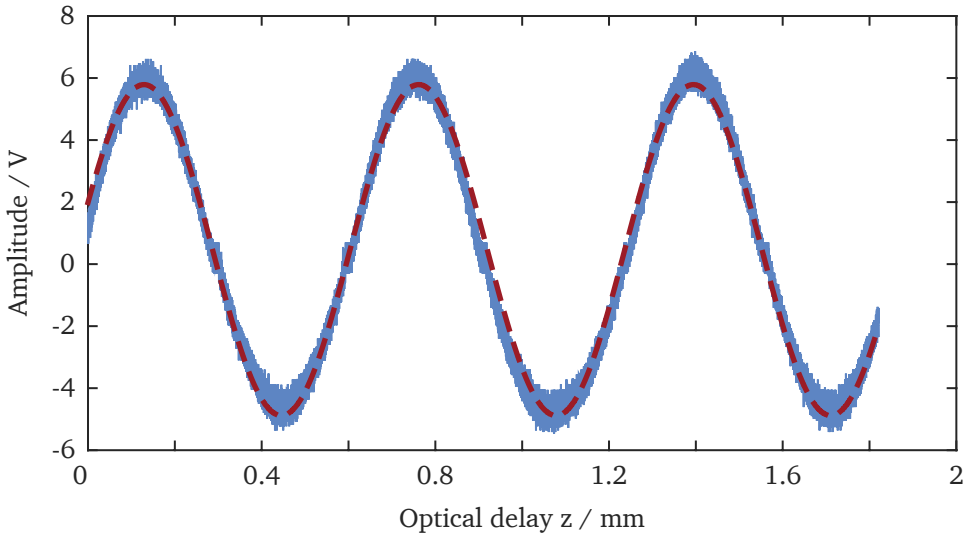

Figure 4.6.: Signal amplitude measured at the receiver PCA RX30A in dependency on the optical delay for a difference frequency of 0.45 THz. The measurement is represented by the solid blue data, while a curve fitting to Eq. 4.2 is shown as dashed red curve.

The measured signal for a difference frequency of 0.45 THz is shown in Fig. 4.6 using the TOPTICA Photonics emitter and receiver PCAs. The optical delay is scanned from 0 to 1.8 mm and as described in Eq. 4.2, the measured amplitude exhibits a sinusoidal shape. Curve fitting of the experimental data to Eq. 4.2 yields a periodicity of 0.63 μm of the signal, which is in good agreement with the expected terahertz wavelength of 0.66 μm calculated from the optical spectra of the two ECDLs. The heterodyne detection scheme represents a very sensitive method to detect both amplitude and phase of the terahertz radiation. Further it operates at room temperature and is capable to measure small signals because of its good dynamic range, which amounts to 80 dB at 0.1 THz and 70 dB at 0.5 THz [149]. The receiver PCA only provides a signal if both optical beat signal and the electric field of the terahertz radiation are temporally overlapping. Therefore, background radiation, which is not in phase averages to zero, which enables high signal-to-noise values of this detection scheme. The noise-equivalent power (NEP) of such a heterodyne detection scheme is in the order of $2E^{-14}\frac{W}{\sqrt{Hz}}$. This corresponds to a one order smaller NEP compared to the NEP of the utilized liquid helium cooled bolometer, which amounts to $1.3E^{-13}\frac{W}{\sqrt{Hz}}$.

4.3. Summary and conclusion

In this chapter a common photomixing scheme for the generation of terahertz radiation was investigated and two different detection methods were applied. Two Jülich PCAs were examined with respect to their emitted terahertz power, which was detected using a liquid helium cooled bolometer. The output power of the PCAs reached a maximum value of 9 nW near 0.2 THz for the PCA M75/117. This is less than 1/100 of the output power provided by the commercial available PCA TX30A. Even if the Jülich PCAs were operated at a lower bias voltage and optical intensity, this advance of the commercial available PCA can not be compensated by an increase of the operation parameters for the Jülich PCAs. Thus, a heterodyne detection scheme was realized using the PCAs provided by TOPTICA Photonics demonstrating

the phase sensitive terahertz detection at room temperature. Due to the high output power of the PCAs provided by TOPTICA Phonics, these excellent PCAs will be used for the subsequent experiments.

5. Homodyne self-mixing

In the previous chapter the photomxing technique has been demonstrated using a PCA for the conversion of an optical beat signal into terahertz radiation. The generated terahertz radiation has been either detected by a second PCA or a liquid helium cooled bolometer. In order to reduce the complexity, costs and number of necessary components of the terahertz experiment, a newly developed concept using the source of radiation simultaneously for the generation and detection of the radiation will now be employed. This concept is well established for lasers, where a portion of the laser radiation is fed back into the laser, which at the same time serves as detector [150, 151]. In the terahertz frequency domain, a promising progress towards improving the compactness of terahertz set-ups has been achieved by combining the terahertz source (transmitter) and detector (receiver) into one device as realized for example by QCL self-mixing [106]. Very recently, a similar approach for the generation and detection of broadband terahertz pulses has been reported involving a complex set-up that includes two fs-lasers and a single PCA [152]. In this chapter a terahertz spectroscopy concept is demonstrated by combining both CW-terahertz radiation generation and phase-sensitive detection in one PCA, which results in a significantly reduced complexity and cost of the terahertz spectroscopy set-up.

5.1. Experimental set-up

The compact experimental set-up is depicted schematically in Fig. 5.1. Two IF-based tunable ECDLs are coupled into polarization-maintaining single-mode fibers and are superimposed by a fiber beamsplitter[D13]. The resulting optical beat signal impinges on the fiber-coupled PCA[D21]. The Toptica PCA features an interdigitated finger structure and a logarithmic spiral antenna with three turns, which emits the terahertz radiation at the difference frequency of the two lasers. A Si-lens focuses the terahertz beam approximately 40 mm behind the PCA with a beam waist w_0 of around 0.56 mm (for 0.54 THz). The PCA is electrically connected to a 9 V battery that provides a constant bias voltage. A revolving chopper wheel[D32](RCW) mounted on a linear translation stage[D29] is placed within the Rayleigh length of the terahertz radiation, which is estimated to about 1.8 mm for a terahertz-wave frequency of 0.54 THz. Its surface generates a back-reflection that is modulated at a chopping frequency up to 2.6 kHz. The size of the selected chopper wheel apertures range from 3 mm to 10 mm and are chosen to minimize diffraction limiting effects [153]. Via the translation stage the phase between the laser beat signal and the back-reflected terahertz radiation is varied. The back-reflection gives rise to an AC photocurrent in the PCA, which is modulated with the frequency of the chopper wheel. This current signal is electrically amplified by a transimpedance amplifier[D30] which separates AC and DC current contributions and amplifies the alternating current by a factor of 10^5 V/A. The output signal of the transimpedance amplifier and the electrical reference frequency of the chopper wheel are fed to a lock-in amplifier and the resulting amplitude and phase signals are monitored on a digital two-channel oscilloscope[D31].

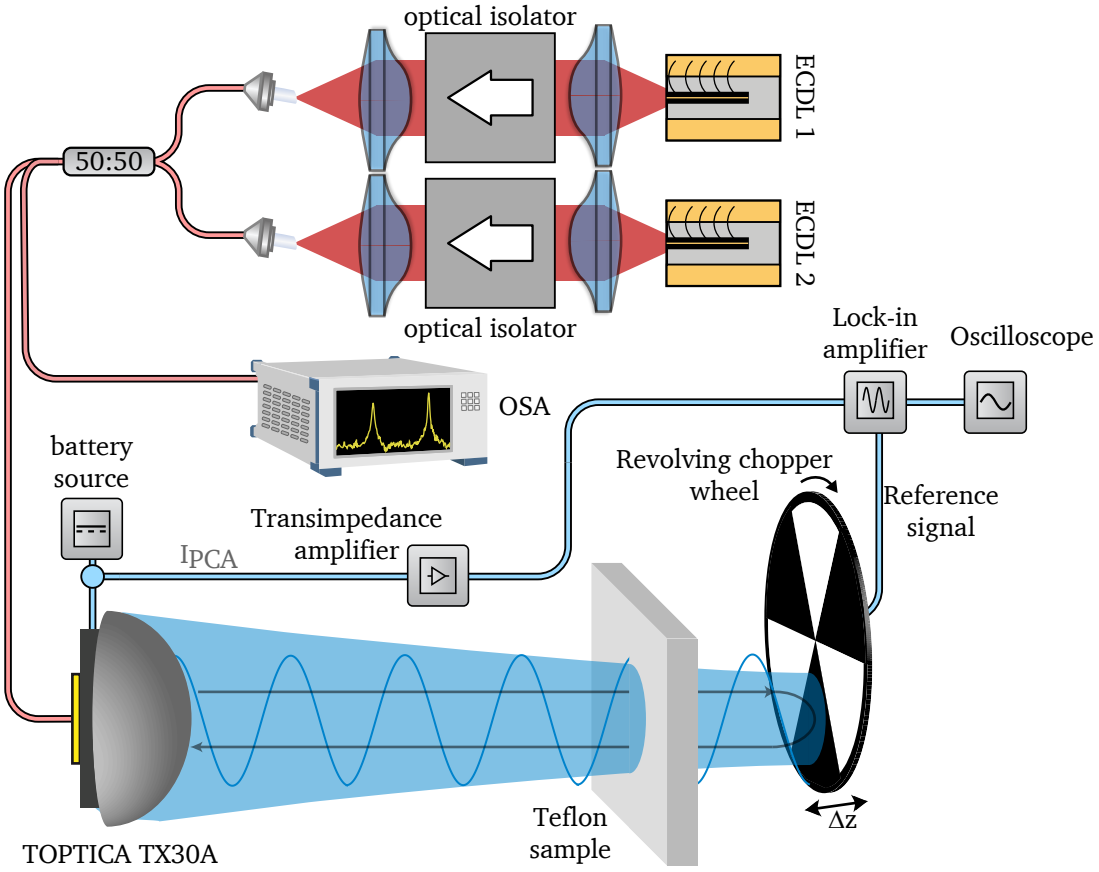

Figure 5.1.: Schematic of the homodyne self-mixing experimental set-up. The terahertz radiation generated by the PCA is back-reflected by a revolving chopper wheel and is detected by the same PCA.

5.2. Results and discussion

The amplitude and phase signals recorded with the oscilloscope are shown in Fig. 5.2(a) and (b) in dependence on the RCW displacement for a terahertz frequency of 0.54 THz, respectively. The amplitude of the signal reveals a squared sinusoidal shape with a periodicity of 130 μm. This periodicity corresponds to approximately four times the wavelength of terahertz radiation. In the phase signal a periodicity of 260 μm is recognized, in which the phase undergoes one discrete switch from $-10°$ to $+150°$, which indicates a sign change of the signal.

To understand these signals in the following the HSM approach is modeled and the time-dependent total current $I(t)$ in the PCA as the product of the induced terahertz voltage $V(t)$ and electrical conductance $G(t)$ is calculated. The time-varying conductance $G(t)$ is modulated at the beat frequency of the two lasers

$$G(t) = G_{Dark} + G_{THz} \cdot (1 + sin(\omega t)), \tag{5.1}$$

where G_{Dark} is the conductance without any laser radiation impinging on the PCA, ω is the frequency of the beat signal and G_{THz} is the conductance proportional to the total average laser power. Besides

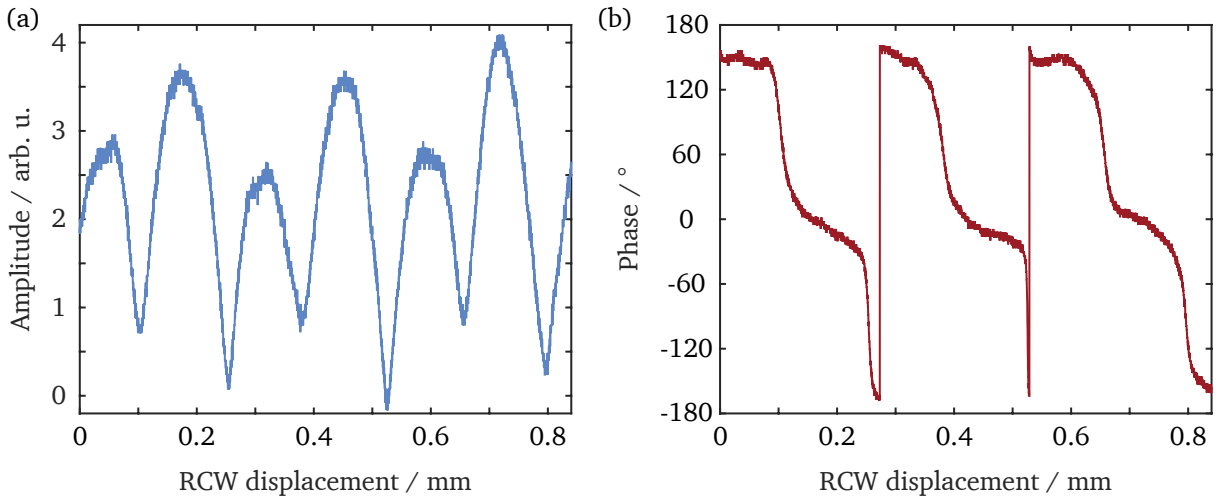

Figure 5.2.: Measured (a) amplitude and (b) phase of the HSM signal at a difference frequency of 0.54 THz.

the constant bias voltage V_0 applied to the PCA, a time- and terahertz phase-dependent voltage $V_{FB}(t)$ is considered, which is induced by the back-reflected terahertz radiation. Considering the voltage $V_{FB}(t)$ with its proportionality factor V_{FB0} the following expression for the total current is obtained

$$\begin{aligned} I(t,\phi) &= G(t) \times V(t) = G(t) \cdot (V_0 + V_{FB0} sin(\omega t + \phi)) \\ &= G_{Dark} V_0 + G_{THz} V_0 + G_{THz} V_0 sin(\omega t) \\ &- \frac{V_{FB0} G_{THz}}{2} cos(2\omega t + \phi) + (G_0 + G_{THz}) V_{FB0} sin(\omega t + \phi) \\ &+ \frac{V_{FB0} G_{THz}}{2} cos(\phi). \end{aligned} \tag{5.2}$$

The mean value of this current on time scales much longer than the period of the terahertz wave is then given by

$$\langle I(t,\phi) \rangle_{t>>T_{THz}} = G_{Dark} V_0 + G_{THz} V_0 + \frac{V_{FB} G_{THz}}{2} cos(\phi). \tag{5.3}$$

The last term in Eq. 5.3 provides information on the path length traveled by the terahertz wave to the RCW and back, since $\phi = 2ks$, where k is the wave number of the terahertz field and s is the displacement of the RCW. Figure 5.3(a) depicts the total instantaneous PCA current in the time-domain for a back-reflected wave of 0.539 THz, calculated from Eq. 5.2 with typical values of 0.04 μS, 1 μS and 1 mV for G_{Dark}, G_{THz} and V_{FB} respectively and omitting the DC contribution of V_0.

In Fig 5.3, the total current clearly exhibits a non-vanishing mean value on time scales much longer than the terahertz period, caused by the nonlinear product in Eq. 5.2. Furthermore, with increasing displacements a decreasing mean current is found, which is indicated by a decreasing minimum towards

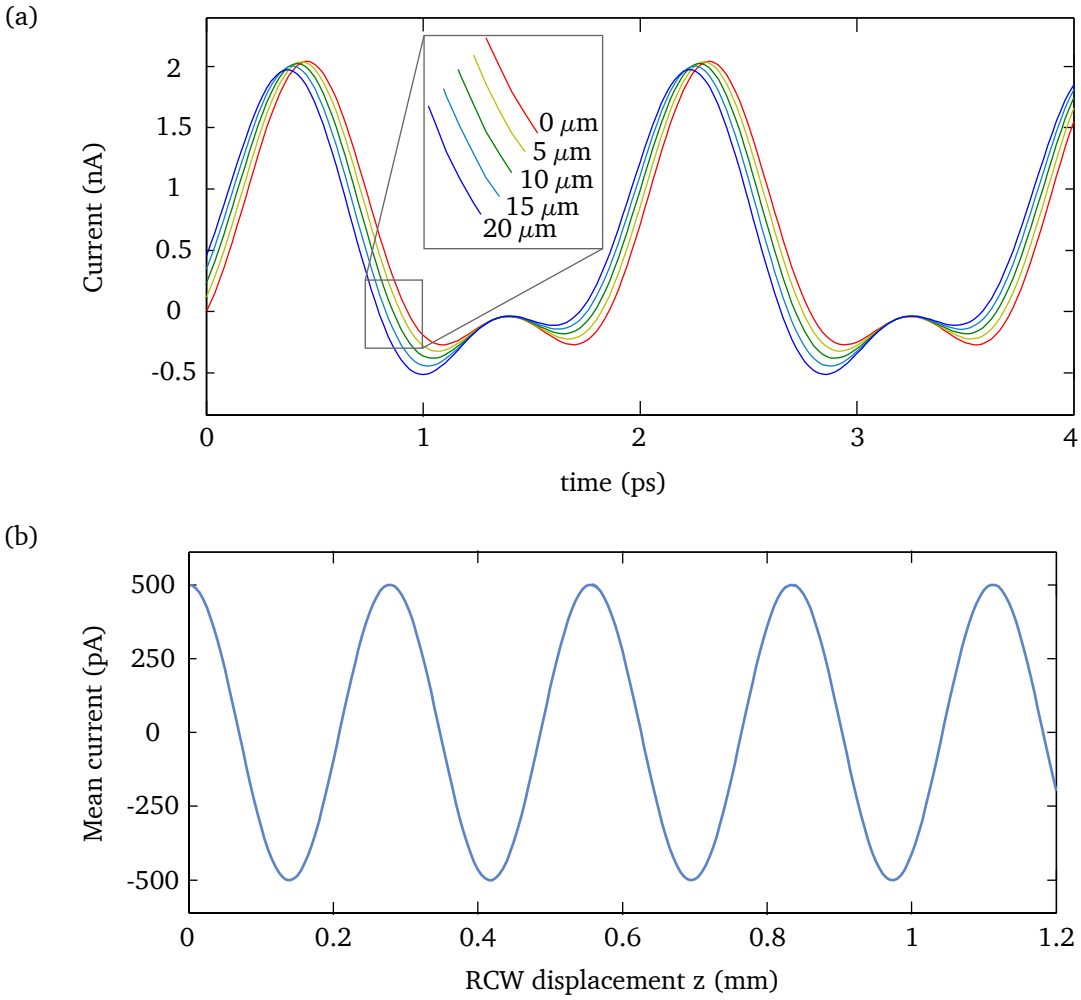

Figure 5.3.: Simulations of the photocurrent induced in the PCA by a back-reflected 0.539 THz wave. (a) Calculated PCA current for a RCW displacement of 0, 5, 10, 15 and 20 μm using Eq. 5.2, but neglecting the contribution of the constant bias voltage V_0. (b) Calculated mean PCA current versus RCW displacement on time scales much longer than the terahertz period using Eq. 5.3.

higher displacements depicted in Fig. 5.3(a). The calculated mean current within the PCA over a displacement from 0 to 1.2 mm and for a back-reflected terahertz wave with a frequency of 0.539 THz exhibits a sinusoidal shape with a period of $\lambda/2$, which is depicted in Fig. 5.3(b).

From these theoretical considerations, the measured signals of the (a) amplitude and (b) phase shown in Fig. 5.2 can be understood. The amplitude shows a periodicity of 130 μm, which corresponds to a quarter of the wavelength of the emitted terahertz radiation. As can be seen in Fig. 5.3(b) the HSM signal switches its sign with a periodicity of half of the terahertz wavelength. This agrees with the experimentally observed phase switches in Fig. 5.2(b) and the amplitude periodicity.

In order to obtain the phase-dependent HSM signal, which is proportional to the electric field of the back-reflected terahertz wave, the measured amplitude (Fig. 5.2(a)) is multiplied numerically with the cosine of the phase (Fig. 5.2(b)). This yields the HSM signal as shown in Fig. 5.4(b), which resembles the calculated results shown in Fig. 5.3(b). The experimentally obtained HSM signal for the frequencies of 0.167 and 0.539 THz are depicted in Fig. 5.4(a) and (b) respectively as a function of the spatial displacement of the RCW. The RCW is translated over 3 mm and 1.2 mm with a constant velocity of 40μm/s. A nearly sinusoidal signal with a periodicity of half of the terahertz wavelength is evident, since the optical delay of the terahertz wave corresponds to twice the RCW displacement. Fitting a sine function to the data yields the periods of 903 μm for the 0.167 THz signal and 275 μm for the 0.539 THz signal. This is in good agreement with the values of 898 μm and 278 μm which are expected from the wavelengths of the terahertz radiation. These detected HSM signals originate from interference generated by the nonlinear product of the back-reflected terahertz wave and the time-dependent conductance of the PCA as described in the theoretical considerations.

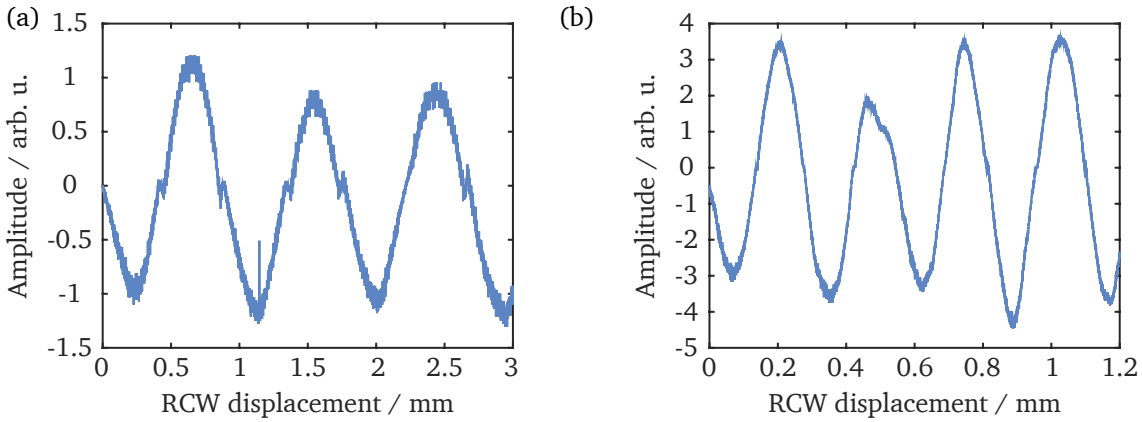

Figure 5.4.: HSM signals in dependency of the RCW displacement for two difference frequency of (a) 0.167 THz (b) 0.54 THz.

In order to exploit the phase-sensitivity of the presented HSM method and thus to validate the proposed method, now a measurement of the refractive index of Teflon is performed. Teflon samples of different thickness are placed between the PCA and the RCW as indicated in Fig. 5.1. The terahertz frequency is tuned to 0.167 THz, thus a periodicity of the HSM signal of 898 μm is expected. For each sample the HSM signal is recorded over a linear translation of the RCW by 3 mm, with each scan starting from the same position. The experimental results are plotted in Fig. 5.5 for selected Teflon samples of thickness $d_1 = 1.1$ mm (a), $d_2 = 9.8$ mm (b) and $d_3 = 10.85$ mm (c), while the reference measurement without Teflon sample is shown in Fig. 5.4(a). All of the traces show the expected sinusoidal shape of the HSM signal with a periodicity of 903 μm. The phase of the HSM signals varies with the sample thickness which can be explained by the different optical path lengths of the terahertz wave within the sample. In fact, the total terahertz path consists of 3 contributions:

- The base displacement of the RCW (s_0)
- The path travelled through the linear translation stage (z)

- The additional optical path length by the Teflon sample ($d \times (n-1)$)

To retrieve the refractive index of Teflon at 0.167 THz, a curve fitting of the experimental data to the following set of equations is performed:

$$I(z, d_i) = I_0(d_i) \cdot cos\left(\frac{4\pi}{\lambda}\left[s_0 + z + (d_i + \Delta d(d_i)) \cdot \left(n_{Teflon} - 1\right)\right]\right), \tag{5.4}$$

$$i \in \{0, 1, 2, 3\}\,. \tag{5.5}$$

Here, I_0 denotes the amplitude of the HSM signal, λ the terahertz wavelength, d_i the geometric thickness of the Teflon sample measured with a caliper, Δd a correction factor considering a possible uncertainty of this thickness measurement and n_{Teflon} the real part of the refractive index of Teflon. Parameters determined by the curve fitting are I_0, $\Delta d(d_i)$, n_{Teflon}, s_0 and λ, while the thickness d_i of the Teflon samples is given by measurements using a caliper. The result of the curve fitting is plotted in Fig. 5.5 as red dashed curve together with the experimental data. A good qualitative agreement between modeling results

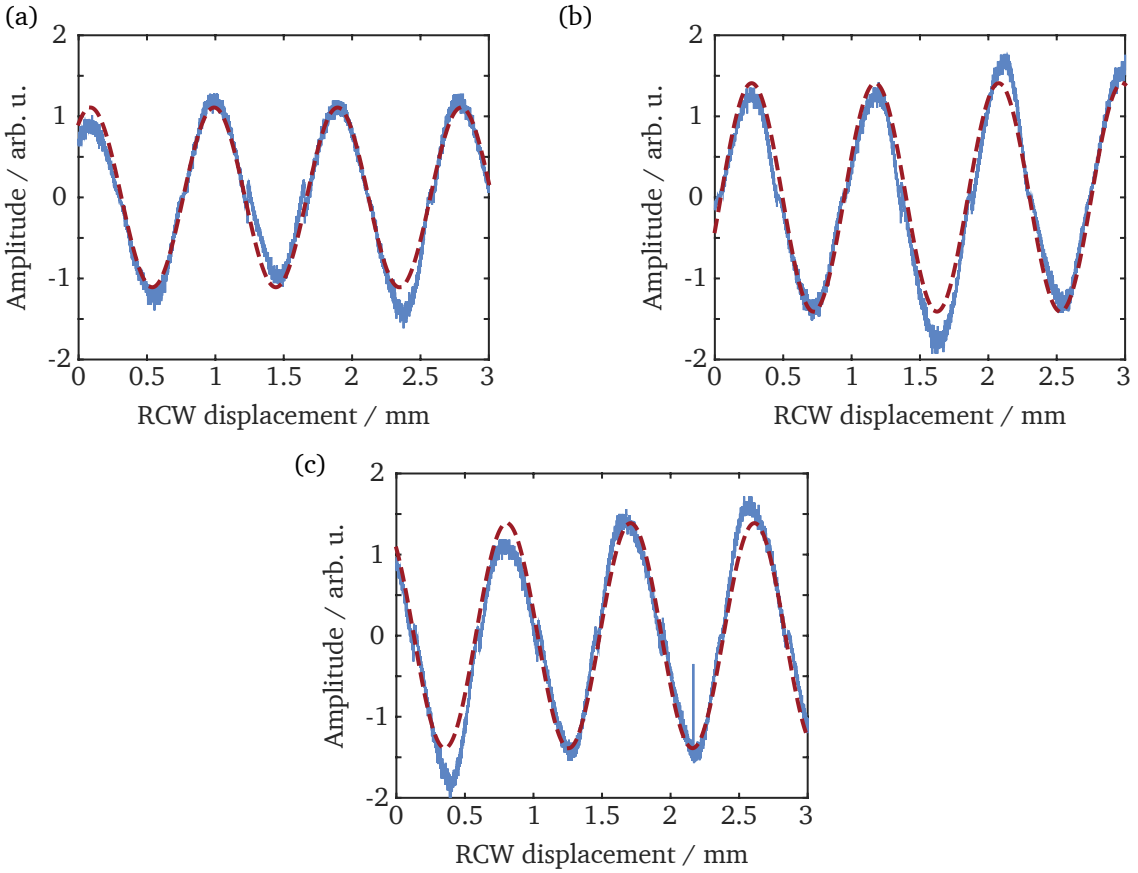

Figure 5.5.: Measured HSM signals as a function of the displacement z of the RCW for selected Teflon samples of thickness (a) $d_1 = 1.1\,\text{mm}$, (b) $d_2 = 9.8\,\text{mm}$ and (c) $d_3 = 10.9\,\text{mm}$ (solid blue). The dashed red curves are the result of a curve fitting according to Eq. 5.4.

Table 5.1.: Curve fitting parameters used for the determination of the refractive index of Teflon. i denotes the Teflon sample index, where $i = (1, 2, 3)$ corresponds to the sample thicknesses of $(1.1, 9.8, 10.9)$ mm .

Parameter	Value
Amplitude of HSM signal:	
I_0(no Teflon)	0.95
$I_0(d_i)$	1.11, 1.41, 1.39
Thickness correction $\Delta d(d_i)$ for Teflon sample	(291, 42, −103) μm
Start displacement of RCW s_0	40 mm
Wavelength of terahertz radiation λ	1807 μm
Refractive index of Teflon n_{Teflon}	1.41

and experiment is obtained for the individual Teflon samples. A summary of the evaluated parameters is given in Tab. 5.1.

The curve fitting yields a terahertz wavelength of 1807 μm. Although the obtained value of Δd_1 is surprisingly high, which could be attributed to possible deviations of the ideally plane sample surface or deposits on the surface, the value of the achieved terahertz wavelength agrees within 0.6% with the calculated wavelength of 1796 μm, which is derived from measurements of the optical spectra of the two lasers. It is notable that the amplitudes $I_0(d_i)$ of the HSM signal increase with thicker Teflon samples placed between the PCA and the RCW. At first, this indicates that the absorption coefficient of Teflon at the chosen wavelength of 1807 μm is very low. Second, an increase in the amplitude indicates a slight misalignment between the initial RCW position s_0 and the focal point of the terahertz radiation, which is corrected by the additional optical path length through the thick Teflon samples. A reason for this misalignment could be the deviation of the focal length position at a wavelength of 1807 μm compared to the theoretical distance of 40 mm from the PCA. This deviation arises from the 'active region' of the logarithmic spiral antenna, which emits the major part of the terahertz radiation. Due to constructive and destructive interference of the radiation, the size of this region turns out to be frequency-dependent. With increasing wavelength respectively lower frequency, the area of this region increases [154, 155], which leads to a more distant virtual point source. The last parameter obtained by the curve fitting yield the refractive index of Teflon, which amounts to 1.41 at 0.167 THz. This is very close to the literature value of 1.44 [156].

In order to give an estimate of the responsivity (R_{ep}) and noise equivalent power (NEP) of the HSM approach, a measurement of the frequency dependent current at the PCA under back reflected terahertz radiation is evaluated. The back reflected radiation is modulated near 2.5 kHz as can be seen in Fig. 5.6. The current at the PCA is separated in its DC and AC components and amplified by a transimpedance amplifier (10^5 V/A). Now the AC part is connected to an ESA[D33] and shown in Fig. 5.6 from 0 to 4 kHz using a resolution bandwidth of 1 Hz. The frequency of the back reflected terahertz radiation is

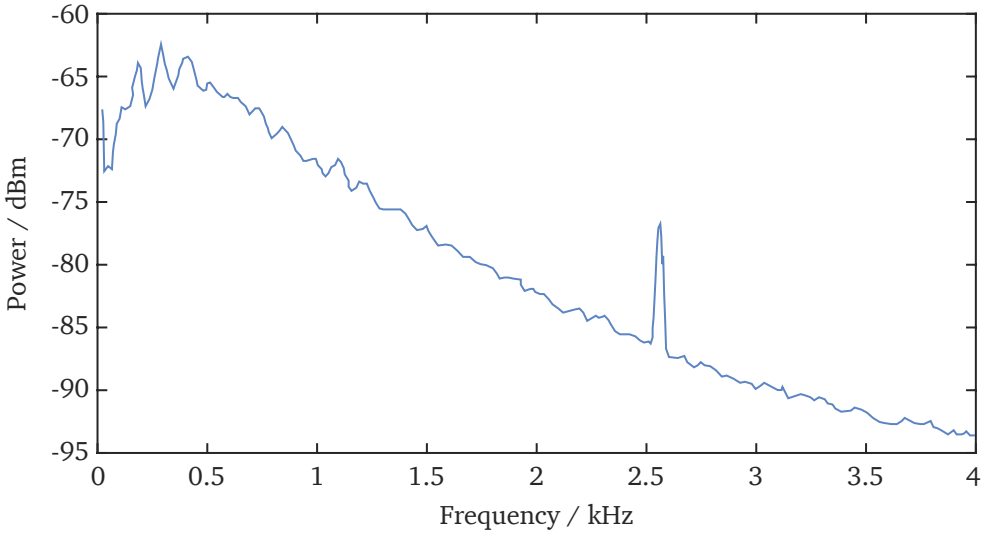

Figure 5.6.: Measured AC part of the PCA current from 0 to 4 kHz using an ESA with a resolution bandwidth of 1 Hz. The peak near 2.5 kHz corresponds to the current induced by the back-reflected terahertz radiation.

approximately 0.55 THz. As specified by TOPTICA Photonics, the optical output power P_{THz} of the PCA at 0.55 THz is 0.55 μW. The HSM signal amplitude is determined from Fig. 5.6 and amounts $P_{elec,THz} = -76.7$ dBm. From the signal amplitude and the output power the value of R_{ep} amounts to

$$R_{ep} = 65\frac{V}{W}. \tag{5.6}$$

The NEP can be calculated as the quotient of the noise power spectral density, which is the baseline in Fig. 5.6 and R_{ep} at the chopping frequency of 2.5 kHz. From this a NEP of

$$NEP = 160\frac{nW}{\sqrt{Hz}}. \tag{5.7}$$

is calculated. These values represent the lowest (R_{ep}) / highest (NEP) values and thus a worst case estimation of the responsivity and the NEP, since an ideal back reflection and no further loses are considered. In a more realistic scenario the reflectivity of the untreated rough surface of the chopper wheel would not exceed 30%. Considering this fact the R_{ep} and NEP improve to

$$R_{ep} = 217\frac{V}{W} \tag{5.8}$$

$$NEP = 48\frac{nW}{\sqrt{Hz}}. \tag{5.9}$$

Typical NEP values for sophisticated techniques like the terahertz time-domain spectroscopy and far-infrared Fourier transform spectroscopy amount to 10^{-7} and 0.1 $\frac{nW}{\sqrt{Hz}}$, respectively [157]. Regarding these values it is quite obvious that further improvements to the HSM concept has to be done to compete with

these techniques. An improvement can be expected by using a higher modulation frequency. As can be seen from Fig. 5.6 the noise of the current at the PCA decreases with increasing frequency. Since the PCA is biased by a battery source and the current in absence of back-reflected terahertz radiation depends on the intensity of the two lasers according to Eq. 2.4, the dominant part of noise introduced to the current of the PCA is caused by optical power fluctuations of the lasers. The characterization of the lasers in section 3 revealed a frequency dependent noise of the emitted intensity until a threshold frequency, from which on the RIN is constant. These threshold frequencies are located between 10 kHz and 300 kHz. An increase of the modulation frequency of the back-reflected terahertz radiation above this threshold frequency, therefore would result in much better values of the responsivity and NEP. An increase of the terahertz modulation frequency could be achieved by different terahertz modulation techniques including all-electric, thermal, magnetic and all-optical schemes [158]. In this way, pulses of terahertz radiation with a width of 10 ns have been generated [159], which would result in a modulation frequency up to 50 MHz.

5.3. Summary and conclusion

In conclusion, an experimental method for the generation and detection of CW-terahertz radiation utilizing only one PCA was demonstrated. The PCA simultaneously acts as emitter and receiver for CW terahertz radiation which is reflected off a rotating chopper wheel. This terahertz spectroscopic set-up infers a cost reduction and relaxes the demand on high laser power as only one PCA is needed. The proposed method lends itself to the realization of compact terahertz assemblies. However, so far the values of the responsivity are quite low and the NEP is rather high. To improve these values one key point is the increasing of the chopper frequency, since the dominant part of current noise at the PCA is contributed by the intensity noise of the ECDLs. The expectable absolute lower noise limit of the HSM approach should be the shot noise limit of the current at the PCA. Taking into account a current of 1 mA and an amplification of 10^5 V/A of the transimpedance amplifier, the noise floor measured at the ESA amounts to -141 dBm. This would result in a NEP of $7.4 \times 10^{-2} \frac{nW}{\sqrt{Hz}}$ and a SNR of 64 dB, which is comparable to the achieved SNR of highly developed and commercially available standard photomixing set-ups.

The introduced HSM approach allows the implementation of compact spectroscopic set-ups in the terahertz frequency domain. As a proof-of-concept experiment this is demonstrated in the following chapter by the realization of a two-dimensional terahertz tomography set-up. This not only allows to create 2D images of sample objects, revealing the inner geometry of the sample but further allows for spatially resolved chemical composition identification using spectroscopic imaging.

6. Tomographic terahertz imaging

Tomographic terahertz imaging is on the way of becoming an excellent tool for a plurality of industrial applications [37]. In general, terahertz imaging benefits from the opacity of many materials and the specific spectral fingerprints of a multitude of substances located in the terahertz domain. These characteristics offer the opportunity of a contact-free identification of hidden objects in security tasks [28] and the visualization of objects in quality control applications [160]. In order to realize an insight into a hidden object, rather than imaging a projection, tomographic reconstruction techniques can be applied. This for example is useful in security applications and a plurality of industrial processes [37]. Since the photon energy of terahertz radiation is non-ionizing, there are lower safety requirements compared to x-rays, easing the implementation of terahertz systems. Therefore, tomographic terahertz imaging can become an alternative to x-ray tomography in several fields of application.

6.1. Homodyne self-mixing approach

To realize a compact tomographic imaging set-up in the terahertz frequency domain, first the developed HSM approach is applied. This allows spectroscopic imaging by a change of the optical beat frequency and phase sensitive detection.

6.1.1. Experimental set-up

As in the original HSM experiment described in chapter 5 a single PCA is used to achieve simultaneous generation and detection of terahertz radiation. To accomplish two-dimensional imaging of weak absorbing objects the original experimental set-up is expanded with a rotational and an additional linear translation[D34] stage. The sample object is a hollow core Teflon cylinder with a height $h = 20\,\text{mm}$, a cylinder diameter $d = 18.5\,\text{mm}$ and a wall-thickness $t = 4.25\,\text{mm}$ as indicated in Fig. 6.1. Measurements are performed with the sample object filled with α-Lactose monohydrate powder and without filling, respectively. The sample is placed between the PCA and RCW and is mounted on the linear translation stage allowing for a movement orthogonal to the terahertz beam (Δx direction) related to the displacement (z) of the RCW. A further rotation around the center axes of the Teflon cylinder is realized by the rotation platform. In this manner the sample is scanned over a range of 27 mm in 1 mm steps in x-direction. For every x-position of the sample, the RCW which is mounted on a second linear translation stage[D34], is translated over a displacement Δz of 1.2 mm. For each scan the RCW displacement starts from the same initial displacement z_0. Both phase and amplitude of the HSM signal are measured by the lock-in amplifier[D25] and recorded by the oscilloscope[D31]. The amplitude $I_{x_i,0}$ of the back-reflected terahertz radiation is extracted by fitting the measured data to

$$I_{x_i}(z) = I_{x_i,0} \cdot cos\left(\frac{4\pi}{\lambda} \cdot (z_0 + z) + \phi)\right). \tag{6.1}$$

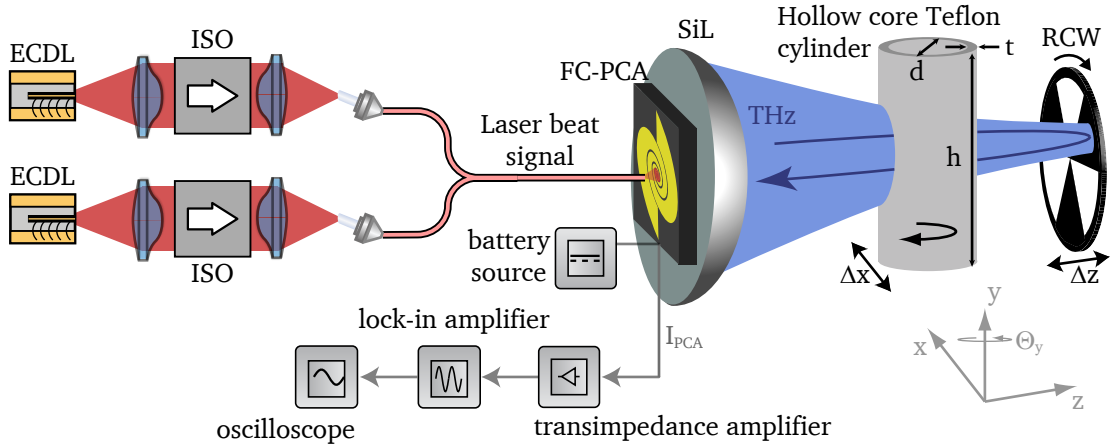

Figure 6.1.: Scheme of the experimental set-up, which is used to realize tomographic terahertz imaging applying the HSM method.

Here, λ is the wavelength of the terahertz radiation, z_0 is the initial distance between of the RCW and PCA, z is the displacement of the linear translation stage and ϕ is an additional phase introduced by the sample object. The phase ϕ is described by

$$\phi = \frac{4\pi}{\lambda} \cdot g \cdot \left(n_{sample} - 1\right), \tag{6.2}$$

with the distance g which the terahertz radiation travels through the object and n_{sample} the refractive index of the sample material. After the linear scan of the sample object, the rotational stage rotates the sample by 30° and the linear scan in x-direction is repeated. The procedure is performed for a total of 6 rotation angles Θ_y between 0° and 150°.

6.1.2. Results and discussion

First, the two ECDLs are tuned to a difference frequency of 0.539 THz, which corresponds to a wavelength of 556 μm. As described in the experimental set-up for each x-position of the cylinder, the HSM signal is recorded over a RCW displacement Δz of 1200 μm. Figure 6.2 shows the measured HSM signals at two selected sample x-positions, which correspond to no sample between PCA and RCW ($x = 0$ mm, (a)) and the position, where the center of the PCA and Teflon cylinder are congruent ($x = 14$ mm, (b)). At a displacement of $x = 14$ mm the parameter g in Eq. 6.2 is equal to the double wall thickness t of the hollow-core Teflon cylinder, because the terahertz radiation passes the cylinder front- and back-wall on its way to the RCW and Eq. 6.1 depends on the distance between the PCA and RCW. Therefore, the wall thickness t can be determined by a curve fitting of Eq. 6.1 to the measured HSM signal at $x = 14$ mm. The refractive index n Teflon at 0.539 THz is assumed to be 1.44 [156]. Parameters that are obtained by the curve fitting are the object thickness g, the terahertz wavelength λ and the initial displacement z_0. The results of the curve fitting yields a terahertz wave frequency of 0.542 THz and an object thickness g of 8.8 mm. Both values are in good agreement with the calculated difference frequency of 0.539 THz and

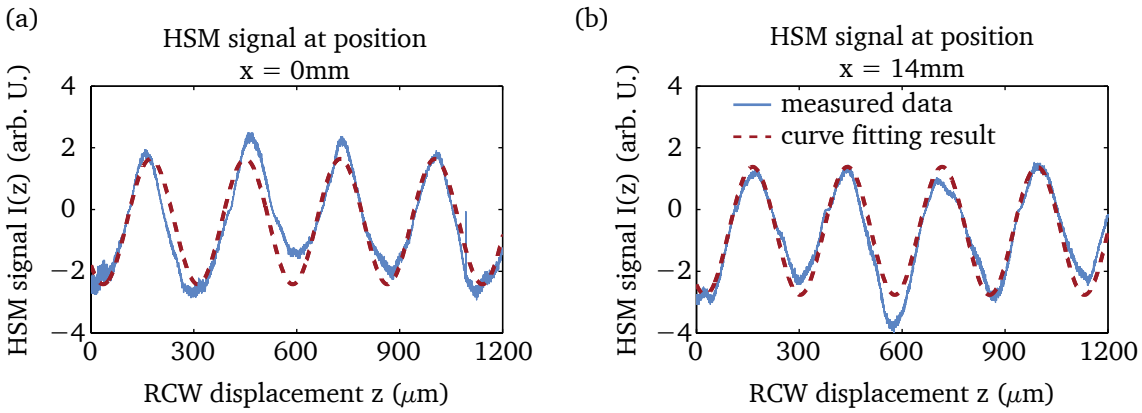

Figure 6.2.: Measured HSM signals (solid, blue) at a terahertz frequency of 0.539 THz without sample (a) and with sample center congruent to PCA center (b) versus displacement z of the RCW. (Dashed, red) Curve fitting of measured data to Eq. 6.1.

two times the wall-thickness of the hollow-core Teflon cylinder as determined by a caliper measurement (8.5 mm).

In order to perform two-dimensional imaging of the hollow-core Teflon cylinder, a complete set of measurements for all rotation angles Θ_y of the sample is performed. The total measurement time depends on the investigated terahertz wavelength. For longer wavelengths the RCW displacement increases, leading to longer measurement times. In the case of a terahertz frequency of 0.19 THz, one HSM signal measurement, i.e. at one specific angle Θ_y and one x-position, lasts roughly 40 seconds which results in an overall time duration of two hours for one tomographic measurement of 6 angles with 27 x-positions each. After measuring all HSM signals, a curve fitting to Eq. 6.1 for each HSM signal yields the HSM signal intensity $I_{x_i,0}$ for each x-position and rotation angle Θ_y, considering different DC offsets by an additional constant factor in Eq. 6.1. This fitting is done in order to perform an automated data processing and to avoid false signals with the wrong wavelength at low signal amplitudes. Besides the signal amplitude, the curve fitting provides also the signal phase, which may be useful in future investigations. An normalized example of these measured signal intensities $I_{x_i,0}$ for $\Theta_y = 0°$ at each x-position are shown in Fig. 6.3 for a terahertz frequencies of 0.19 THz and in Fig. 6.4 for a frequency of 0.539 THz. As a guide to the eye a photograph of half of the investigated Teflon cylinder is scaled to the axis dimensions and shown in the background in both graphs. The filled circles in blue represent a scan of the Teflon cylinder filled with α-Lactose monohydrate powder, whereas the empty circles in red show a scan of the empty hollow-core Teflon cylinder. The hollow-core Teflon cylinder filled with powder clearly shows negligible transmission through the whole sample at a terahertz frequency of 0.539 THz (Fig. 6.4, blue circles). Only in the periphery outside the Teflon cylinder, from $x = 0$ to $x = 4$ mm and from $x = 22$ to $x = 26$ mm marked as regions I, a considerable transmission is observed. In contrast, for the empty cylinder at a terahertz frequency of 0.539 THz (Fig. 6.4, red empty circles) and for the filled cylinder for a terahertz frequency of 0.19 THz (Fig. 6.3, blue filled circles) a high transmission through the center of the sample can be seen (region III), whereas no transmission through the side walls of the Teflon cylinder ($x = 6$ to $x = 10$ mm and $x = 15$ to $x = 20$ mm) is observed in both cases (region II). Responsible for the absence of any signal in case of the filled cylinder at 0.539 THz is not the scattering by the powder, but rather the characteristic

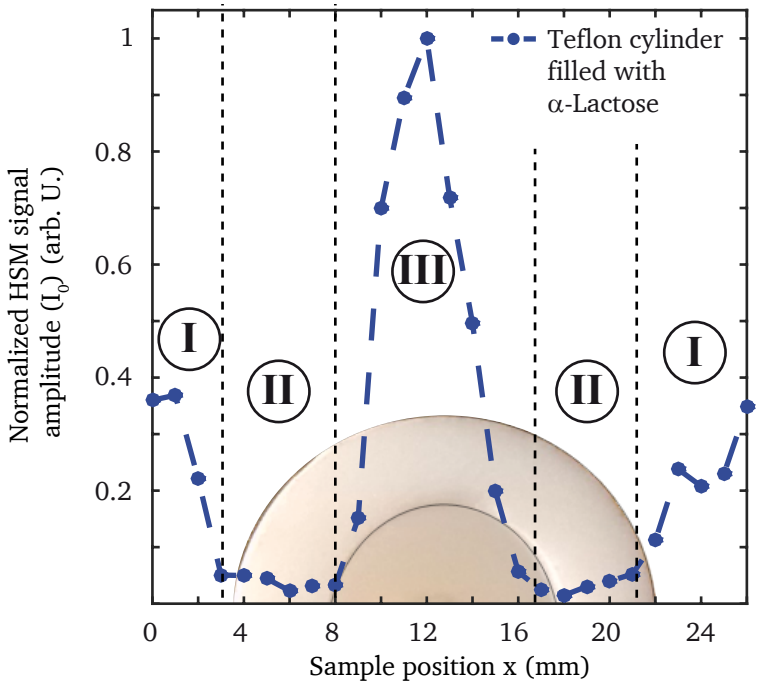

Figure 6.3.: Experimentally obtained HSM signal amplitudes I_0 for a sample scan in x-direction for a rotation angle Θ_y of 0° with α-Lactose filling for a terahertz frequency of 0.19 THz. A photograph of half of the investigated Teflon cylinder scaled to the axis dimensions should serve as a guide to the eye.

absorption line of α-Lactose near the selected frequency of 0.539 THz [161].

In case of 0.19 THz three different transmission regions are identified and marked in Fig. 6.3.

(I) A HSM signal amplitude of approximately 0.4 is observed in the case of no sample between PCA and RCW.

(II) By moving the sample into the THz beam path a region of no transmission is observed.

(III) A surprisingly high signal of around twice the amplitude according to (I) is found at the position, in which the center of the PCA and sample are congruent.

Coming from the well established x-ray tomographic imaging, the measured projections of the Teflon cylinder showing these three regions appear unusual, since a smooth attenuation of the signal depending on the thickness of the Teflon cylinder is expected when moving it into the terahertz beam path [119]. As x-rays only experience a small refraction at boundary surfaces, the path from the source of the radiation to the detector can be approximated as a straight line. Hence, the measured signal amplitude at the detector only depends on the attenuation of the sample between source and detector. In contrast, optical effects like refraction and diffraction play an important role for terahertz radiation [119, 120]. Therefore, the experimental set-up from Fig. 6.1 is studied for a frequency of 0.19 THz by ray tracing using the software ZEMAX in the non-sequential mode. The investigated geometrical set-up is depicted on the left side of

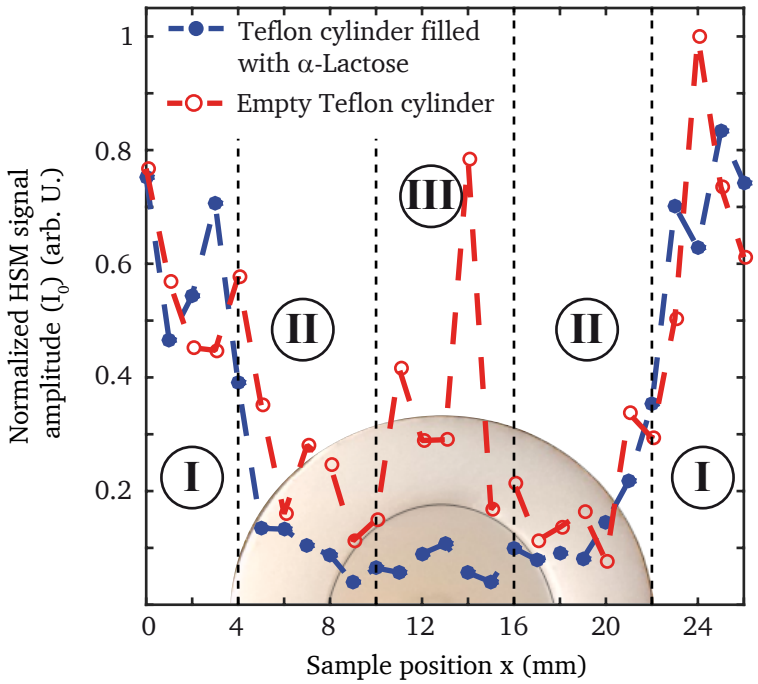

Figure 6.4.: Experimentally obtained HSM signal amplitudes I_0 for a sample scan in x-direction for a rotation angle Θ_y of 0° without (empty red circles) and with (filled blue circles) α-Lactose filling for a terahertz frequency of 0.54 THz. A photograph of half of the investigated Teflon cylinder scaled to the axis dimensions should serve as a guide to the eye.

Fig. 6.5 for different displacements of the Teflon cylinder filled with α—Lactose, representing the regions (I), (II) and (III). The source is a circular Gaussian source with a radius of 4 mm followed by a paraxial lens with a focal length of 21 mm. The sample is modeled by two cylinders with refractive indices of 1.44 (Teflon) [156] and 1.79 (α—Lactose) [161] and which are displaced in x-direction. At a distance of 40 mm from the source a mirror back-reflects the calculated rays to the detector, which has the same size and is located at the same position as the source. By summing up the total power of the incident rays at the detector for different x-positions of the Teflon cylinder, one projection of the cylinder is simulated. The projection is shown on the right side of Fig. 6.5. The intensity has been normalized with respect to the maximum calculated intensity at the detector and is shown over a total displacement of 26 mm in 1 mm steps. As in the experimentally obtained data, the simulated projection exhibits the same three regions.

In region (I) there is no sample placed between the PCA and the RCW respectively the mirror. Here the loss of intensity originates from the deviation of the focal point position at 0.19 THz compared to the theoretical distance of 40 mm from the PCA. This deviation arises from the 'active region' of the logarithmic spiral antenna, which emits the major part of the terahertz radiation. Due to constructive and destructive interference of the radiation, the size of this region turns out to be frequency-dependent. With increasing wavelength respectively lower frequency, the area of this region increases [154, 155], which leads to a more distant virtual point source. In combination with the mounted Si-lens, this contributes to a shift of the focal point of the terahertz radiation towards the Si-lens. The absence of any signal in

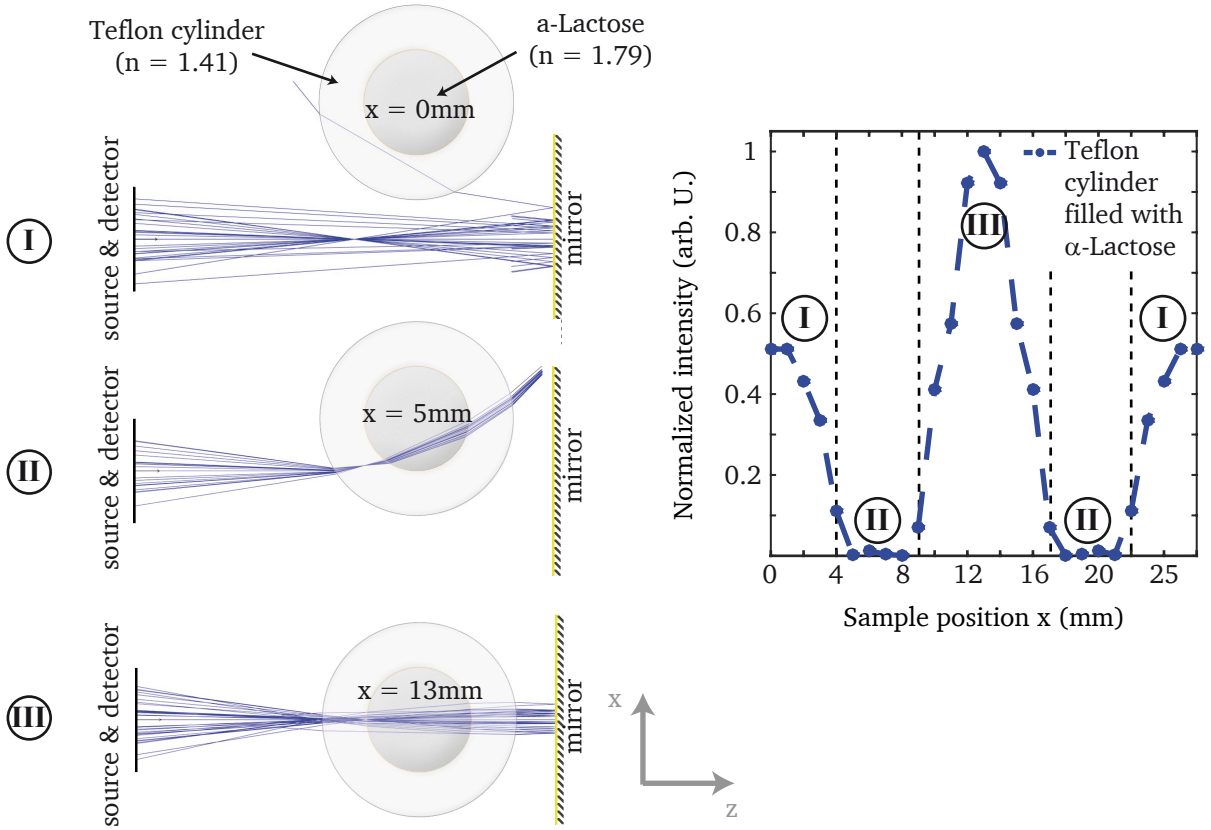

Figure 6.5.: (left) Exemplary geometrical set-ups used for the analysis with the ray tracing software ZEMAX. The source is a circular Gaussian source with a radius of 4 mm followed by a paraxial lens with a focal length of 21 mm. The sample is modeled by two cylinders with refractive indices of 1.41 (Teflon) and 1.79 (α—Lactose) which are displaced in x-direction. At a distance of 40 mm from the source a mirror back-reflects the calculated rays to the detector, which is located at the source position. (right) By the ray tracing software ZEMAX calculated normalized intensities at the detector versus the displacement of the Teflon cylinder in x-direction.

region (II) of both the simulated and experimentally obtained projection of the Teflon cylinder becomes evident by regarding the second set-up in Fig. 6.5 ($x = 5$ mm). The emitted terahertz radiation gets strongly refracted by the curved surface of the Teflon cylinder, resulting in the total loss of the radiation. In contrast, region (III) exhibits an amplitude of approximately twice the amplitude in (I) in accordance with experimental and simulated data. Here the Teflon cylinder acts like a lens making sure that the whole terahertz radiation gets back reflected to the PCA.

After understanding the influence of refraction on the raster scan a reconstruction of the object using all 6 projection angles Θ_y for the tomographic 2D image of the Teflon cylinder is investigated. In order to avoid aliasing in the rasterisation of the projections, necessary for the 2D reconstruction, the received transmission projections for every rotation angle Θ_y are up-scaled by a linear interpolation. The

dependency of the projections of the filled sample object regarding the rotation angle Θ_y is recorded. These projections are used to reconstruct the two-dimensional transmission profile of the sample object. The back projection can be performed using a multitude of algorithms, which are well-established in the field of tomography. In agreement with literature [107] it is noticed, that the inverse Radon transformation suffers from the small number of performed projections. It is well accepted that iterative algorithms are superior to Back Fourier algorithms for low numbers of projections [107]. Here the SART [118] implemented in the ASTRA Tomography Toolbox [162] provides the best image quality and therefore is chosen. By even considering the Gaussian beam shape of the terahertz radiation, it would be possible to further improve the quality of the reconstructed image [122]. This also becomes clear by viewing the smooth transition between air and Teflon cylinder in Fig. 6.3, where the absence of the expected sharp transition indicates a Gaussian beam profile. However, for simplicity of this proof of concept experiment, parallel beams are assumed in the reconstruction method.

The reconstructed two-dimensional images of the Teflon cylinder filled with α-Lactose monohydrate powder for both investigated terahertz frequencies of 0.19 THz and 0.539 THz are depicted in Fig. 6.6(a) and (b), respectively. In case of a terahertz frequency of 0.19 THz a transmission through the surrounding air can be seen at the edges of the Teflon cylinder by the yellow and orange region. The side-walls of the Teflon cylinder are defined by a blue area of no transmittance, due to strong refraction on the curved surface of the Teflon cylinder. The transition region from air to the Teflon cylinder appears to be a little bit blurred. In contrast, the 1D-projections for both frequencies and the reconstructed 2D image at 0.539 THz (Fig. 6.6(b)) exhibit a sharp transition between air and the Teflon cylinder. Therefore, it seems likely that this blurring effect is a consequence of the refraction of the terahertz radiation at the curved surface. A part of the outer Teflon ring appears transparent for measurements in a configuration shown in Fig. 6.5 III. But under a rotation of the Teflon cylinder the same part of the outer Teflon ring seems to be highly absorbing as illustrated in Fig. 6.5 II. These two contradictory transmission behaviors may result in a blurring effect in the reconstruction. The center of the reconstructed image at 0.19 THz (Fig. 6.6(a)) clearly shows a high transmission despite the α-Lactose inside the Teflon cylinder, which confirms our assumption that the scattering at the terahertz wavelength does not affect our transmission experiment. Figure 6.6(b) shows a large blue region of no transmission, from which the outer shape of the Teflon cylinder is recognized. Here, only a transmission through the air surrounding the cylinder can be seen. A comparison of the two images received from the chosen terahertz frequencies reveal the hollow core of the Teflon cylinder, since a high transmission in case of a terahertz frequency of 0.19 THz is observed, whereas no transmission is measured at 0.539 THz. With the knowledge about the absorption line of α-Lactose at 0.539 THz, finally the filling of the hollow core Teflon cylinder can be identified. In this manner frequency-dependent imaging can be used to identify substances or even to indicate specific regions in tomographic images, which would be unrecognized in single frequency imaging.

The investigated tomographic terahertz experiments using the HSM approach, demonstrated the capability to reconstruct the dimensions of a hollow core Teflon cylinder and further allowed the identify of the α-Lactose filling by its specific absorption line. The optical effects of refraction on the experimentally determined 1D projections of the sample could be clearly identified by the modeling of the experimental set-up in ZEMAX. These results show a very good agreement between experiment and theory and allow for a better understanding of the refraction effects. Also, the influence of refraction onto the reconstructed image of the sample is discussed. In order to investigate on the influence of refraction effects on

tomographic terahertz imaging different imaging techniques are discussed by ray tracing simulations in the next chapter. Therefore, a specific ray tracing software is developed in Matlab allowing the easy implementation of different detection schemes, which are raster scanning using detectors with small and large surface, multi-pixel detectors and single-pixel imaging. All of these detection schemes are studied under the aspect of tomographic imaging.

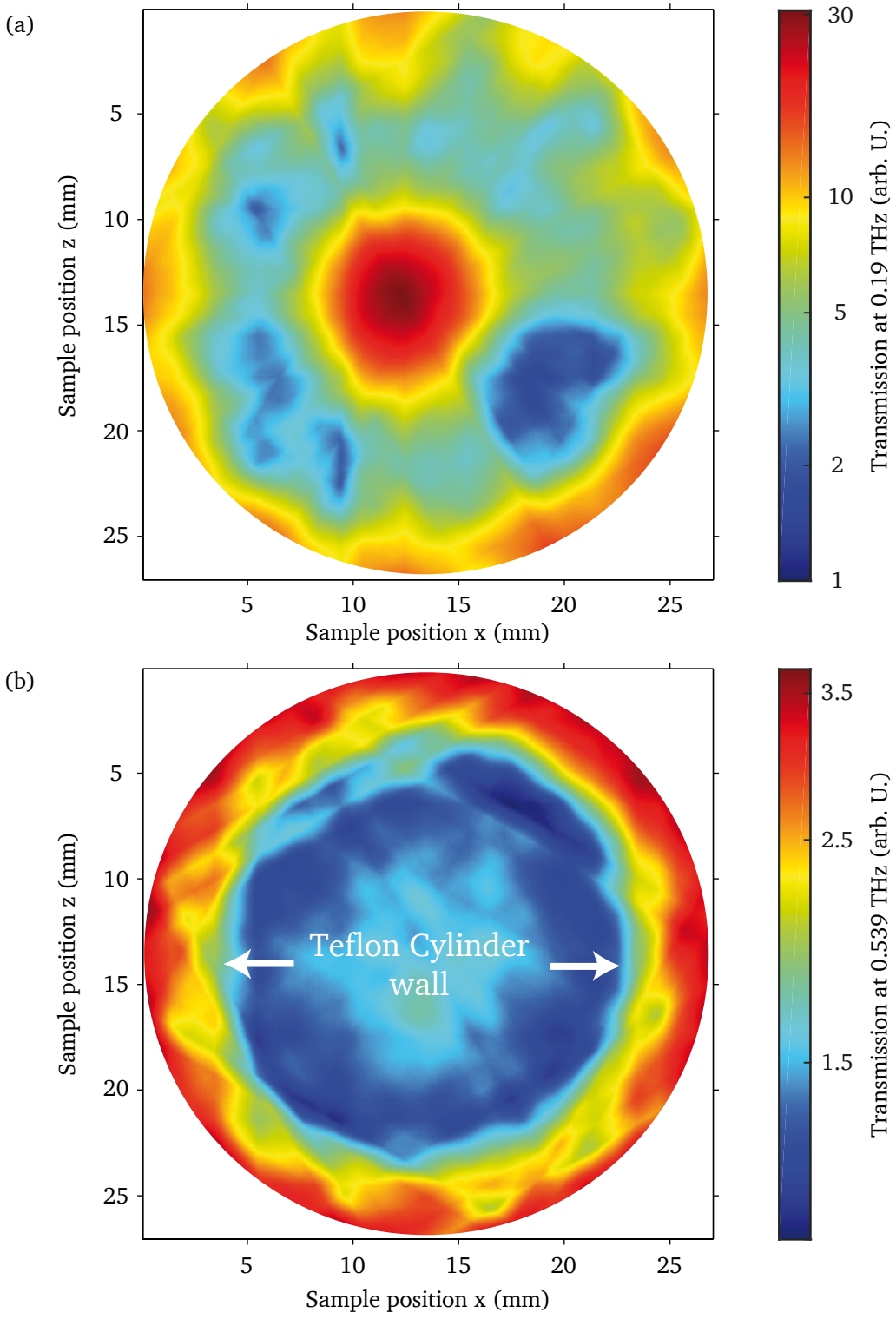

Figure 6.6.: Reconstructed two-dimensional image in a logarithmic transmission representation at a terahertz frequency of (a) 0.19 THz and (b) 0.54 THz of the Teflon cylinder filled with α-Lactose utilizing the SART algorithm.

6.2. Optical ray tracing simulations

In the previous section 6.1.2, optical ray tracing using ZEMAX has been proven to accurately simulate projections measured in the terahertz frequency domain. Therefore, optical ray tracing is used in this section to simulate two-dimensional tomographic imaging using different detection techniques. The investigated detection schemes are raster scanning using detectors with small (Fig. 6.7(a)) and large surface (Fig. 6.7(a)), multi-pixel detectors (Fig. 6.8(a)) and single-pixel imaging (Fig. 6.8(a)). The most popular detection scheme so far used in tomographic imaging in the terahertz frequency domain is the raster scanning of the sample object. This technique has been also used in the previously HSM tomographic imaging approach. Often the usable detector area is small compared to the object under investigation, for example in the HSM experiment the Si lens collecting the terahertz radiation has a diameter of 12.7 mm, but only the radiation focused in the tiny gap between the electrodes of the PCA is detected. This case is simulated by sending a bundle of parallel rays towards a detector which is twice as large as the ray bundle. This arrangement is shown in Fig. 6.7(a).

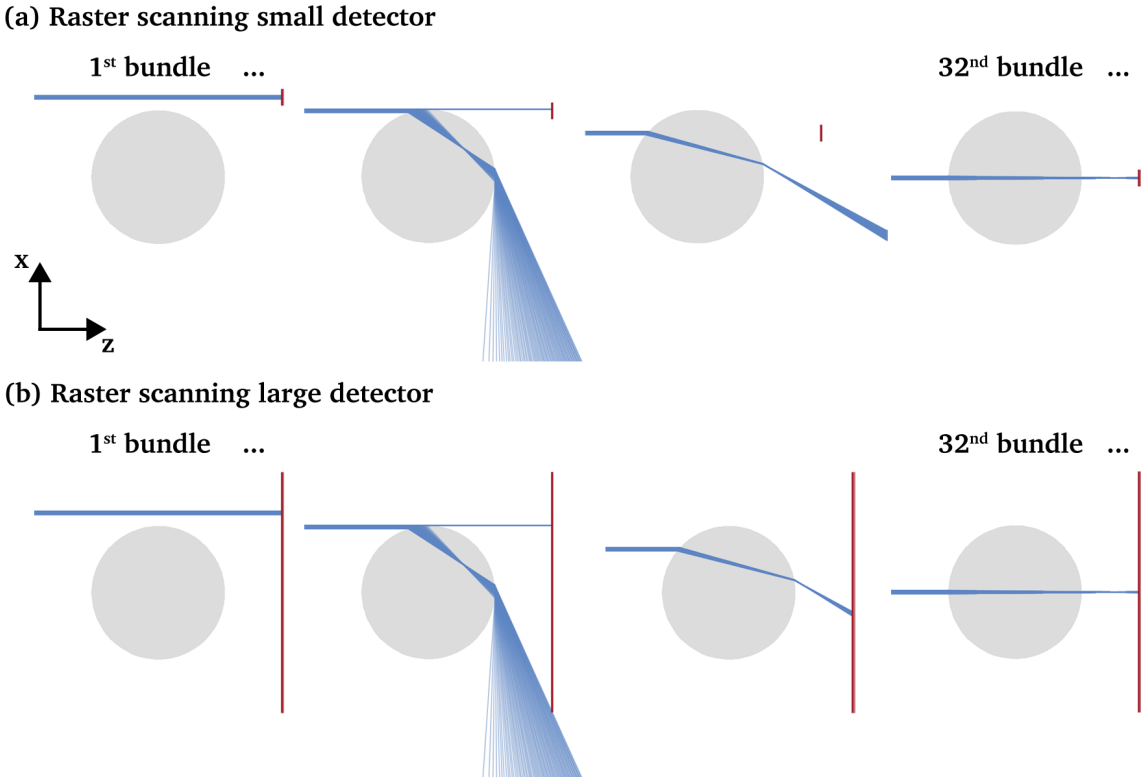

Figure 6.7.: Ray tracing simulations for the projection imaging of a circular sample object using raster scanning of the object with a (a) small and (b) large detector surface.

The circular sample object with a refractive index of 1.5 and an absorption coefficient of 1 cm^{-1} is placed between the source and detector, while for the ambient a refractive index of 1 is assumed. The object has a radius of 7 mm and the distance between source and detector is 26 mm. A ray is described by its

starting point $\vec{s}$ and its direction $\vec{m}$, with $|\vec{m}| = 1$. For each ray a possible intersection with the circle of radius r and with a center position $\vec{c}$ is checked using the inequation:

$$B^2 - 4AC > 0 \tag{6.3}$$

$$A = m_x^2 + m_y^2 \tag{6.4}$$

$$B = 2\left[(s_x - c_x) \cdot m_x + \left(s_y - c_y\right) \cdot m_y\right] \tag{6.5}$$

$$C = (s_x - c_x)^2 + \left(s_y - c_y\right)^2 - r^2 \tag{6.6}$$

Further an intersection between each ray and the detector is checked using the three inequations 6.7 and the three Eqs. 6.8 - 6.10:

$$q \leqslant 1 \;\&\; q \geqslant 0 \;\&\; p > 0 \tag{6.7}$$

$$q = \begin{cases} \frac{s_y - d_{1,y}}{d_{2,y} - d_{1,y}}, & d_{2,y} \neq d_{1,y} \;\&\; |m_y| = 0 \;\&\; |m_x| \neq 0 \\ \frac{d_{1,x} - s_x - \frac{m_x}{m_y}(d_{1,y} - s_y)}{\eta} \end{cases} \tag{6.8}$$

$$\eta = \frac{m_x}{m_y}\left(d_{2,y} - d_{1,y}\right) - \left(d_{2,x} - d_{1,x}\right) \tag{6.9}$$

$$p = \begin{cases} \frac{d_{1,x} + \left(d_{2,x} - d_{1,x}\right) \cdot q - s_x}{m_x}, & d_{2,y} \neq d_{1,y} \;\&\; |m_y| = 0 \;\&\; |m_x| \neq 0 \\ \frac{d_{1,y} - s_y + (d_{2,y} - d_{1,y}) \cdot q}{m_y} \end{cases} \tag{6.10}$$

Here, the detector is represented by a line spanned by the two points $\vec{d_1}$ and $\vec{d_2}$. If a ray intersects with both the detector and the circle, the distance between the starting position $\vec{s}$ of the ray and the intersection points $\vec{h}$ is calculated. In case the ray hits the detector first the ray ends and is marked as detected. Otherwise a new ray is casted, with its starting position at the intersection point and a direction calculated using Snell's law. The intensity of rays traveling through the circle gets attenuated considering the absorption coefficient of the sample and the length traveled through the object. Also losses due to reflection are taken into account using the Fresnel equations for unpolarized light and non-magnetic media.

Figure 6.7(a) exemplary shows the ray tracing results of four ray bundle and detector arrangements as they are found during the raster scanning of a circular object. First the ray bundle passes the object and is directly measured by the detector. Second a minor part of the rays still passes the object and reaches the detector. But the majority of rays get strongly refracted on the bended surface of the circular object and therefore do not reach the small surface of the detector. By moving the detector and the ray bundle towards the center of the circular object, as shown in the third case, all the rays get refracted away from the detector. In the last case the ray bundle is at the same height as the center of the circle. Here, the rays get focused onto the detector by the bended surface of the object. But the intensity of the rays is

lowered due to the absorption of the sample object. A simulated projection of the circular object is shown in Fig.6.9(a) using the raster scanning method and a small detector area. The object is scanned using 64 start positions of the ray bundle and the detector. Aside from the object a maximum transmission through the surrounding atmosphere can be seen. This suddenly changes when the rays intersect the object and the detected intensity approaches zero very fast. The intensity stays at zero until the ray bundle approaches the center of the circular sample object. Due to the lensing effect, the rays get focused on the detector and an intensity according to the absorption of the object is detected. The achieved simulated projection resembles the projection measured using the HSM technique in the case of a unfilled Teflon cylinder shown in Fig. 6.4.

Next, the small detector is replaced by a detector with a large surface as shown in Fig. 6.7(b). Again the circular sample object is scanned using 64 ray bundles starting from different x-positions, but this time the detector stays at a fixed position. From the ray tracing simulations it can be seen, that even strongly refracted rays reach the detector surface. For each ray bundle the intensity of the rays reaching the detector is summed up and correlated to the x-position of the corresponding bundle. In this way, the simulated projection shown in Fig. 6.9(b) is obtained. Besides two sharp transmission minimums at the sample boarder, the projection looks similar to the projection received using x-ray tomography of a circular shaped object. But the actual values of the intensity at the detector might differ, since the rays get refracted and might travel a longer distance inside the absorbing media in case of terahertz tomography. This causes a stronger absorption compared to rays propagating on straight lines, which is the case for x-rays.

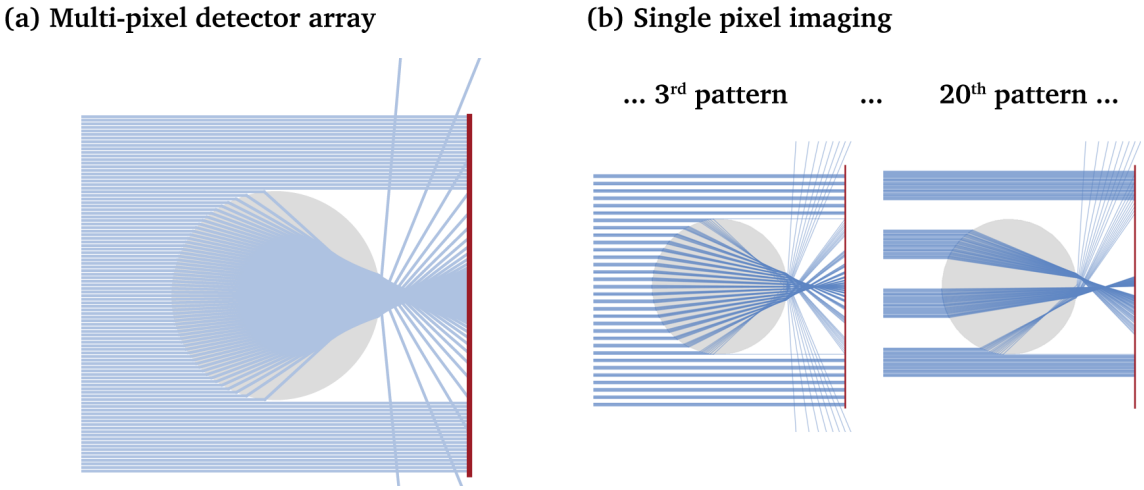

Figure 6.8.: Ray tracing simulations for the projection imaging of a circular sample object using (a) a multi-pixel detector and (b) the single-pixel imaging approach. In (b) two out of the 128 necessary irradiation patterns are selected and shown as example.

Another possibility to measure the projection of an object is the use of a detector array as shown in Fig. 6.8(a). Here, the red line indicates 64 equally sized and spaced detectors, each summing up the intensity of rays hitting the corresponding pixel. In that way the intensity for each pixel is recorded and

an image of the object is take. A total of 10^4 equally spaced rays are casted and their traces to the detector are calculated. For clarity, Fig. 6.8(a) only shows the trace of every hundredth ray. The evaluation of the intensities measured at each detector pixel is shown in Fig. 6.9(c). The intensities on the left (0 to 5 mm) and right (20 to 25 mm) side of the projection mostly represent the rays passing the object. However, coming from the boarders of the projection, the intensity increases slowly when approaching the object boarder. This increase in intensity is caused by rays, which intersect with the top and bottom part of the object and as a result get strongly refracted. The simulated projection shows an abrupt decline of the intensity at the positions 5 and 20 mm, which corresponds to the top and bottom border of the object. Followed by these two positions towards the center of the projection, the intensity rises and reaches a small plateau of a maximum transmission through the object. This maximum reaches an intensity level close to the transmission level through the surrounding atmosphere. This can be understood by regarding the circular object as a lens, which focus the rays onto the two central pixels of the detector. Thus, a displacement of the detector in z-direction would lead to a different appearance of sample projection.

The last imaging approach investigated here is the so-called single-pixel imaging already introduced in

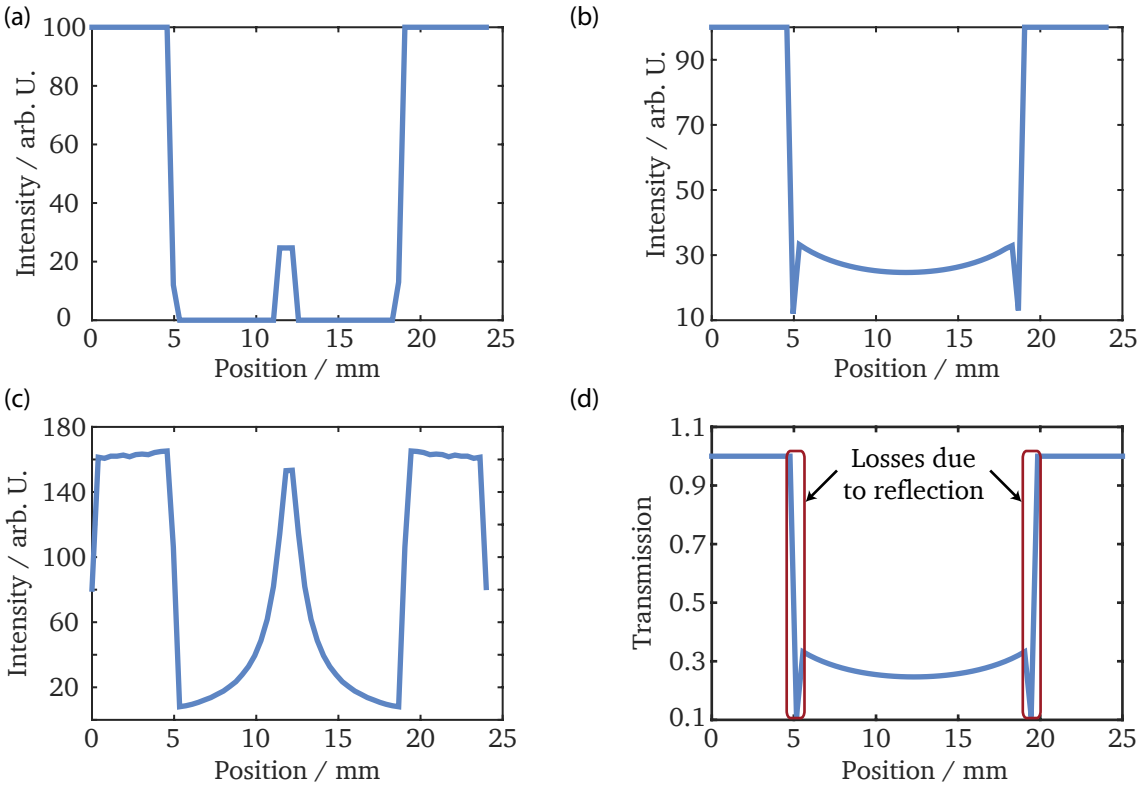

Figure 6.9.: Simulated projections of a cylindrical sample object with a refractive index of 1.5 and an absorption coefficient of 1 cm^{-1} using ray tracing of the different imaging concepts. The object projections are obtained by raster scanning of the object using (a) a small and (b) a large detector, (c) taking an image using a multi-pixel detector and (d) calculating the image using the single-pixel imaging technique.

section 2.3.2. The utilized detector is the same bucket detector as in the case of the previously described raster scanning using a large surface detector. But instead of raster scanning the object with 64 ray bunches, rays forming different masks defined by a 64×64 Hadamard matrix are casted towards the object. The results of the ray tracing simulations are shown exemplary for the 3^{rd} and 20^{th} pattern mask in Fig. 6.8(b). The detector measures the total intensity for each radiation pattern to obtain the measurement vector $\vec{M}$, from which afterwards the projection of the object is calculated using Eq. 2.23. The reconstructed projection is shown in Fig. 6.9(d). It is noted, that the projection employing single-pixel imaging looks the same as the projection received using raster scanning in combination with a large area detector (Fig. 6.9(b)). As already discussed before, the projection resembles a projection using x-rays. The only differences are two absorption spikes near the positions 5 and 20 mm, which are the result of strongly refracted rays. Further, the rays at these positions incident on the object under large angles, which leads to high losses due to reflection.

Since the investigated object possesses a rotational symmetry, the reconstruction of the two-dimensional

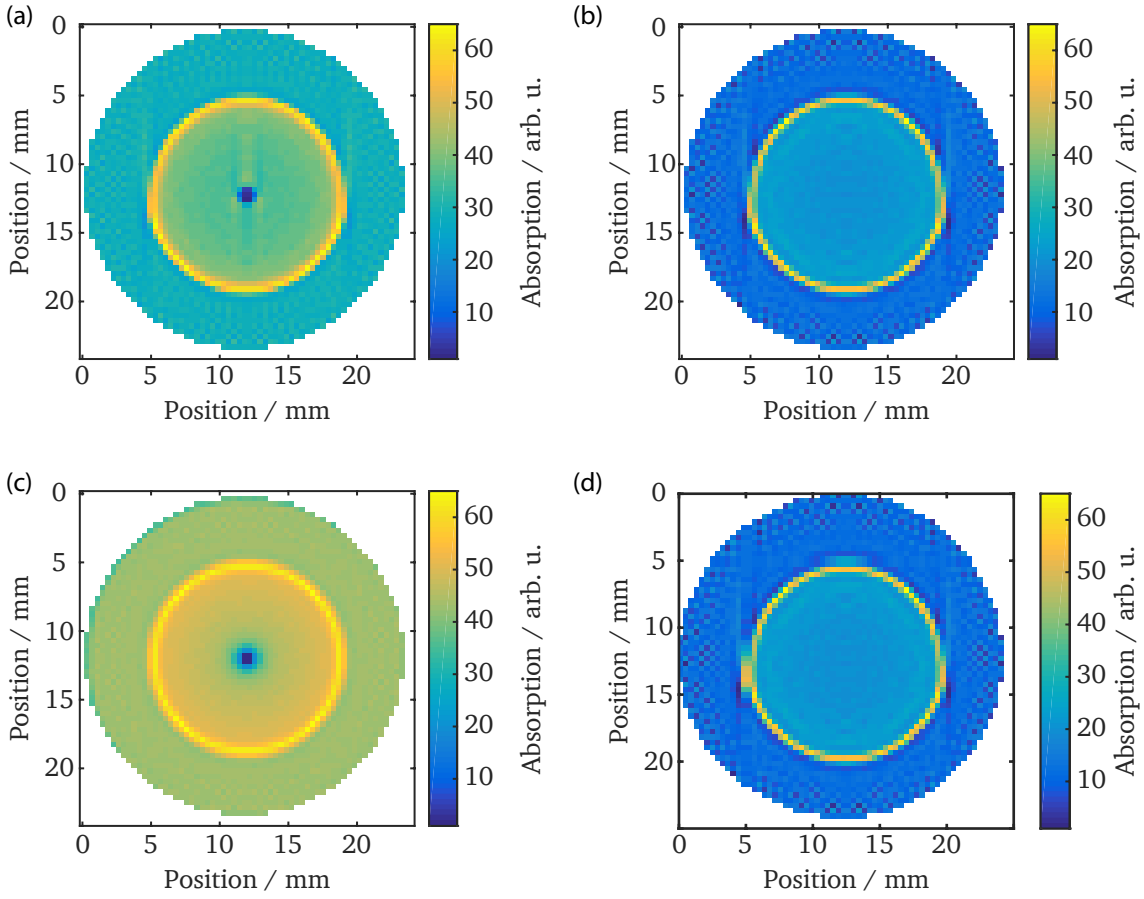

Figure 6.10.: Resulting reconstructions using the simulated projection employing raster scanning using (a) a small and (b) a large detector surface, (c) a multi-pixel detector and (d) the single-pixel approach.

shape using the introduced methods can be performed using the corresponding projection shown in Fig. 6.9 for each rotation angle. The reconstruction is performed using the SART algorithm of the ASTRA toolbox [162] for each of the four investigated imaging methods. The resulting reconstructions using projection angles from 0° to 180° in 5° iterations are shown in Fig.6.10(a-d) for the employed raster scanning using a small and a large detector surface, a multi-pixel detector and the single-pixel approach, respectively. In all the reconstructed images, the border of the object is apparent by a yellow circle of high absorption. However, the inner appearance of the sample object is quite different for the different investigated approaches. In case of raster scanning using a small detector (Fig.6.10(a)) the inner of the object in the reconstructed image has an absorption value of 35, which is close to the absorption of the surrounding atmosphere. Further, the homogeneous absorption value of the sample object is not reflected in the reconstructed image. In the center of the image a circle with a low absorption coefficient is observed. The same low absorbing feature is also realized in the center of the reconstructed image using the projection employing a multi-pixel detector (Fig. 6.10(c)). But in that case, the contrast between the inner of the sample object and this absorption feature is even higher. The only two reconstructed images that correctly reflect the homogeneous absorption coefficient of the sample object are shown in Fig. 6.10(b,d). The reconstruction of these images is based on the projections obtained by the raster scanning with a large detector and single-pixel approach. The inner of the object is represented by a cyan colored absorption value of 21, while the surrounding atmosphere is represented by a blue one with an absorption value of 12. Solely the yellow circle at the border between air and sample object distorts the reconstructed image. One reason for the good reconstruction results achieved by using the projections of these two techniques is the additional information about the origin of each ray. The origin of a ray does not get lost due to refraction, since the patterns and ray bundles are generated in front of the sample object, which does not hold true for imaging using a multi-pixel detector. Because of the good results obtained in the ray tracing simulations using the single-pixel approach, in the following chapter the approach will be experimentally investigated.

6.3. Hadamard imaging for terahertz tomography

The superiority regarding tomographic terahertz imaging of the the raster scanning approach using a large area detector and the single-pixel technique has been demonstrated in the previous section using ray tracing simulations. Both techniques obtained the same results for the projection of a circular object. Further these results are very similar to the expected projections employing x-ray imaging. Even if both techniques yield the same results in tomographic imaging, there are some advantages in the implementation of single-pixel imaging compared to raster scanning. The measured intensities for each pattern are always a sum of intensities arising from multiple transparent regions defined by the corresponding pattern and are therefore higher as in case of an intensity measurement for each pixel on its own. These higher intensities lead to a better signal to noise ratio at the detector, which is one of the advantages of the single-pixel imaging. Further it does not require mechanical movement of the terahertz source or the sample object. Also promising progress of the single-pixel method has been achieved in the scope of near field imaging, leading for example to sub-wavelength spatial resolution [125]. Motivated by these considerations, a two-dimensional tomographic imaging experiment using the single-pixel approach is investigated in this section.

6.3.1. Experimental set-up

The experiment is integrated in a Bruker Vertex 80V Fourier transform infrared (FTIR) spectrometer as shown in Fig. 6.11. The spectrally filtered radiation of a built-in mercury-arc lamp serves as a broadband terahertz source emitting radiation between 0.45 and 3 THz. This frequency range is caused by the combination of a beamsplitter installed in the spectrometer, a far-infrared cut-off filter incorporated into the detecting bolometer[D24] and the outer vacuum window of the bolometer, which is a wedged white polyethylene window. The bolometer filter is a 1 mm thick diamond wedged crystal quartz coated on

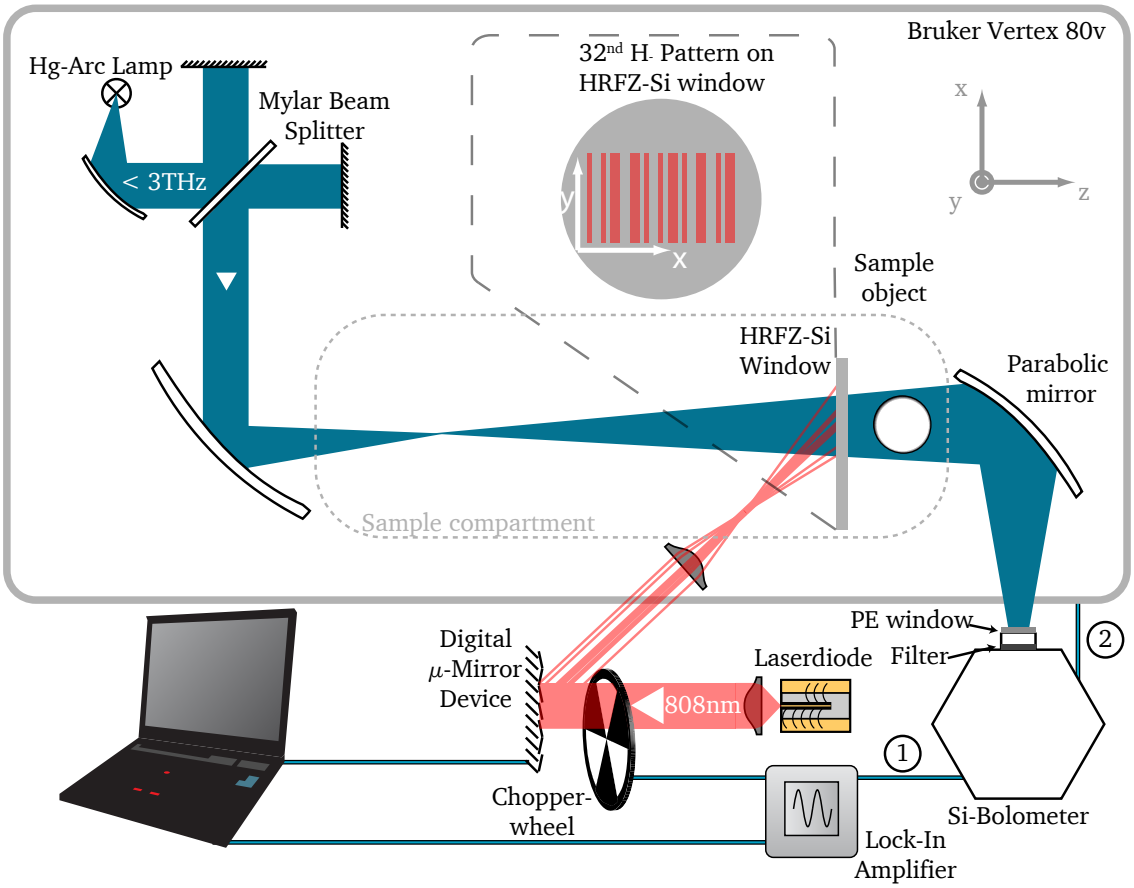

Figure 6.11.: Schematic depiction of the 2D single-pixel tomographic imaging set-up. The inset shows exemplary the 32nd pattern as it is radiated on the HRFZ-Si window by the 808 nm LD.

one face with garnet powder and ensures that only radiation below 3 THz is measured by the bolometer. The terahertz radiation is collimated and passes the Michelson interferometer, whose two arms are fixed at the zero delay position for the experiment. After passing the beamsplitter, the radiation is focused into the sample compartment. Here it is transmitted through a 1 mm thick HRFZ-Si window[D35] and the object under investigation. Finally a parabolic mirror focuses the radiation onto the liquid helium cooled bolometer, which measures the total optical intensity collected by this mirror. The HRFZ-Si window is irradiated by a 1 W 808 nm LD[D36], whose collimated beam is spatially modulated by a digital micromirror device[D37] (DMD). To realize a lock-in detection of the bolometer signal, additional to the

spatial modulation, the LD is temporally modulated by a chopper wheel. Because of the relatively low frequency bandwidth of the bolometer, the modulation frequency amounts to 200 Hz. The so-called photodoping of the HRFZ-Si window by the 808 nm laser beam leads to a change of its transmission characteristics in the terahertz spectral domain [163], transferring the temporal and spatial modulation of the near-infrared radiation into the terahertz radiation, yielding the spatial resolution of the imaging scheme. By the photodoping technique it is possible to achieve a modulation of the terahertz radiation in a broad spectral range from below 0.1 to over 3 THz [164]. The effect of photodoping on the utilized HRFZ-Si window is described in more detail in the next section (6.3.2). Finally, the signal of the bolometer is fed to a lock-in amplifier[D25] as indicated by connection 1 in Fig. 6.11, which extracts the signal amplitude and is readout by a computer. Alternatively, the bolometer can be connected directly to the FTIR spectrometer to perform spectrally resolved measurements as indicated by the connection 2 in Fig. 6.11. For this purpose the temporal modulation of the LD is not necessary and the chopper wheel is turned off.

The used DMD from Texas Instruments possesses 608 mirrors in x- and 684 mirrors in y-direction, which are combined to 32 stripes consisting of 19 mirrors in x-direction and 684 mirrors in y-direction. Thus, a spatial resolution of 32×1 pixels is realized in the terahertz frequency domain. The maximum number of used pixels is determined by the measurement time (more pixels correspond to longer measurement times) and is limited by a minimum reasonable width of each pixel at the HRFZ-Si window, which on the other hand is determined by the investigated wavelength of the radiation. In the realized set-up, the width of one pixel at the HRFZ-Si window amounts to approximately 0.6 mm, which is in the order of the wavelength of the used radiation. In order to gain spatial informations about the transmission properties of the sample object, the HRFZ-Si window and thus the terahertz radiation is spatially modulated by a multitude of patterns, consisting of 32 pixels in x-direction, defined by a 32×32 Hadamard matrix $\mathbf{H}$. Since the Hadamard matrix only consists of the values $+1$ and -1, each row of $\mathbf{H}$ represents two patterns. The instruction for the creation of the patterns is exemplary shown in Fig. 2.13(a) for the first two and last two patterns. The H_+ patterns are created by transparent regions represented by $+1$ entries and opaque regions for the -1 entries, while this is reversed for the H_- patterns. As an example, the resulting 32nd H_- pattern is shown as inset in Fig. 6.11, as it is radiated on the HRFZ-Si window by the 808 nm LD. For each of the 64 patterns ($32 \times H_+$ and $32 \times H_-$) the total transmitted terahertz radiation is measured by the bolometer, resulting in two measurement vectors $\vec{M}_+$ and $\vec{M}_-$, which are related to $\mathbf{H}$ by Eq. 2.24. With these two measurement vectors the image can be reconstructed using Eq. 2.25 and Eq.2.23. Hence, the spatially resolved transmission of the sample object can directly be calculated from the two measurement vectors and the Hadamard matrix.

Before every tomographic measurement an image of the terahertz beam profile is taken using the formalism described above and with no sample object placed in the sample compartment. This beam profile is used to normalize the transmission through the sample object, which is realized by dividing the object image by the measured beam profile. In this way a normalized object transmission is received, which is then converted into absorption values and which are used for the tomographic image reconstruction. Figure 6.12 shows the beam profile of the utilized mercury-arc lamp at the sample compartment of the spectrometer. On the left (pixel position $1-6$) and right side (pixel position $22-29$) of the beam profile the intensity rises, reaching an intensity maximum of 12.5 and 13 (in arb. u.), respectively. In between these two maxima a drop of intensity is observed, which is caused by a window for an adjustment laser in

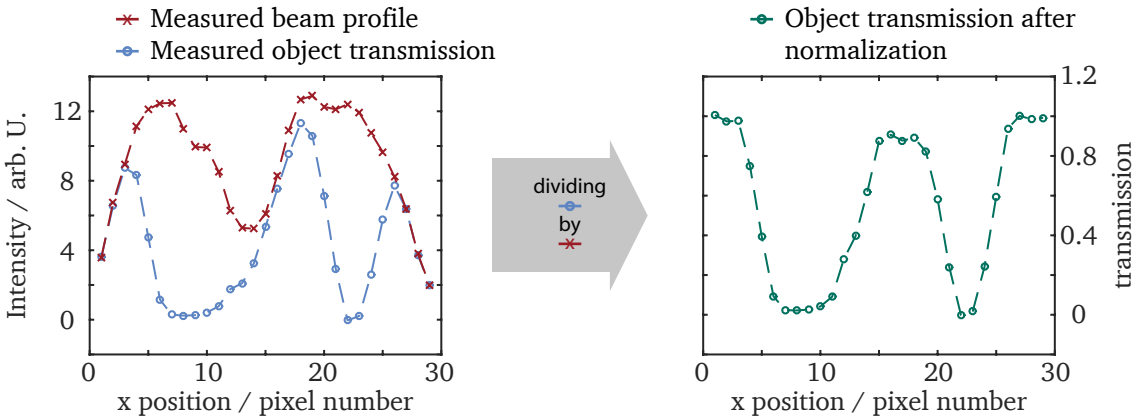

Figure 6.12.: Exemplary measured beam profile and raw object transmission for a cuboid sample object under a rotation angle of 120°. The object projection is divided by the beam profile to achieve the normalized transmission of the object as shown on the right. The normalized transmissions are then converted into absorption values, which are used for the tomographic image reconstruction.

the center of the beam splitter installed inside the spectrometer. This drop of the intensity is removed from the object transmission by the normalization procedure as can be seen in Fig. 6.12.

6.3.2. Photodoping of a high resistivity float zone silicon window

There exist a multitude of possible techniques to modulate terahertz radiation in the temporal domain. These technique include all-electric, thermal, magnetic and all-optical schemes and furthermore often make use of meta materials [158]. In the all-optical scheme, mostly visible or NIR radiation is temporally modulated and subsequently this modulation is transferred onto the terahertz radiation. This transfer can be realized by thin disks of a semiconductor material. As described in the experimental set-up the visible or NIR radiation is irradiated on the semiconductor, which leads to the generation of free carriers if the energy of the radiation is higher than the band-gap of the material. These free carriers modify the optical properties of the semiconductor in the terahertz frequency domain. Due to the fast recombination times in semiconductors its optical properties return back to equilibrium, if no visible or NIR radiation is irradiated any more. In this way, pulses of terahertz radiation with a width of 10 ns have been generated [159]. One benefit of the all-optical modulation technique is the possibility to easily achieve not only temporal modulation of the terahertz radiation, but also spatial modulation [164]. Due to the development of spatial light modulators for visible and NIR radiation it is possible to spatially distribute the intensity of this radiation onto the semiconductor. As a result the optical properties of the semiconductor in the terahertz frequency domain are spatially modulated and again transfer the intensity distribution of the visible or NIR light to the terahertz radiation. Using this technique optically reconfigurable terahertz components [165] and graded index gratings [166] in the terahertz frequency domain have been realized.

The influence of free carriers generated by photoexcitation to the optical properties of a semiconductor

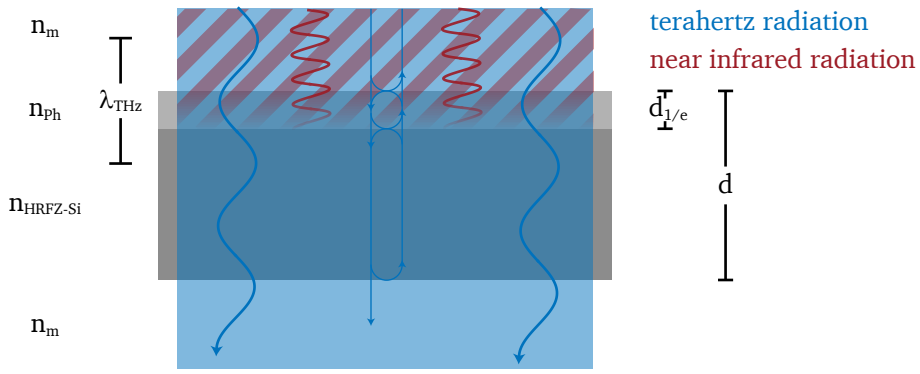

Figure 6.13.: Optical layer model that describes the photodoping of a HRFZ-Si window of thickness d. 63% of the NIR radiation is absorbed after a depth of $d_{1/e}$ by the window.

in the terahertz frequency domain can be described by the dielectric function derived from the Drude model [167]. This semiclassical model describes the charge transport in a solid under the acceleration of an external electric field. The response of the solid to an alternating electric field with an angular frequency of $\omega = 2\pi f$ is given by the well known Drude dielectric response function

$$\epsilon(\omega) = \epsilon_\infty - \frac{\omega_p^2}{\omega^2 + i\gamma\omega}. \tag{6.11}$$

Here ϵ_∞ is the background dielectric constant, ω_p is the plasma frequency and γ is the carrier scattering rate of the semiconductor. By photodoping, the free carriers density N of the semiconductor is changed and therefore the plasma frequency ω_p shifts according to

$$\omega_p = \sqrt{\frac{N \cdot e^2}{\epsilon_0 \cdot m^*}}, \tag{6.12}$$

with ϵ_0 the permittivity of vaccum, e the electron charge and m^* the effective electron mass.

The incident terahertz and NIR radiation impinge on the interface between the ambient and a photodoped layer of the semiconductor as schematically depicted in Fig. 6.13. The photodoped layer of the semiconductor is described by its complex refractive index $n_{Ph} = \sqrt{\epsilon(\omega)}$ and the thickness $d_{1/e}$. Since the NIR radiation is strongly absorbed by the semiconductor, the photodoped layer can be regarded as a very thin layer with a homogeneous refractive index n_{Ph} [167]. The length on which the intensity of the NIR radiation declines to a 1/e fraction of the initial intensity defines the thickness $d_{1/e}$ of the photodoped layer of semiconductor. After the photodoped layer, the terahertz radiation impinges on the interface between the photodoped and unphotodoped semiconductor, on which the radiation is partly reflected and transmitted. The thickness of this second layer is given by the total thickness d of the semiconductor minus the thickness $d_{1/e}$ of the photodoping layer. Finally, the terahertz radiation is partly reflected and transmitted due to the interface between the semiconductor and the ambient. On its way through the semiconductor the terahertz radiation gets reflected back and forth multiple times by the different interfaces, which results in constructive and destructive interference of the terahertz radiation. The total

intensity transmittance T of the terahertz radiation can be calculated using a matrix formulation [168] of the system depicted in Fig 6.13. A single layer can be described using the refractive index n_j, the layer thickness d_j, the angle of incident θ_j and the wavelength of the terahertz radiation λ_{THz} by the matrix

$$\mathbf{M_j} = \begin{pmatrix} cos(\delta_j) & \frac{i}{\eta_j} sin(\delta_j) \\ i\eta_j sin(\delta_j) & cos(\delta_j) \end{pmatrix} \tag{6.13}$$

$$\delta_j = \frac{2\pi}{\lambda_{THz}} \left(n_j d_j cos(\theta_j) \right) \tag{6.14}$$

$$\eta_j = \begin{cases} \frac{n_j}{cos(\theta_j)} & p-polarization \\ n_j cos(\theta_j) & s-polarization \end{cases} \tag{6.15}$$

Using these matrices, the transmission coefficient t of the system is given by

$$t = \frac{2\eta_m}{\eta_m E_m + H_m} \tag{6.16}$$

$$\begin{pmatrix} E_m \\ H_m \end{pmatrix} = \mathbf{M_{ph}} \mathbf{M_{Si}} \begin{pmatrix} 1 \\ \eta_m \end{pmatrix}, \tag{6.17}$$

from which the total intensity transmittance T can be calculated

$$T = \frac{\eta_m}{\eta_m} |t|^2 = |t|^2 . \tag{6.18}$$

Applying the described model of the photodoping process, the terahertz transmittance and reflectance with and without NIR radiation impinging on the HRFZ-Si window of the experimental set-up can be simulated. The material properties of the HRFZ-Si window are assumed to 3×10^{-13} s for the scattering time $\tau = \frac{1}{\gamma}$, 11.7 for ϵ_∞, $10^{12}\,\mathrm{cm}^{-3}$ for the carrier density without photodoping and $0.26\,\mathrm{m}_0$ for m^*, where m_0 is the free electron mass [169]. Further, for the investigated HRFZ-Si window it was found that the density of free carriers saturates at a maximum value of $2.25 \times 10^{16}\,\mathrm{cm}^{-3}$ [169]. The HRFZ-Si window possesses a thickness of 1 mm and the absorption coefficient of silicon is $945\,\mathrm{cm}^{-1}$ [170] at a wavelength of 808 nm, which results in a thickness of the photodoping layer of $d_{1/e} \approx 11\,\mu$m. Figure 6.14(a,b) shows the calculated transmission of the HRFZ-Si window (a) without and (b) with saturated photodoping using a wavelength of 808 nm for the terahertz frequency range from 0.5 to 3.5 THz. In both cases an inset shows a zoom of the transmission spectra in the range from 0.75 to 1 THz. With and without photodoping, the transmission shows multiple Fabry-Pérot fringes due to the multiple reflections and the consequent constructive and destructive interference. The spacing between these fringes is determined by the thickness of the undoped layer and therefore varies slightly between the two cases without and with photodoping. For the case in which no NIR radiation impinges on the HRFZ-Si window (Fig. 6.14(a)), the transmission is modulated between 0.3 and 1, which corresponds to a Fabry-Pérot interferometer with an finesse of 2.5. From Fig. 6.14(b) it can be seen that due to the saturated photodoping of the HRFZ-Si window, a frequency-dependent absorption lowers the maximum transmission. The rising absorption coefficient of the illuminated HRFZ-Si window is caused by the absorption of the terahertz radiation by the increasing number of free carriers. This can also be seen in the plasma frequency ω_p, which amounts

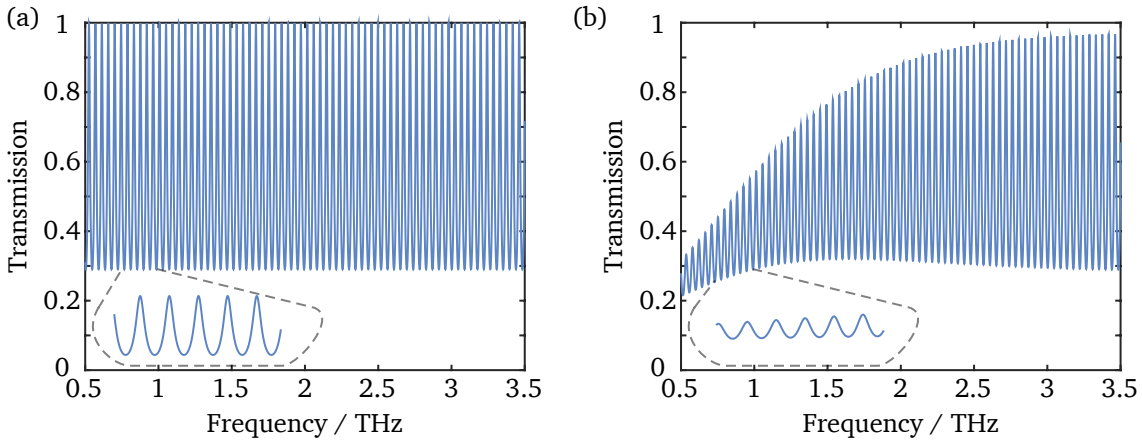

Figure 6.14.: (a) Calculated terahertz transmission through the HRFZ-Si window (a) in the absence of NIR radiation and (b) under saturated photodoping conditions.

to 0.11 THz for the HRFZ-Si window without illumination and 16.6 THz in case of saturated doping of the window. Radiation with a frequency above the plasma frequency experience no absorption within the material, while the material absorbs radiation with a frequency below ω_p. Starting from a value of 0.33 at 0.5 THz, the transmission maximum rises with increasing frequency and converges towards 1 beyond a frequency of 3.5 THz. Also the minimum transmission values are lower compared to the transmission curve without photodoping of the HRFZ-Si window (Fig. 6.14(a)). The minimum transmission values of the photodoped HRFZ-Si window exhibit a frequency-dependent curve, which is not as pronounced as in case of the maximum values. The difference in the minimum transmission values between with and without photodoping indicates, that beside the transmission of the window also the reflection changes under the influence of photodoping. Figure 6.15(a,b) shows the calculated reflectance of the HRFZ-Si window (a) without and (b) with saturated photodoping using a wavelength of 808 nm for the terahertz frequency range from 0.5 to 3.5 THz. In both cases an inset shows a zoom of the reflectance spectra in the range from 0.75 to 1 THz. With and without photodoping, the reflectance shows multiple Fabry-Pérot fringes as already observed in the transmission spectra. For the case in which no NIR radiation impinges on the HRFZ-Si window (Fig. 6.15(a)), the reflectance varies between 0 and 0.7. A reflectance of 0 is given at frequencies where the transmission is 1, while 0.7 is reached at frequencies with a transmission value of 0.3. Due to the illumination with 808 nm radiation the minimum and maximum reflectance changes, as can be seen in Fig. 6.15(b). Starting from a value of 0.45 at 0.5 THz, the reflectance maximum rises with increasing frequency and converges towards 0.7. For the minimum reflectance between 0.5 and 2 THz higher values are observed compared to the reflectance curve without photodoping of the HRFZ-Si window. These higher reflectance values converge to the original reflectance value of 0 shortly beyond a frequency of 2 THz.

In order to depict the frequency-dependent change of transmission and reflection, an envelope of the transmission and reflection spectra is obtained. Afterwards the mean transmission $< T >$ and reflection

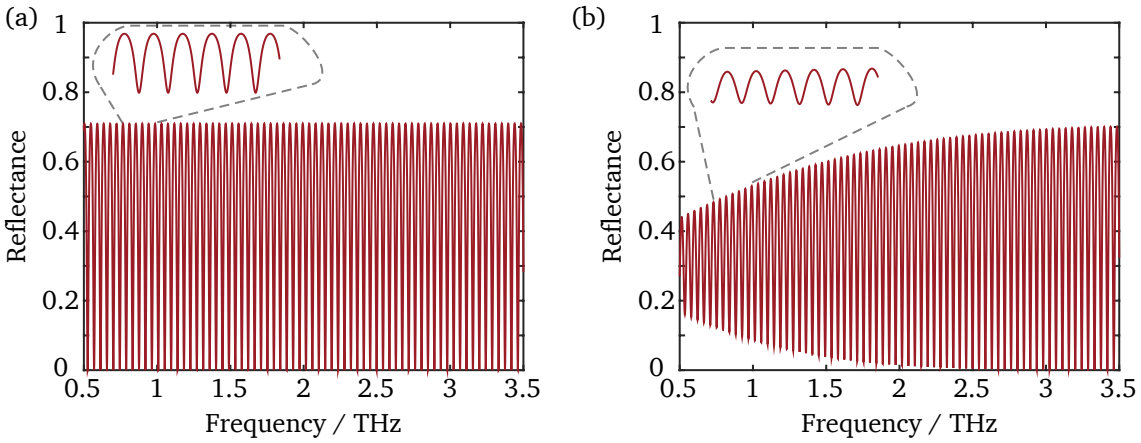

Figure 6.15.: (a) Calculated terahertz reflectance through the HRFZ-Si window (a) in the absence of NIR radiation and (b) under saturated photodoping conditions.

$< R >$ is calculated in each case by the sum of the upper and lower envelope divided by two. The achievable modulation depth for transmitted D_t and reflected D_r terahertz radiation is calculated using

$$D_t = 1 - \frac{< T_{with} >}{< T_{without} >} \tag{6.19}$$

$$D_r = 1 - \frac{< R_{with} >}{< R_{without} >}. \tag{6.20}$$

Here the indices $without$ and $with$ correspond to the plain HRFZ-Si window and the HRFZ-Si window under saturated photodoping, respectively. The frequency-dependent modulation depth for reflected and transmitted terahertz radiation is shown in Fig. 6.16 in the frequency range of 0.5 to 3.5 THz. A maximum modulation depth of nearly 60 % is obtained for the transmission at a frequency of 0.5 THz. With increasing frequency the modulation depth drops and reaches 10 % at 2 THz. Afterwards the modulation depth further decreases and slowly approaches 0 % beyond the x-axis limit of the plot of 3.5 THz. Overall, the modulation depth for reflected terahertz radiation is lower compared to the achieved modulation depth of the transmitted terahertz radiation. Here, a maximum modulation depth of 15 % is achieved at 0.5 THz. As for the transmitted terahertz radiation, the modulation depth decreases with increasing frequency. But the decrease occurs at a much smaller gradient compared to the modulation depth of the transmitted terahertz radiation between 0.5 and 2 THz. At 2 THz the curves of the reflected and transmitted modulation depth cross and proceed at a similar gradient.

In general, higher modulation depths for the transmitted terahertz radiation can be achieved by increasing the thickness $d_{1/e}$ of the photodoped layer. This can be realized by a wavelength shift of the NIR radiation towards lower energies. For example, for a wavelength of 950 nm a thickness $d_{1/e}$ of 65 μm is calculated for silicon, which is six times larger compared to the investigated wavelength of 808 nm. Of course, the optical power of the NIR radiation has to be sufficient larger in order to create enough free carriers in the extended photodoping volume.

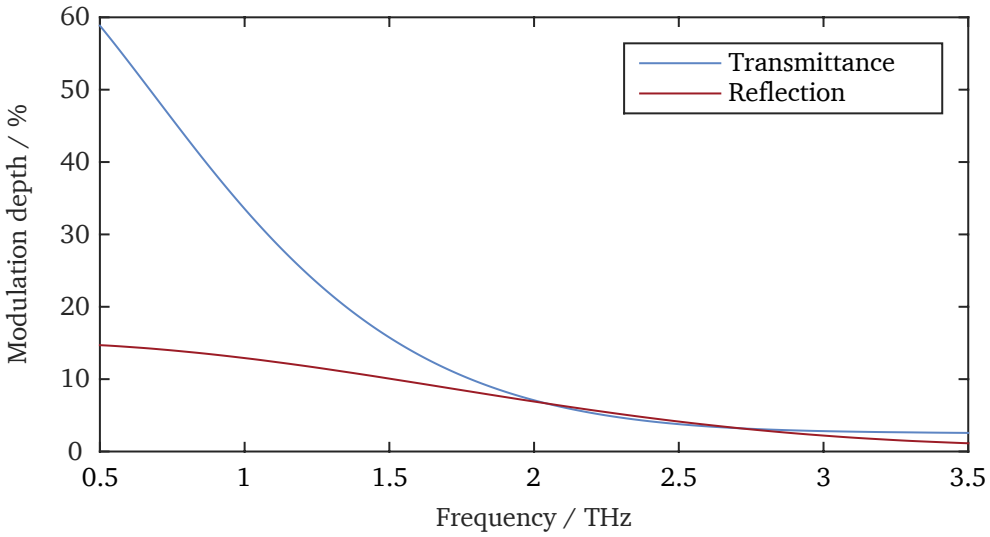

Figure 6.16.: Calculated frequency-dependent modulation depth for reflected and transmitted terahertz radiation.

After these theoretical considerations the transmission of the HRFZ-Si windows used for the single-pixel imaging approach under photodoping is investigated. For this purpose, the experimental set-up shown in Fig. 6.11 is used, but the DMD is replaced by an ordinary gold mirror. Further the measurements are performed under vacuum conditions (≈ 4 mbar) and a metal aperture with a diameter of 3 mm is placed directly on the HRFZ-Si window. This aperture is homogeneously illuminated by the terahertz and the NIR radiation and ensures that only terahertz radiation is measured, which overlaps with the NIR radiation on the HRFZ-Si window. The intensity of the terahertz radiation is measured by the bolometer, which either is connected to the lock-in amplifier or the FTIR-spectrometer, providing the intensity integrated over the whole terahertz frequency range of the source (connection 1 in Fig. 6.11) or the spectrally resolved intensity (connection 2 in Fig. 6.11), respectively.

Two spectra taken with and without NIR radiation impinging onto the HRFZ-Si window are shown in Fig. 6.17. As in case of the simulated transmissions, the spectra both show Fabry-Pérot fringes. The actual overall shape of the spectra is caused by different components in the FTIR-spectrometer like the beamsplitter, the cut-off filter in front of the bolometer and the real spectra of the mercury-arc lamp as described in section 6.3.1. The spectra shows two broad emission domains with their intensity maxima located at 1.25 and 2.6 THz. The left domain extends between 0.5 and 1.6 THz and is separated by a gap of no emission from the second domain, which extends from 1.9 to 3.5 THz. The spectrum shown as a dotted red line in Fig. 6.17 represents the transmission through the plain HRFZ-Si window. The amplitude of the left and right domain approach 1.5 and 2, respectively. By illuminating the HRFZ-Si window with an intensity of 87 mW/mm^2 at a wavelength of 808 nm, the transmission in both domains decreases. This is shown as solid blue line in Fig. 6.17. As already seen in the calculated transmissions, the measured spectra of the illuminated HRFZ-Si window exhibits a decreased maximum transmission and also the minima of the fringes are slightly lower compared to the plain window. From the measured spectra a maximum modulation depth between 24 and 32% is recognized.

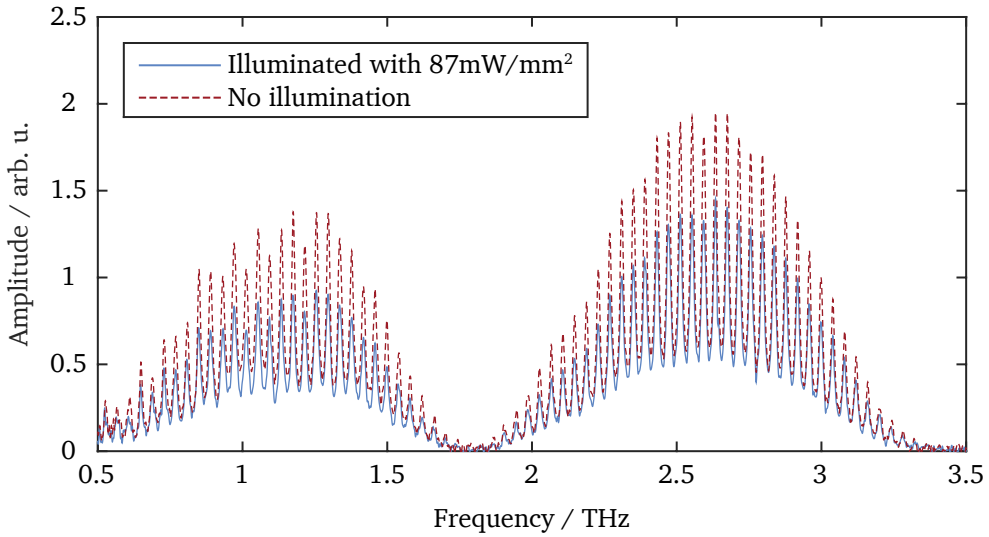

Figure 6.17.: Measured terahertz transmission through a 1 mm thick HRFZ-Si window in the absence of NIR radiation (dashed, red) and under photodoping with an optical power of 87 mW/mm^2 (solid, blue).

In order to investigate now the dependency of the photodoping modulation technique on the intensity of the incident NIR radiation the bolometer is directly connected to the lock-in amplifier and the NIR radiation is temporally modulated with a frequency of 200 Hz. Hence, the lock-in amplifier measures the terahertz transmission difference between the photodoped and plain HRFZ-Si window integrated over the whole terahertz spectra (by using connection 1 in Fig. 6.11) depicted in Fig. 6.17. The intensity of the 808 nm LD is tuned by its pump current from 0 to 87 mW/mm^2 and the lock-in signal is recorded as shown in Fig. 6.18(a). Between an intensity of 20 mW/mm^2 and the maximum intensity a linear dependency is observed and the lock-in signal rises to a maximum of 18 mV. The amplitude of the lock-in amplifier still shows no saturation at an intensity of 87 mW/mm^2, which indicates that the number of free carriers is still below 2.25×10^{16} cm^{-3} inside the photodoped volume of the HRFZ-Si window.

During the investigations on the photodoping based terahertz modulation technique, a temporal dependence of the lock-in amplitude has been noticed. At the beginning of the illumination of the HRFZ-Si window with NIR radiation, the lock-in amplitude rises from 8 mV to 12.5 mV during a duration of 10 minutes. This is shown in Fig. 6.18(b) by the measurement points inside the first green area. After these 10 minutes the NIR radiation is blocked, while the window remains under vacuum conditions. The measured lock-in amplitude drops to zero, since the terahertz radiation is no longer modulated as shown within the first red area in Fig. 6.18(b). Another 10 minutes later, the window is again exposed to the NIR radiation and only a small difference to the former lock-in amplifier amplitude after 10 minutes of irradiation can be seen. Afterwards, the NIR radiation is blocked for 12.5 minutes, but this time the window remains under ambient conditions. At the end of this time the vacuum conditions are restored and the NIR laser is revealed to the window. As at the beginning of the measurement, the signal amplitude

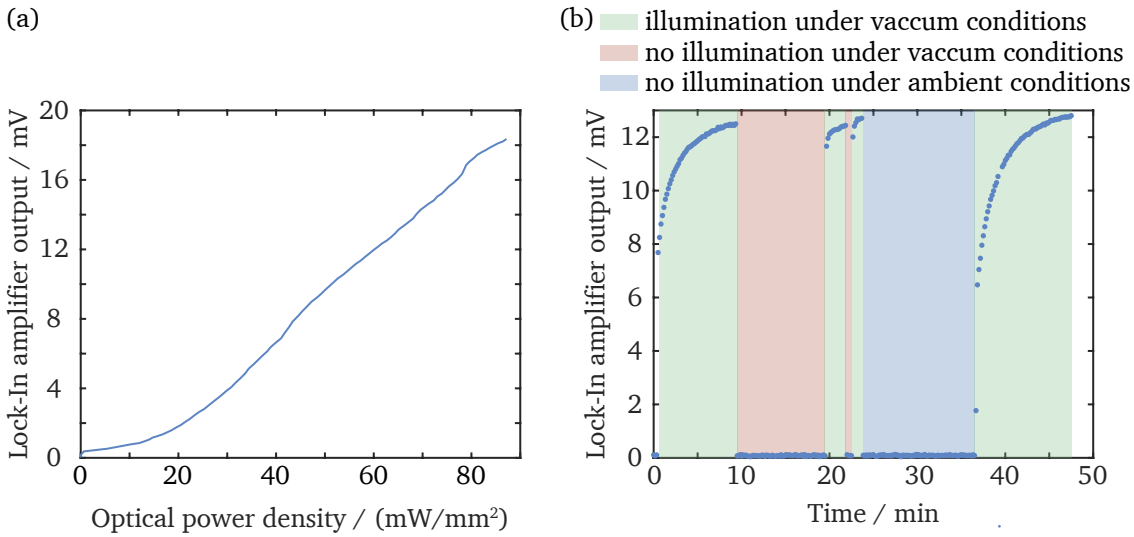

Figure 6.18.: (a) Difference of the transmitted intensity through an irradiated and plain HRFZ-Si window measured with a bolometer for different intensities of the NIR radiation. (b) Temporal dynamics of the signal measured in (a) right after irradiation of the HRFZ-Si window with temporally modulated NIR radiation.

exponentially increases and reaches a maximum after approximately 10 minutes. A possible reason for this phenomenon could be the deposition of heat inside the HRFZ-Si window by the NIR radiation. By blocking the NIR radiation, but leaving the window under vacuum conditions the heat dissipation could be so low that the window does not reach its initial temperature within the 10 minutes. However, the increased temperature provoke more free carriers inside the silicon [171], which would lead to a reduction of the modulation depth and therefore the lock-in signal should decrease. Another possibility could be the desorption of molecules from the surface of the window. The deposited energy of the NIR laser could lead to the desorption of gas molecules and therefore influence the transmission properties in the terahertz frequency domain, as it has been observed for graphene [172] and active carbon [173]. While the window remains under vacuum conditions (≈ 3 mbar) and is not illuminated there are only very few molecules, which could adsorb on the surface of the window. Therefore, the lock-in amplifier signal is still the same before and after the intermediate time with no irradiation. This changes if the window remains under ambient conditions and molecules could adsorb on the window. A detailed investigation of this phenomenon is out of scope of this thesis. However, it is an interesting topic for further extensive investigations. In the following, the NIR light is irradiated onto the HRFZ-Si window until the lock-in amplitude reaches its maximum and subsequently the measurement is performed.

6.3.3. Results and discussion

Now that the terahertz radiation can be modulated using the photodoping approach in the spatial and temporal domain, the single-pixel imaging set-up described in section 6.3.1 is investigated for tomographic terahertz imaging using the connection scheme 1 shown in Fig. 6.11. First of all, two metallic M4 screws are arranged on a base plate and are used as sample object. They are positioned on the rotation stage behind the HRFZ-Si window and a projection is recorded using the Hadamard formalism. For this purpose, successively one of the H_+ and H_- pattern is alternately projected onto the HRFZ-Si window and the transmitted terahertz radiation is measured by the bolometer. In this way, the M_+ and M_- measurement vector is determined, from which the projection of the sample object is calculated using Eq. 2.23. Figure 6.19(a) shows the $\vec{M}_+$ and $\vec{M}_-$ measurement vectors. Each value is the average of 25 measurements for the corresponding pattern taken with a separation of 1 s and an integration time of 300 ms at the lock-in detector. The shown error bars represent the mean square error of these 25 measurements. The first pattern of H_+ represents the total intensity transmitted through the object and

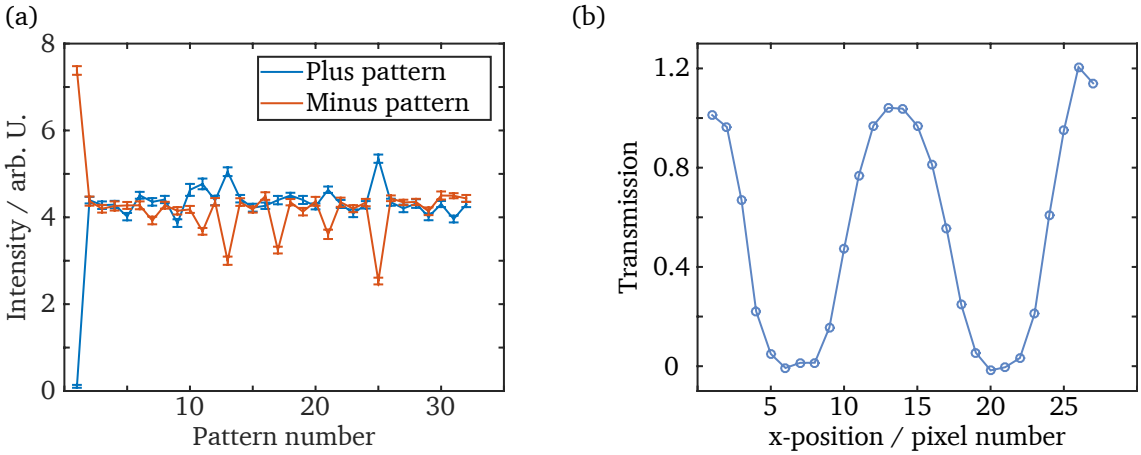

Figure 6.19.: (a) Measurement vectors $\vec{M}_+$ and $\vec{M}_-$ for a measured projection of the two M4 screws under a rotation angle of 0°. (b) Result of the projection calculation using the measurement vectors of (a) and Eq. 2.23.

consequently has the highest value of all measurement points. With a value of 8 %, the mean square error of the measurement points is very low and therefore the delicate differences in the various patterns is measured within a good accuracy. Indeed, the difference between most of the plus pattern and their counterpart the minus pattern is small. Besides the first pattern, only the 11th, 13th, 17th, 21st and 25th pattern show a large difference on their intensities. By multiplying the difference of the two measurement vectors with the inverse of the Hadamard matrix the projection for a rotation angle of 0° of the two M4 screws is obtained. This projection is depicted in Fig. 6.19(b). The two screws are clearly visible by two peaks of no transmission, while the surrounding atmosphere is mostly transparent. Now the screws are rotated by 20° and another projection is measured. This procedure is repeated until projections for rotation angles between 0° and 170° in 20° iterations are measured for the two screws. The resulting 2D absorption profile in dependence on the position and the rotation angle, the so-called sinogram, is shown in Fig. 6.20. In order to avoid aliasing in the rasterisation of the projections, occurring in the reconstruction algorithm for the 2D reconstruction, the resolution of the obtained transmission projections

Table 6.1.: Definition of quantities for an objective expression of the image quality. The values in the last column refer to the quality of the reconstructed image of the two M4 screws shown in Fig. 6.21.

Quantity	Definition	Value
Visibility	$v = \frac{<A_{obj}> - <A_{env}>}{<A_{obj}> + <A_{env}>}$	0.56
Contrast-to-noise ratio	$CNR = \frac{<A_{obj}> - <A_{env}>}{\sigma}$	17.2

for every rotation angle θ_y is increased by a factor of 10 using a linear interpolation in between the measured points. Beginning at an angle of 0° the two screws, which are represented by the two separated yellow areas, first enlarge their spacing to each other. The two screws reach a maximum distance between each other at 40° and beyond this angle they again approach each other. The two screws start to join each other between 120° and 160° and at an angle of 140° only one screw is visible and afterwards they again start to separate from each other.

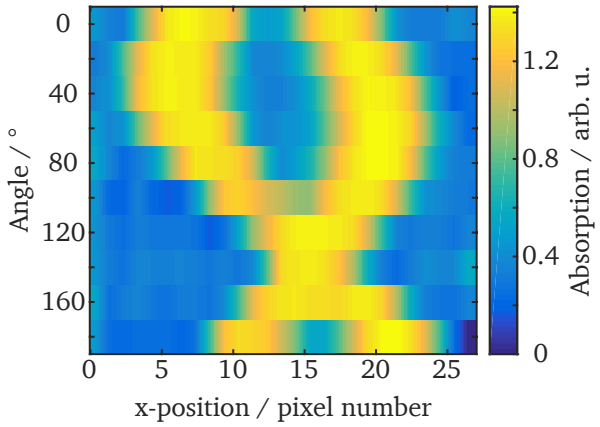

Figure 6.20.: Measured sinogram of two M4 screws.

In order to obtain a two dimensional image of the arrangement of the two screws, the SART implemented in the ASTRA toolbox [162] is applied to the sinogram shown in Fig. 6.20. The reconstructed image of the scene is depicted in Fig. 6.21. Two yellow highly absorbing circular spots are noticed in the image representing the screws. The two screws possess a diameter of 3.14 mm, which coincides with the size of five pixels in the image. Apparently the image exhibits a good contrast, since the screws are well distinguishable from the surrounding atmosphere. The overall image quality is described by several quantities as for example the contrast-to-noise ratio CNR and the visibility v. The mathematical definitions of these quantities are given in table 6.1, where $< A_{obj} >$ and $< A_{env} >$ are the mean amplitudes of the object and the environment, respectively and σ is the standard deviation of a pixel in the image. For

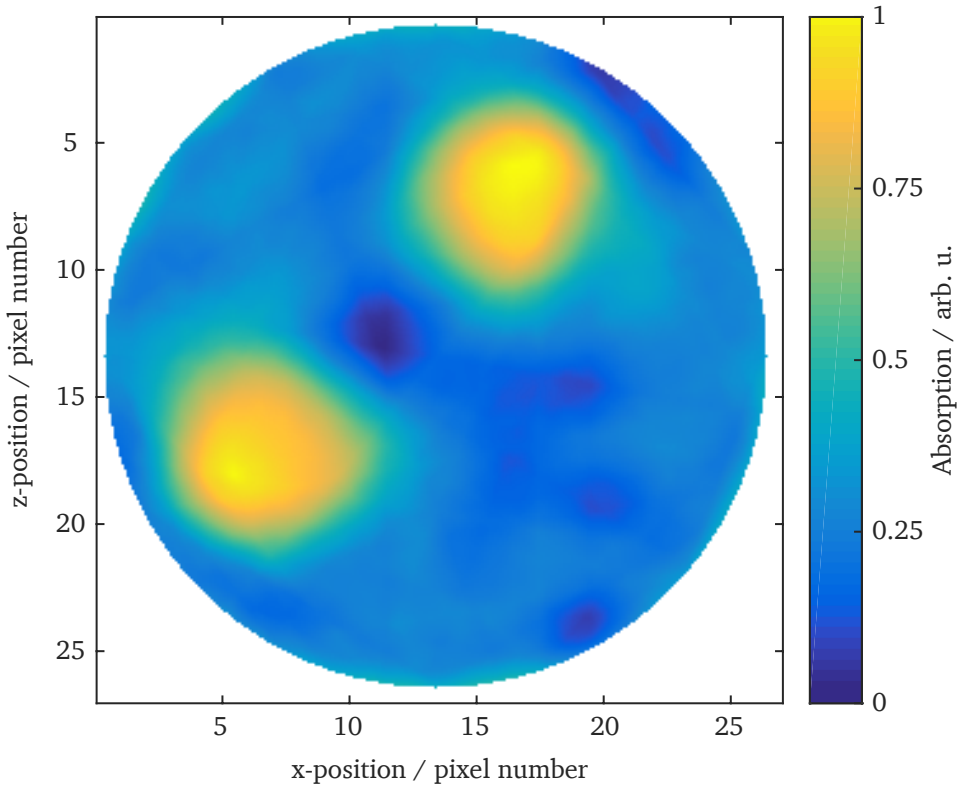

Figure 6.21.: Reconstructed image of two M4 screws using the SART.

the CNR an constant standard deviation for the environment and the object is assumed. The visibility indicates how large the difference in amplitude of the environment A_{env} and the object A_{obj} is and gives information how pronounced the object appears. A visibility of 1 is achieved if the amplitude of the environment is zero and therefore represents the upper limit. The lowest visibility is reached in case of equal amplitudes for the object and the environment, which is expressed by a visibility of 0 since the object is not distinguishable from the environment at all. The investigated metal screws are totally opaque for the terahertz radiation and therefore cause a maximum achievable contrast between the environment and the sample object. However, the visibility of a metal screw shown in Fig. 6.21 does not approach the maximum visibility of 1, but rather amounts to 0.56. This is caused by atmospheric absorption of the terahertz radiation, which ranges from $10^{-4}\,\frac{1}{cm}$ at 500 GHz to $10^{-1}\,\frac{1}{cm}$ at 3 THz [174]. All tomographic imaging experiments are performed under ambient conditions and the contrast between the sample and the surrounding atmosphere is lower due to this atmospheric absorption compared to the contrast between sample and vacuum. In order to set the visibility of the object in relation to the noise of the image, the difference in amplitudes is divided by the standard deviation of the pixel values, which gives the CNR. The range of possible CNR values is not limited to a specific interval as in case of the visibility, but a value of 1 corresponds to an amplitudes difference ($< A_{obj} > - < A_{env} >$) equal to the standard deviation. In that case objects would not be distinguishable from noise, which represents the worst case scenario. With higher CNR values, the object clearly gets more distinguishable from random fluctuations. The reconstructed image in Fig. 6.21 exhibits a CNR of 17.2, which also indicates that the metal screws

are well distinguishable from noise.

Even if the two metal screws are a suitable test object to discuss on the maximum potential visibility and *CNR* values, they do not offer the possibility to realize an insight into the object because of their high absorption coefficient. However, this look inside a sample object is often desirable when applying tomographic imaging. Therefore, the introduced single-pixel tomographic imaging concept is now applied to cylindrically and cuboid shaped sample objects consisting of polypropylene (PP). The synthetic material PP exhibits a low absorption coefficient of near 1 cm^{-1} and a refractive index of 1.5 between 0.3 and 4 THz [175, 176]. Again the sample objects are placed on the rotational table and x-direction resolved projections of the sample object are measured using single-pixel imaging at each rotation angle from 0° to 180° in 10° iterations. An exemplary projection (Fig. 6.22(a)) and the sinogram (Fig. 6.22(b)) of a solid PP cylinder with a diameter of 14 mm is shown in Fig. 6.22.

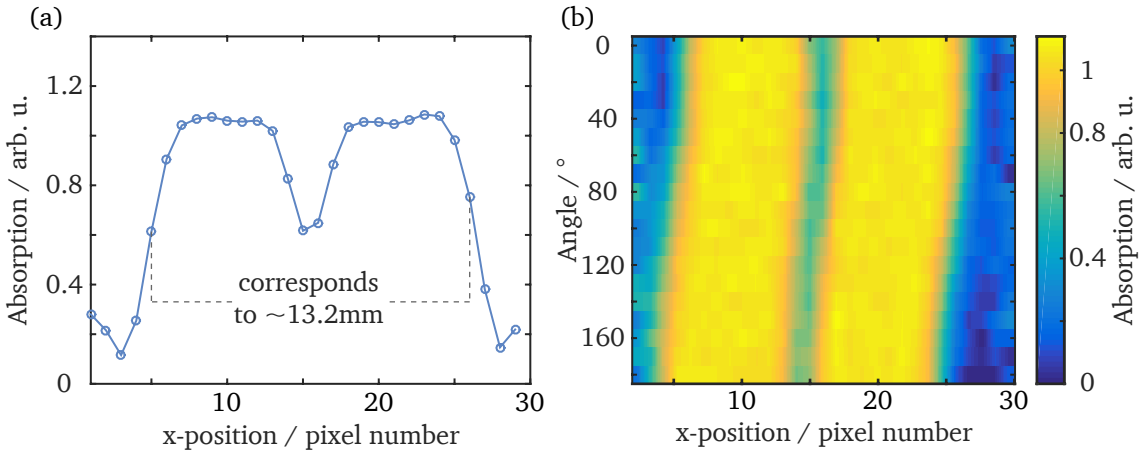

Figure 6.22.: (a) Measured projection under a rotation angle of 0° and (b) measured sinogram of a cylindrical PP sample with a diameter of 14 mm. From the projection (a), the diameter of the cylinder can be estimated between 13 and 14.5 mm.

At first, the projection shows a low absorption through the atmosphere in the periphery at the positions 0 to 3 and 27 to 28. In the area in between, the absorption rises to a maximum of approximately 1 forming plateaus of no terahertz transmission. In the center (position 15) of the projection a reduced absorption peak is observed. In the terahertz spectral domain, this kind of projection shape is typical for a cylindric object, and has also been observed for the HSM tomography experiment in section 6.1, the Raytracing simulations in section 6.2 and by others [119, 120]. Here, the plateaus do not represent regions of the sample object with a high absorption coefficient, they are rather the result of combined refraction and reflection effects. These optical effects have a particularly large impact on the measured projections in the terahertz frequency spectrum, leading to a lens-like focusing of the radiation after a circular shape. A rotation of the cylindrical sample objects shows no change in the shape of the measured projections, as can be seen from the sinogram in Fig. 6.22(b). Only a slight shift of the central transmission peak can be observed, indicating a small difference of the rotational table axis and the cylinder center.

While the measured projections of the cylindrical sample object show strong influences of refraction and reflection effects caused by the bended surface, a cuboid sample object with one of its flat faces orthogonal to the beam propagation direction should only show some additional losses due to reflection, since the rays incident parallel to the surface normal. Two different projections measured at a rotation angle of 180° (Fig. 6.23(a)) and 120° (Fig. 6.23(b)) and the measured sinogram (Fig. 6.23(d)) of a cuboid PP sample with side lengths of 14×7 mm are shown in Fig. 6.23. It is noticeable that in the case of a 180° rotational angle of the sample (Fig. 6.23(a)), which corresponds to a geometric arrangement, where the rays incident parallel to the surface normal, a multitude of features can be observed. These features do

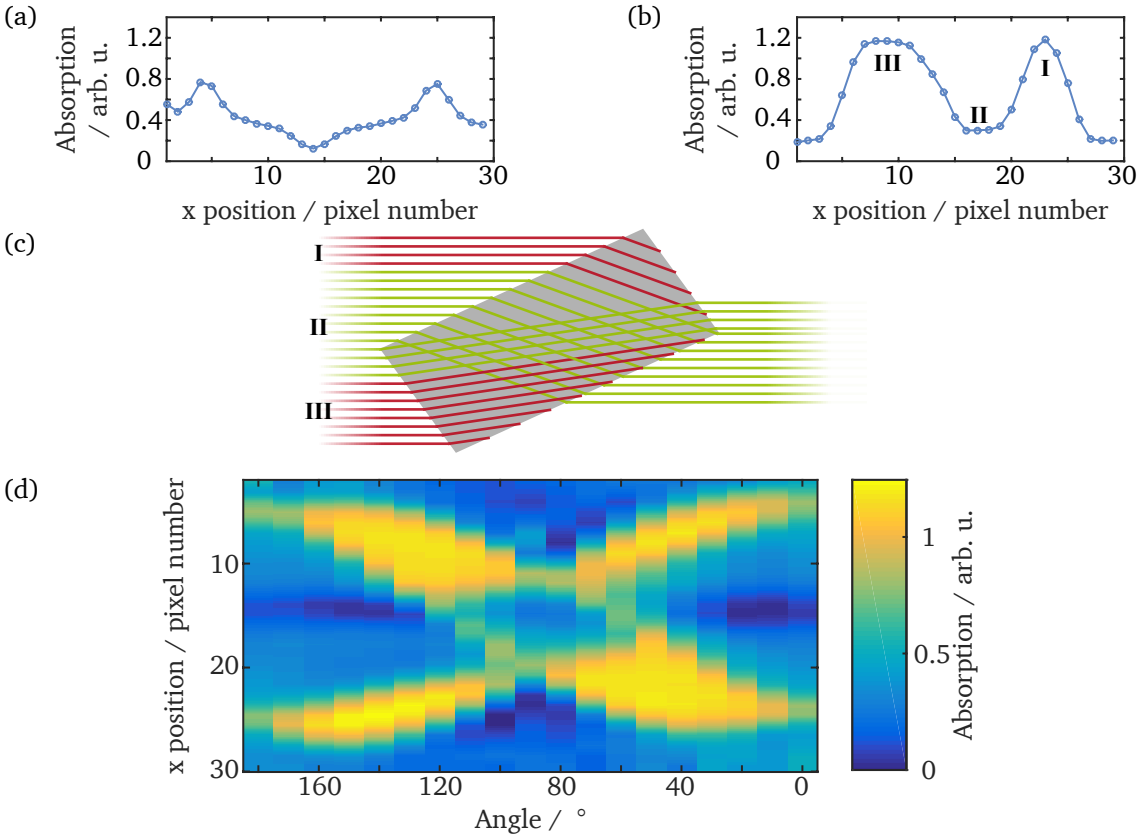

Figure 6.23.: Two measured projections under a rotation angle of (a) 180° and (b) 120° and (d) measured sinogram of a cuboid PP sample with edge lengths of 14×7 mm. (c) Ray tracing simulation for a rectangular object with edge lengths of 14×7 mm and a refractive index of 1.5 under a rotation of 120°. Red colored rays indicate rays which get totally reflected on the rear side, while green rays can pass the object.

not agree with the previous assumption that only some additional reflection losses occur, but rather can be attributed to diffraction effects. The outer dimensions of the cuboid sample object can be recognized due to the two absorption peaks located at position 4 and 25, which indicate the side edges. In contrast to the high absorption plateaus of the cylindrical sample object, there is still some transmission of terahertz radiation at these two absorption peaks. Next to each of the two peaks, there are two regions of slowly decreasing absorption (positions 7-11 and 17-22) representing the inner of the sample. In the center of

the measured projection a small dip of low absorption is recognized. The described shape of the projection changes quite a lot, if the sample object is rotated as can be seen in Fig. 6.23(b). Here, the first positions (1-3) show a low absorption through the atmosphere, followed by a broad region (positions $7-11$) of no transmission. Subsequently, a region with a constant lower absorption coefficient follows, which is slightly higher than the absorption of the atmosphere. The last characteristic is a broad peak at the positions $20-26$, in whose maximum no terahertz radiation is transmitted. These three differently sized regions of transmittance can be understood as various refraction zones of the tilted cuboid, as can be seen in Fig. 6.23(c). Figure 6.23(c) shows the results for a ray tracing simulation of a 14×7 mm large rectangle with a refractive index of 1.5 and under a rotation of 120°. First, there is radiation which incidents on the long front side, but is refracted to the short side (I). Secondly, there is a region, where the radiation incidents on the long side and is able to pass the object (II) and lastly the radiation incidents on the short side of the sample (III). Total reflection (red rays) has a large impact on the absorption coefficients in the first and third case, since radiation inside the object hits the surface under large angles. The size of each of the three regions vary with the rotation angle of the object, which can be seen in the measured sinogram depicted in Fig. 6.23(d).

The measured sinogram of the cylindrical (Fig. 6.22(b)) and cuboid (Fig. 6.23(d)) PP samples are now used to reconstructed their two dimensional shape using the SART. The reconstructed images are shown in Fig. 6.24(a) and (b) for the cylindrical and cuboid PP sample, respectively. The red circular shape of the cylindrical PP sample (Fig. 6.24(a)) with absorption values between 0.75 and 1 is clearly visible, whereas the surrounding atmosphere is represented by green and yellow coloring, representing absorption values between 0.5 and 0.65. As already indicated in the sinogram (Fig. 6.22(b)), the cylinder is not centered. The visibility of the PP cylinder is calculated using the mean absorption value of the red area as object amplitude $< A_{obj} >$ and the mean absorption value of the surrounding atmosphere $< A_{env} >$, here represented by the green and yellow colored area in Fig. 6.24(a). A relatively low visibility of 0.13 and a CNR of 6.1 is determined, which on the one hand is caused by a smaller difference in the absorption coefficients of PP and the atmosphere, compared to metal screws and atmosphere. On the other hand refraction effects distort the reconstructed image as indicated by an additional low absorbing region in the center of the PP cylinder. This fully transparent blue area in the center is an artifact caused by the lens like behavior of the PP cylinder and leads to a distortion of the otherwise homogeneous sample object.

The reconstructed 2D image of the cuboid PP sample shows a lot of distortions and its shape is difficult to recognize. The shorter 7 mm sides of the cuboid can be seen as red areas with an absorption between 0.75 and 1 in Fig. 6.24(b), while the longer 14 mm sides are yellow areas with absorption values around 0.65, which can be hardly differentiated via the color from the surrounding atmosphere. This is also revealed by the different visibility values of the long and short side. While the long side still exhibits a visibility of 0.27 and a CNR of 11.5, the short side has a very low visibility of 0.08 and a CNR of 2.7. Actually, the object consists of a homogeneous PP cuboid and therefore the reconstructed image should show a rectangle of constant absorption. However, the interior is represented as a large dark blue area enclosed by the red and yellow surfaces of the sample object. The main reason for these distortions of the reconstructed images originate in the used reconstruction algorithm, which actually has been developed for x-ray tomography, i.e. wavelengths between 5 and 60 pm, thus being much smaller than the object dimensions. Moreover, the refractive index of matter differs very little from unity in the x-rays spectral domain, hence the algorithm assumes straight rays, which penetrate the sample object and get attenuated

depending on the spatially distributed absorption coefficient and the optical path length through the objects. This circumstance is not given in case of tomographic terahertz imaging, since refraction of the rays, losses due to reflection and diffraction effects occur and strongly influence the measured projections. For this purpose, both new concepts for the field of tomographic terahertz imaging have to be developed, and improvements of the experimental set-ups, like for example refractive index matching [121], or special reconstruction algorithms [119] are needed. Also a good understanding of the impact of refraction, reflection and diffraction effects on terahertz tomography is required in the later case, in order to include these effects to the tomographic reconstruction. For this purpose, a model combining ray tracing and scalar diffraction theory is developed in the following chapter.

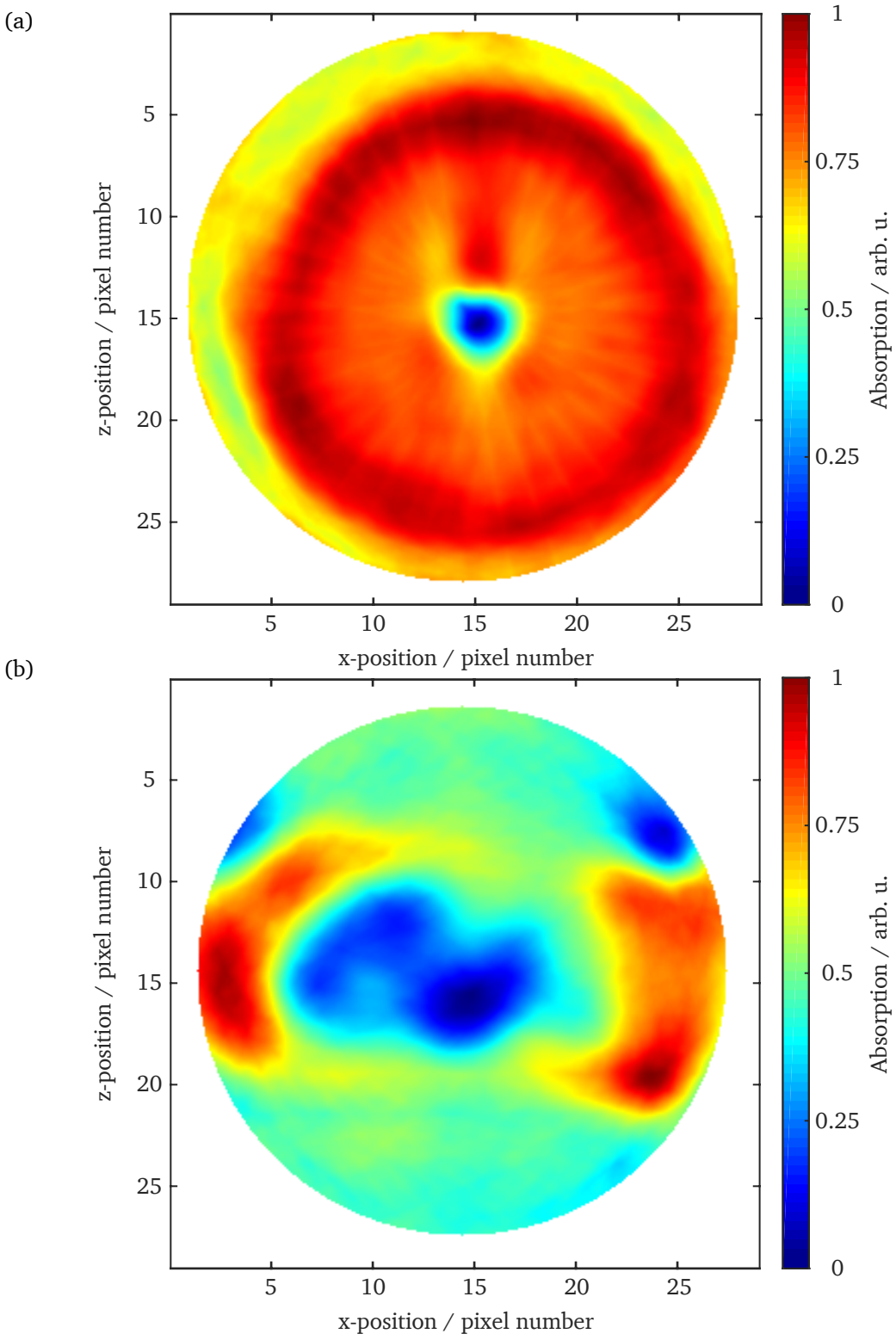

Figure 6.24.: Reconstructed images of (a) a cylindrical and (b) a cuboid PP sample using the measured sinograms and performing the reconstruction by applying the SART algorithm.

6.3.4. Refraction, reflection and diffraction modeling for tomographic terahertz imaging

The measured projections from section 6.3.3 clearly demonstrate the impact of refraction, reflection and diffraction effects. The influence of refraction can be well observed in case of the cylindrical object in Fig. 6.22(a), the effect of reflection as can be seen in Fig. 6.23(b) and Fig. 6.23(a) shows strong diffraction effects. In oder to get a better understanding and to verify these observations a model is developed, which takes all these effects into account. The model is designed to take the same two sample geometries (rectangular and circular), as in the case of the performed experiments and to calculate the resulting sinogram for the selected sample object using the single-pixel imaging technique taking into account the previously mentioned optical effects. Therefore, the model will be capable to reproduce the measured sinograms, which can also serve as a benchmark for the developed model.

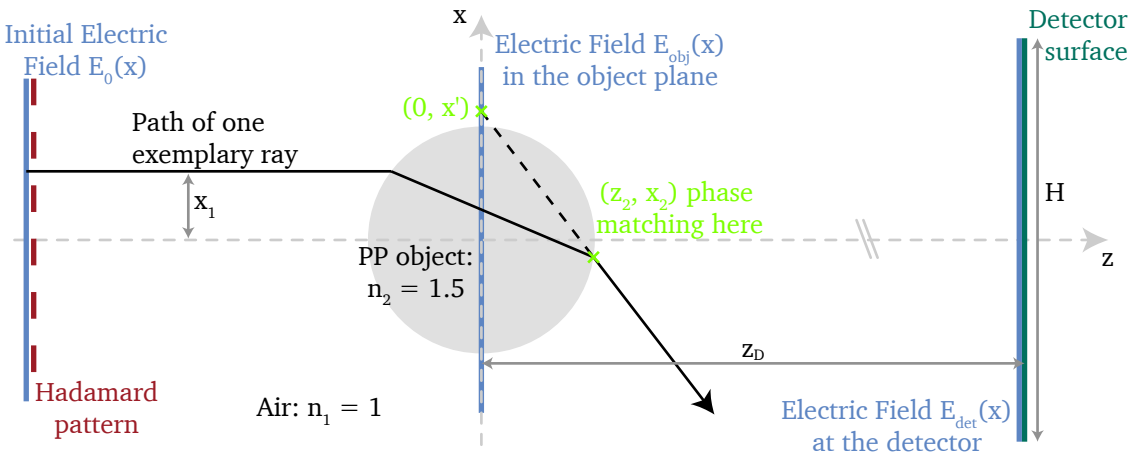

Figure 6.25.: Schematic sketch of the model combining Hadamard imaging and refraction, reflection and diffraction effects for projection calculations of a circular PP object.

The basic concept of the model is taken from [177] and it is adapted to the single-pixel tomographic imaging set-up. The model is based on a hybrid ansatz combining ray tracing for reflection and refraction effects with diffractive light propagation using the Rayleigh-Sommerfeld diffraction solution. A sketch for the case of a cylindrical sample object is depicted in Fig. 6.25. First, the initially constant electric field E_0 passes the Hadamard mask H_i. Therefore, the electric field after each of the 64 binary Hadamard transmission masks is calculated using the Rayleigh-Sommerfeld diffraction solution [178]:

$$E_{obj}(z=0,x) = \frac{d}{i\lambda}\int_{-\infty}^{+\infty} H_i(x')\cdot E_0 \cdot \frac{exp\,(ikr_{12})}{{r_{12}}^2}dx', \tag{6.21}$$

$$r_{12} = \sqrt{(x'-x)^2+d^2}.$$

Here d is the distance between the Hadamard pattern and the object plane, λ is the wavelength, k is the wavenumber and r_{12} is the distance between a position on the Hadamard mask and the object plane. These electric fields serve as source fields in the object plane at $z = 0$ and are divided into one part incident on the object and another part passing the object. The strength of the electric field incident on

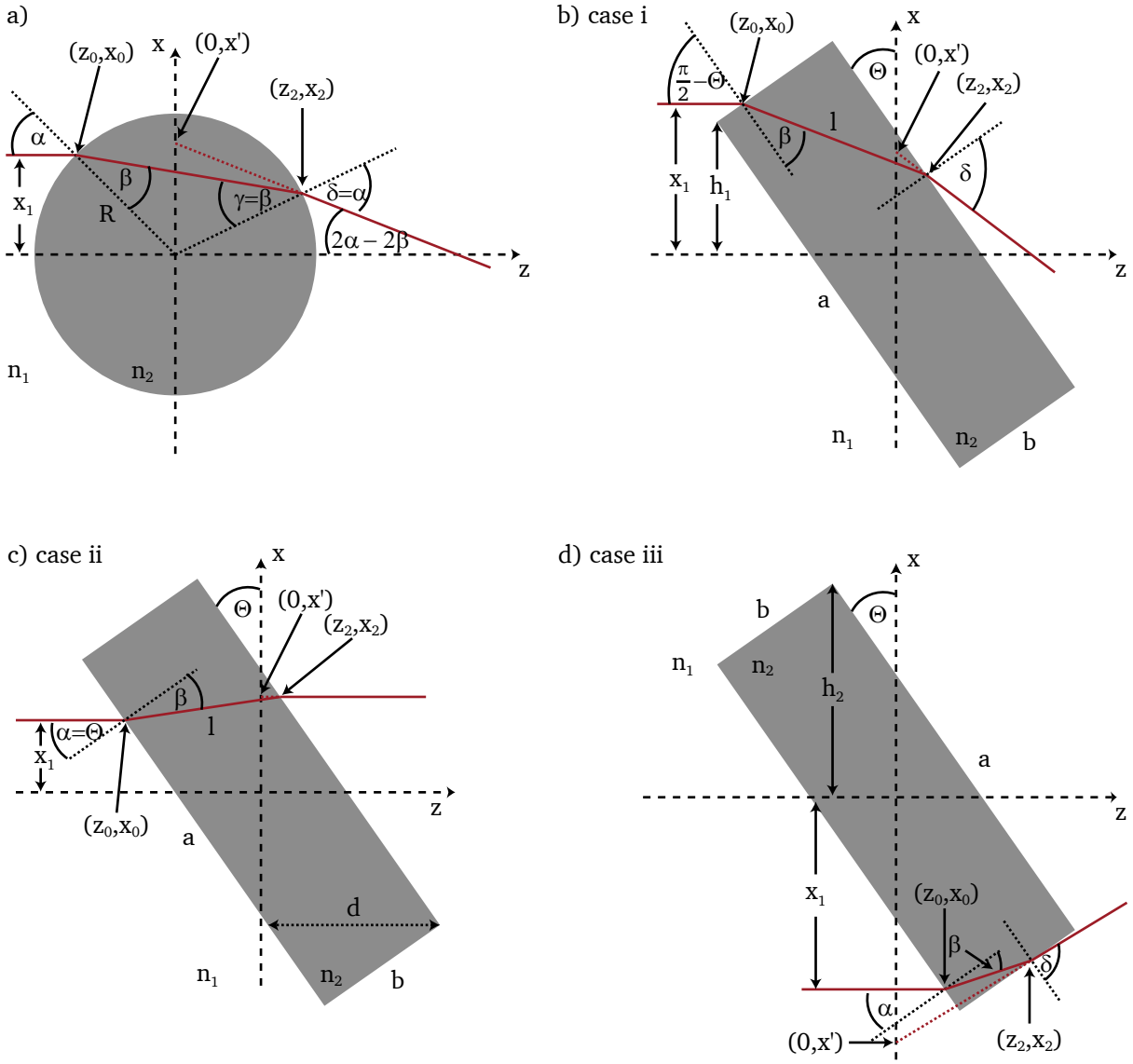

Figure 6.26.: Rays passing the sample object are depicted as solid red lines. (a) Geometric positions and relations of important points necessary for the projection calculation of a circular sample object. (b-d) Geometric positions and relations of important points necessary for the projection calculation of a rectangular sample object. (b) Rays incident on the side b get refracted to the rear side a. (c) Rays incident on the front side a and get refracted to the rear side a. (d) Rays incident on the front side a and get refracted to the side b.

the object is corrected by the Fresnel formulas and the Lambert-Beer law for each x_1 coordinate, taking into account x_1 dependent incident angles and optical path lengths through the object. Furthermore, the phase of the electric field incident on the object is corrected to match the phase at the position (z_2, x_2) (which is the position at which the ray leaves the object), while the ray seems to come from the position $(0, x')$. The coordinates $(0, x')$ and (z_2, x_2) depend on the original x-displacement x_1 and the geometry of the investigated object. In order to obtain these coordinates optical ray tracing is performed for a circle and an arbitrarily rotated rectangle.

A ray with a displacement x_1 from the x-axis incidents on the surface of a circle with radius R under the angle

$$\alpha = arcsin\left(\frac{x_1}{R}\right), \tag{6.22}$$

as illustrated in Fig. 6.26(a). Inside the circle the ray gets refracted depending on the refractive indices n_1 of the ambient and n_2 of the material, which the circle consists of. The angle of refraction is given by

$$\beta = arcsin\left(\frac{n_1 x_1}{n_2 R}\right). \tag{6.23}$$

After the ray travels the distance $l = 2R \cdot cos(\beta)$ thought the circle, it gets again refracted on the backside of the circle and finally reaches the detector plane. For an observer remaining in this plane, the ray seems to originate from the coordinate $(0, x')$, which is given by

$$x' = R\frac{sin(\alpha)}{cos(2\alpha - 2\beta)}. \tag{6.24}$$

Hence, the values of the electric field at the position $(0, x_1)$ are shifted to the coordinates $(0, x')$ for the calculation of the electric field at the detector plane. But before this final electric field is calculated, the phase and amplitude of the electric field is corrected due to the influence of the sample object. First, the amplitude is corrected by the factor a for absorption losses using the Lambert-Beer law

$$a = exp(-\kappa \cdot l), \tag{6.25}$$

where κ is the absorption coefficient of the cylinder material. Next the losses due to reflection are incorporated using the Fresnel equations

$$t = \frac{t_{TE} + t_{TM}}{2} \tag{6.26}$$

$$t_{TE} = \frac{4n_1 N_2 cos(\alpha) cos(\gamma)}{(n_1 cos(\alpha) + N_2 cos(\beta)) \cdot (N_2 cos(\gamma) + n_1 cos(\delta))} \tag{6.27}$$

$$t_{TM} = \frac{4n_1 N_2 cos(\alpha) cos(\gamma)}{(N_2 cos(\alpha) + n_1 cos(\beta)) \cdot (n_1 cos(\gamma) + N_2 cos(\delta))}, \tag{6.28}$$

with N_2 the complex refractive index of the circle. The angle γ represents the incident angle of a ray propagating inside the object to the interface object-ambient, while δ is the corresponding angle of refraction. As illustrated in Fig. 6.26(a) in case of a circular object the relationships $\gamma = \beta$ and $\delta = \alpha$

Table 6.2.: Summary of important quantities used for the projection calculation of circular and rectangular sample object.

	Circle	Rectangle (case i)	Rectangle (case ii)	Rectangle (case iii)
z_0	$-R \cdot cos(\alpha)$	$z_2 - l \cdot cos(\alpha - \beta)$	$z_2 - l \cdot cos(\alpha - \beta)$	$z_2 - l \cdot cos(\alpha - \beta)$
x'	$R\frac{sin(\alpha)}{cos(2\alpha - 2\beta)}$	$z_2 \cdot tan(\alpha - \delta) + x_2$	x_2	$z_2 \cdot tan(\alpha + \delta - 90°) + x_2$
x_2	$Rsin(2\beta - \alpha)$	$x_1 - lsin(\alpha - \beta)$	$l \cdot tan(\alpha - \beta) + x_1$	$x_1 + l \cdot sin(\alpha - \beta)$
z_2	$Rcos(2\beta - \alpha)$	$\frac{d}{2}\frac{x_2}{tan(\alpha)}$	$\frac{d}{2} - \frac{x_2}{tan(90° - \alpha)}$	$x_1 tan(\alpha) - \frac{d}{2} + lcos(\alpha - \beta)$
l	$2Rcos(\beta)$	$\left(b - \frac{x_1 - h_1}{sin(\alpha)}\right)\frac{1}{sin(\beta)}$	$\frac{b}{cos(\beta)}$	$\frac{n_2(h_2 - x_1)}{n_1 \cdot sin(\alpha) \cdot cos(\alpha)}$
α	$arcsin\left(\frac{x_1}{R}\right)$	$90° - \Theta$	Θ	Θ
γ	β	$90° - \beta$	β	$90° - \beta$
δ	α	$arcsin\left(\frac{n_2}{n_1}sin(\gamma)\right)$	α	$arcsin\left(\frac{n_2}{n_1}sin(\gamma)\right)$

hold true. In order to account for the extra optical path length Δl the rays travel, the phase of the electric field is matched at the position (z_2, x_2). For an observer positioned in the detector plane the ray with a displacement x_1 from the x-axis travels the distance $n_1 \cdot \sqrt{z_2^2 + (x' - x_2)^2}$ from $(0, x')$ to (z_2, x_2), but due to the sample object the actual distanced traveled by the ray is longer. To take this into account the electric field is multiplied with an additional phase factor

$$\phi = exp\left(i\frac{2\pi\Delta l}{\lambda}\right) \tag{6.29}$$

$$\Delta l = n_2 l + n_1 z_0 - n_1 \cdot \sqrt{z_2^2 + (x' - x_2)^2}. \tag{6.30}$$

Here λ is the wavelength of the radiation and (z_0, x_0) denotes the position on which the ray first incident on the object. After these corrections of the electric field, the total electric field at the detector surface is again calculated utilizing the Rayleigh-Sommerfeld diffraction solution for the unchanged electric field passing the object plus the corrected electric field incident on the object. Finally, the intensity at the detector surface is summed up for each Hadamard mask and the single-pixel imaging formalism is used to calculate the projection of the sample object.
To apply the same model to a rectangular sample object with the side length $a \times b$ and a rotational angle Θ, the important positions (z_0, x_0), $(0, x')$ and (z_2, x_2) and parameters α, β, γ, δ and l have to be determined. Here, three different cases have to be distinguished:

(i) Rays incident on the side (b) get refracted to the rear side (a) (Fig. 6.26(b))

(ii) Rays incident on the front side (a), which get refracted to the rear side (a) (Fig. 6.26(c))

(iii) Rays incident on the front side (a), which get refracted to the side (b) (Fig. 6.26(d))

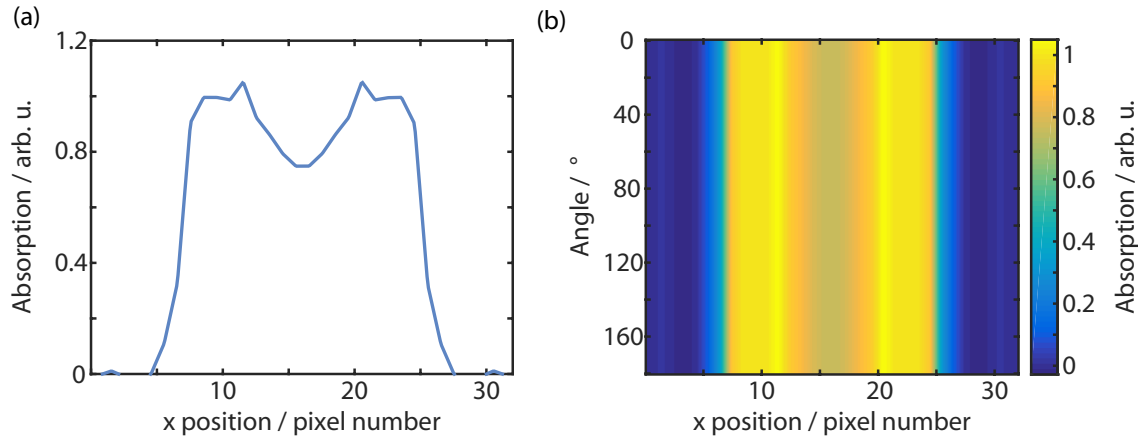

Figure 6.27.: (a) Calculated projection under an arbitrary rotation angle and (b) sinogram of a cylindrical PP sample with diameter of 14 mm at a frequency of 1 THz.

By the evaluation of the different geometric arrangements depicted in Fig. 6.26(b-d), the important positions and parameters for each scenario are obtained. Table 6.2 summarizes the resulting relations for a circular sample object and the three different cases of a rectangular sample object.

After the development of these relations the model is now used to calculate the projections of circular and rectangular objects under arbitrary rotation angles. As in the measurements in section 6.3.3, the objects consist of PP, which possess a refractive index of approximately 1.5 and an absorption coefficient in the order of 1 cm^{-1} at the terahertz frequency under investigation [175]. The object under investigation is rotated from 0° to 180° in 1° iterations and for each rotation angle the projection is calculated at a frequency of 1 THz. As in the case of the measured projections, which are normalized by the beam profile shown in Fig. 6.12, first of all a calculation of the intensity distribution is performed without an object, which is used to normalize the calculated projections including an object. Thus, absorption values of 1 correspond to fully opaque regions for the terahertz radiation, whereas an absorption of 0 implies a fully transparent region. Since the cylindrical object possesses a rotational symmetry only one projection is calculated and used for all rotation angles. The calculated projection for a PP cylinder with a diameter of 14 mm is shown in Fig. 6.27(a) together with the corresponding sinogram (Fig. 6.27(b)). Both sides of the projection show no absorption through the atmosphere, which changes quickly at the object borders. Here, the object appears as fully opaque plateaus, which are only interrupted in the center of the projection by a valley of reduced absorption. The calculated projection resembles the measured one shown in Fig. 6.22(a), only the width and depth of the central peak differ slightly. This may be caused by the broad frequency range of the used terahertz radiation in the experiment, which influences the measured sinogram, since parameters like the refraction index and absorption coefficient depend on the wavelength.

The model is now applied to a rectangularly shaped PP sample object, for which two calculated projections at a rotation angle of 180° (Fig. 6.28(a)) and 120° (Fig. 6.28(b)) as well as the sinogram (Fig. 6.28(c)) are shown in Fig. 6.28. The effects of diffraction are especially apparent in the case of the 180° projection, because no refraction effects occur, which is caused by the perpendicular incidence of the radiation on

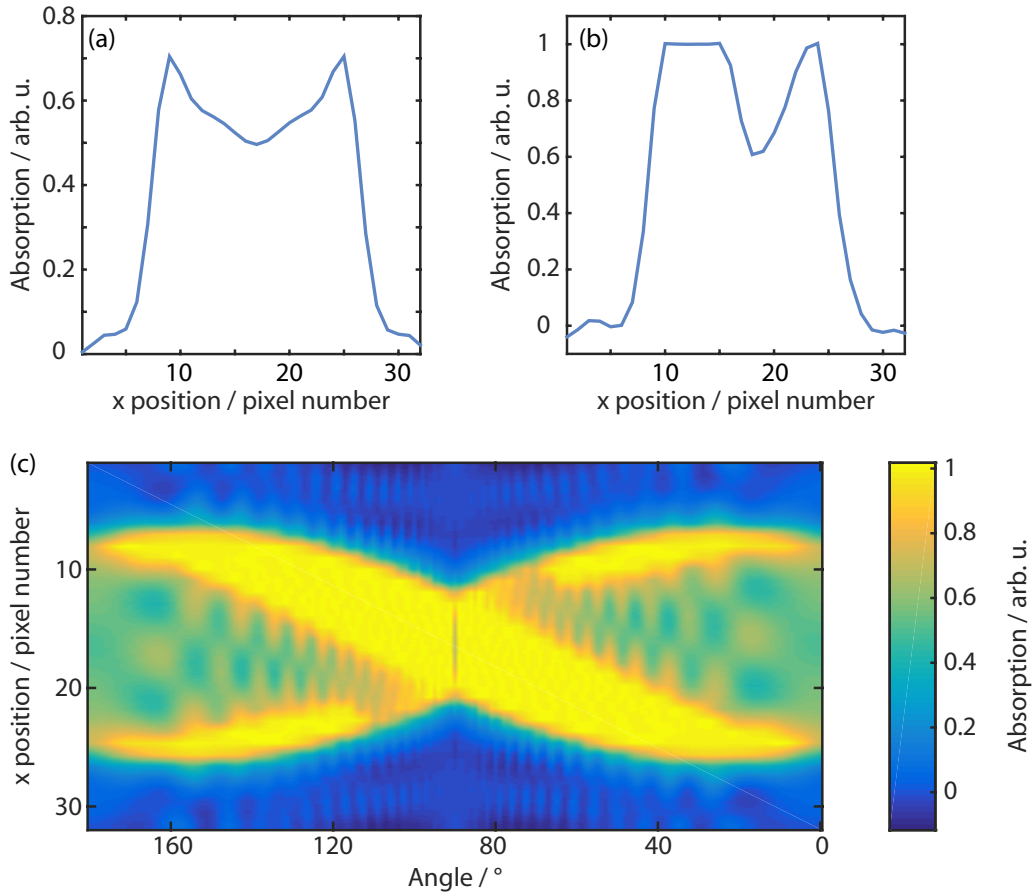

Figure 6.28.: Calculated projections under a rotation angle of (a) 180° and (b) 120° and (c) sinogram of a rectangular PP sample with edge lengths of 14 × 7 mm at a frequency of 1 THz.

the surface of the rectangular sample object. Nevertheless, the projection exhibits some characteristics which do not depend on the absorption of the sample object. The same absorption peaks on positions 9 and 25 are visible as in case of the measured projection shown in Fig. 6.23(a). As before, these two peaks occur at the transition from the surrounding atmosphere to the sample object. Furthermore, the interior of the object's projection at 180° also resembles the measured one. In between the two absorption peaks, the absorption decreases slowly and leads to an absorption minimum in the center of the object. By rotating the object the contributions of refraction and reflection effects to the projections increase and are the dominant source of distortions, as shown in the sinogram by yellow regions of high absorption (Fig. 6.28(c)). The yellow x-shaped structure in the sinogram can be attributed to the three regions as described in section 3 and depicted in Fig. 6.23(c). The radiation incident on the object's top and bottom sides (region I and III) leads to non-transmitting zones of the object, while the sizes of these zones are dependent on the rotational angle. In Fig. 6.28(b) the projection of the rectangular PP object at a rotational angle of 120° clearly shows these three different transmission zones.

In order to reconstruct the 2D images of both the circular and rectangular PP objects, again the SART

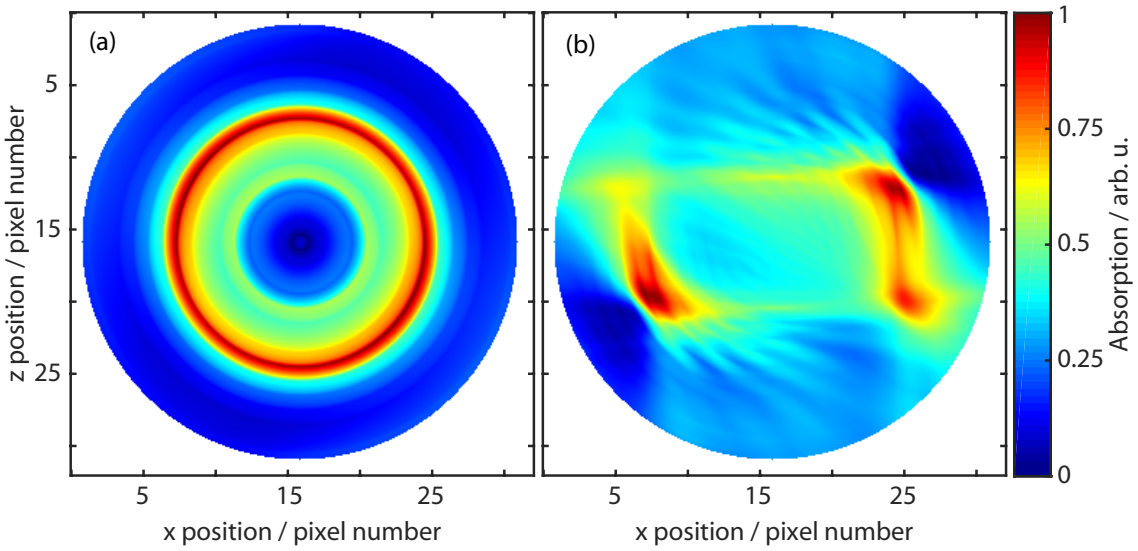

Figure 6.29.: Reconstructed images of modeled (a) cylindrical and (b) rectangular PP samples using the calculated sinograms for a frequency of 1 THz and performing the reconstruction by applying the SART algorithm.

algorithm from the ASTRA toolbox is used. The resulting images are shown in Fig. 6.29(a) and (b) for the circular and rectangular samples at a frequency of 1 THz, respectively. Here the circular PP object is shown as a hollow circle, a fact which can be attributed to the lensing effect of the object, but clearly stands out from the surrounding atmosphere. The good contrast between the atmosphere and object reduces in case of the rectangular shaped sample as can be seen in Fig. 6.29(b). The left and right sides of the rectangular are each represented by a thick red vertical line and are clearly emphasized in relation to the surrounding atmosphere, whereas the front and rear sides are only visible as thin yellow horizontal lines. Finally, the interior of the rectangle does not even contrasts from the atmosphere, which makes the object appear to be hollow as also observed in the measured 2D image of the rectangular sample depicted in Fig. 6.24(b). The results of the developed modeling approach for 2D Hadamard terahertz tomography are in good agreement with the observations obtained from the experimentally realized tomographic imaging. Calculated projections of both circular and rectangular objects under different rotation angles reproduce the findings of the measurements and clarify the effects of refraction, reflection and diffraction in the field of terahertz imaging.

However, the results of the measurements and simulations both do not match the expectations of the ray tracing simulation result from section 6.2 regarding the single-pixel imaging approach. The projection obtained by these pure ray tracing simulations resemble the expected projection shape of a homogeneous cylinder that is measured by x-ray tomography. In contrast, the measurements, as well as the simulations obtained by the hybrid ansatz both yield projections, which still show the lens like behavior of the sample cylinder. Since the hybrid ansatz reproduces the measurements very well, it can be concluded that the hybrid ansatz is superior to pure ray tracing simulations, due to the implementation of refraction, reflection and diffraction of the radiation. However, the pure ray tracing simulations clearly revealed

a dependency of the projections on the detector size, as can be seen by comparing Fig. 6.9(a) and (b). This detector size is equivalent to the collection angle, under which radiation is captured by the detector. Figure. 6.25 shows, that the tangents of the collection angle is determined by the fraction of half the detector size H and the distance between the object center and the detector z_D

$$\Psi = arctan\left(\frac{H}{2 \cdot z_d}\right). \tag{6.31}$$

A smaller collection angle implies less detected radiation, which is refracted or diffracted by the sample object. The collection angle value of the employed experimental set-up is defined by the FTIR, but is a free parameter in the developed model, which allows the calculation of the projections employing arbitrary collection angles. Hence, the influence of the collection angle on the projections obtained by the tomographic single-pixel imaging scheme can be investigated. The same circular sample object as

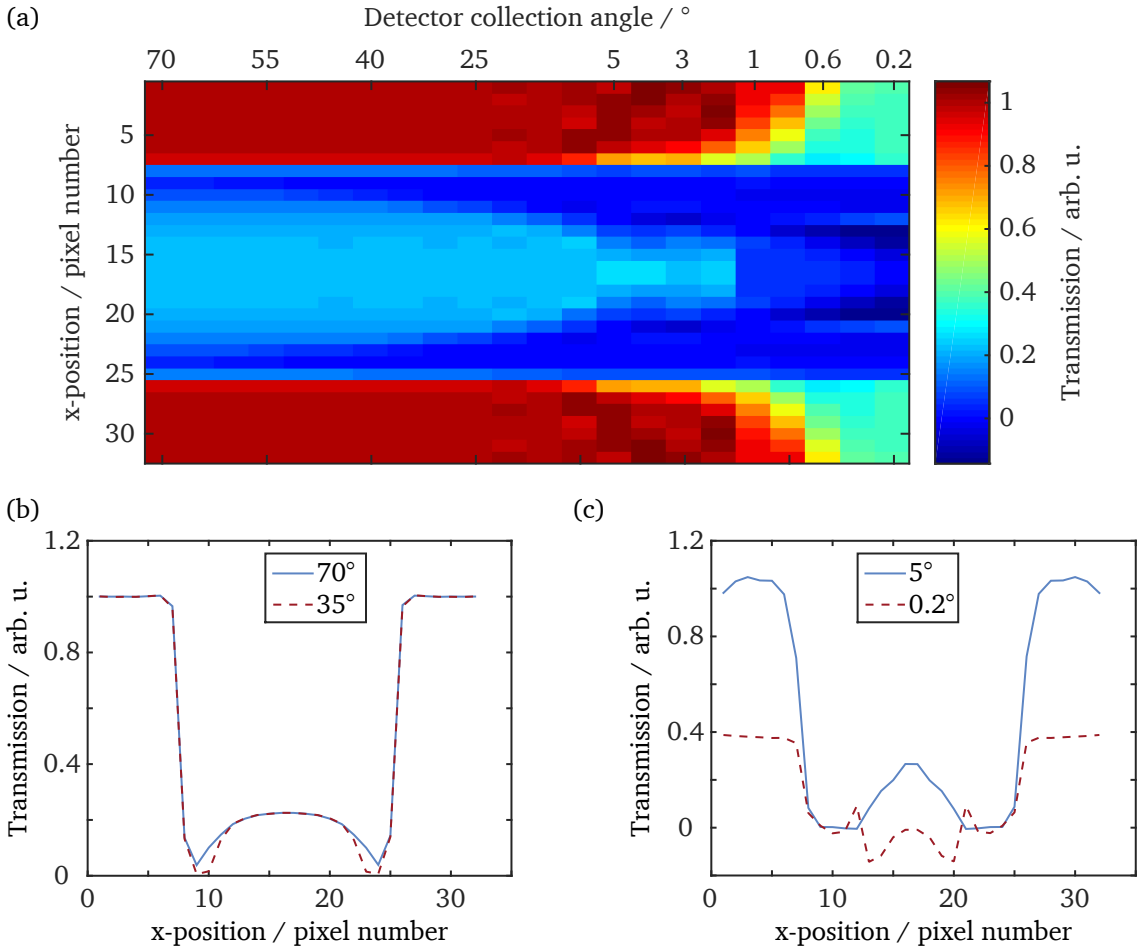

Figure 6.30.: (a) Shape of the calculated projections for a circular PP sample with respect to the collection angle Ψ of the detector. Four exemplary projections are shown for collection angles of (b) 70° (solid, blue), (b) 35° (dashed, red), (c) 5° (solid, blue) and (c) 0.2° (dashed, red).

used in the simulations before is now investigated for collection angles ranging from 0.1° to 70°. For each collection angle a projection of the circular sample is calculated using the hybrid ansatz of the tomographic single-pixel imaging scheme. The projection is afterwards normalized by the intensity profile calculated in the absence of the sample object. The resulting map in Fig.6.30(a) shows the transmission resolved for the x-position and the collection angle. For collection angles above 1°, the surrounding atmosphere is represented by red areas, which correspond to a transmission value of 1. The x-positions of the atmosphere range from 1 to 7 and from 26 to 32. With smaller collection angles, suddenly the transmission through the atmosphere drops below 1. First, this transmission drop is limited to a region near the interface between the sample object and the atmosphere, but with further reduced collection angle the drop expands towards the image outlines. Finally, at the lowest collection angle of 0.1° the transmission through the atmosphere again appears as a homogeneously colored area, but with a reduced transmission of 0.4. Also the appearance of the sample object undergoes a large change with a reduction of the collection angle. Through all investigated collection angles, the object border is depicted as a sudden drop in transmission at the positions 8 and 25, only the steepness of the drop slightly increases with decreasing collection angle. In contrast, the inner of the sample object is reflected quite differently for the different collection angles. Starting from each of the two atmosphere-to-object-interfaces, which can be identified by the steep decrease in transmission, the transmission increases towards the center of the sample object for collection angles between 70° and 2°. But with decreasing collection angle the transmission values after the atmosphere-to-object-interfaces approach 0. Further they remain at a value of 0 for an increasing number of pixels with decreasing collection angle. Afterwards the transmission always increases to values around 0.3 towards the center of the object. This leads to fully opaque regions at the x-positions $8-13$ and $20-25$ between the atmosphere and a reduced region of the sample object transmission (position 14—19) for a collection angle of 2°. A further reduction of the collection angle leads to a transmission profile, which cannot explicitly be correlated to the sample object. The transmission in the center of the object decreases towards zero and even negative transmission values are observed.

Figures 6.30(b) and (c) show four exemplary projections calculated for the collection angles 70°, 35°, 5° and 0.2°. A reduction of the collection angle from 70° to 35° only exhibits some small deviations in the calculated projection as can be seen in Fig. 6.30(b). The two projections only differ in the transmission drop at the atmosphere-to-sample interface, which is more pronounced in case of a collection angle of 35°. A further reduction of the collection angle to 5° causes an even broader region of no transmission behind the atmosphere-to-sample interface. This is exemplary shown in Fig. 6.30(c). As for the calculated projections in Fig. 6.30(b), behind its fully opaque regions the projection calculated for an collection angle of 5° shows an increasing transmission towards its center, but due to the broader opaque region the gradient is larger. While the transmission maxima at 70° and 35° have a flat top, for a collection angle of 5° the maximum transmission exhibits an additional dip in its center. When moving to an even smaller collection angle of 0.2°, there are plenty of changes in the shape of the calculated projection. First of all, a drop in the transmission through the surrounding atmosphere to a value of 0.4 is recognized. As before, the contour of the object is visible due to a sharp transmission drop at the atmosphere-to-sample interface. But behind this transmission drop, the inner part of the sample object shows a complex projection, with multiple maxima and minima. Even negative transmission values are observable, which indicate a non-physical solution. These negative transmission values only occur at very small collection angles below 1°. The influence of the collection angle on the projection shape is clearly visible from the calculated projections shown in Fig. 6.30(a). In the region between 70° and 40° the shape of the

projection undergoes only small changes. Below this collection angle the informations about the inner shape of the sample object is compressed to a smaller area, since the atmosphere-to-object interface gets more pronounced. Due to the unphysical negative transmission values, the collection angle in an experimental realization of the single-pixel imaging approach must be larger than 1°.

Following these investigations on the influence of the detection angle, the model will be used for tomographic reconstruction of the experimentally obtained sinograms.

6.3.5. Tomographic reconstruction using the developed model

The development model successfully reproduces the measurements and will now be used to reconstruct the shape of the investigated sample objects. For this purpose a genetic algorithm, implemented by the Matlab® function "ga", is used to minimize the mean squared error (MSE). For this purpose, the "ga" function creates a sequence of populations after an initial random population. A population contains many individuals and each individual represents a set of parameters for the optimization problem. From the individuals of the current population a new population is generated by three different mechanisms. First, elite children are selected, which are given by individuals in the current generation with the best MSE values. Second, crossover children are generated by combining two parents and third, children are created by mutations like random changes. By these mechanisms, the individuals approach the best solution of the optimization problem with increasing population. For the investigated tomographic reconstruction, the optimization problem is defined as

$$MSE = \frac{1}{n} \sum_{\theta_y} \sum_{x} \left(Data(\theta_y, x) - Model(\theta_y, x, a, b, s) \right)^2 . \tag{6.32}$$

Here n is the number of measurement points, θ_y and x are the rotational angle and the x-position of the object respectively, $Data(\theta_y, x)$ represents a measurement point of the sinogram and $Model(\theta_y, x, a, b, s)$ is the function of the developed model. The parameters a, b and s are the fitting parameters of the model, by which the genetic algorithm tries to minimize the MSE.

Here, s has an integer value of 0 in case the object is of rectangular shape or 1 in case the object is of circular shape. Depending on the value of s, the parameter a represents the diameter of the circle or the first edge length of the rectangle, while the length of the second edge is represented by the parameter b, which is unused in case of a circular shape.
The results of the fitting process to the measured sinogram of both samples are shown in table 6.3. At first, it is apparent from the results, that the optimization algorithm results in the correct shape for each sample object. In case of the rectangular sample object (Fig. 6.23(d)) the s parameter is 0, while the parameter is 1 in case of the circular object (Fig. 6.22(b)). However, the estimated size of the sample objects is too small in both cases, due to a multitude of different factors. Size affecting factors are the refractive index and the absorption coefficient of the sample object and the collection angle of the detector, which are all defined in the model. Also, the broad frequency range of the used terahertz radiation influences the measured sinogram, since parameters like the absorption coefficient and optical effects like diffraction depend on the wavelength. Here, an extension of the model from the currently used single frequency calculations towards calculations using a broad frequency spectrum is needed. Or alternatively, the measurements can

Table 6.3.: Results for the fitting of the measured sinograms to the developed model. The initial values of the fit parameters are $a = 10$ and $b = 10$ for both objects, while s has an initial value of 0, in case of the circular object and 1, in case of the rectangular object, in order to prevent a prepossession of the algorithm.

a (Diameter / Edge one)	b (Edge two)	s (Shape)	MSE	Measurement data	Sample object dimensions
11.3 mm	-	1 (circular)	0.03	Fig. 6.22(b)	14 mm
12.4 mm	4.1 mm	0 (rectangular)	0.06	Fig. 6.23(d)	14 × 7 mm

be performed at a single terahertz frequency. So far, the presented method can simulate the sinogram of rectangular and circular objects of different sizes and thereby is a proof-of-concept demonstration of tomographic image reconstruction in the terahertz frequency domain, which has to be extended in the future, to allow tomographic imaging of arbitrarily shaped sample objects.

One possibility of achieving single frequency images is given by the spectroscopic capability of the FTIR. Therefore the connection scheme of the bolometer has to be changed from connection 1 to connection 2 as indicated in Fig. 6.11. This is done in the following chapter to obtain spectrally resolved images using the single-pixel approach.

6.3.6. Spectroscopic single-pixel imaging

One advantage of the single-pixel approach is that only correlations between pattern masks and intensities have to be measured. Hence, a spatially resolving detector is not required and the intensities can be measured in a number of ways. So far, the total intensity of the spectrally filtered mercury-arc lamp was integrated by the bolometer for each pattern. In order to achieve spectrally resolved imaging in the terahertz frequency domain, the bolometer is now directly connected to the FTIR spectrometer as indicated by connection 2 in Fig. 6.11. For each pattern a spectrum of the mercury-arc lamp is measured in the frequency range from 0.8 to 1.6 THz. The result is a two dimensional map of amplitudes with the frequency on one axis and the pattern number on the other axis. From this map an image for each frequency component of the spectrum can be calculated using Eq. 2.23.
A frequency-resolved image of the beam profile of the mercury-arc lamp is recorded using the single-pixel scheme. The resulting image is shown in Fig. 6.31. Like the integrated beam profile from section 6.3.1, the frequency resolved beam profile exhibits two maxima separated by a drop in intensity. This local intensity minimum is caused by a window for an adjustment laser in the center of the beam splitter installed inside the spectrometer. The shape of the beam profile remains the same along the frequency axis, showing no frequency dependency. The gaps from 1.08 to 1.2 THz and from 1.4 to 1.44 THz in the beam profile along the frequency axis in Fig. 6.31 originate from low intensities of the corresponding frequency. At these frequencies the SNR is too small, such that an calculation of the image was not possible. Generally, the signal-to-noise ratio is lower in the frequency-resolved measurement compared to the previous intensity integrating ones in section 6.3.3, since no lock-in detection scheme is used. Therefore, it was not possible to achieve imaging of a complex object like a α—Lactose filled hollow core Teflon cylinder as used in

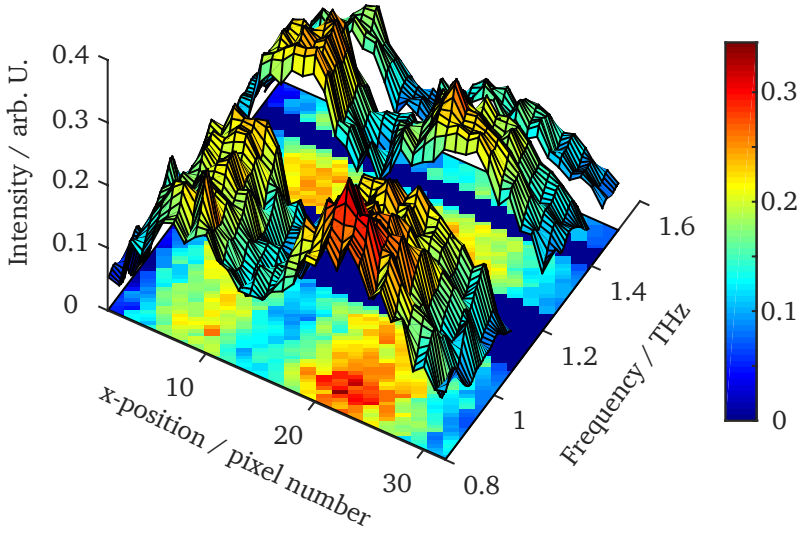

Figure 6.31.: Frequency resolved image of the 1D beam profile of the used mercury-arc lamp.

section 6.1. To achieve spectroscopic imaging of such complex objects further improvements are necessary to increase the signal-to-noise ratio. For example, the step-scan mode of the Bruker Vertex 80v can be used to combine the spectroscopic capability of the FTIR with a lock-in detection scheme. Nevertheless, the frequency-resolved measurement of the beam profile represents a proof-of-principle experiment for spectroscopic terahertz imaging and demonstrates the simple implementation of spectroscopic aspects into the single-pixel imaging approach.

6.4. Summary and conclusion

In this chapter terahertz imaging was investigated by different experimental realizations and theoretical considerations. First the developed HSM method was used to achieve spectrally resolved two-dimensional images of a hollow core Teflon cylinder. Here, the object was scanned through the terahertz beam giving 1D projections of the sample object. The phase information of the HSM signals was used to determine the wall thickness of the cylinder. By projection measurements of the sample object under rotation angles between 0° and 150° tomographic imaging was realized. Not only the inner shape of the sample object, but also its composition was revealed by taking one image at a specific fingerprint absorption line and a second image far away from that line. The measured projections showed strong influences on refraction effects, which was confirmed by modelling the experimental set-up in ZEMAX. These ray tracing simulations were in good agreement with the experimental data and revealed the lens like behaviour of the cylindrical sample object.

In order to get a better understanding of refraction and reflection effects using different terahertz imaging techniques, a ray tracing software was developed in MATLAB. This software was able to characterize the different imaging schemes with respect to tomographic terahertz imaging. Therefore, projections for a refractive circular sample object were calculated using raster scanning of the object with a small and large area detector, a multi-pixel detector and the single-pixel imaging approach. Here, raster scanning using a

large surface detector and the single-pixel imaging approach exhibited the most promising results for the reconstructed images, since these methods provide information about the origin of each ray.

Stimulated by these findings, a tomographic single-pixel terahertz imaging experiment was realized. The capability to modulate terahertz radiation by photodoping of a thin HRFZ-Si window was investigated by measurements and simulations. In order to implement the single-pixel imaging scheme, the photodoping technique was used to transfer the spatial modulation of a NIR LD onto the terahertz radiation.

1D projection measurements of a cylindrical and a cuboid PP sample object under different rotation angles showed the need for a detailed understanding of diffraction effects in tomographic terahertz imaging besides the already investigated refraction and reflection effects. Therefore, a hybrid ansatz combining ray tracing for reflection and refraction effects with diffractive light propagation using the Rayleigh-Sommerfeld diffraction solution was investigated. The developed model was used to simulate the experimentally obtained sinograms for the cylindrical and cubid sample object and a good agreement between the measured and simulated sinograms was found.

Next, the developed hybrid ansatz model was used for the reconstruction of the sample object shape. For this purpose, a genetic algorithm was used to solve a formulated optimization problem. The method was capable to reproduce the shape of the investigated object from the experimental data. However, the dimensions of the objects were in general estimated as too small.

Lastly, the single-pixel imaging set-up was used for spectroscopic imaging, which was easily implemented since a high-sensitive single pixel bolometer can be used. Therefore, the FTIR spectrometer was used to measure a spectrum for every pattern mask. In that way, a spectrally resolved image of the beam profile of the mercury-arc lamp was obtained. The easy integration of spectroscopic imaging represents one advantage of the single-pixel imaging approach over conventional imaging schemes.

7. Summary and outlook

More than 100 years after the terahertz gap was first mentioned by H. Rubens and E. F. Nichols, the field of terahertz research still attracts a lot of attention. Indeed, continuous research efforts through the years gradually closed this gap in the electromagnetic spectrum. Due to a unique set of properties, including spectral fingerprints of molecules, transparency of materials like plastics and paper and the non-ionizing nature, a plurality of possible applications have been proposed for the terahertz spectral domain. Most of these applications must compete with other sensor technologies, which are often well established in the industrial processes. Therefore, still a lot of effort is necessary in finding an industrial breakthrough application of terahertz radiation [179]. Key aspects demanded for the generation and detection of terahertz radiation are robustness and room temperature operation. For this purpose, promising devices capable to generate and detect terahertz radiation are photoconductive antennas (PCAs). Both short terahertz pulses and continuous-wave terahertz radiation can be generated and detected using these devices in combination with well-established optical technologies, as fs-pulse and single frequency lasers.

In the first part of this work the continuous-wave generation and detection of terahertz radiation using such PCAs in combination with two single frequency external cavity diode lasers (ECDLs) was investigated. A new concept for the simultaneous generation and phase sensitive detection using a single PCA was developed. This homodyne self-mixing (HSM) concept leads to a cost reduction and paves the way for extremely compact terahertz spectroscopy assemblies. Also, it relaxes the demand on high laser power because only one PCA is needed.

In chapter 3 and 4 the basic elements for the HSM concepts were investigated, namely the ECDLs and the PCA devices. Two IF- and one grating-based ECDLs were developed and characterised in chapter 3. The ECDLs were characterised according to their intensity and spectral stabilities. For this purpose, long time measurements of the output power and spectra were taken and the relative intensity noise and spectral linewidth were investigated. The result of this characterization was summarized in table 3.1 and identified the suitability of the ECDLs for high resolution terahertz spectroscopy employing photomixing. Subsequently chapter 4 described the generation of terahertz radiation using two Jülich PCAs and a commercial available PCA provided by TOPTICA Photonics. The Jülich PCAs were characterized according to their output power and compared to the commercial one. This analysis pointed out the high-quality of the TOPTICA Photonics PCA, which exhibited a near-infrared to terahertz radiation conversion efficiency of 33×10^{-6} at 0.2 THz. In contrast, the Jülich PCAs only exhibited a conversion efficiency of 0.6×10^{-6}. A common photomixing set-up using the TOPTICA Photonics PCA TX30A as emitter and the PCA RX30A as receiver was realized.

The subsequent miniaturization of this common photomixing set-up towards the new compact HSM method was discussed in chapter 5. The terahertz radiation emitted by a single PCA is back-reflected from a revolving chopper wheel to the same PCA, where the incoming radiation gives rise to an AC current

modulated at the frequency of the chopper wheel. This AC current depends on the amplitude and phase of the back-reflected terahertz radiation. A sinusoidal shape of the HSM signals was observed in dependency of the chopper wheel displacement. This finding was confirmed by theoretical investigations on the PCA current under the influence of back-reflected terahertz radiation. To demonstrate the phase sensitivity of the HSM signal, the refractive index of a Teflon sample was successfully determined at a frequency of 0.17 THz.

In the second part of this thesis two-dimensional tomographic imaging in the terahertz frequency domain was studied. As a proof-of-principle experiment, the developed HSM concept was applied to two-dimensional tomographic terahertz imaging in chapter 6.1. Measurements for two different terahertz frequencies were performed for a Teflon cylinder filled with α-Lactose. The reconstructed image revealed the dimensions of the Teflon cylinder and allowed for an identification of the α-Lactose filling due to a specific absorption line. The optical effect of refraction on the experimentally determined 1D projections of the sample was clearly identified by the modelling of the experimental set-up in ZEMAX. These results showed a remarkable agreement between experiment and theory and allowed for a better understanding of the refraction effects.

Motivated by the ZEMAX ray tracing results, a detailed discussion of different imaging schemes with respect to tomographic terahertz imaging was performed in chapter 6.2. For this purpose, a ray tracing software was developed in MATLAB capable to perform ray tracing simulations involving different geometrical shapes. The developed software was used to simulate projections of a circular sample object using different imaging schemes. The investigated schemes included imaging by raster scanning of the object using detectors with a small and large surface, a multi-pixel detector and the single-pixel imaging approach. Here, raster scanning using a large surface detector and the single-pixel imaging approach exhibited the most promising results, since these methods provide information about the origin of each ray and therefore the object imaging can be more precise.

Stimulated by these findings, a tomographic single-pixel terahertz imaging experiment was realized. Photodoping of a thin high resistivity float zone silicon window by an 808 nm laser diode and a digital micromirror device was used to transfer the spatial modulation of a near infrared laser diode to the terahertz radiation. Patterns defined by a 32×32 Hadamard matrix were used to measure 1D projections of different sample objects. By subsequent 1D projection measurements of the samples under different rotation angles, the simultaneous algebraic reconstruction technique was used to reconstruct the 2D image of the samples. After two metal screws having served as fully opaque demo sample objects, a cylindrical and cuboid PP sample were investigated. These two sample objects with a refractive index of 1.5 and an absorption coefficient of approximately 1 cm^{-1} revealed the need for a detailed understanding of refraction, reflection and diffraction effects in tomographic terahertz imaging. Therefore, a hybrid ansatz combining ray tracing for reflection and refraction effects with diffractive light propagation using the Rayleigh-Sommerfeld diffraction solution was investigated. The developed model was used to simulate the experimentally obtained sinograms for the cylindrical and rectangular sample objects. An excellent agreement between the measured and simulated sinograms was found. Further, the developed model was used to investigate the influence of the detector collection angle on the projection of an object. A collection angle between 70° and 40° was found to have a small influence on the shape of the projection. Below this collection angle the information about the inner shape of the sample object was compressed

to a smaller area and an even further reduction of the collection angle below 1° resulted in negative transmission values. This study showed that good results are obtained within a large range of collection angles and that the collection angle should be larger than 1°, which is easily achieved in the experiment.

Compared to x-ray tomography, the projections of sample objects measured in the terahertz frequency domain exhibit an extraordinary shape. Because of refraction effects occurring in the terahertz spectral domain, rays do not travel on straight lines through the object, as it is expected and required for the reconstruction methods coming from x-ray tomography. To overcome this requirement a reconstruction method including the developed hybrid ansatz was introduced in chapter 6.3.5. Therefore, a genetic algorithm was used to solve the formulated optimization problem. Here, the dimensions of the objects were generally estimated a little bit too small. However, the method was capable to reproduce the shape of the investigated object from the experimental data.

After the successful implementation of a tomographic single-pixel terahertz imaging set-up, the capability of this set-up with respect to spectroscopic imaging, as it was already realized for the HSM approach in chapter 6.1, was investigated. Due to the single-pixel imaging approach, which does not require a spatial resolution of the detector, the Fourier transform infrared spectrometer was used to measure a spectrum for every pattern mask. In that way, a spectrally resolved image of the beam profile of the mercury-arc lamp was obtained. The easy integration of spectroscopic imaging demonstrated one of the advantages of the single-pixel imaging approach over conventional imaging schemes.

In conclusion, this work contributed to two essential fields of terahertz research. First a new concept for the generation and detection of terahertz radiation was established and secondly, the application of tomographic terahertz imaging was investigated by various experimental realizations and theoretical studies.

The developed hybrid ansatz model enables the realistic reconstruction of circular and cuboid refractive objects using terahertz tomography. However, so far the computational time is very long and amounts to several hours. In order to gain lower computational times of the hybrid ansatz model the graphics processing unit of the computer could be used to calculate the projections of sample. The reduced computational time would allow the implementation of more complex shapes into the model, which would lead to a larger variety of sample geometries.

With this enhanced tomographic reconstruction method, realistic image reconstruction can be performed for arbitrary refractive objects in the terahertz domain. Spectroscopic single-pixel tomography could be realized by combing the full capabilities of the Fourier-transform infra-red spectrometer with a lock-in amplifier detection scheme. This could be realized by using the so-called "step-scan" modus of the spectrometer, which allows the interconnection of a lock-in amplifier.

Inspired by the results achieved in the field of terahertz modulation realized by a transfer from the near-infrared to the terahertz domain, this modulation technique could be used to increase the terahertz modulation frequency in the HSM concept. As discussed in chapter 5 this will lead to an increase of the detectivity and a decrease of the noise-equivalent power. This will combine its conceptual advantages

with a low noise-equivalent power and therefore enables a variety of applications. Further the optical modulation scheme allows the implementation of single-pixel imaging in the HSM concept.

8. Zusammenfassung und Ausblick

Auch mehr als 100 Jahre nach der ersten Erwähnung des sogenannt "terahertz gap" durch H. Rubens und E. F. Nicholes, herrscht ein großes Interesse in der Forschung für den Frequenzbereich zwischen 0.1 und 10 THz. In der Tat wurde diese Lücke des elektromagnetischen Spektrums durch fortwährende Erfolge in der Forschung immer weiter geschlossen, der Durchbruch hin zu industriellen Anwendungen wurde jedoch noch nicht erzielt [179]. Dabei könnte dieser Spektralbereich durch seine einzigartigen Eigenschaften, wie den spektralen Fingerabdrücken vieler Moleküle, der Transparenz von Materialen wie Kunststoff und Papier und dem nicht ionisierenden Charakter eine Vielzahl von Anwendungen ermöglichen. So wurde bereits eine Vielzahl an möglichen Anwendungen entwickelt, jedoch müssen sich diese gegen die in der Industrie schon gut etablierten Sensortechnologien behaupten. Eine wichtige Bedingung für den industriellen Nutzen der Terahertzstrahlung ist eine robuste Erzeugung und Detektion bei Raumtemperatur. Vielversprechende Bauteile zur Erzeugung und Detektion von Terahertzstrahlung stellen sogenannte photoleitende Antennen (engl. photoconductive antenna (PCA)) dar. In Kombination mit etablierten optischen Systemen wie fs-Pulslasern bzw. Einmodenlasern sind sie in der Lage, kurze Terahertzpulse bzw. kontinuierliche Terahertzstrahlung zu erzeugen.

Der erste Teil dieser Arbeit befasste sich mit der Erzeugung und Detektion von kontinuierlicher Terahertzstrahlung unter Verwendung dieser PCAs und einem selbst entwickeltem Lasersystem (engl. external cavity diode laser (ECDL)). Darüber hinaus wurde ein neuartiges Konzept zur gleichzeitigen Erzeugung und phasensensitiven Detektion durch nur eine einzige PCA erarbeitet. Dieses HSM (engl. homodyne self-mixing) genannte Konzept kann zu einer Kostenreduktion führen, da nur eine PCA benötigt wird und bereitet den Weg für extrem kompakte Spektroskopie-Aufbauten im Terahertzfrequenzbereich.

Kapitel 3 und 4 befassten sich mit den fundamentalen Elementen des HSM Konzeptes, welche sich aus dem ECDL und der PCA zusammensetzen. Im Rahmen dieser Arbeit wurden zwei ECDLs basierend auf einem Interfernzfilter und ein ECDL basierend auf einem optischen Gitter entwickelt. Diese wurden in Kapitel 3 ausführlich hinsichtlich ihrer Stabilität der Ausgangsleistung und Spektren untersucht. Hierzu wurden Langzeitmessungen der Leistung und Spektren durchgeführt und das relative Intensitätsrauschen und die Linienbreite der Laser bestimmt. Die Resultate dieser Charakterisierung sind in Tabelle 3.1 zusammengefasst. Diese Ergebnisse belegen die Eignung der entwickelten Lasersysteme zur hochaufgelösten Terahertzspektroskopie unter Verwendung von PCAs. Anschließend zu diesem Ergebnis befasste sich Kapitel 4 mit der Erzeugung und Detektion von Terahertzstrahlung unter Verwendung von zwei PCAs des Forschungszentrums Jülich und einer kommerziell erhältlichen PCA, welche von TOPTICA Photonics bereitgestellt wurde. Die vom Forschungszentrums Jülich bereitgestellten PCAs wurden hinsichtlich ihrer Ausgangsleistung untersucht und mit der kommerziell erhältlichen PCA verglichen. Dieser Vergleich zeigte die hohe Qualität der kommerziell erhältlichen PCA, welche die nah-infrarote Strahlung mit einer Konversionseffizienz von 33×10^{-6} bei einer Emissionsfrequenz von 0.2 THz in Terahertzstrahlung konvertiert. Im Vergleich hierzu zeigten die PCAs des Forschungszentrums Jülich lediglich eine Konversionseffizienz von

0.6×10^{-6}. Aus diesem Grund wurden die PCAs der Firma TOPTICA Photonics für einen Standardaufbau zur Erzeugung und Detektion von Terahertzstrahlung mittels PCAs verwendet. Hierfür wurde die PCA TX30A als Sender und die PCA RX30A als Empfänger verwendet.

Die Reduzierung dieses Standardaufbaus hin zur Erzeugung und Detektion der Terahertzstrahlung mittels einer einzigen PCA wurde in Kapitel 5 beschrieben. Hierbei wurde die von der PCA emittierte Terahertzstrahlung von einem sich drehenden Chopperrad zurück auf dieselbe PCA reflektiert. An dieser wurde durch die zurückreflektierte Terahertzstrahlung ein Wechselstrom erzeugt, welcher von der Amplitude und Phase der Terahertzstrahlung abhängt. Ein sinusförmiger Zusammenhang zwischen einer longitudinalen Verschiebung des Chopperrads und des gemessenen Stroms wurde beobachtet. Bestätigt wurde diese Beobachtung durch theoretische Überlegungen zum Stromfluss durch die PCA unter Berücksichtigung der zurückreflektierten Terahertzstrahlung. Um die Phasensensitivität der HSM Methode zu demonstrieren, wurde beispielhaft der Brechungsindex einer Teflonscheibe aus den HSM Signalen erfolgreich bei einer Frequenz von 0.17 THz bestimmt.

Der zweite Teil dieser Arbeit befasste sich mit der zweidimensionalen tomographischen Bildgebung im Terahertzspektralbereich. Diese diente zunächst als Demonstrationsexperiment der HSM Methode wie in Kapitel 6.1 beschrieben. Hierzu wurden eindimensionale Projektionen eines hohlen Teflonzylinders, welcher mit α-Lactose befüllt war, für zwei verschiedene Frequenzen gemessen. Das rekonstruierte zweidimensionale Bild des Zylinders gab Aufschluss über die Dimensionen des Zylinders und erlaubte es, die α-Lactose Füllung über eine spezifische Absorptionslinie zu identifizieren. Die gemessenen eindimensionalen Projektionen wurden stark durch Brechungseffekte am Zylinder beeinflusst. Diese konnten durch eine Modellierung des Aufbaus im Programm ZEMAX identifiziert werden. Die Ergebnisse dieser Modellierung spiegelten die experimentellen Ergebnisse in guter Übereinstimmung wider und trugen zum Verständnis über den Einfluss dieser optischen Effekte bei.

Motiviert durch die vorangegangenen ZEMAX Modellierungen, wurden detaillierte Simulationen unter Verwendung von optischem Raytracing für verschiedene Bildgebungsverfahren in Kapitel 6.2 behandelt. Hierzu wurde eine Raytracing Software in MATLAB entwickelt, welche es erlaubte, Simulationen für Testobjekte mit verschiedenen Geometrien durchzuführen. Die entwickelte Software wurde dazu verwendet, die eindimensionalen Projektionen eines kreisförmigen Testobjekts unter Verwendung von verschiedenen Bildgebungsverfahren zu simulieren. Dabei wurden die Projektionen unter Verwendung der Rasterscan Methode mittels kleiner und großer Detektorfläche, eines räumlich auflösenden Detektors und des "Single-Pixel" Bildgebungsverfahrens bestimmt. Die Information über die Herkunft eines Strahls, bevor dieser das Testobjekt passiert, geht bei den Methoden des "Single-Pixel" Bildgebungsverfahrens und des Rasterscannens mittels großer Detektorfläche nicht verloren. Daher zeigten diese Methoden die besten Resultate und erwiesen sich als am vielversprechendsten.

Stimuliert durch dieses Ergebnis, wurde ein Experiment zur tomographischen Bildgebung unter Verwendung des "Single-Pixel" Bildgebungsverfahrens realisiert. Hierfür wurde die mittels eines Mikrospiegelaktors räumlich modulierte Strahlung einer nah-infraroten Laserdiode über ein dünnes HRFZ-Si Fenster in den Terahertzfrequenzbereich transferiert. Dieser Transfer basiert auf der Erzeugung von freien Ladungsträgern im Fenstermaterial durch die nah-infrarote Strahlung, welche eine Änderung der optischen Eigenschaften im Terahertzfrequenzbereich mit sich bringt. Die verschiedenen Muster, welche

für das "Single-Pixel" Bildgebungsverfahren nötig sind, wurden durch eine 32×32 Hadamard-Matrix vorgegeben. Zunächst dienten zwei metallische M4 Schrauben als Testobjekt, von welchen eindimensionale Projektionen unter verschieden Drehwinkeln aufgenommen wurden. Aus diesen Projektionen konnte unter Verwendung der simultanen algebraischen Rekonstruktionstechnik ein zweidimensionales Bild der Schraubenanordnung rekonstruiert werden. Im Anschluss wurden die zwei Schrauben durch zylindrische und quaderförmig Testobjekte bestehend aus Polypropylen ersetzt. Polypropylen besitzt einen Brechungsindex von 1.5 und einen Absorptionskoeffizienten von ungefähr 1 cm^{-1} im Terahertzfrequenzbereich. Der Einfluss von Brechung, Reflektion und Beugung war klar am Verlauf dieser Testobjektprojektionen zu erkennen. Aus diesem Grund, wurde ein Hybridansatz entwickelt, welcher Raytracing Simulationen mit der Lichtpropagation unter Verwendung des Rayleigh-Sommerfeld Beugungintegrals vereint. Schließlich, wurde dieses Model dazu verwendet, die experimentell erhaltenen Sinogramme für beide Testobjekte zu simulieren und es wurde eine hervorragende Übereinstimmung mit den experimentellen Ergebnissen gefunden. Der Aufnahmewinkel des Detektors ist in der experimentellen Realisierung nicht zugänglich, jedoch zeigten die vorherigen Raytracing Simulationen aus Kapitel 6.2 einen Einfluss dieser Größe auf die erhaltenen Projektionen. Daher wurde dieser durch Simulationen in einem Bereich zwischen 70° und 0.2° untersucht. Eine Variation des Winkels zwischen 70° und 40° zeigte nur einen sehr kleinen Einfluss auf die Form der Projektion. Simulierte Projektionen mit einem Winkel unterhalb von 40° wiesen jedoch eine Kompression der inneren Geometrie des Objekts auf. Für sehr kleine Aufnahmewinkel unterhalb von 1° wurden sogar negative Transmissionen gefunden. Diese Untersuchung zeigte, dass gute Resultate innerhalb eines breiten Spektrums an Aufnahmewinkeln möglich sind und das der Aufnahmewinkel im Experiment größer als 1° sein sollte, was sich jedoch ohne größeren Aufwand realisieren lässt.

Aus Sicht der auf Röntgenstrahlung basierenden tomographischen Bildgebung wiesen die im Terahertzbereich erzielten Projektionen durchaus eine ungewöhnliche Form auf. Diese ließ sich durch die an den Grenzflächen auftretende Brechung erklären, welche bei der Verwendung von Röntgenstrahlung nicht auftritt. Da bei der auf Röntgenstrahlung basierenden Tomographie angenommen wird, dass die Strahlung auf geraden Linien von der Quelle zum Detektor gelangt, beruhen auch die Rekonstruktionsalgorithmen auf diesem Prinzip. Um diese Limitierung zu überwinden, wurde das oben entwickelte Hybridansatz Modell zur Rekonstruktion der Testobjekte verwendet. Dazu wurde ein Optimierungsproblem formuliert, welches mit Hilfe eines evolutionären Algorithmus gelöst wurde. Die Dimensionen der Objekte wurden generell als zu klein ermittelt. Jedoch ermöglichte es die entwickelte Methode, basierend auf den experimentellen Daten die Objektform erfolgreich zu bestimmen.

Nachdem ein tomographisches "Single-Pixel" Terahertz Bildgebungssystem erfolgreich implementiert wurde, wurde dieses Konzept hinsichtlich spektral auflösender Bildgebung untersucht, wie dies schon in Abschnitt 6.1 bei der HSM Methode angewendet wurde. Durch den verwendeten "Single-Pixel" Ansatz, welcher zur Bildgebung keinen räumlich auflösenden Detektor benötigt, ließ sich dies einfach durch ein an das FTIR Spektrometer angeschlossene Bolometer realisieren. Hierfür wurde für jedes Muster ein Spektrum gemessen und so ein spektral aufgelöstes Bild des Strahlprofils der Quecksilber-Bogenlampe aufgenommen. Durch diese unkomplizierte Realisierung der spektral aufgelösten Bildgebung, wurde ein weiterer Vorteil des "Single-Pixel" Bildgebungsverfahrens gegenüber konventionellen Bildgebungsverfahren aufgezeigt.

Abschließend kann gesagt werden, das in dieser Arbeit ein wichtiger Beitrag zu zwei wesentlichen Be-

reichen der Terahertzforschung erbracht wurde. Erstens wurde ein neuartiges Konzept zur Erzeugung und Detektion von Terahertzstrahlung eingeführt und zweitens wurde die Anwendung der tomographischen Bildgebung mittels Terahertzstrahlung in verschiedensten experimentellen Realisierungen und theoretischen Untersuchungen erforscht.

Das in dieser Arbeit entwickelte Hybrid-Model ermöglicht die realistische Rekonstruktion von kreisförmigen und rechteckigen lichtbrechenden Objekten, welche mit Hilfe von Terahertz-Tomographie vermessen wurden. Jedoch beträgt die hierfür benötigte Rechenzeit einige Stunden. Um diese zu verkürzen, könnten die Berechnungen des Models auf der Grafikkarte des Computers durchgeführt werden. Dies würde die Implementierung von deutlich komplexeren Objekten erlauben und somit die Anzahl der rekonstruierbaren Objektformen erhöhen.

Durch diese tomographische Rekonstruktionsmethode könnten realistische Bilder von willkürlich geformten lichtbrechenden Objekten durch Terahertz-Tomographie aufgenommen werden. Eine spektral aufgelöste Single-Pixel Tomographie könnte durch den Einsatz des Fourier-Transform-Infrarotspektrometers in Kombination mit einem Lock-In Verstärker realisiert werden. Hierzu könnte das Spektrometer im sogenannten "Step-Scan" Modus betrieben werden, welcher es erlaubt den Lock-In Verstärker zwischenzuschalten.

Inspiriert durch die Ergebnisse der optischen Modulation der Terahertzstrahlung im Single-Pixel Experiment, könnte dieses Modulationskonzept auf die HSM Methode übertragen werden. Hierdurch könnte eine deutliche Erhöhung der Modulationsfrequenz erreicht werden. Wie in Kapitel 5 diskutiert, würde dies zu einer Erhöhung der Detektivität und einer Verringerung der rauschäquivalenten Leistung führen. Die somit erreichte Kombination der konzeptionellen Vorteile des HSM Ansatzes mit einer hohen Detektivität würde viele Anwendungsbereiche ermöglichen. Des Weiteren könnte durch die optische Modulationstechnik das HSM Konzept durch Single-Pixel Bildgebung erweitert werden.

A. List of abbreviations

AOM	acousto-optic modulator
AR	anti-reflective
ART	algebraic reconstruction technique
BS	beam splitter
CW	continuous wave
DFG	difference frequency generation
ECDL	external cavity diode laser
EO	electro optic
ESA	electrical spectrum analyser
FWHM	full with at half maximum
HITRAN	high-resolution transmission molecular absorption
HRFZ-Si	high resistivity float zone silicon
HSM	homodyne self-mixing
IF	interference filter
ISO	optical isolator
LD	laser diode
LT-GaAs	low-temperature Gallium Arsenide
NDC	negative-differential-conductance
NEP	noise equivalent power
NIR	near-infrared
PCA	photoconductive antenna
PCB	printed circuit board
PM	partially reflective mirror

PP	polypropylene
QCL	quantum cascade laser
RIN	relative intensity noise
RTD	resonant-tunneling diode
SART	simultaneous algebraic reconstruction technique
SNR	signal-to-noise ratio

B. List of devices

[D1] Thorlabs C610TME-B, EFL= 4 mm, NA= 0.6

[D2] Thorlabs GR13-1208, 1200 Grooves/mm

[D3] Laser Components LC-830HBP3.2-25 Bandpassfilter, CWL= 830 nm, BW= 3.2 nm

[D4] Layertec Output Coupler, R= 40% at 850 nm

[D5] Thorlabs C280TMD-B, EFL= 18.4 mm, NA= 0.15

[D6] ISOWAVE I-80-SD-5M and Halbo Optics Model IS79

[D7] Thorlabs BSW29

[D8] Anritsu MS9710C Spectrum Analyzer

[D9] Melles Griot 13SAM045

[D10] Coherent FieldMaster, VIS-15K08

[D11] HP 8568B Spectrum Analyzer 100 Hz - 1.5 GHz

[D12] IntraAction Corp. AOM-40N

[D13] Thorlabs FC830-50B-APC

[D14] Menlo Systems FPD 510

[D15] Rohde & Schwarz FSC Spectrum Analyzer 9 kHz - 6 GHz

[D16] Anti-reflection coated laser diode provided by the Ferdinand-Braun-Institut

[D17] JDSU, Diode Lasersm Single-mode 200 mW 830 nm, 5430-J1 Series

[D18] Oclaro SM830-200-TO56-R01

[D19] TPT Wire Bonder HB10

[D20] Batop FSL-D20-f50 -Focusing silicon lens

[D21] GaAs-based photomixer, model EK-000831, TOPTICA Photonics

[D22] Thorlabs C220TME-B, f= 11 mm, NA= 0.25

[D23] HP 8110A Pulse generator

[D24] Infrared Laboratories, 4.2 K Silicon Bolometer

[D25] Stanford Research Systems SR530 Lock-In Amplifier

[D26] Keithley 2100 6 1/2 Digit Multimeter

[D27] Thorlabs FC830-90B-APC

[D28] Thorlabs F24APC-780

[D29] Newport Inc. ESP300

[D30] FEMTO DLPCA-200

[D31] Tektronix TDS3022

[D32] Scitec Instruments Inc.

[D33] Tektronix Spektrumanalysator RSA6000

[D34] Thorlabs MTS50/M-Z8

[D35] Tydex W-HRFZ-SI-D25.4-T1

[D36] Roithner Lasertechnik S8081WG, 808 nm, 1 *W*

[D37] Texas Instruments Lightcrafter, DLP3000

[D38] Roithner Lasertechnik LED820-01AV

C. Development of a photodetector for RIN measurements in the low frequency regime

In order to get information about the fluctuations of the optical power for the different ECDL configurations the RIN is measured. For this measurement the optical output power of the ECDL is translated into a current by a photodiode [180, 181]. Further this current has to be separated into its DC and AC contribution in the relevant frequency range, lasting from $100\,Hz$ to $1\,MHz$. To achieve this low frequency separation a detection scheme introduced for the purpose of rejecting ambient light [182] and for the detection of 'Violin-Mode' resonances in advanced Laser Interferometer Gravitational wave Observatories [183] is employed. A circuit diagram of developed photo detector is shown in Fig. C.1 and the values of the used electrical components are summarized in table C.1.

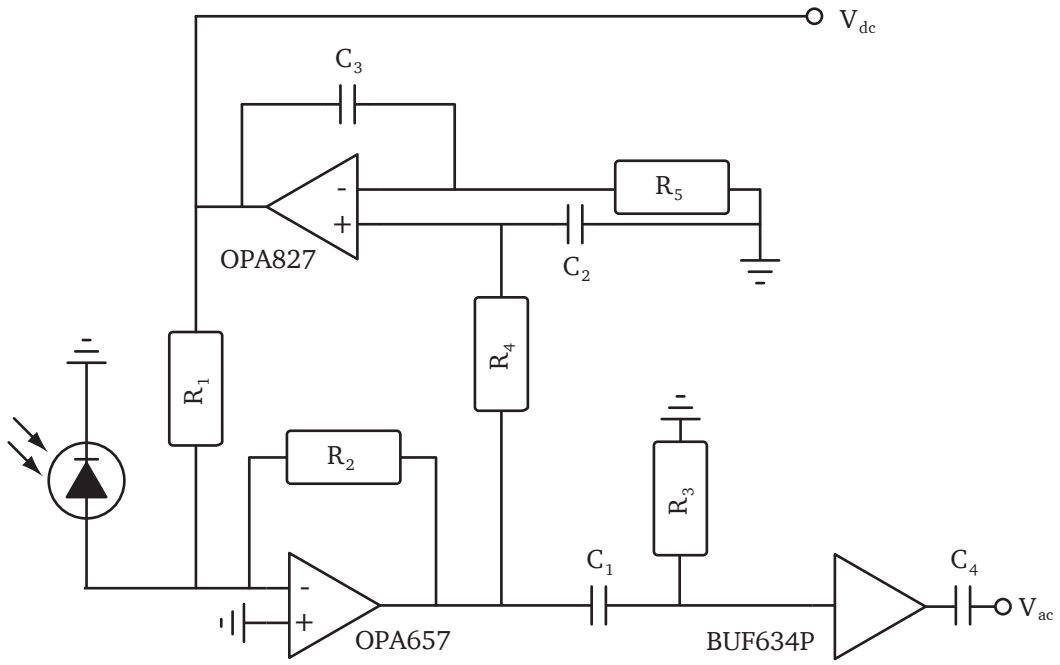

Figure C.1.: Circuit diagram of the developed photo detector for RIN measurement in the frequency range from $100\,Hz$ to $1\,MHz$.

The detector is composed of a transimpedance amplifier ($OPA657$ and R_2), an integrator ($OPA827$, R_4, R_5, C_2 and C_3), a buffer amplifier ($BUF634P$) and an electrical high pass filter (C_1 and R_3). The separation of the current generated at the photodiode is realized due to feedback of the non-inverting integrator.

Table C.1.: Electrical components of the realized photo detector and the corresponding values.

Component	R_1	R_2	R_3	$R_{4,5}$	$C_{1,2,3}$	C_4
Value	$120\,k\Omega$	$1.2\,M\Omega$	$10\,k\Omega$	$100\,k\Omega$	$100\,nF$	$45\,\mu F$

This feedback forces the DC current to flow over the resistance R_1 and the AC part into the input of the transimpedance amplifier. Therefore, a voltage proportional to the DC current at V_{dc} and a voltage proportional to the AC current at V_{ac} can be measured. These voltages are given by

$$V_{dc} = -I_{dc} \cdot R_1 \tag{C.1}$$

$$V_{ac} = -I_{ac} \cdot R_2, \tag{C.2}$$

but in case of V_{ac} additional frequency dependent components like the high pass filter and feedback of the integrator have to be considered.

The measured DC and AC amplification of the developed photodetector is shown in Fig. C.2. The DC amplification is measured using a near-infrared LED[D38] shining onto the photodiode and a simultaneous current measurement by a multimeter in series to the photodiode. By a change of the LED injection current, the current at the photodiode is varied from $\approx 6\,\mu$A to $24\,\mu$A and the output voltage is measured at V_{dc}. The resulting linear dependency between the photocurrent and the measured voltage can be seen in Fig. C.2(a), from which an amplification of $-119.4\,$kV/A is obtained by curve fitting.

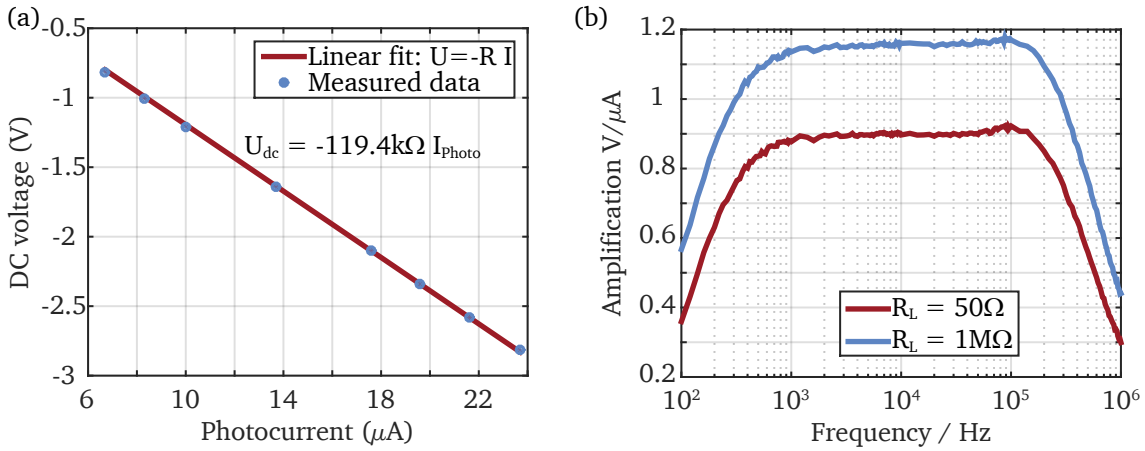

Figure C.2.: (a) DC voltage measured at V_{dc} in dependency of a DC photocurrent at the photodiode. (b) Frequency dependent AC amplification for two different load resistors R_L.

The AC amplification of the photodetector is measured using the same LED, but injected with a constant current plus a small sinusoidal current modulation. The ratio between DC and AC current is fixed to 10 and the output voltage V_{ac} is measured for modulation frequencies between 100 Hz and 1 MHz using an oscilloscope. The resulting amplification for two different load resistors is shown in Fig. C.2(b). For both load resistors a constant amplification is visible between 1 kHz and 100 kHz and amounts to $0.9\,$V/μA

and 1.15 V/μA for a load resistor of 50 Ω and 1 MΩ, respectively. For the RIN measurements the ratio between the AC and DC gain is of interest. Therefore the LED is operated as described before, but the output is directly connected to the used ESA. The AC amplitudes measured at the ESA are correlated to the corresponding DC voltages providing the gain ratio shown in Fig. C.3.

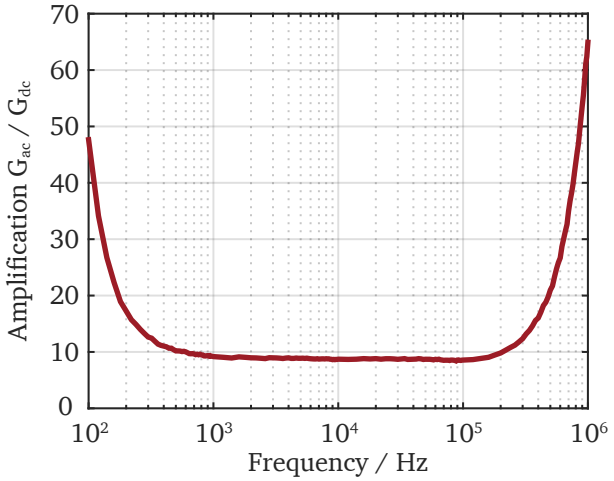

Figure C.3.: Measured ratio of the AC and DC amplification used to calculate the RIN values. The ratio is determined using the same ESA as for the actual RIN measurement.

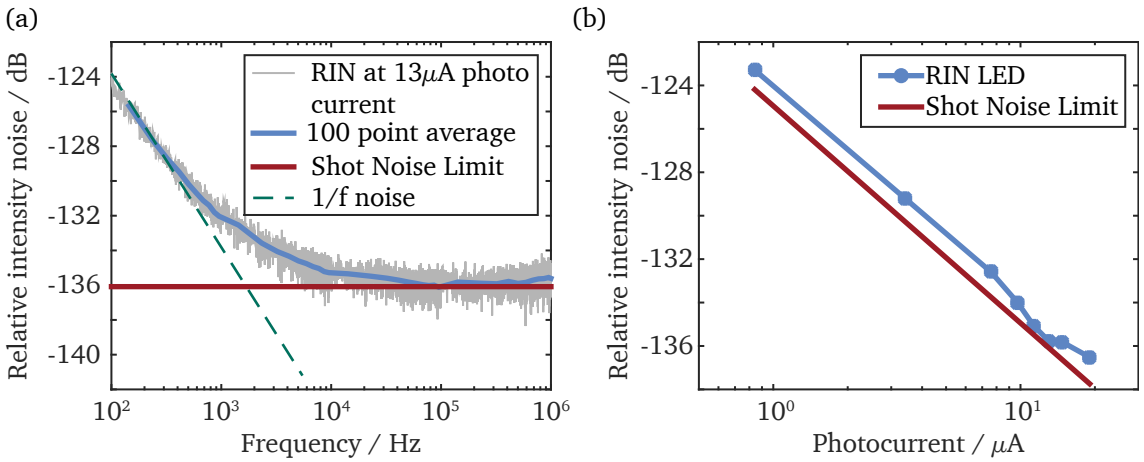

Figure C.4.: (a) Measured RIN of a LED generating a DC photocurrent of 13 μA at the photodiode. (b) Mean RIN values calculated using the RIN of the last decade from 100 kHz to 1 MHz for different DC photocurrents at the photodiode.

After the detailed characterization of the developed photodetector, the RIN of the same near-infrared LED as before is measured injecting different DC currents. The measured RIN in dependency of the frequency is shown in Fig. C.4(a) for a DC photocurrent of 13 μA of the photodiode. Starting at -124 dB the value of the RIN decreases with increasing frequency and finally approaches the shot noise limit of -136 dB at approx. 100 kHz. From this frequency, the RIN value remains constant at the shot noise limit.

As can be seen from Eq. 3.6, the shot noise limit depends on the DC photocurrent of the photodiode. Therefore, an increase of the injection current of the LED, which increases the output power and consequently the photocurrent, leads to a reduction of the RIN. The frequency resolved RIN is measured for 8 different injection currents of the LED and a mean RIN value is calculated using the frequency range of constant RIN values (100 kHz to 1 MHz). The resulting RIN in dependency of the photocurrent is shown in Fig. C.4(b). The RIN values are in good agreement with the shot noise limit and the maximum deviation from this limit amounts to 0.9dB. These results point out that the developed photodetector is suitable for RIN measurement for frequencies between 100 Hz and 1 MHz.

Bibliography

[1] J. C. MAXWELL. A Dynamical Theory of the Electromagnetic Field. Philosophical Transactions of the Royal Society of London **155** (1865), 459–512.

[2] J. M. CHAMBERLAIN. Where optics meets electronics: recent progress in decreasing the terahertz gap. Philosophical Transactions of the Royal Society of London A: Mathematical, Physical and Engineering Sciences **362** (2004), 199–213.

[3] H. RUBENS and O. von BAEYER. On extremely long waves, emitted by the quartz mercury lamp. Philosophical Magazine **21** (1911), 689–695.

[4] M. KIMMITT. Restrahlen to T-Rays – 100 Years of Terahertz Radiation. Journal of Biological Physics **29** (2003), 77–85.

[5] M. PLANCK. Über das Gesetz der Energieverteilung im Normalspectrum. Annalen der Physik **309** (1901), 553–563.

[6] H. RUBENS and E. F. NICHOLS. Heat Rays Of Great Wave Length. Phys. Rev. (Series I) **4** (1897), 314–323.

[7] I. GORDON *et al.* The HITRAN2016 molecular spectroscopic database. Journal of Quantitative Spectroscopy and Radiative Transfer (2017).

[8] M. FEIGINOV, C. SYDLO, O. COJOCARI, and P. MEISSNER. Resonant-tunnelling-diode oscillators operating at frequencies above 1.1 THz. Appl. Phys. Lett. **99** (2011), 233506.

[9] A. MAESTRINI, B. THOMAS, H. WANG, C. JUNG, J. TREUTTEL, Y. JIN, G. CHATTOPADHYAY, I. MEHDI, and G. BEAUDIN. Schottky diode-based terahertz frequency multipliers and mixers. Comptes Rendus Physique **11** (2010). Terahertz electronic and optoelectronic components and systems, 480–495.

[10] J. M. CHAMBERLAIN and R. MILES. New Directions in Terahertz Technology. Springer Netherlands 2012.

[11] T. H. MAIMAN. Stimulated Optical Radiation in Ruby. Nature **187** (1960), 493–494.

[12] A. CROCKER, H. A. GEBBIE, M. F. KIMMITT, and L. E. S. MATHIAS. Stimulated Emission in the Far Infra-Red. Nature **201** (1964), 250–251.

[13] G. DODEL. On the history of far-infrared (FIR) gas lasers: Thirty-five years of research and application. Infrared Physics & Technology **40** (1999), 127–139.

[14] F. KEILMANN, V. N. SHASTIN, and R. TILL. Pulse buildup of the germanium far-infrared laser. Applied Physics Letters **58** (1991), 2205–2207.

[15] R. F. KAZARINOV and R. A. SURIS. Possibility of the amplification of electromagnetic waves in a semiconductor with a superlattice. Sovie Physics - Semiconductors **5** (1971), 707–709.

[16] J. FAIST, F. CAPASSO, D. L. SIVCO, C. SIRTORI, A. L. HUTCHINSON, and A. Y. CHO. Quantum Cascade Laser. Science **264** (1994), 553–556.

[17] R. KÖHLER, A. TREDICUCCI, F. BELTRAM, H. E. BEERE, E. H. LINFIELD, A. G. DAVIES, D. A. RITCHIE, R. C. IOTTI, and F. ROSSI. Terahertz semiconductor-heterostructure laser. Nature **417** (2002), 156–159.

[18] P. R. SMITH, D. H. AUSTON, and M. C. NUSS. Subpicosecond photoconducting dipole antennas. IEEE Journal of Quantum Electronics **24** (1988), 255–260.

[19] D. H. AUSTON and M. C. NUSS. Electrooptical generation and detection of femtosecond electrical transients. IEEE Journal of Quantum Electronics **24** (1988), 184–197.

[20] D. GRISCHKOWSKY, S. KEIDING, M. van EXTER, and C. FATTINGER. Far-infrared time-domain spectroscopy with terahertz beams of dielectrics and semiconductors. J. Opt. Soc. Am. B **7** (1990), 2006–2015.

[21] K. A. MCINTOSH, E. R. BROWN, K. B. NICHOLS, O. B. MCMAHON, W. F. DINATALE, and T. M. LYSZCZARZ. Terahertz photomixing with diode lasers in low-temperature-grown GaAs. Appl. Phys. Lett. **67** (1995), 3844.

[22] W. SHI, Y. J. DING, N. FERNELIUS, and K. VODOPYANOV. Efficient, tunable, and coherent 0.18–5.27-THz source based on GaSe crystal. Opt. Lett. **27** (2002), 1454–1456.

[23] R. B. BARNES, W. S. BENEDICT, and C. M. LEWIS. The Far Infrared Spectrum of H_2O. Phys. Rev. **47** (1935), 918–921.

[24] T. MOHR, S. BREUER, G. GIULIANI, and W. ELSÄSSER. Two-dimensional tomographic terahertz imaging by homodyne self-mixing. Opt. Express **23** (2015), 27221–27229.

[25] A. BRAHM, A. TÜNNERMANN, F. WICHMANN, C. GERTH, M. TYMOSHCHUK, S. RIEHEMANN, and G. NOTNI. Terahertz Computed Tomography Helps ID Chemical Substances. Photonics Spectra December **12** (2011), 40–43.

[26] K. KAWASE, Y. OGAWA, Y. WATANABE, and H. INOUE. Non-destructive terahertz imaging of illicit drugs using spectral fingerprints. Opt. Express **11** (2003), 2549–2554.

[27] Y. C. SHEN, T. LO, P. F. TADAY, B. E. COLE, W. R. TRIBE, and M. C. KEMP. Detection and identification of explosives using terahertz pulsed spectroscopic imaging. Applied Physics Letters **86** (2005), 241116.

[28] M. C. KEMP, P. F. TADAY, B. E. COLE, J. A. CLUFF, A. J. FITZGERALD, and W. R. TRIBE. Security applications of terahertz technology. Proc. SPIE **5070** (2003), 44–52.

[29] G. J. WILMINK and J. E. GRUNDT. Invited Review Article: Current State of Research on Biological Effects of Terahertz Radiation. Journal of Infrared, Millimeter, and Terahertz Waves **32** (2011), 1074–1122.

[30] R. M. WOODWARD, V. P. WALLACE, R. J. PYE, B. E. COLE, D. D. ARNONE, E. H. LINFIELD, and M. PEPPER. Terahertz Pulse Imaging of ex vivo Basal Cell Carcinoma. Journal of Investigative Dermatology **120** (2003), 72–78.

[31] C. JÖRDENS, M. SCHELLER, B. BREITENSTEIN, D. SELMAR, and M. KOCH. Evaluation of leaf water status by means of permittivity at terahertz frequencies. Journal of Biological Physics **35** (2009), 255–264.

[32] R. GENTE and M. KOCH. Monitoring leaf water content with THz and sub-THz waves. Plant Methods **11** (2015), 15.

[33] E. CASTRO-CAMUS, M. PALOMAR, and A. A. COVARRUBIAS. Leaf water dynamics of Arabidopsis thaliana monitored in-vivo using terahertz time-domain spectroscopy. Scientific Reports **3** (2013), 2910.

[34] D. BANERJEE, W. von SPIEGEL, M. D. THOMSON, S. SCHABEL, and H. G. ROSKOS. Diagnosing water content in paper by terahertz radiation. Opt. Express **16** (2008), 9060–9066.

[35] B. HILS, W. von SPIEGEL, T. LÖFFLER, and H. ROSKOS. Berührungsfreie Prüfung von Materialoberflächen mit THz-Strahlung. Technisches Messen **75** (2009), 45–50.

[36] B. PRADARUTTI, R. MÜLLER, C. BRÜCKNER, S. RIEHEMANN, G. NOTNI, A. TÜNNERMANN, G. MATTHÄUS, and S. NOLTE. Mehrkanalige THz-Bildgebung zur Qualitätskontrolle. Technisches Messen **75** (2008), 58–63.

[37] J. P. GUILLET, B. RECUR, L. FREDERIQUE, B. BOUSQUET, L. CANIONI, I. MANEK-HÖNNINGER, P. DESBARATS, and P. MOUNAIX. Review of Terahertz Tomography Techniques. Journal of Infrared, Millimeter, and Terahertz Waves **35** (2014), 382–411.

[38] L.-H. XU, R. M. LEES, E. C. C. VASCONCELLOS, S. C. ZERBETTO, L. R. ZINK, and K. M. EVENSON. Methanol and the optically pumped far-infrared laser. IEEE Journal of Quantum Electronics **32** (1996), 392–399.

[39] G. W. CHANTRY. Long Wave Optics: The Science and Technology of Infrared and Near-Millimeter Waves : Applications. Academic Pr 1984.

[40] Y.-S. LEE. Principles of Terahertz Science and Technology. Springer US 2009.

[41] H.-W. HÜBERS, S. G. PAVLOV, and V. N. SHASTIN. Terahertz lasers based on germanium and silicon. Semiconductor Science and Technology **20** (2005), S211.

[42] R. N. HALL, G. E. FENNER, J. D. KINGSLEY, T. J. SOLTYS, and R. O. CARLSON. Coherent Light Emission From GaAs Junctions. Phys. Rev. Lett. **9** (1962), 366–368.

[43] S. NAKAMURA, M. SENOH, S.-i. NAGAHAMA, N. IWASA, T. YAMADA, T. MATSUSHITA, H. KIYOKU, and Y. SUGIMOTO. InGaN-Based Multi-Quantum-Well-Structure Laser Diodes. Japanese Journal of Applied Physics **35** (1996), L74.

[44] M. RAZEGHI, S. SLIVKEN, Y. BAI, and R. DARVISH. The Quantum Cascade Laser: A Versatile and Powerful Tool. Optics and Photonics News **19** (2008), 42–47.

[45] O. CATHABARD, R. TEISSIER, J. DEVENSON, J. C. MORENO, and A. N. BARANOV. Quantum cascade lasers emitting near 2.6 μm. Applied Physics Letters **96** (2010), 141110.

[46] G. SCALARI, C. WALTHER, L. SIRIGU, M. L. SADOWSKI, H. BEERE, D. RITCHIE, N. HOYLER, M. GIOVANNINI, and J. FAIST. Strong confinement in terahertz intersubband lasers by intense magnetic fields. Phys. Rev. B **76** (2007), 115305.

[47] K.-E. PEIPONEN, A. ZEITLER, and M. KUWATA-GONOKAMI. Terahertz Spectroscopy and Imaging. Springer-Verlag GmbH 2012.

[48] S. FATHOLOLOUMI, E. DUPONT, C. CHAN, Z. WASILEWSKI, S. LAFRAMBOISE, D. BAN, A. MÁTYÁS, C. JIRAUSCHEK, Q. HU, and H. C. LIU. Terahertz quantum cascade lasers operating up to $\sim$ 200 K with optimized oscillator strength and improved injection tunneling. Opt. Express **20** (2012), 3866–3876.

[49] L. LI, L. CHEN, J. ZHU, J. FREEMAN, P. DEAN, A. VALAVANIS, A. G. DAVIES, and E. H. LINFIELD. Terahertz quantum cascade lasers with >1 W output powers. Electronics Letters **50** (2014), 309–311.

[50] B. S. WILLIAMS. Terahertz quantum-cascade lasers. Nature Photonics **1** (2007), 517–525.

[51] C. WALTHER, M. FISCHER, G. SCALARI, R. TERAZZI, N. HOYLER, and J. FAIST. Quantum cascade lasers operating from 1.2 to 1.6 THz. Applied Physics Letters **91** (2007), 131122.

[52] A. W. M. LEE, B. S. WILLIAMS, S. KUMAR, Q. HU, and J. L. RENO. Tunable terahertz quantum cascade lasers with external gratings. Opt. Lett. **35** (2010), 910–912.

[53] M. A. BELKIN, F. CAPASSO, F. XIE, A. BELYANIN, M. FISCHER, A. WITTMANN, and J. FAIST. Room temperature terahertz quantum cascade laser source based on intracavity difference-frequency generation. Applied Physics Letters **92** (2008), 201101.

[54] Y. JIANG, K. VIJAYRAGHAVAN, S. JUNG, F. DEMMERLE, G. BOEHM, M. C. AMANN, and M. A. BELKIN. External cavity terahertz quantum cascade laser sources based on intra-cavity frequency mixing with 1.2–5.9 THz tuning range. Journal of Optics **16** (2014), 094002.

[55] H. KANAYA, R. SOGABE, T. MAEKAWA, S. SUZUKI, and M. ASADA. Fundamental Oscillation up to 1.42 THz in Resonant Tunneling Diodes by Optimized Collector Spacer Thickness. Journal of Infrared, Millimeter, and Terahertz Waves **35** (2014), 425–431.

[56] M. FEIGINOV, H. KANAYA, S. SUZUKI, and M. ASADA. Operation of resonant-tunneling diodes with strong back injection from the collector at frequencies up to 1.46 THz. Applied Physics Letters **104** (2014), 243509.

[57] S. SUZUKI, M. SHIRAISHI, H. SHIBAYAMA, and M. ASADA. High-Power Operation of Terahertz Oscillators With Resonant Tunneling Diodes Using Impedance-Matched Antennas and Array Configuration. IEEE Journal of Selected Topics in Quantum Electronics **19** (2013), 8500108.

[58] G. CARPINTERO, E. GARCIA-MUNOZ, H. HARTNAGEL, S. PREU, and A. RÄISÄNEN. Semiconductor TeraHertz Technology: Devices and Systems at Room Temperature Operation (Wiley - IEEE). Wiley-IEEE Press 2015.

[59] T. W. CROWE. GaAs Schottky barrier mixer diodes for the frequency range 1–10 THz. International Journal of Infrared and Millimeter Waves **10** (1989), 765–777.

[60] H. EISELE, A. RYDBERG, and G. I. HADDAD. Recent advances in the performance of InP Gunn devices and GaAs TUNNETT diodes for the 100-300-GHz frequency range and above. IEEE Transactions on Microwave Theory and Techniques **48** (2000), 626–631.

[61] W. SHI, Y. J. DING, N. FERNELIUS, and K. VODOPYANOV. Efficient, tunable, and coherent 0.18–5.27-THz source based on GaSe crystal. Opt. Lett. **27** (2002), 1454–1456.

[62] Y. J. DING and I. B. ZOTOVA. Second-order nonlinear optical materials for efficient generation and amplification of temporally-coherent and narrow-linewidth terahertz waves. Optical and Quantum Electronics **32** (2000), 531–552.

[63] G. GALLOT, J. ZHANG, R. W. MCGOWAN, T.-I. JEON, and D. GRISCHKOWSKY. Measurements of the THz absorption and dispersion of ZnTe and their relevance to the electro-optic detection of THz radiation. Applied Physics Letters **74** (1999), 3450–3452.

[64] A. TOMASINO, A. PARISI, S. STIVALA, P. LIVRERI, A. C. CINO, A. C. BUSACCA, M. PECCIANTI, and R. MORANDOTTI. Wideband THz Time Domain Spectroscopy based on Optical Rectification and Electro-Optic Sampling. Scientific Reports **3** (2013).

[65] A. G. STEPANOV, J. HEBLING, and J. KUHL. Efficient generation of subpicosecond terahertz radiation by phase-matched optical rectification using ultrashort laser pulses with tilted pulse fronts. Applied Physics Letters **83** (2003), 3000–3002.

[66] K. L. VODOPYANOV, M. M. FEJER, X. YU, J. S. HARRIS, Y.-S. LEE, W. C. HURLBUT, V. G. KOZLOV, D. BLISS, and C. LYNCH. Terahertz-wave generation in quasi-phase-matched GaAs. Applied Physics Letters **89** (2006), 141119.

[67] M. C. HOFFMANN and J. A. FÜLÖP. Intense ultrashort terahertz pulses: generation and applications. Journal of Physics D: Applied Physics **44** (2011), 083001.

[68] K. AOKI, J. SAVOLAINEN, and M. HAVENITH. Broadband terahertz pulse generation by optical rectification in GaP crystals. Applied Physics Letters **110** (2017), 201103.

[69] M. P. FISCHER, J. BÜHLER, T. KURIHARA, G. FITZKY, A. LEITENSTORFER, and D. BRIDA. Coherent Field Transients below 15 THz from Phase-Matched Difference Frequency Generation in 4H-SiC. In: Conference on Lasers and Electro-Optics. Optical Society of America 2017, STu3J.5.

[70] BATOP GMBH. PCA - Photoconductive Antenna for Terahertz waves, $\lambda \sim 800\,\mathrm{nm}$. 2017. URL: http://www.batop.de/products/terahertz/photoconductive-antenna/photoconductive-antenna-800nm.html (visited on 10/24/2017).

[71] N. T. YARDIMCI, S. H. YANG, C. W. BERRY, and M. JARRAHI. High-Power Terahertz Generation Using Large-Area Plasmonic Photoconductive Emitters. IEEE Transactions on Terahertz Science and Technology **5** (2015), 223–229.

[72] Y. C. SHEN, P. C. UPADHYA, E. H. LINFIELD, H. E. BEERE, and A. G. DAVIES. Ultrabroadband terahertz radiation from low-temperature-grown GaAs photoconductive emitters. Applied Physics Letters **83** (2003), 3117–3119.

[73] S. H. YANG, M. R. HASHEMI, C. W. BERRY, and M. JARRAHI. 7.5% Optical-to-Terahertz Conversion Efficiency Offered by Photoconductive Emitters With Three-Dimensional Plasmonic Contact Electrodes. IEEE Transactions on Terahertz Science and Technology **4** (2014), 575–581.

[74] D. BLÖMER. Erzeugung und Anwendung von Dauerstrich-Terahertz-Strahlung unter Verwendung von Halbleiterkomponenten. PhD thesis. Technische Universität Darmstadt, 2015.

[75] C. W. BERRY, M. R. HASHEMI, S. PREU, H. LU, A. C. GOSSARD, and M. JARRAHI. High power terahertz generation using 1550nm plasmonic photomixers. Applied Physics Letters **105** (2014), 011121.

[76] A. ROLLAND, G. DUCOURNAU, G. DANION, G. LOAS, M. BRUNEL, A. BECK, F. PAVANELLO, E. PEYTAVIT, T. AKALIN, M. ZAKNOUNE, J. F. LAMPIN, F. BONDU, M. VALLET, P. SZRIFTGISER, D. BACQUET, and M. ALOUINI. Narrow Linewidth Tunable Terahertz Radiation By Photomixing Without Servo-Locking. IEEE Transactions on Terahertz Science and Technology **4** (2014), 260–266.

[77] E. R. BROWN, K. A. MCINTOSH, K. B. NICHOLS, and C. L. DENNIS. Photomixing up to 3.8 THz in low-temperature-grown GaAs. Applied Physics Letters **66** (1995), 285–287.

[78] A. J. DENINGER, A. ROGGENBUCK, S. SCHINDLER, and S. PREU. 2.75 THz tuning with a triple-DFB laser system at 1550 nm and InGaAs photomixers. Journal of Infrared, Millimeter, and Terahertz Waves **36** (2015), 269–277.

[79] M. TANI, S. MATSUURA, K. SAKAI, and S.-i. NAKASHIMA. Emission characteristics of photoconductive antennas based on low-temperature-grown GaAs and semi-insulating GaAs. Appl. Opt. **36** (1997), 7853–7859.

[80] A. WADE, G. FEDOROV, D. SMIRNOV, S. KUMAR, B. S. WILLIAMS, Q. HU, and J. L. RENO. Magnetic-field-assisted terahertz quantum cascade laser operating up to 225 K. Nature Photonics **3** (2008), 41–45.

[81] R. HUBER, A. BRODSCHELM, F. TAUSER, and A. LEITENSTORFER. Generation and field-resolved detection of femtosecond electromagnetic pulses tunable up to 41 THz. Applied Physics Letters **76** (2000), 3191–3193.

[82] P. LIU, X. ZHANG, D. XU, Y. LI, X. ZHANG, W. SHI, J. YAO, and Y. WU. Efficient and widely-tunable THz-wave difference frequency generation with organic crystals DSTMS and OH1. In: 2016 41st International Conference on Infrared, Millimeter, and Terahertz waves (IRMMW-THz). 2016, 1–2.

[83] T. TANABE, K. SUTO, J. NISHIZAWA, T. KIMURA, and K. SAITO. Frequency-tunable high-power terahertz wave generation from GaP. Journal of Applied Physics **93** (2003), 4610–4615.

[84] E. B. PETERSEN, W. SHI, A. CHAVEZ-PIRSON, N. PEYGHAMBARIAN, and A. T. COONEY. Efficient parametric terahertz generation in quasi-phase-matched GaP through cavity enhanced difference-frequency generation. Applied Physics Letters **98** (2011), 121119.

[85] P. L. RICHARDS. Bolometers for infrared and millimeter waves. Journal of Applied Physics **76** (1994), 1–24.

[86] GENTEC-EO. THZ-B THz Detectors - Gentec-EO. 2017. URL: https://www.gentec-eo.com/products/thz-detectors/THZ-B (visited on 08/16/2017).

[87] S. HOFFMANN and M. HOFMANN. Generation of Terahertz radiation with two color semiconductor lasers. Laser & Photonics Reviews **1** (2007), 44–56.

[88] I. PARK, C. SYDLO, I. FISCHER, W. ELSÄSSER, and H. L. HARTNAGEL. Generation and spectroscopic application of tunable continuous-wave terahertz radiation using a dual-mode semiconductor laser. Measurement Science and Technology **19** (2008), 065305.

[89] K. A. MCINTOSH, K. B. NICHOLS, S. VERGHESE, and E. R. BROWN. Investigation of ultrashort photocarrier relaxation times in low-temperature-grown GaAs. Applied Physics Letters **70** (1997), 354–356.

[90] A. W. JACKSON, J. P. IBBETSON, A. C. GOSSARD, and U. K. MISHRA. Reduced thermal conductivity in low-temperature-grown GaAs. Applied Physics Letters **74** (1999), 2325–2327.

[91] I. S. GREGORY, C. BAKER, W. R. TRIBE, I. V. BRADLEY, M. J. EVANS, E. H. LINFIELD, A. G. DAVIES, and M. MISSOUS. Optimization of photomixers and antennas for continuous-wave terahertz emission. IEEE Journal of Quantum Electronics **41** (2005), 717–728.

[92] K. A. MCINTOSH, E. R. BROWN, K. B. NICHOLS, O. B. MCMAHON, W. F. DINATALE, and T. M. LYSZCZARZ. Terahertz measurements of resonant planar antennas coupled to low-temperature-grown GaAs photomixers. Applied Physics Letters **69** (1996), 3632–3634.

[93] P. R. SMITH, D. H. AUSTON, and M. C. NUSS. Subpicosecond photoconducting dipole antennas. IEEE Journal of Quantum Electronics **24** (1988), 255–260.

[94] J. V. RUDD and D. M. MITTLEMAN. Influence of substrate-lens design in terahertz time-domain spectroscopy. J. Opt. Soc. Am. B **19** (2002), 319–329.

[95] P. U. JEPSEN and S. R. KEIDING. Radiation patterns from lens-coupled terahertz antennas. Opt. Lett. **20** (1995), 807–809.

[96] J. DAI, J. ZHANG, W. ZHANG, and D. GRISCHKOWSKY. Terahertz time-domain spectroscopy characterization of the far-infrared absorption and index of refraction of high-resistivity, float-zone silicon. J. Opt. Soc. Am. B **21** (2004), 1379–1386.

[97] B. B. HU and M. C. NUSS. Imaging with terahertz waves. Opt. Lett. **20** (1995), 1716–1718.

[98] S. PREU, G. H. DÖHLER, S. MALZER, L. J. WANG, and A. C. GOSSARD. Tunable, continuous-wave Terahertz photomixer sources and applications. J. Appl. Phys. **109** (2011), 061301.

[99] A. J. SEEDS, M. J. FICE, K. BALAKIER, M. NATRELLA, O. MITROFANOV, M. LAMPONI, M. CHTIOUI, F. van DIJK, M. PEPPER, G. AEPPLI, A. G. DAVIES, P. DEAN, E. LINFIELD, and C. C. RENAUD. Coherent terahertz photonics. Opt. Express **21** (2013), 22988.

[100] P. JEPSEN, D. COOKE, and M. KOCH. Terahertz spectroscopy and imaging - Modern techniques and applications. Laser & Photonics Reviews **5** (2010), 124–166.

[101] H.-B. LIU, H. ZHONG, N. KARPOWICZ, Y. CHEN, and X.-C. ZHANG. Terahertz Spectroscopy and Imaging for Defense and Security Applications. Proceedings of the IEEE **95** (2007), 1514–1527.

[102] J. F. FEDERICI, B. SCHULKIN, F. HUANG, D. GARY, R. BARAT, F. OLIVEIRA, and D. ZIMDARS. THz imaging and sensing for security applications—explosives, weapons and drugs. Semiconductor Science and Technology **20** (2005), S266–S280.

[103] K. J. SIEBERT, T. LÖFFLER, H. QUAST, M. THOMSON, T. BAUER, R. LEONHARDT, S. CZASCH, and H. G. ROSKOS. All-optoelectronic continuous wave THz imaging for biomedical applications. Physics in Medicine & Biology **47** (2002), 3743.

[104] P. H. SIEGEL, W. DAI, R. A. KLONER, M. CSETE, and V. PIKOV. First millimeter-wave animal in vivo measurements of L-Glucose and D-Glucose: Further steps towards a non-invasive glucometer. In: 2016 41st International Conference on Infrared, Millimeter, and Terahertz waves (IRMMW-THz). 2016, 1–3.

[105] R. GENTE, S. F. BUSCH, E. M. STÜBLING, L. M. SCHNEIDER, C. B. HIRSCHMANN, J. C. BALZER, and M. KOCH. Quality Control of Sugar Beet Seeds With THz Time-Domain Spectroscopy. IEEE Transactions on Terahertz Science and Technology **6** (2016), 754–756.

[106] P. DEAN, Y. L. LIM, A. VALAVANIS, R. KLIESE, M. NIKOLIĆ, S. P. KHANNA, M. LACHAB, D. INDJIN, Z. IKONIĆ, P. HARRISON, A. D. RAKIĆ, E. H. LINFIELD, and A. G. DAVIES. Terahertz imaging through self-mixing in a quantum cascade laser. Optics Letters **36** (2011), 2587.

[107] B. RECUR, A. YOUNUS, S. SALORT, P. MOUNAIX, B. CHASSAGNE, P. DESBARATS, J.-P. CAUMES, and E. ABRAHAM. Investigation on reconstruction methods applied to 3D terahertz computed tomography. Opt. Express **19** (2011), 5105.

[108] B. FISCHER, M. HOFFMANN, H. HELM, G. MODJESCH, and P. U. JEPSEN. Chemical recognition in terahertz time-domain spectroscopy and imaging. Semiconductor Science and Technology **20** (2005), S246.

[109] R. A. HADI, H. SHERRY, J. GRZYB, Y. ZHAO, W. FORSTER, H. M. KELLER, A. CATHELIN, A. KAISER, and U. R. PFEIFFER. A 1 k-Pixel Video Camera for 0.7 - 1.1 Terahertz Imaging Applications in 65-nm CMOS. IEEE Journal of Solid-State Circuits **47** (2012), 2999–3012.

[110] J. ZDANEVIČIUS, M. BAUER, S. BOPPEL, V. PALENSKIS, A. LISAUSKAS, V. KROZER, and H. G. ROSKOS. Camera for High-Speed THz Imaging. Journal of Infrared, Millimeter, and Terahertz Waves **36** (2015), 986–997.

[111] M. P. EDGAR, G. M. GIBSON, R. W. BOWMAN, B. SUN, N. RADWELL, K. J. MITCHELL, S. S. WELSH, and M. J. PADGETT. Simultaneous real-time visible and infrared video with single-pixel detectors. Scientific Reports (2015), 10669.

[112] B. SUN, M. P. EDGAR, R. BOWMAN, L. E. VITTERT, S. WELSH, A. BOWMAN, and M. J. PADGETT. 3D Computational Imaging with Single-Pixel Detectors. Science **340** (2013), 844–847.

[113] J. RADON. Über die Bestimmung von Funktionen durch ihre Integralwerte längs gewisser Mannigfaltigkeiten. Akad. Wiss. **69** (1917), 262–277.

[114] A. C. KAK and M. SLANEY. Principles of Computerized Tomographic Imaging (Classics in Applied Mathematics). Society for Industrial and Applied Mathematics 2001.

[115] X. PAN, E. Y. SIDKY, and M. VANNIER. Why do commercial CT scanners still employ traditional, filtered back-projection for image reconstruction? Inverse Problems **25** (2009), 123009.

[116] R. GORDON, R. BENDER, and G. T. HERMAN. Algebraic Reconstruction Techniques (ART) for three-dimensional electron microscopy and X-ray photography. Journal of Theoretical Biology **29** (1970), 471–481.

[117] S. JAYARAMAN, T. V. T, and S. ESAKKIRAJAN. Digital Image Processing. McGraw Hill Education 2017.

[118] A. H. ANDERSEN and A. C. KAK. Simultaneous Algebraic Reconstruction Technique (SART): A Superior Implementation of the Art Algorithm. Ultrasonic Imaging **6** (1984), 81–94.

[119] S. MUKHERJEE, J. FEDERICI, P. LOPES, and M. CABRAL. Elimination of Fresnel Reflection Boundary Effects and Beam Steering in Pulsed Terahertz Computed Tomography. Journal of Infrared, Millimeter, and Terahertz Waves **34** (2013), 539–555.

[120] A. BRAHM, S. MERX, M. TYMOSHCHUK, G. NOTNI, and A. TUNNERMANN. Optical effects at projection measurements for Terahertz tomography. In: 2014 39th International Conference on Infrared, Millimeter, and Terahertz waves (IRMMW-THz). Institute of Electrical & Electronics Engineers (IEEE) 2014.

[121] J. B. PERRAUD, J. B. SLEIMAN, B. RECUR, H. BALACEY, F. SIMOENS, J. P. GUILLET, and P. MOUNAIX. Liquid index matching for 2D and 3D terahertz imaging. Applied Optics **55** (2016), 9185.

[122] B. RECUR, J. P. GUILLET, I. MANEK-HÖNNINGER, J. C. DELAGNES, W. BENHARBONE, P. DESBARATS, J. P. DOMENGER, L. CANIONI, and P. MOUNAIX. Propagation beam consideration for 3D THz computed tomography. Opt. Express **20** (2012), 5817.

[123] M. F. DUARTE, M. A. DAVENPORT, D. TAKHAR, J. N. LASKA, T. SUN, K. F. KELLY, and R. G. BARANIUK. Single-pixel imaging via compressive sampling. IEEE Signal Processing Magazine **25** (2008), 83–91.

[124] W. L. CHAN, K. CHARAN, D. TAKHAR, K. F. KELLY, R. G. BARANIUK, and D. M. MITTLEMAN. A single-pixel terahertz imaging system based on compressed sensing. Appl. Phys. Lett. **93** (2008), 121105.

[125] R. I. STANTCHEV, B. SUN, S. M. HORNETT, P. A. HOBSON, G. M. GIBSON, M. J. PADGETT, and E. HENDRY. Noninvasive, near-field terahertz imaging of hidden objects using a single-pixel detector. Science Advances **2** (2016).

[126] E. J. CANDES, J. ROMBERG, and T. TAO. Robust uncertainty principles: exact signal reconstruction from highly incomplete frequency information. IEEE Transactions on Information Theory **52** (2006), 489–509.

[127] D. SHREKENHAMER, C. M. WATTS, and W. J. PADILLA. Terahertz single pixel imaging with an optically controlled dynamic spatial light modulator. Opt. Express **21** (2013), 12507.

[128] M. MIKULICS, E. A. MICHAEL, M. MARSO, M. LEPSA, A. van der HART, H. LÜTH, A. DEWALD, S. STANČEK, M. MOZOLIK, and P. KORDOŠ. Traveling-wave photomixers fabricated on high energy nitrogen-ion-implanted GaAs. Applied Physics Letters **89** (2006), 071103.

[129] A. PINE, R. SUENRAM, E. BROWN, and K. MCINTOSH. A Terahertz Photomixing Spectrometer: Application to SO_2 Self Broadening. Journal of Molecular Spectroscopy **175** (1996), 37–47.

[130] E. R. BROWN, K. A. MCINTOSH, F. W. SMITH, M. J. MANFRA, and C. L. DENNIS. Measurements of optical-heterodyne conversion in low-temperature-grown GaAs. Appl. Phys. Lett. **62** (1993), 1206.

[131] K. A. MCINTOSH, E. R. BROWN, K. B. NICHOLS, O. B. MCMAHON, W. F. DINATALE, and T. M. LYSZCZARZ. Terahertz photomixing with diode lasers in low-temperature-grown GaAs. Applied Physics Letters **67** (1995), 3844–3846.

[132] M. TANI, P. GU, M. HYODO, K. SAKAI, and T. HIDAKA. Generation of coherent terahertz radiation by photomixing of dual-mode lasers. Optical and Quantum Electronics **32** (2000), 503–520.

[133] N. KIM, H.-C. RYU, D. LEE, S.-P. HAN, H. KO, K. MOON, J.-W. PARK, M. Y. JEON, and K. H. PARK. Monolithically integrated optical beat sources toward a single-chip broadband terahertz emitter. Laser Physics Letters **10** (2013), 085805.

[134] M. MAIWALD, B. EPPICH, J. FRICKE, A. GINOLAS, F. BUGGE, B. SUMPF, G. ERBERT, and G. TRÜNKLE. Dual-Wavelength Y-Branch Distributed Bragg Reflector Diode Laser at 785 Nanometers for Shifted Excitation Raman Difference Spectroscopy. Applied Spectroscopy **68** (2014), 838–843.

[135] R. NEUHAUS. Ohne Sprünge zu neuen Anwendungen. Best of Physik Journal (2016), 18–22.

[136] J. ALNIS, A. MATVEEV, N. KOLACHEVSKY, T. UDEM, and T. W. HÄNSCH. Subhertz linewidth diode lasers by stabilization to vibrationally and thermally compensated ultralow-expansion glass Fabry-Perot cavities. Phys. Rev. A **77** (2008), 053809.

[137] B. LEONHÄUSER-REIN, L. DRZEWIETZKI, F. SCHAD, and W. ELSÄSSER. Investigations of mode beat frequencies of external cavity semiconductor lasers. Applied Physics B **113** (2013), 215–220.

[138] B. LEONHÄUSER-REIN. Untersuchung des Emissionsverhaltens von Quantenkaskadenlasern unter optischer Rückkopplung. Master-Thesis. Technische Universität Darmstadt, 2011.

[139] D. J. THOMPSON and R. E. SCHOLTEN. Narrow linewidth tunable external cavity diode laser using wide bandwidth filter. Rev. Sci. Instrum. **83** (2012), 023107.

[140] S. L. RUMYANTSEV, M. S. SHUR, Y. BILENKO, P. V. KOSTERIN, and B. M. SALZBERG. Low frequency noise and long-term stability of noncoherent light sources. Journal of Applied Physics **96** (2004), 966–969.

[141] K. I. KALLIMANI and M. J. O'MAHONY. Relative intensity noise for laser diodes with arbitrary amounts of optical feedback. IEEE Journal of Quantum Electronics **34** (1998), 1438–1446.

[142] T. OKOSHI, K. KIKUCHI, and A. NAKAYAMA. Novel method for high resolution measurement of laser output spectrum. Electronics Letters **16** (1980), 630–631.

[143] A. TECHNOLOGIES. Optical Spectrum Analysis - Application Note 1550-4. Ed. by A. TECHNOLOGIES. 2000.

[144] YOKOGAWA. AQ6373 Optical Spectrum Analyzer. Ed. by YOKOGAWA. 2013, 55.

[145] J. OLIVERO and R. LONGBOTHUM. Empirical fits to the Voigt line width: A brief review. Journal of Quantitative Spectroscopy and Radiative Transfer **17** (1977), 233–236.

[146] L. RICHTER, H. MANDELBERG, M. KRUGER, and P. MCGRATH. Linewidth determination from self-heterodyne measurements with subcoherence delay times. IEEE Journal of Quantum Electronics **22** (1986), 2070–2074.

[147] T. FÜHRER. Modellierung und Anwendung eines neuartigen Verfahrens zur aktiven Regelung und Kontrolle von Wellenlänge und Linienbreite eines Diodenlasers mit externem Resonator. PhD thesis. Darmstadt: Technische Universität, 2012.

[148] K. KIKUCHI and T. OKOSHI. Dependence of semiconductor laser linewidth on measurement time: evidence of predominance of 1/f noise. Electronics Letters **21** (1985), 1011–1012.

[149] T. PHOTONICS. TOPTICA Photonics AG: GaAs and InGaAs Photomixers. 2017. URL: http://www.toptica.com/products/terahertz-systems/frequency-domain/gaas-and-ingaas-photomixers/ (visited on 10/25/2017).

[150] Y. MITSUHASHI, J. SHIMADA, and S. MITSUTSUKA. Voltage change across the self-coupled semiconductor laser. IEEE Journal of Quantum Electronics **17** (1981), 1216–1225.

[151] G. GIULIANI, M. NORGIA, S. DONATI, and T. BOSCH. Laser diode self-mixing technique for sensing applications. Journal of Optics A: Pure and Applied Optics **4** (2002), S283.

[152] S. BUSCH, T. PROBST, M. SCHWERDTFEGER, R. DIETZ, J. PALACÍ, and M. KOCH. Terahertz transceiver concept. Opt. Express **22** (2014), 16841.

[153] D. MITTLEMAN, R. JACOBSEN, and M. NUSS. T-ray imaging. IEEE J. Select. Topics Quantum Electron. **2** (1996), 679–692.

[154] M. LANGENBACH, A. ROGGENBUCK, I. C. MAYORGA, A. DENINGER, K. THIRUNAVUKKUARASU, J. HEMBERGER, and M. GRÜNINGER. Group Delay in THz Spectroscopy with Ultra-Wideband Log-Spiral Antennae. Journal of Infrared, Millimeter, and Terahertz Waves **35** (2014), 918–931.

[155] M. MCFADDEN. Analysis of the Equiangular spiral Antenna. PhD thesis. Georgia Institude of Technology, 2009.

[156] P. D. CUNNINGHAM, N. N. VALDES, F. A. VALLEJO, L. M. HAYDEN, B. POLISHAK, X.-H. ZHOU, J. LUO, A. K.-Y. JEN, J. C. WILLIAMS, and R. J. TWIEG. Broadband terahertz characterization of the refractive index and absorption of some important polymeric and organic electro-optic materials. J. Appl. Phys. **109** (2011), 043505.

[157] P. Y. Han, M. Tani, M. Usami, S. Kono, R. Kersting, and X.-C. Zhang. A direct comparison between terahertz time-domain spectroscopy and far-infrared Fourier transform spectroscopy. Journal of Applied Physics **89** (2001), 2357–2359.

[158] M. Rahm, J.-S. Li, and W. J. Padilla. THz Wave Modulators: A Brief Review on Different Modulation Techniques. Journal of Infrared, Millimeter, and Terahertz Waves **34** (2012), 1–27.

[159] T. Nozokido, H. Minamide, and K. Mizuno. Modulation of submillimeter wave radiation by laser-produced free carriers in semiconductors. Electronics and Communications in Japan (Part II: Electronics) **80** (1997), 1–9.

[160] B. S.-Y. Ung, B. M. Fischer, B. W.-H. Ng, and D. Abbott. Towards quality control of food using terahertz. In: BioMEMS and Nanotechnology III. Ed. by D. V. Nicolau, D. Abbott, K. Kalantar-Zadeh, T. D. Matteo, and S. M. Bezrukov. SPIE-Intl Soc Optical Eng 2007.

[161] A. Roggenbuck, H. Schmitz, A. Deninger, I. C. Mayorga, J. Hemberger, R. Güsten, and M. Grüninger. Coherent broadband continuous-wave terahertz spectroscopy on solid-state samples. New Journal of Physics **12** (2010), 043017.

[162] W. van Aarle, W. J. Palenstijn, J. D. Beenhouwer, T. Altantzis, S. Bals, K. J. Batenburg, and J. Sijbers. The ASTRA Toolbox: A platform for advanced algorithm development in electron tomography. Ultramicroscopy **157** (2015), 35–47.

[163] P. Weis, J. L. Garcia-Pomar, M. Höh, B. Reinhard, A. Brodyanski, and M. Rahm. Spectrally Wide-Band Terahertz Wave Modulator Based on Optically Tuned Graphene. ACS Nano **6** (2012), 9118–9124.

[164] S. Busch, B. Scherger, M. Scheller, and M. Koch. Optically controlled terahertz beam steering and imaging. Opt. Lett. **37** (2012), 1391–1393.

[165] L.-J. Cheng and L. Liu. Optical modulation of continuous terahertz waves towards cost-effective reconfigurable quasi-optical terahertz components. Opt. Express **21** (2013), 28657–28667.

[166] T. P. Steinbusch, H. K. Tyagi, M. Schaafsma, G. Georgiou, and J. G. Rivas. Active terahertz beam steering by photo-generated graded index gratings in thin semiconductor films. Opt. Express **22** (2014), 26559–26571.

[167] R. Ulbricht, E. Hendry, J. Shan, T. F. Heinz, and M. Bonn. Carrier dynamics in semiconductors studied with time-resolved terahertz spectroscopy. Rev. Mod. Phys. **83** (2011), 543–586.

[168] M. Bass, C. Decusatis, and J. M. Enoch. Handbook of Optics, Volume IV: Optical Properties of Materials, Nonlinear Optics, Quantum Optics. MCGRAW HILL BOOK CO 2009. 1152.

[169] F. P. Mezzapesa, L. L. Columbo, M. Brambilla, M. Dabbicco, M. S. Vitiello, and G. Scamarcio. Imaging of free carriers in semiconductors via optical feedback in terahertz quantum cascade lasers. Appl. Phys. Lett. **104** (2014), 041112.

[170] D. E. Aspnes and A. A. Studna. Dielectric functions and optical parameters of Si, Ge, GaP, GaAs, GaSb, InP, InAs, and InSb from 1.5 to 6.0 eV. Phys. Rev. B **27** (1983), 985–1009.

[171] S. Nashima, O. Morikawa, K. Takata, and M. Hangyo. Temperature dependence of optical and electronic properties of moderately doped silicon at terahertz frequencies. Journal of Applied Physics **90** (2001), 837–842.

[172] F. R. BAGSICAN, A. WINCHESTER, S. GHOSH, X. ZHANG, L. MA, M. WANG, H. MURAKAMI, S. TALAPATRA, R. VAJTAI, P. M. AJAYAN, J. KONO, M. TONOUCHI, and I. KAWAYAMA. Adsorption energy of oxygen molecules on graphene and two-dimensional tungsten disulfide. Scientific Reports **7** (2017), 1774.

[173] H. ZHAN, S. WU, R. BAO, K. ZHAO, L. XIAO, L. GE, and H. SHI. Water adsorption dynamics in active carbon probed by terahertz spectroscopy. RSC Adv. **5** (2015), 14389–14392.

[174] D. M. SLOCUM, E. J. SLINGERLAND, R. H. GILES, and T. M. GOYETTE. Atmospheric absorption of terahertz radiation and water vapor continuum effects. Journal of Quantitative Spectroscopy and Radiative Transfer **127** (2013), 49–63.

[175] J. R. BIRCH. The far-infrared optical constants of polypropylene, PTFE and polystyrene. Infrared Physics **33** (1992), 33–38.

[176] B. UNG, A. MAZHOROVA, A. DUPUIS, M. ROZÉ, and M. SKOROBOGATIY. Polymer microstructured optical fibers for terahertz wave guiding. Opt. Express **19** (2011), B848–B861.

[177] D. J. BUTLER and G. W. FORBES. Fiber-diameter measurement by occlusion of a Gaussian beam. Appl. Opt. **37** (1998), 2598–2607.

[178] D. G. VOELZ. Computational Fourier Optics: A MATLAB Tutorial. SPIE 2011.

[179] D. van MECHELEN. An Industrial THz Killer Application? Optics & Photonics News (2015).

[180] T. GENSTY. Untersuchungen des Intensitätsrauschens von Quantenkaskadenlasern in verschiedenen Konfigurationen. PhD thesis. Technische Universität Darmstadt, 2005.

[181] T. GENSTY, W. ELSÄSSER, and C. MANN. Intensity noise properties of quantum cascade lasers. Opt. Express **13** (2005), 2032–2039.

[182] M. JOHNSON. Photodetection and Measurement. McGraw-Hill Education - Europe 2003. 298 Seiten.

[183] N. A. LOCKERBIE and K. V. TOKMAKOV. A low-noise transimpedance amplifier for the detection of “Violin-Mode” resonances in advanced Laser Interferometer Gravitational wave Observatory suspensions. Rev. Sci. Instrum. **85** (2014), 114705.

Publications and Proceedings

Journal papers

1. T. Mohr, S. Breuer, D. Blömer, M. Simonetta, S. Patel, M. Schlosser, A. Deninger, G. Birkl, G. Giuliani, and W. Elsäßer, „Terahertz homodyne self-mixing transmission spectroscopy“, Appl. Phys. Lett., Vol. 106, 061111 (2015).

2. T. Mohr, S. Breuer, G. Giuliani, and W. Elsäßer, „Two-dimensional tomographic terahertz imaging by homodyne self-mixing“, Opt. Express, Vol. 23(21), 27221-27229 (2015).

3. A. Molitor, T. Mohr, S. Hartmann, and W. Elsäßer, „Investigations on Spectro-Temporally Resolved Stokes Polarization Parameters of Transverse Multi-Mode Vertical-Cavity Surface-Emitting Lasers“, IEEE J. Quantum Elect., Vol. 52(2), 2400109 (2016).

Conference proceedings

1. T. Mohr, and W. Elsäßer, „Spectroscopic ellipsometry of highly ordered pyrolytic graphite in the far infrared wavelength regime“, 8th Workshop Ellipsometry 2014, Dresden, Germany (poster).

2. T. Mohr, S. Breuer, D. Blömer, M. Simonetta, S. Patel, M. Schlosser, A. Deninger, G. Birkl, G. Giuliani, and W. Elsäßer, „Terahertz homodyne self-mixing: A new spectroscopic technique - Basics and two-dimensional tomographic imaging applications“, 6th International Conference on Semiconductor Mid-IR Materials and Optics 2015, Prague, Czech Republic, (invited talk).

3. T. Mohr, S. Breuer, D. Blömer, M. Simonetta, S. Patel, M. Schlosser, A. Deninger, G. Birkl, G. Giuliani, and W. Elsäßer, „Terahertz homodyne self-mixing and its application to two-dimensional tomographic terahertz imaging“, Conference on Lasers and Electro-optics 2015, Munich, Germany, (talk).

4. A. Molitor, T. Mohr, S. Hartmann, and W. Elsäßer, „Spectro-temporally resolved Stokes polarization parameters of transverse multi-mode oxide-conned Vertical-Cavity Surface-Emitting Lasers“, Conference on Lasers and Electro-optics 2015, Munich, Germany, (poster).

5. T. Mohr, S. Breuer, D. Blömer, M. Simonetta, S. Patel, M. Schlosser, A. Deninger, G. Birkl, W. Elsäßer, and G. Giuliani „Terahertz homodyne self-mixing as a new tomographic tool“, SPIE Photonics West 2016, San Francisco, USA, (invited talk).

6. T. Mohr, S. Breuer, G. Giuliani, and W. Elsäßer, „Two-dimensional tomographic terahertz imaging by homodyne selfmixing“, 7th International Workshop on Terahertz Technology and Applications 2016, Kaiserslautern, Germany, (poster).

7. T. Mohr, S. Breuer, D. Blömer, M. Simonetta, S. Patel, M. Schlosser, A. Deninger, G. Birkl, G. Giuliani, and W. Elsäßer, EMN Meeting on Terahertz 2016, San Sebastian, Spain (invited talk).

8. T. Mohr, S. Breuer, D. Blömer, M. Simonetta, S. Patel, M. Schlosser, A. Deninger, G. Birkl, G. Giuliani, and W. Elsäßer, The 24th International Conference on Advanced Laser Technologies 2016, Galway, Ireland (invited talk).

9. D. Laukhardt, T. Mohr, S. Blumenstein, and W. Elsäßer, „Single Pixel Imaging and its application in beam profile analysis “, DPG Früjahrstagung 2017, Mainz, Germany, (talk).

10. T. Mohr, and W. Elsäßer, „Single pixel detection tomographic terahertz imaging“, Conference on Lasers and electro-optics 2017, Munich, Germany, (poster).

11. T. Mohr, and W. Elsäßer, „Two novel experimental schemes for terahertz tomography“, 19th International Conference on Transparent Optical Networks 2017, Girona, Spain, (invited talk).

12. A. Gollert, D. Laukhardt, T. Mohr, S. Blumenstein, A. Herdt, and W. Elsäßer, „Single Pixel Imaging and its application in beam profile analysis “, 12th International Symposium on Emerging and Industrial DLP Technology Applications 2017, Hanau, Germany, (talk).

13. T. Mohr, A. Herdt, and W. Elsäßer, „2D Terahertz-Tomografie mittels Single-Pixel Bildgebungsverfahren am Bruker Vertex 80v “, Bruker Anwendertreffen 2017, Ettlingen, Germany (talk).

14. A. Herdt, T. Mohr, D. Lenstra, and W. Elsäßer, „Injection dynamics of mutually delay-coupled non-identical quantum cascade lasers “, International Symposium on Physics and Applications of Laser Dynamics 2017, Paris, France (talk).

Summer schools

1. 20.-24. Mai 2013: TERA-MIR Radiation: Materials, Generation, Detection and Applications, „Determination of optical material parameters in the MIR and THz regime using ellipsometry“, (poster).

2. 04.-10. Juli 2015: 25th International Travelling Summer School on Microwaves and Lightwaves, „Terahertz homodyne self-mixing and its application to two-dimensional tomographic terahertz imaging“, (talk).

Supervised Theses

- Sanketkumar Patel, „Relative intensity noise and mode stability of an external cavity diode laser“, Technische Universität Darmstadt, M.Sc. 2016.
- Andreas Herdt, „Novel Mid-Infrared Gas Sensor Based On Mutually Coupled Quantum Cascade Lasers“, Technische Universität Darmstadt, M.Sc. 2017.
- Daniel Laukhardt, „Untersuchungen zum Single Pixel Bildgebungsverfahren und dessen Anwendung in der Strahlprofilanalyse“, Technische Universität Darmstadt, B.Sc. 2017.

Curriculum Vitae

Persönliche Daten

Till Mohr
geboren am 02.02.1985 in Frankfurt am Main

Ausbildung

07/2001 bis 06/2004	Alfred-Delp-Schule, Dieburg Allgemeine Hochschulreife

Hochschulausbildung

10/2005 bis 02/2010	Technische Universität Darmstadt Bachelor of Science Physik
04/2010 bis 09/2012	Technische Universität Darmstadt Master of Science Physik
01/2013 bis 12/2017	Technische Universität Darmstadt Promotion

Danksagung

An dieser Stelle möchte ich mich bei all denen bedanken, die mich während meiner Promotionszeit begleitet und unterstützt haben.

Herrn Prof. Dr. Wolfgang Elsäßer danke ich, dass er mir die Durchführung meiner Promotion in seiner Arbeitsgruppe Halbleiteroptik an der Technischen Universität Darmstadt ermöglicht hat. Besonders möchte ich Ihm danken für die exzellente Betreuung und die Unterstützung meiner Arbeit. In der Zeit meiner Promotion konnte ich viel von Ihm lernen und wurde stets dazu ermutigt eigenverantwortlich wissenschaftlich zu arbeiten.

Herrn Prof. Dr. Thomas Walther danke ich für das Interesse an dieser Arbeit und die Übernahme des Zweitgutachtens.

Ich danke allen Mitwirkenden des LOEWE Forschungsschwerpunktes "Sensors Towards Terahertz", in welchem ich einen Großteil meiner Promotion arbeiten durfte. Besonderer Dank gilt hierbei Prof. Dr. Norbert Nicoloso, der durch konstruktive Diskussionen zum Erfolg des Projekts beigetragen hat. Darüber hinaus gilt mein besonderer Dank Dr. Anselm Deninger und TOPTICA Photonics die mir durch eine Leihgabe ihrer PCAs die Umsetzung vieler Ideen ermöglicht haben.

Besonderer Dank gilt auch Dr. Martin Mikulics vom Forschungszentrum Jülich, der mir freundlicherweise seine PCA Chips zur Verfügung gestellt hat und Prof. Dr. Lambert Alff und Dr. Philipp Komissinskiy die mich bei der Kontaktierung dieser unterstützt haben.

Dr. Marcello Simonetta und Prof. Dr. Guido Giuliani von der Università di Pavia danke ich für die Kooperation und Ihre Unterstützung die zu der erfolgreichen Realisierung der HSM Methode beigetragen hat.

Ich danke den Mitarbeitern des Instituts für Angewandte Physik der Technischen Universität Darmstadt. Insbesondere danke ich Prof. Dr. Gerhard Birkl und Dr. Malte Schlosser dafür, dass Sie es mir überbrückungsweise ermöglicht haben zwei Ihrer ECDL Systeme für meine Experimente zu nutzen. Außerdem danke ich Holger John für viele konstruktive Gespräche und Prof. Dr. Reinhold Walser und Martin Sturm für die Einführung in ZEMAX.

Allen Mitarbeitern der feinmechanischen Werkstatt danke ich für die hervorragende Beratung und Herstellung vieler opto-mechanischer Komponenten.

Wolfgang Rök danke ich für die große Hilfsbereitschaft und stets kompetente Beratung bei Elektrotech-

nischen Problemstellungen.

Dr. Sébastien Blumenstein, Dr. Dominik Blömer, Dr. Stefan Breuer, Dr. Lukas Drzewietzki, Andreas Herdt, Dr. Andreas Molitor und Christoph Weber danke ich für die gemeinsame Doktorandenzeit und ihre vielen fachlich kompetenten Hilfestellungen und Ideen. Allen Kollegen der Arbeitsgruppe Halbleiteroptik danke ich darüber hinaus für zahlreiche Diskussionen und Anregungen und die stets angenehme Arbeitsatmosphäre.

Frau Maria Musso Pantaleo danke ich vielmals für die Unterstützung bei vielen Formalitäten und die Gespräche die durch Ihrer ehrliche direkte Art positiv geprägt wurden.

Mein größter Dank gilt meinen Eltern Günther und Ramona, meiner Partnerin Sarah und meinen Freunden. Vielen Dank für eure Unterstützung, euer Verständnis und eure Geduld. Ohne euch wäre das alles nicht möglich gewesen.